

See discussions, stats, and author profiles for this publication at: <https://www.researchgate.net/publication/269705642>

Mixed Galerkin and Least-Squares formulations for Isogeometric analysis

Thesis · March 2014

DOI: 10.13140/2.1.1546.1442

CITATIONS

11

READS

6,443

1 author:



[Chennakesava Kadapa](#)

Edinburgh Napier University

59 PUBLICATIONS 595 CITATIONS

[SEE PROFILE](#)

MIXED GALERKIN AND LEAST-SQUARES FORMULATIONS FOR ISOGEOMETRIC ANALYSIS

by

Chennakesava Kadapa

M.Tech (IIT Kanpur)

A thesis

submitted to Swansea University

in fulfilment of the requirements

for the Degree of

Doctor of Philosophy

Swansea University

2014

Declarations

1. This work has not previously been accepted in substance for any degree and is not being concurrently submitted in candidature for any degree.

Signed (candidate)

Date

2. This work is the result of my own work and investigation, except where otherwise stated. Other sources have been acknowledged by giving explicit references. A bibliography is appended.

Signed (candidate)

Date

3. I hereby give consent for my thesis, if accepted, to be available for photocopying and for inter-library loan, and for the title and summary to be made available to outside organisations.

Signed (candidate)

Date

Dedicated to
My parents

Acknowledgements

I would like to express my profound gratitude to my thesis supervisors Dr. Wulf Dettmer and Prof. Djordje Perić for their excellent guidance, invaluable suggestions, continuous encouragement, constructive criticism and openness to implement new ideas during the entire course of of this research work.

I am very thankful to College of Engineering for providing the financial support by awarding me the Zienkiewicz scholarship. My special thanks go to Dr. Dettmer for agreeing to work with me and recommending me for the scholarship. I would like to thank College of Engineering and the University as a whole for providing a very supportive and encouraging environment to carry out the research work.

I extend my thanks to all my colleagues with whom I had many interesting discussions and exchange of ideas regarding my research work. I would like to thank all my friends and all those who, directly or indirectly, made my stay in Swansea very enjoyable throughout the course of this work.

I am deeply grateful to my family for their constant support and motivation all the way through my career.

Last but not the least, I extend my thanks to the internet communities and open source software groups which provided an invaluable support and free software tools to enhance my skills that were substantially helpful in carrying out my research.

Abstract

This work is concerned with the use of isogeometric analysis based on Non-Uniform Rational B-Splines (NURBS) to develop efficient and robust numerical techniques to deal with the problems of incompressibility in the fields of solid and fluid mechanics. Towards this, two types of formulations, mixed Galerkin and least-squares, are studied.

During the first phase of this work, mixed Galerkin formulations, in the context of isogeometric analysis, are presented. Two-field and three-field mixed variational formulations — in both small and large strains — are presented to obtain accurate numerical solutions for the problems modelled with nearly incompressible and elasto-plastic materials. The equivalence of the two mixed formulations, for the considered material models, is derived; and the computational advantages of using two-field formulations are illustrated. Performance of these formulations is assessed by studying several benchmark examples. The ability of the mixed methods, to accurately compute limit loads for problems involving elasto-plastic material models; and to deal with volumetric locking, shear locking and severe mesh distortions in finite strains, is illustrated.

Later, finite element formulations are developed by combining least-squares and isogeometric analysis in order to extract the best of both. Least-squares finite element methods (LSFEMs) based on the use of governing differential equations directly — without the need to reduce them to equivalent lower-order systems — are developed for compressible and nearly incompressible elasticity in both the small and finite strain regimes; and incompressible Navier-Stokes. The merits of using Gauss-Newton scheme instead of Newton-Raphson method to solve the underlying nonlinear equations are presented. The performance of the proposed LSFEMs is demonstrated with several benchmark examples from the literature. Advantages of using higher-order NURBS in obtaining optimal convergence rates for non-norm-equivalent LSFEMs; and the robustness of LSFEMs, for Navier-Stokes, in obtaining accurate numerical solutions without the need to incorporate any artificial stabilisation techniques, are demonstrated.

Contents

1	Introduction	1
1.1	The Aim of the Thesis	6
1.2	Layout of the Thesis	6
2	NURBS and Isogeometric Analysis	8
2.1	A brief review of NURBS	8
2.1.1	Bézier curve	8
2.1.2	Rational Bézier curve	9
2.1.3	B-Spline basis functions	9
2.1.4	B-Spline curves	10
2.1.5	NURBS curves	11
2.1.6	NURBS in higher dimensions	11
2.2	NURBS refinement strategies	13
2.2.1	Knot insertion (or h -refinement)	13
2.2.2	Degree elevation (p -refinement)	14
2.2.3	k -refinement	15
2.3	NURBS with multiple patches	16
2.4	Isogeometric analysis — NURBS as approximating functions	17
2.4.1	NURBS to approximate field variables	19
2.4.2	Numerical integration	19
3	Formulation of Boundary Value Problems for Solids and Fluids	22
3.1	Kinematics	22
3.1.1	Deformation gradient	23
3.1.2	Strain measures	24
3.2	Stress measures	25
3.3	Equilibrium	26
3.4	Boundary conditions	27
3.5	Boundary Value Problem in solid mechanics	27
3.5.1	BVP in small strain regime	27
3.5.2	BVP in finite strain regime	28
3.6	Constitutive relations	28
3.6.1	Linear elasticity	29

3.6.2	Small strain elasto-plasticity	29
3.6.3	Hyperelastic materials	31
3.6.4	Large strain elasto-plasticity	32
3.7	BVP in fluid mechanics	32
4	Galerkin formulation	34
4.1	Galerkin formulation in small strains	34
4.1.1	Displacement formulation	36
4.1.2	Two-field mixed variational formulation	38
4.1.3	Three-field mixed variational formulation	39
4.2	Galerkin formulation in finite strains	41
4.2.1	Displacement formulation	41
4.2.2	Two-field mixed variational formulation	42
4.2.3	Three-field mixed variational formulation	43
4.2.4	Stability conditions for mixed formulations	45
4.3	NURBS spaces for mixed methods	46
4.3.1	Solving discrete equations arising from mixed formulations	47
4.3.2	Equivalence of the two mixed formulations	47
5	Galerkin formulation - Numerical Examples	51
5.1	Numerical examples - small strain	51
5.1.1	Elastic plate with a circular hole	51
5.1.2	Thick cylinder under internal pressure	54
5.1.3	Cook's membrane with nearly incompressible linear elastic material	57
5.1.4	Strip Footing collapse	59
5.1.5	Double-edge notched specimen	66
5.2	Numerical examples - Finite strain	68
5.2.1	Cook's membrane with Neo-Hookean material	68
5.2.2	Cook's membrane with von Mises elasto-plastic material	71
5.2.3	Compression of a plane-strain block	73
5.2.4	Plane strain localization problem	76
5.2.5	Pinched Torus	78
5.2.6	Torsion of a square prism	80
5.2.7	Necking of a cylindrical bar	81
5.2.8	Compression of a block in three dimensions	83
5.2.9	Bending of a thick cylindrical shell	85
6	Least-Squares formulation	89
6.1	Formulation of general LSFEMs	89
6.2	Boundary conditions and the issue of norm-equivalence	91
6.3	Solid Mechanics	92
6.3.1	Governing equations	92
6.3.2	Compressible linear elasticity	93

6.3.3	Nearly incompressible linear elasticity	95
6.3.4	Compressible nonlinear elasticity	97
6.3.5	Nearly incompressible non-linear elasticity	100
6.4	Fluid Mechanics	102
6.4.1	The incompressible Navier-Stokes	102
7	Least-Squares Formulation - Numerical Examples	104
7.1	NURBS spaces	104
7.2	Numerical Examples - Solid Mechanics	105
7.2.1	Cook's membrane with nearly incompressible linear elasticity	105
7.2.2	1-D bar under body force	106
7.2.3	Plane-strain block under body force	109
7.2.4	Cook's membrane with compressible Neo-Hookean material	112
7.2.5	Cook's membrane with nearly incompressible Neo-Hookean material	114
7.3	Numerical Examples - Fluid Mechanics	115
7.3.1	Kovaszny flow	115
7.3.2	Flow in lid driven cavity	119
8	Conclusions	123
8.1	Achievements and Conclusions	123
8.2	Scope for future research work	125
A	Newton-Raphson method	126
B	Computing second derivatives	128
B.1	For an uniform cartesian grid	129

List of Figures

2.1	NURBS objects in 1D, 2D and 3D.	12
2.2	Knot insertion	14
2.3	Degree elevation	15
2.4	Combined p - and h - refinements.	16
2.5	A plate with two holes modelled using two NURBS patches shown in green and blue colours.	17
2.6	Analogy between <i>iso-geometric</i> analysis and the classical finite element analysis.	18
2.7	Mapping of the physical element to parametric domain and then to master element space.	20
3.1	A general motion of a deformable body in space.	23
3.2	Components of Cauchy stress in three-dimensions.	26
4.1	B-Spline basis functions for 1D patch of 4-elements with all the internal knots having multiplicity = 1. All the spaces have $\mathcal{C}^{a-1}/\mathcal{C}^{a-2}$ continuity.	47
5.1	Plate with a circular hole: geometry, loading and material prop- erties	52
5.2	Plate with a circular hole: coarse mesh and its control net. . . .	52
5.3	Plate with a circular hole: meshes generated by h -refinement, with reparameterization in first knot direction.	53
5.4	Plate with a circular hole: contour plots of stress σ_{xx} obtained with Q_2 NURBS.	53
5.5	Thick cylinder under internal pressure: geometry, loading and material properties.	54
5.6	Thick cylinder under internal pressure.	55
5.7	Thick cylinder under internal pressure: partly plastified cross- section.	55
5.8	Thick cylinder under internal pressure: applied pressure versus displacement.	55
5.9	Thick cylinder under internal pressure: von Mises stress at dif- ferent load levels for 32×32 mesh with Q_2 NURBS.	56
5.10	Thick cylinder under internal pressure: hoop and radial stress distribution along radial coordinate.	56

5.11	Cook's membrane: geometry, loading and material properties . .	57
5.12	Cook's membrane: meshes generated by h -refinement	58
5.13	Cook's membrane with linear elastic material: vertical displacement of the top right corner against number of elements per side.	58
5.14	Cook's membrane with linear elastic material: hydrostatic pressure for mesh-5 with cubic NURBS.	59
5.15	Cook's membrane with linear elastic material: von Mises stress for mesh-5 with cubic NURBS	59
5.16	Strip footing collapse: a.) Geometry, loading, boundary conditions and material properties b.) Initial control mesh of two patch geometry.	60
5.17	Strip footing collapse: meshes considered for the analysis.	60
5.18	Strip footing collapse - coarse mesh: load-displacement curve. . .	61
5.19	Strip footing collapse - coarse mesh: equivalent plastic strain with displacement formulation.	62
5.20	Strip footing collapse - coarse mesh: equivalent plastic strain with mixed formulation.	62
5.21	Strip footing collapse - coarse mesh: hydrostatic pressure with displacement formulation.	63
5.22	Strip footing collapse - coarse mesh: hydrostatic pressure with mixed formulation.	63
5.23	Strip footing collapse - fine mesh: load-displacement curve. . . .	64
5.24	Strip footing collapse - fine mesh: equivalent plastic strain with displacement formulation.	65
5.25	Strip footing collapse - fine mesh: equivalent plastic strain with mixed formulation.	65
5.26	Double-edge notched tensile specimen: geometry, loading and material properties.	66
5.27	Double-edge notched specimen: load-displacement curve.	67
5.28	Double-edge notched specimen: equivalent plastic strain with displacement formulation.	67
5.29	Double-edge notched specimen: equivalent plastic strain with mixed formulation.	68
5.30	Cook's membrane with Neo-Hookean material: convergence of vertical displacement of top right corner with respect to number of elements.	69
5.31	Cook's membrane with Neo-Hookean material: hydrostatic pressure for mesh-5 with Q_3 NURBS.	70
5.32	Cook's membrane with Neo-Hookean material: equivalent stress for mesh-5 with Q_3 NURBS.	70
5.33	Cook's membrane with elasto-plastic material: convergence of vertical displacement of top right corner with respect to number of elements.	71

5.34	Cook's membrane with elasto-plastic material: equivalent plastic strain for mesh-5 with Q_3 NURBS.	72
5.35	Cook's membrane with elasto-plastic material: von Mises stress for mesh-5 with Q_3 NURBS.	73
5.36	Plane-strain block under compression: geometry, loading and boundary conditions.	74
5.37	Plane-strain block under compression: compression level for Q_1/Q_0 NURBS compared to LQ-Fbar.	75
5.38	Plane-strain block under compression: compression level for different orders of NURBS under different loading conditions. . . .	75
5.39	Plane-strain block under compression: contour plots of hydrostatic pressure for 32×32 mesh with Q_3 NURBS for $p/p_0=60$. .	76
5.40	Plane-strain block under compression: contour plots of von Mises equivalent stress for 32×32 mesh with Q_3 NURBS for $p/p_0=60$	76
5.41	Necking of an elasto-plastic strip: geometry, loading and boundary conditions.	77
5.42	Necking of an elastoplastic strip.	77
5.43	Necking of an elasto-plastic strip: deformed shape and von Mises stress for Q_3/Q_2 NURBS.	78
5.44	Pinched torus: geometry, loading and boundary conditions. . . .	79
5.45	Pinched torus: load-displacement curve.	79
5.46	Pinched torus: contour plots of Cauchy stress component σ_{yy} . .	80
5.47	Torsion of a prism: (a) Geometry, loading and boundary conditions, (b) An intermediate deformed shape and (c) von Mises stress contour plot at 720 deg rotation for Q_2/Q_1 NURBS. . . .	81
5.48	Necking of a cylindrical bar.	82
5.49	Necking of a cylindrical bar: variation of necking force with respect to applied displacement.	82
5.50	Necking of a cylindrical bar: variation of neck displacement with respect to applied displacement.	83
5.51	Block under compression in 3D: boundary conditions and loading. 84	
5.52	Block under compression in 3D: comparison, of convergence of compression level, between Q_1/Q_0 NURBS and standard F-bar element.	84
5.53	Block under compression in 3D: compression level for different orders of NURBS.	85
5.54	Block under compression in 3D: contour plots of vertical displacement (UZ) and von Mises equivalent stress.	85
5.55	Thick cylindrical shell in 3D: geometry, loading and material properties.	86
5.56	Thick cylindrical shell in 3D: boundary conditions and a typical mesh used for the analysis.	87

5.57	Thick cylindrical shell in 3D: vertical displacement of point A with respect to number of elements in the circumferential direction for different order of NURBS with displacement and mixed formulation.	87
5.58	Thick cylindrical shell in 3D: contour plots of vertical displacement (uz) and shear stress σ_{xy}	88
7.1	Cook's membrane with nearly incompressible linear elasticity: vertical displacement of the top right corner against number of elements per side with different orders of NURBS basis functions.	106
7.2	Cook's membrane with nearly incompressible linear elasticity: contour plots of hydrostatic pressure and von Mises stress for mesh-5 with Q_3 NURBS.	106
7.3	1-D bar under body force: geometry, loading and boundary conditions.	107
7.4	1-D bar under body force: displacement of mid point against number of elements per side with different orders of NURBS basis functions with LSFEM LSFEM-CC and LSFEM-RC. . . .	107
7.5	1-D bar under body force: displacement of mid point against number of elements per side with different orders of NURBS basis functions with LSFEM-CC and GFEM.	108
7.6	Plane-strain block under body force: geometry, loading and boundary conditions.	109
7.7	Plane-strain block under body force: displacement of mid point against number of elements per side, for different orders of NURBS, with LSFEM-CC and GFEM; Dirichlet boundary conditions are enforced strongly for GFEM and weakly for LSFEM-CC.	110
7.8	Plane-strain block under body force: convergence of Gauss-Newton iterations for two different discretisations with LSFEM-CC; Dirichlet boundary conditions are enforced weakly.	111
7.9	Plane-strain block under body force: downward displacement of mid point against number of elements per side with different orders of NURBS with LSFEM-CC and GFEM; Dirichlet boundary conditions are enforced strongly for both GFEM and LSFEM-CC.	111
7.10	Plane-strain block under body force: contour plots of displacements, shear stress and von Mises stress for 32×32 mesh for Q_4 NURBS with LSFEM-CC; Dirichlet boundary conditions are enforced weakly.	112
7.11	Cook's membrane with compressible Neo-Hookean material: vertical displacement of the top right corner against number of elements per side with different orders of NURBS basis functions with LSFEM-CC and GFEM.	113

7.12	Cook's membrane with compressible Neo-Hookean material: convergence of Gauss-Newton iterations for two different discretisations with LSFEM-CC.	113
7.13	Cook's membrane with nearly incompressible Neo-Hookean material: vertical displacement of the top right corner against number of elements per side with different orders of NURBS.	114
7.14	Cook's membrane with nearly incompressible Neo-Hookean material: contour plots of hydrostatic pressure and von Mises stress for mesh-5 with Q_3 NURBS.	115
7.15	Kovaszny flow: error norms for $Re = 40$	117
7.16	Kovaszny flow: Contour plots for 20×20 mesh with Q_2 and Q_3 NURBS.	118
7.17	Lid driven cavity: a.) Geometry and boundary conditions and b.) A typical mesh used for the analysis.	119
7.18	Lid driven cavity: velocity profiles for 20×20 mesh with $Re = 100$.	120
7.19	Lid driven cavity: velocity profiles for 40×40 mesh with $Re = 1000$	120
7.20	Lid driven cavity: velocity profiles for 150×150 mesh with $Re = 10000$	121
7.21	Lid driven cavity: streamlines and pressure contour lines for 20×20 mesh with Q_4 NURBS for $Re = 100$	121
7.22	Lid driven cavity: streamlines and pressure contour lines for 40×40 mesh with Q_4 NURBS for $Re = 1000$	122
7.23	Lid driven cavity: streamlines and pressure contour lines for 150×150 mesh with Q_4 NURBS for $Re = 10000$	122

Chapter 1

Introduction

Characterisation of the behaviour of systems in nature, ranging from the motion of atoms to the movement of stars, can be formulated by differential equations. Based on the dependence on time these differential equations can be classified into Boundary Value Problems (BVPs), Initial Value Problems (IVPs) and a more general Initial Boundary Value Problems (IBVPs). Obtaining the solution of differential equations is one of the important and classical branches of mathematics, which dates back to several centuries. Analytical solution techniques can only be used for some simple problems involving simple geometries but they are useless for complex problems encountered in real life scenarios. But the invention of numerical techniques to obtain solutions of differential equations has made it possible to obtain solutions of complex problems. The invention of numerical computing machines has changed the paradigm of numerical techniques like never imagined before and lead to newer and more efficient techniques. Among the several numerical methods Finite Difference Method (FDM) [83, 88], Finite Element Method (FEM) [7, 40, 68, 92], Finite Volume Method (FVM) [50, 89], Boundary Element Method (BEM) [3, 10, 22, 35, 72] and meshless methods [28, 51, 53, 54] were introduced to solve the differential equations over complicated geometries which are often encountered in science and engineering.

Engineering design is a very complex and time consuming process. Until recently complete design was done in drawing rooms using pencils and drawing boards and then the finalised design is sent to the prototype testing to check if the design sustains the intended loading environment. This process was mainly limited by the human ability to perform complicated calculations and the amount of time and money required for prototype testing. So, there was little scope for optimisation of designs. But, the invention of numerical computing machines has totally changed the paradigm of engineering design by taking burden of computations away from the engineers and allowing them to perform optimisations, thereby enabling them to create better designs and/or reduce the total time.

Modern day engineering design has turned into *simulation driven design* where Computer Aided Design (CAD) and/or Computer Aided Engineering

(CAE) tools are used to perform numerical simulations in order to enhance productivity and produce better designs. Engineers of today do indeed have a wide range of such simulation tools to deploy throughout the product development process. Some of the more powerful of these tools include: first-pass tools for performing analysis early in the design cycle; advanced optimization technology for refining product designs; and virtual prototyping methods for evaluating how products will perform in actual operating conditions. Moreover, the ever increasing need for safety, norms induced by regulatory authorities to control exhausts, use of advanced materials etc., push the limits of design and hence, require more and more numerical simulations. A complete design cycle ranges from several days to several decades depending upon the complexity of the system to be designed; and amount and types of numerical simulations to be performed. An understanding of modern day engineering design cycle shows that it can be divided into three main steps.

- a.) Modelling in CAD.
- b.) Meshing and
- c.) Analysis and post-processing of results.

In many cases these three steps are applied in an iterative manner, during product optimisation, to improve the performance by creating better designs. Experience with the industry reveals that the first two steps consume about 80% of the total time because of the several underlying difficulties. Cleaning up the CAD geometry and developing meshes for complicated geometries with intricate shapes is often an annoying and time consuming task. Once a mesh is developed the underlying geometry model is discarded as it has nothing to do with the analysis. When a design fails during the analysis stage the design team modifies the design and new design configuration is sent to the analysis team to perform the analysis. During every such modification the mesh has to be modified accordingly to incorporate design changes. This mesh modification is often time consuming and in some cases, meshes developed once are to be discarded and completely new meshes might need to be created. This way, of using different file systems in design and analysis teams, creates a bottleneck in the design cycle and hampers seamless movement of data between the two teams which causes severe ambiguity issues and leads to delays.

In addition to the above mentioned difficulties, another disadvantage of conventional FEM is that the discretisation only approximates geometry, which introduces a geometry error into the numerical solution. So, if a numerical analysis technique, which can make use of the geometry definition, is developed many of the issues discussed above can be eliminated, by paving the way for better designs and/or reduction in the design cycle times. With this motivation in view Hughes *et al.* [29, 41] introduced a numerical technique called isogeometric analysis (IGA) based on Non-Uniform Rational B-Splines (NURBS) which are the standard mathematical tools used to represent geom-

etry in CAD. IGA uses the definition of geometry in CAD models for the purpose of analysis. Several advantages of IGA are,

- a.) Exact representation of the geometry in most cases. So the numerical solution is free of errors due to mismatch in geometry.
- b.) As the discretisation is linked directly to the geometry mesh modifications are quite easy and can be automated.
- c.) The data transfer between different teams would be seamless as a master CAD model can be maintained and circulated among several teams. A single file serves the purpose of geometry and mesh as well.
- d.) Great improvements in terms of accuracy as NURBS help attain higher continuity across element boundaries via a new refinement scheme — called k -refinement — which not only increases the continuity across element boundaries but also minimises the number of additional degree of freedom (DOF).

The IGA has proven to be an efficient alternative for the conventional FEM. In the literature, this technique has been applied to study several phenomenon in various fields of physics and engineering: Bazilevs *et al.* studied fluid-structure interaction [8] using isogeometric analysis; Cottrell *et al.* applied isogeometric analysis to structural vibrations [30]; and Gomez *et al.* extended this technique to phase-transition phenomenon [37]. But only a few papers [33, 57, 87] have reported on the use of IGA to the problems involving incompressible and nearly incompressible materials, especially elasto-plastic materials.

Simulations involving incompressible or nearly incompressible materials — like rubber, elastomers, and elasto-plastic materials — are very common in engineering analysis. The foremost important problem with such materials is "volumetric locking", which arises due to incompressibility. When Poisson's ratio approaches 0.5 or when the material is in plastic zone the material becomes very stiff to further application of load. For such problems, use of finite element formulations based on the pure displacements show very stiff behaviour and gives less accurate results. In order to obtain results with the desired accuracy one has to either use an extremely fine mesh or develop special treatments to circumvent or control the problem of locking. In general, remedies followed to overcome locking are: using reduced or selectively reduced integration [40]; use of B-bar formulation for small-strain problems [40, 82, 92] and F-bar formulation for large-strain problems [60, 62]; and use of hybrid or enhanced strain or enhanced stress elements [4, 64, 78, 79, 81].

Despite its advantages, NURBS based isogeometric analysis with displacement based Galerkin formulation, is not an ideal tool to deal with difficulties posed by incompressibility as it still suffers from locking phenomenon and require the above mentioned special treatments to deal with incompressibility in solid mechanics. Towards this, Elguedj *et al.* [33] introduced $\bar{\mathbf{B}}$ and $\bar{\mathbf{F}}$

projection methods; and Taylor [87] and Mathisen *et al.* [57] extended 3-field mixed variational formulations. But, the mathematics of $\bar{\mathbf{B}}$ and $\bar{\mathbf{F}}$ projection methods is too complicated and these methods are computationally expensive (because of the number of terms involved in stiffness matrix and force vectors and matrix inversions that need to be performed at every Gauss point); and the 3-field formulation increases the number of DOF substantially for higher order NURBS because of the tensor-product structure and therefore, requires more computational resources and solver time. Moreover, for most of the material models encountered in engineering simulations, 3-field formulations prove to be superfluous and 2-field formulations are sufficiently generic. These factors served as a motivation to extend the 2-field formulations to NURBS based isogeometric analysis.

Two-field mixed formulations can be developed based either on the classical Galerkin formulations or the less-popular least-squares formulations. In this work NURBS based two-field mixed methods based on both the Galerkin and least-squares formulations are studied. During the first phase of this work two-field mixed Galerkin formulations are implemented for solid mechanics. Performance of these methods is illustrated with several benchmark examples.

Mixed Galerkin formulations, however, still pose difficulties when applied to isogeometric analysis. The most important of them include: unsymmetrical matrix systems when applied to non-self-adjoint systems; effective stabilisation techniques for advection dominated problems in fluid mechanics [41]; and strategies to circumvent or satisfy Ladizhenskaya-Babuška-Brezzi (LBB) or inf-sup condition in both fluid and solid mechanics [33, 41, 87, 57]. Many of the strategies developed for Galerkin finite element formulations with Lagrangian basis functions have to be reformulated to overcome those difficulties. So, as an alternative to overcome these difficulties Least-Squares finite element methods (LSFEMs) are applied to NURBS based IGA in Chapters 6 and 7 of this work.

Until recently, LSFEMs are less popular compared to their Galerkin counterparts because they either require a high degree of continuity of the basis functions or, lead to systems with more number of DOF when field equations are written as an equivalent lower-order system. However, LSFEMs result in symmetric and positive definite matrix systems even for non-self adjoint systems and are not subjected to LBB condition. These advantages and increase in computational power have attracted scientists and engineers towards LSFEMs, over the last decade. Bochev and Gunzburger [13, 14, 15, 16, 17, 18, 19] have extensively studied and developed mathematical theory of LSFEMs; Bo-Nan Jiang *et al* [42, 43, 45, 46, 91], Bramble *et al* [21], Pontaza and Reddy [67, 66], and others [58, 31] studied LSFEMs for the problems of fluid flow; and the application of LSFEM to the problems of elasticity, elasto-plasticity and nonlinear elasticity is presented in [44, 47, 24, 25, 26, 75, 84, 85, 56].

However, majority of least-squares based finite element formulations encountered in the literature use equivalent lower order system of equations by introducing auxiliary variables. This is because of the fact that straight-forward

implementation of LSFEMs to higher-order BVPs requires higher continuities in the entire domain, compared to the GFEMs where the continuity requirement is weakened using integration by parts. The degree of continuity of the basis functions should be at least equal to the degree of the highest derivative in the governing equations reduced by one; and constructing such basis function was deemed to be extremely difficult. Moreover, the continued trend to use standard Lagrange basis functions, which are only C^0 continuous across element boundaries, has forced researchers to reformulate the governing equations into equivalent first-order equation systems by introducing auxiliary variables. But it is clearly evident that this approach increases the size of the system substantially and requires larger computational resources.

Another important aspect to be concerned with LSFEMs is norm equivalence. Norm-equivalent LSFEMs result in optimal convergence rates and non-norm-equivalent formulations result in sub-optimal convergence. Norm-equivalent LSFEMs are constructed by defining norms of boundary residuals in appropriate fractional subspaces or by defining spectrally equivalent norms. But, both approaches are extremely difficult and highly impractical to implement in a finite element setting. Pontaza and Reddy [66] have shown that optimal convergence rates can be achieved even with non-norm-equivalent LSFEMs by using higher order basis functions.

The motivation to study NURBS based LSFEMs stems from the following arguments:

- LSFEMs always result in an unconstrained minimisation problem but never a saddle-point problem. So, they are not subjected to the LBB condition. Therefore, equal order basis functions can be used for all the independent variables.
- The resulting matrix systems are always symmetric and positive definite. This has a far-reaching effect in large-scale simulations.
- In case of fluid flow problems, no stabilisation techniques are required in order to obtain oscillation-free solutions. So, independent of free parameters to be tuned, LSFEMs result in very robust solution methods.
- NURBS offer basis functions with higher-order continuities across element boundaries, which makes NURBS an ideal tool to apply straightforward LSFEMs to boundary value problems, thereby eliminating the need to introduce auxiliary variables.
- Use of higher-order NURBS might improve convergence rates for non-norm-equivalent LSFEMs.

Study of properties of such a computational tool satisfying the above arguments is always alluring. NURBS based LSFEMs are developed for some selected problems in solid and fluid mechanics; and their performance is illustrated with several benchmark problems in the literature.

1.1 The Aim of the Thesis

The aim of this thesis is to develop robust, accurate and efficient numerical schemes for the solution of BVPs in solid and fluid mechanics using NURBS based isogeometric analysis. During the first phase of this work, the focus is on applying Galerkin based mixed formulations to deal with nearly incompressible materials in both small and finite strain regimes. Later, the objective is to develop finite element formulations by combining NURBS and least-squares – for nearly incompressible linear and nonlinear elasticity; and incompressible fluid flow – in order to extract the best of both.

1.2 Layout of the Thesis

Chapter 2. A brief discussion about preliminary concepts useful in modelling geometry using NURBS is given. Several strategies used to refine the discretisation of the geometry are discussed. Use of NURBS as basis functions to approximate the field variables towards obtaining numerical solutions of BVPs is discussed.

Chapter 3. In this chapter, important quantities used in deriving the governing differential equations are introduced and the governing differential equations characterising the behaviour of fluids and solids are presented. Several constitutive laws are also discussed; the content is limited to the type of material models used in the present work.

Chapter 4. Formulation of Galerkin based finite element methods for both small and finite strain regimes to deal with the problems of incompressibility is presented. Underlying difficulties in solving matrix systems resulting from mixed methods are discussed and methods to overcome those difficulties are presented. NURBS spaces used as approximation functions for the numerical solutions using mixed methods are presented. Then the equivalence of 2-field and 3-field mixed formulations for the material models considered in the current analysis is demonstrated.

Chapter 5. Numerical examples to demonstrate the performance of NURBS based Galerkin formulations are presented. Several classical benchmark problems are studied to demonstrate the robustness and accuracy of the mixed formulations in both the small and finite strains, under different loading conditions – compression, elongation and twisting. The ability of the mixed methods to calculate the limit loads in case of elasto-plastic materials is demonstrated. The superiority of the mixed methods for problems under severe deformations is demonstrated with torsion of a square prism example.

Chapter 6. An introduction to least-square based finite element formulations is given and their advantages and disadvantages over the Galerkin formulations are discussed. Then, formulation of finite element methods with least-squares

is presented in a general sense. Later, least-square based finite element formulations are developed for the problems involving compressible and nearly incompressible elasticity in both the small strain and finite strain regimes. Finally, least-squares based finite element formulations are developed for the incompressible Navier-Stokes equations for fluid flow.

Chapter 7. Numerical examples for least-square based finite element formulations are presented. One-dimensional bar under body force is studied to study the relative performances of least-square based formulations in current and reference configurations. Two-dimensional block under body force allows for the study of the effect of application of Dirichlet boundary conditions in strong and weak sense. Cook's membrane with different material models is studied in order to demonstrate the performance of the proposed methods. Later, Kovasznay flow problem, with an analytical solution, is studied and error estimates are presented to illustrate the performance of least-square based formulations to incompressible Navier-Stokes. Finally, the classical problem of flow in a lid-driven cavity is analysed for different Reynold's numbers.

Chapter 8. A summary of the important observations made during the course of this work and achievements of this work is given and conclusions are drawn. The thesis is concluded with suggestions and discussion about the scope for future research.

Chapter 2

NURBS and Isogeometric Analysis

In this chapter a brief overview of NURBS and the construction of geometry using NURBS is presented. Several refinement strategies and the use of NURBS as approximating functions in the isogeometric analysis are discussed.

2.1 A brief review of NURBS

NURBS are standard tools in CAD and computer graphics (CG) to model complex geometries. NURBS represent a generalisation of B-Splines. B-Splines are parametric piecewise polynomial curves which are composed of linear combinations of B-Spline basis functions; and B-Splines are a generalisation of Bézier curves. This section gives a brief overview about B-Spline basis functions and constructing geometries using NURBS. For elaborate discussion on these topics the reader is suggested to refer to [34, 65, 71].

2.1.1 Bézier curve

The Bézier curve is the most utilized representation of geometry in computer graphics and geometric modelling. A Bézier curve is usually defined by a set of control points $\{P_0, P_1, \dots, P_n\}$. An n th-degree Bézier curve is defined by,

$$\mathbf{C}(\xi) = \sum_{i=0}^n B_{i,n}(\xi) P_i \quad \text{for } 0 \leq \xi \leq 1 \quad (2.1)$$

where $B_{i,n}$ are the basis functions — the classical n th-degree Bernstein polynomials — given by,

$$B_{i,n}(\xi) = \frac{n!}{i!(n-i)!} \xi^i (1-\xi)^{n-i} \quad (2.2)$$

2.1.2 Rational Bézier curve

A regular Bézier curve is not sufficient to model conic sections and one has to use rational Bézier curves for that purpose. An n th-degree rational Bézier curve is defined by,

$$\mathbf{C}(\xi) = \sum_{i=0}^n R_{i,n}(\xi) P_i \quad \text{for } 0 \leq \xi \leq 1 \quad (2.3)$$

where $R_{i,n}(\xi)$ are the rational basis functions, given as,

$$R_{i,n}(\xi) = \frac{B_{i,n}(\xi) w_i}{\sum_{j=0}^n B_{j,n}(\xi) w_j} \quad (2.4)$$

and w_i are the scalars — called as *weights*. Rational curves have an elegant geometric interpretation that yield efficient processing and compact data storage. The idea, here, is to use *homogeneous coordinates*, see [65], to represent a rational curve in n -dimensional space as a polynomial curve in $(n+1)$ -dimensional space. In homogeneous coordinates, a rational Bézier curve is defined as,

$$\mathbf{C}(\xi) = \sum_{i=0}^n B_{i,n}(\xi) P_i^w \quad \text{for } 0 \leq \xi \leq 1 \quad (2.5)$$

where $P_i^w = (w_i x_i, w_i y_i, w_i z_i, w_i)$ are the *weighted control points* which are calculated from control points $P_i = (x_i, y_i, z_i)$ and weights w_i . Use of homogeneous coordinates offers many advantages in mathematical treatment as well as programming.

2.1.3 B-Spline basis functions

A B-Spline basis function consists of a number of piecewise polynomials joined with the desired continuity. The definition of a B-Spline polynomial requires a *knot* vector and the order of the polynomial. A *knot* vector is a set of non-decreasing sequence of real numbers and each real number in that set is called a *knot*. For a given *knot* vector, $\Xi = \{\xi_0, \xi_1, \dots, \xi_m\}$ and degree of polynomial p (order= $p+1$), the i th B-Spline basis function, denoted by $N_{i,p}(\xi)$, is defined as,

$$N_{i,0}(\xi) = \begin{cases} 1 & \text{if } \xi_i \leq \xi \leq \xi_{i+1} \\ 0 & \text{otherwise} \end{cases}$$

$$N_{i,p}(\xi) = \frac{\xi - \xi_i}{\xi_{i+p} - \xi_i} N_{i,p-1}(\xi) + \frac{\xi_{i+p+1} - \xi}{\xi_{i+p+1} - \xi_{i+1}} N_{i+1,p-1}(\xi) \quad (2.6)$$

Some of the important properties of B-Spline basis functions are

1. Local support: $N_{i,p}(\xi) = 0$ if ξ is outside the interval $[\xi_i, \xi_{i+p+1})$.
2. In any given knot span, $[\xi_j, \xi_{j+1})$, at most $(p+1)$ of the $N_{i,p}$ are non-zero, namely the functions $N_{j-p,p}, \dots, N_{j,p}$.

3. Non-negativity: Each basis function is non-negative, i.e., $N_{i,p}(\xi) \geq 0$ for all i, p , and ξ . (This has important consequence in dynamic analyses, because the coefficients of mass matrix computed from B-Spline basis functions are non-negative).
4. Partition of unity: For any given value of ξ , the sum of all the basis function is equal to unity. i.e., $\sum_{i=0}^n N_{i,p}(\xi) = 1, \forall \xi$.
5. All derivatives of $N_{i,p}(\xi)$ exist in the interior of a knot span. At the knot, $N_{i,p}(\xi)$ is $(p - k)$ times continuously differentiable, where k is the multiplicity of the knot.
6. For a knot vector with $(m + 1)$ knots and degree of polynomial p there are $n + 1$ basis functions, where $n = m - p - 1$.

2.1.4 B-Spline curves

A p th-degree B-Spline curve is defined as,

$$\mathbf{C}(\xi) = \sum_{i=0}^n N_{i,p}(\xi) \mathbf{P}_i \quad (2.7)$$

where, \mathbf{P}_i are the control points, and $N_{i,p}(\xi)$ are the B-Spline basis functions of degree p , defined on a knot vector,

$$\Xi = \{\underbrace{a, \dots, a}_{p+1}, \xi_{p+1}, \dots, \xi_{m-p-1}, \underbrace{b, \dots, b}_{p+1}\}$$

consisting of $(m + 1)$ knots. Unless stated otherwise, it is assumed that $a = 0$ and $b = 1$. Some of the important properties of B-Spline curves are:

1. If $n = p$ and $\Xi = \{0, \dots, 0, 1, \dots, 1\}$, then $\mathbf{C}(\xi)$ is a Bézier curve.
2. $\mathbf{C}(\xi)$ is a piecewise polynomial curve, since $N_{i,p}(u)$ are piecewise polynomials).
3. End-point interpolation: $\mathbf{C}(0) = \mathbf{P}_0$ and $\mathbf{C}(1) = \mathbf{P}_n$. (This property is very important because it enables straightforward application of Dirichlet boundary conditions.)
4. Affine invariance: An affine transformation of a B-Spline curve is obtained by applying transformation to its control points.
5. Local modification scheme: Moving a control point \mathbf{P}_i changes $\mathbf{C}(\xi)$ only in the interval $[\xi_i, \xi_{i+p+1})$.
6. Variation diminishing property: No plane has more intersections with the curve than with the control polygon.

7. Since $\mathbf{C}(\xi)$ is just a linear combination of the basis functions $N_{i,p}(u)$, the continuity and differentiability of $\mathbf{C}(\xi)$ follow from that of the $N_{i,p}(\xi)$. Thus, $\mathbf{C}(\xi)$ is infinitely differentiable in the interior of knot intervals, and it is at least $(p - k)$ times continuously differentiable at a knot of multiplicity k .

2.1.5 NURBS curves

One of the greatest advantages of NURBS is their capability of precisely representing conic sections and circles, as well as free-form curves and surfaces. NURBS curves contain non-rational B-Splines and rational and non-rational Bézier curves as special cases. A p th-degree NUBRS curve is defined as,

$$\mathbf{C}(\xi) = \sum_{i=0}^n R_{i,p}(\xi) \mathbf{P}_i \quad \text{for } a \leq \xi \leq b \quad (2.8)$$

where, \mathbf{P}_i are the control points, and $R_{i,p}(\xi)$ are the p th-degree rational basis functions, defined as,

$$R_{i,p}(\xi) = \frac{N_{i,p}(\xi)w_i}{\sum_{j=0}^n N_{j,p}(\xi)w_j} \quad (2.9)$$

NURBS possess all of the properties of B-Splines and many more. For a detailed discussion on NURBS see [34, 65, 71]. A NURBS curve can also be represented in homogeneous coordinates, similar to a rational Bézier curve 2.5. Using control points in homogeneous coordinates, P_i^w , a NURBS curve is defined as,

$$\mathbf{C}(\xi) = \sum_{i=0}^n N_{i,p}(\xi) P_i^w \quad (2.10)$$

2.1.6 NURBS in higher dimensions

Higher dimensional geometric entities — surfaces and solids — using NURBS, are constructed as tensor products of one dimensional NURBS objects. A B-Spline surface is obtained by taking a bidirectional net of control points, two knot vectors, and the products of univariate B-Spline basis functions,

$$\mathbf{S}(\xi, \eta) = \sum_{i=0}^{n_1} \sum_{j=0}^{n_2} N_{i,p}(\xi) M_{j,q}(\eta) \mathbf{P}_{i,j}^w \quad \text{for } 0 \leq \xi, \eta \leq 1 \quad (2.11)$$

with knot vectors,

$$\Xi_1 = \{\underbrace{0, \dots, 0}_{p+1}, \xi_{p+1}, \dots, \xi_{m_1-p-1}, \underbrace{1, \dots, 1}_{p+1}\} \quad (2.12)$$

$$\Xi_2 = \{\underbrace{0, \dots, 0}_{q+1}, \eta_{q+1}, \dots, \eta_{m_2-q-1}, \underbrace{1, \dots, 1}_{q+1}\} \quad (2.13)$$

The surface is of degree p in ξ direction and degree q in η direction; $\{\mathbf{P}_{i,j}\}$ is called the control net; Ξ_1 has $(m_1 + 1)$ knots, and Ξ_2 has $(m_2 + 1)$ knots; and $n_1 = m_1 - p - 1$ and $n_2 = m_2 - q - 1$.

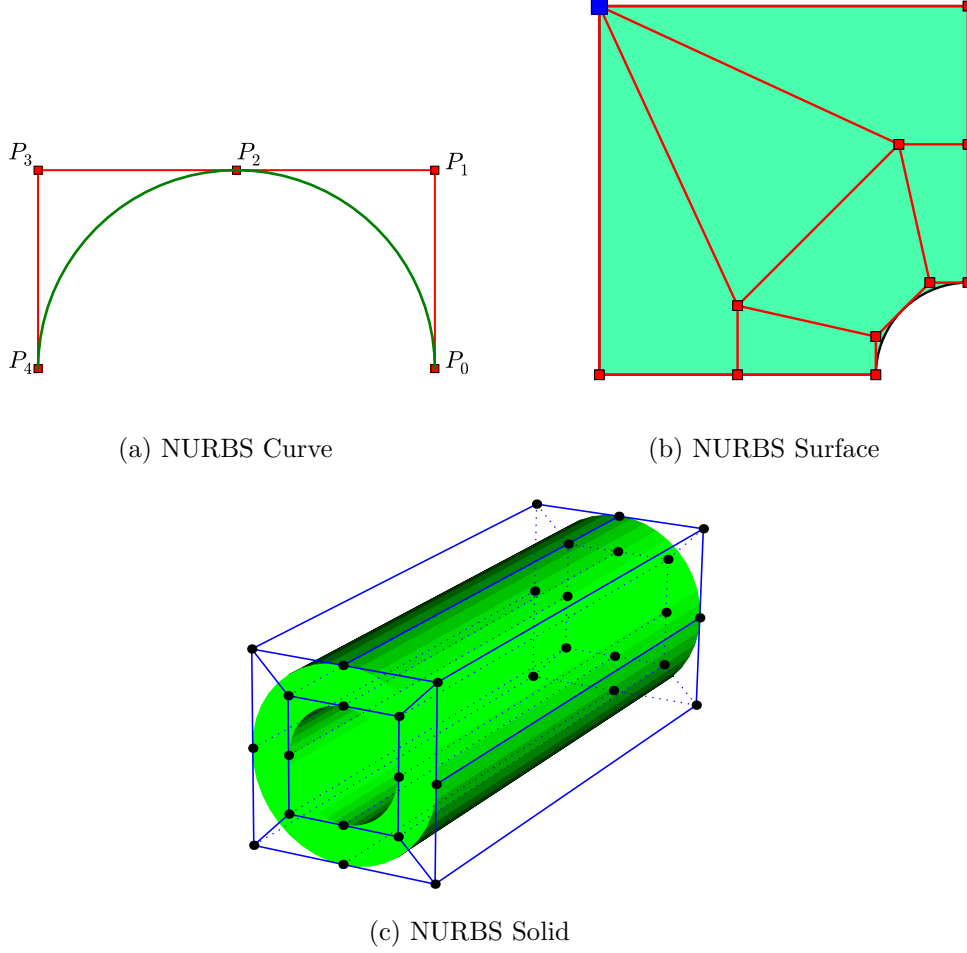


Figure 2.1: NURBS objects in 1D, 2D and 3D.

Tensor product NURBS solids are defined in a similar fashion. For a given control net $\{\mathbf{P}_{i,j,k}^w\}$ and degrees p, q and r respectively in directions ξ, η and ζ , a NURBS solid is defined as,

$$\mathbf{S}(\xi, \eta, \zeta) = \sum_{i=0}^{n_1} \sum_{j=0}^{n_2} \sum_{k=0}^{n_3} N_{i,p}(\xi) M_{j,q}(\eta) L_{k,l}(\zeta) \mathbf{P}_{i,j,k}^w \quad \text{for } 0 \leq \xi, \eta, \zeta \leq 1 \quad (2.14)$$

with knot vectors Ξ_1 and Ξ_2 same as (2.12) and (2.13) respectively, and,

$$\Xi_3 = \underbrace{\{0, \dots, 0\}}_{r+1}, \zeta_{r+1}, \dots, \zeta_{m_3-r-1}, \underbrace{1, \dots, 1}_{r+1} \quad (2.15)$$

and $n_3 = m_3 - r - 1$. As the surfaces and solids are constructed as tensor products of one dimensional objects all the properties of univariate curves and univariate basis functions are applicable to them as well. Figure 2.1 shows NURBS objects in one, two and three dimensions. Sharp corners, in Figure 2.1b, are modelled using multiple control points; there are two control points at the top left corner — shown in blue color.

2.2 NURBS refinement strategies

The mathematical representation of a NURBS object can be refined in several ways: knot insertion, order elevation and a combination of the both. In each of these operations the geometry remains the same but the control net is refined by adding more control points. Refer to [34, 65, 71] for a detailed explanation of these concepts.

2.2.1 Knot insertion (or h -refinement)

Knot insertion is one of the most important algorithms in refining the definition of a NURBS object. Knot insertion is the process of adding new knots to the existing object and calculating new control points. This is analogous to mesh refinement in the conventional finite element analysis, where large elements are split into smaller elements. Knot insertion lowers the degree of differentiability at the place where a new knot is inserted and the loss of differentiability at the new knots depends on the multiplicity of the knot values.

Consider a NURBS curve given by (2.10), defined over a knot vector $\Xi = \{\xi_0, \xi_1, \dots, \xi_m\}$, degree p and control points \mathbf{P}_i^w . In order to insert a new knot $\bar{\xi} = [\xi_k, \xi_{k+1})$ into Ξ , new set of control points need to be calculated and the new curve is given by,

$$\mathbf{C}(\xi) = \sum_{i=0}^n \bar{N}_{i,p}(\xi) \mathbf{Q}_i^w \quad (2.16)$$

where, the new control points \mathbf{Q}_i^w are computed as,

$$\mathbf{Q}_i^w = \alpha_i \mathbf{P}_i^w + (1 - \alpha_i) \mathbf{P}_i^w \quad (2.17)$$

where,

$$\alpha_i = \begin{cases} 1 & 1 \leq k - p \\ \frac{\bar{\xi} - \xi_i}{\xi_{i+1} - \xi_i} & k - p + 1 \leq i \leq k \\ 0 & i \geq k + 1 \end{cases} \quad (2.18)$$

and $\bar{N}_{i,p}(\xi)$ are the basis functions defined over the new knot vector $\bar{\Xi} = \{\xi_0, \xi_1, \dots, \xi_k, \xi_{k+1}, \dots, \xi_m\}$. An example of knot insertion is shown in Figure 2.2. Figures 2.2a and 2.2b show shape functions; and Figures 2.2c and 2.2d

show the curve and corresponding control net, respectively, before and after knot insertion. This process can be repeated to insert more knots. With the insertion of more and more knots the control net approaches the curve.

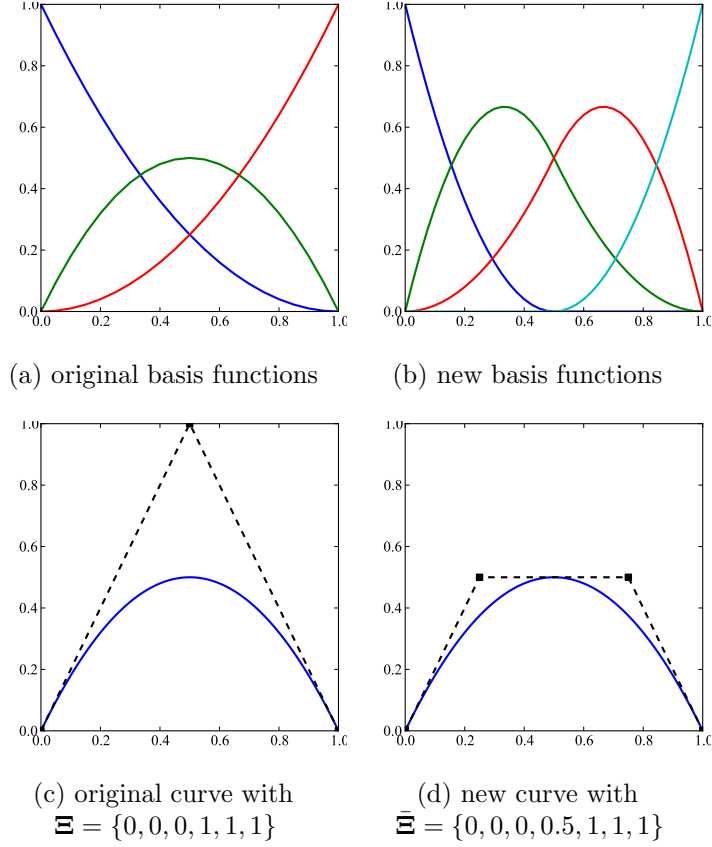


Figure 2.2: Knot insertion

2.2.2 Degree elevation (p -refinement)

Degree elevation is another important algorithm in refining the definition of a NURBS object. In degree elevation the degree (or order) of the basis functions is increased without any change in the geometry or parameterization. This is analogous to p -refinement in conventional finite elements. In order to preserve continuities along the domain, all the existing knot values must be repeated accordingly based on the amount of degree to be raised. The number of new control points to be calculated depends upon the number of knots present and degree to be raised. Refer to [34, 65, 71] for different degree elevation algorithms. An example of degree elevation is depicted in Figure 2.3. Figures 2.3a and 2.3b show shape functions; and Figures 2.3c and 2.3d show the curve and corresponding control net, respectively, before and after degree elevation. This process can be repeated to raise the degree further. Similar to knot insertion, here also, the control net approaches the curve, in the limit.

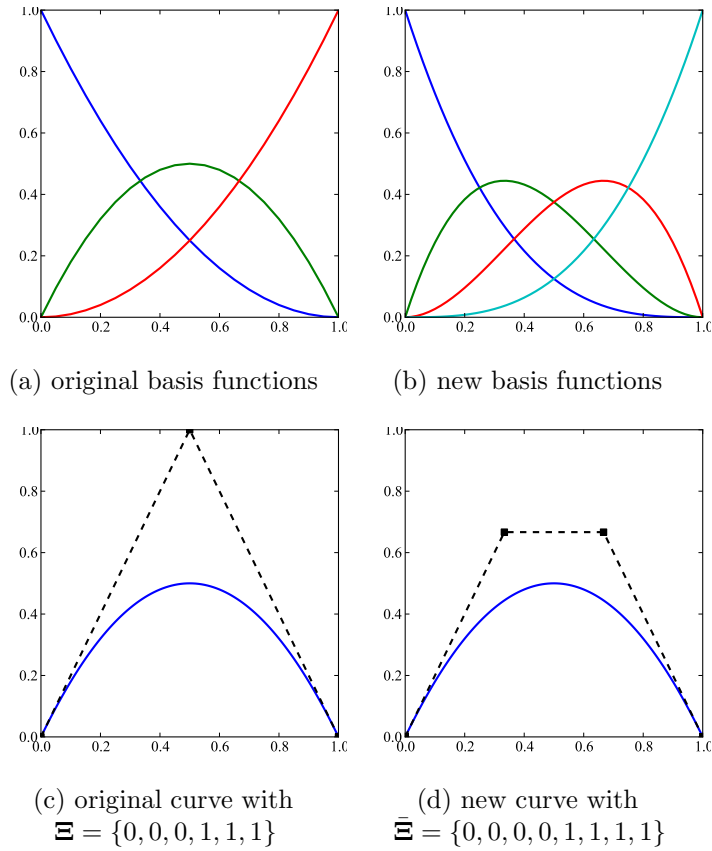


Figure 2.3: Degree elevation

2.2.3 k -refinement

Knot insertion and degree elevation can be combined to construct new refinement strategies. Combining them results in two new algorithms depending upon which of the two operations is applied first: 1.) knot refinement followed by degree elevation and 2.) degree elevation followed by knot refinement. Bazilevs *et al* [41] named the latter as k -refinement. These new algorithms are demonstrated with an example shown in Figure 2.4. As shown in Figure 2.4a, initial basis functions are linear. Inserting two knots — $\frac{1}{3}$ and $\frac{2}{3}$ — and raising the degree to two can be accomplished in two different ways: in the first method, shown on the left portion of Figure 2.4, the knots are inserted first and then degree is raised; and in the second method, shown on the right portion, the degree is raised first and then the knots are inserted.

Clear observation of knot insertion and degree elevation indicates that the two new algorithms do not lead to the same final definition. This is because of the fact that knot insertion and degree elevation do not commute. k -refinement has several advantages over its counterpart: it results in less number of control points and also preserves higher continuities across knot boundaries.

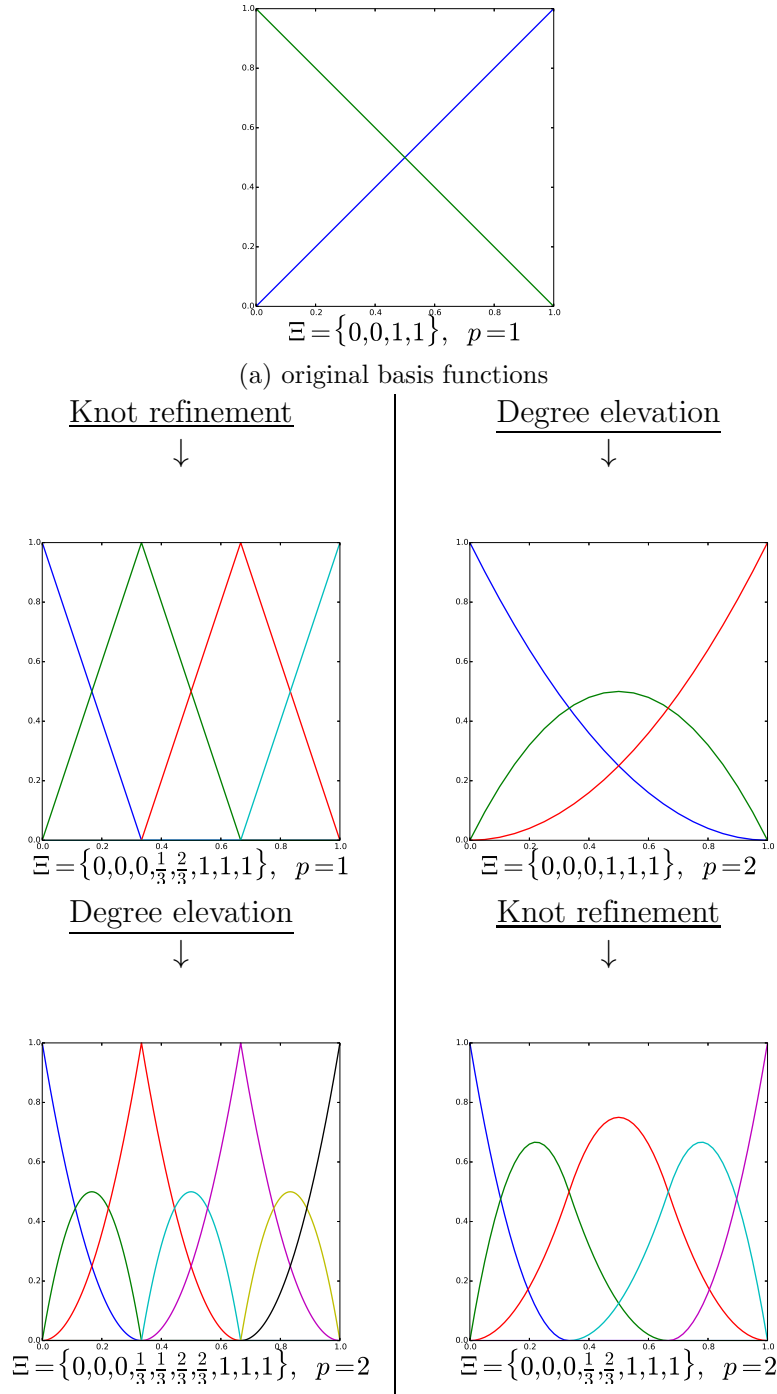


Figure 2.4: Combined p - and h - refinements.

2.3 NURBS with multiple patches

So far, the discussion of NURBS was with respect to simple geometries which can be modelled using a single NURBS patch. But, in order to model complex

geometries, for example multiply connected regions and in the assembly of different parts, one needs to use multiple patches with each patch representing a portion of a geometry and/or different part. Even in case of simple geometries multiple patches are essential for accurately applying the discontinuous boundary conditions during the analysis phase. Figure 2.5 shows a plate with two holes modelled using two patches. Geometries modelled using multiple patches often come at the price of reduced continuities across patch interfaces. In general, only C^0 continuity is maintained because of the computational cost involved in achieving higher continuities and achieving higher-order continuities across patch boundaries is not always possible.

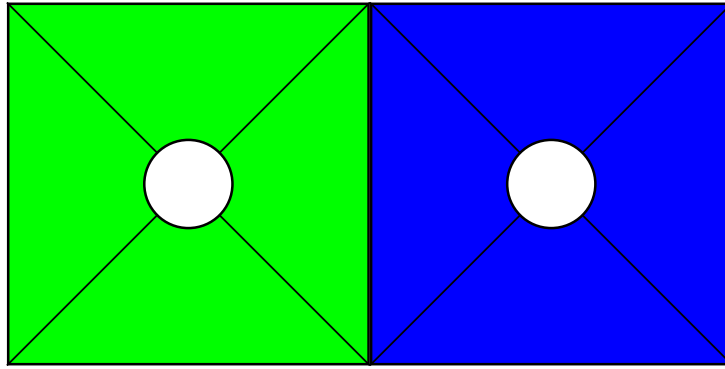


Figure 2.5: A plate with two holes modelled using two NURBS patches shown in green and blue colours.

2.4 Isogeometric analysis — NURBS as approximating functions

The fundamental idea behind isogeometric analysis is to use same basis functions used to construct geometry to also approximate the field variables. This can be viewed as the opposite of the classical finite element analysis where the functions used to approximate the field variables are used to represent the geometry, depicted schematically in Figure 2.6.

Lagrange polynomials are widely used as shape functions in the classical finite element methods. One disadvantage of the Lagrange polynomials is that they are only C^0 continuous across element boundaries. Lagrange polynomials are not suitable for some problems — like finite element analysis of beams and shell structures — where higher-order continuity is required across element boundaries. Achieving such higher-order continuities across element boundaries is a tedious task and special care has to be taken while deriving the shape functions. Hermite polynomials are one such class of polynomials; however, the main disadvantage of Hermite polynomials is that increasing the order increases the complexity in terms of mathematics as well as computer implementation [5, 86]. On the other hand, use of NURBS as shape functions for

approximating field variables overcomes all these difficulties, as NURBS offer several advantages as discussed in Section 2.1. Increasing the order of continuity across element boundaries is straightforward and can be implemented on a computer with much ease compared to other class of polynomials. Moreover, use of high-order shape functions, with higher-order continuities across element boundaries, results in numerical solutions with improved accuracy.

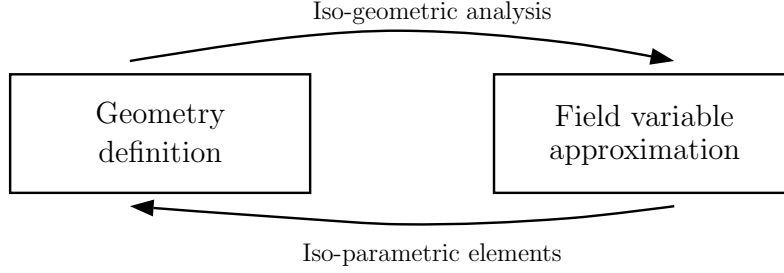


Figure 2.6: Analogy between *iso-geometric* analysis and the classical finite element analysis.

In isogeometric analysis an **element**, in a NURBS patch, is referred to the *non-zero* knot span in one-dimension (or tensor product of *non-zero* knot spans in higher dimensions). For the NURBS patch — a quarter portion of a plate with hole — shown in Figure 2.7, the knot vectors are,

$$\Xi_1 = \{0, 0, 0, 0.25, 0.5, 0.75, 1, 1, 1\} \quad (2.19)$$

$$\Xi_2 = \{0, 0, 0, 0.25, 0.5, 0.75, 1, 1, 1\} \quad (2.20)$$

So, there are *four* elements in the first parameter direction as there are *four* non-zero knot spans, namely $[0 - 0.25]$, $[0.25 - 0.5]$, $[0.5 - 0.75]$ and $[0.75 - 1.0]$. Similarly there are *four* elements in the second parameter direction. Therefore, there are a total of $4 \times 4 = 16$ elements in the entire NURBS patch.

The geometry of a tensor product NURBS solid is given by (2.14) can be written as,

$$\begin{aligned} \mathbf{S}^w(\boldsymbol{\xi}) &= (x(\boldsymbol{\xi}), y(\boldsymbol{\xi}), z(\boldsymbol{\xi}), w(\boldsymbol{\xi})) \\ &= \sum_{i=0}^n N_i(\boldsymbol{\xi}) \mathbf{P}_i^w \quad \text{for } 0 \leq \xi, \eta, \zeta \leq 1 \\ &= \mathbf{N} \mathbf{P}^w \end{aligned} \quad (2.21)$$

where, $\boldsymbol{\xi} = (\xi, \eta, \zeta)$ is a point in parametric coordinates, $N_i(\boldsymbol{\xi})$ are three-dimensional NURBS basis functions, \mathbf{N} is the row vector of N_i , \mathbf{P}^w is the column vector of \mathbf{P}_i^w and n is number of global basis functions.

The geometry of the domain in *initial* or *reference* configuration is given by,

$$\mathbf{X}(\boldsymbol{\xi}) = (X, Y, Z) = \sum_{i=0}^n N_i(\boldsymbol{\xi}) \mathbf{X}_i = \mathbf{N}\mathbf{X} \quad (2.22)$$

and in *current configuration* or *deformed configuration* by,

$$\mathbf{x}(\boldsymbol{\xi}) = (x, y, z) = \sum_{i=0}^n N_i(\boldsymbol{\xi}) \mathbf{x}_i = \mathbf{N}\mathbf{x} \quad (2.23)$$

where, \mathbf{X}_i and \mathbf{x}_i are the control points in reference and current configurations, respectively.

2.4.1 NURBS to approximate field variables

Using the NURBS basis functions $\mathbf{N}(\boldsymbol{\xi})$, a scalar field variable, u , can be approximated as,

$$u(\boldsymbol{\xi}) = \sum_{i=0}^n N_i(\boldsymbol{\xi}) u_i^c \quad (2.24)$$

where, $\{u_i^c\}$ are the control variables — the values of the field variable at the control points of a NURBS patch. Control points can be considered to be similar to *nodes* in the conventional finite element methods except for one difference: while all the nodes are interpolatory the control points are not. Even though the equation (2.24) is defined for a scalar field variable, it can be readily extended to vector and tensor fields.

2.4.2 Numerical integration

Evaluation of element matrices and vectors, for the finite element formulations discussed in the next chapters, require computations of shape functions and also their derivatives. Closed form expressions for element matrices and forces can be derived for simple shape functions; however, in most of the cases — for shape functions of arbitrary degrees and complex polynomials — it is extremely tedious and cumbersome to derive closed form expressions. So, matrices and force vectors are evaluated using numerical integration techniques, like Gauss-Legendre quadrature. In order to use Gauss-Legendre quadrature scheme the integrals have to be transformed from the physical space (Ω^e) to a master (or parent) element domain ($\tilde{\Omega}^e$). But for NURBS this transformation is not straightforward and has to go through an intermediate domain, namely *parametric domain* ($\hat{\Omega}^e$), as shown in Figure 2.7 for a two-dimensional space. Taking $(\tilde{\xi}, \tilde{\eta}, \tilde{\zeta})$ as coordinates in $\tilde{\Omega}^e$, the parametric coordinates (ξ, η, ζ) can be expressed as functions of parent element coordinates as,

$$\xi = \xi(\tilde{\xi}), \eta = \eta(\tilde{\eta}) \quad \text{and} \quad \zeta = \zeta(\tilde{\zeta}) \quad (2.25)$$

There is no cross-coupling between (ξ, η, ζ) and $(\tilde{\xi}, \tilde{\eta}, \tilde{\zeta})$, in relations (2.25). This is due to the reason that an element, e , which is a rectangle $[\xi_i, \xi_{i+1}] \times [\eta_j, \eta_{j+1}]$ in $\hat{\Omega}^e$ is mapped to a square $[-1, 1] \times [-1, 1]$ in $\tilde{\Omega}^e$. Using (2.25), equation (2.23) can be rewritten as,

$$\mathbf{x}(\xi, \eta, \zeta) = \sum_{i=0}^n N_i(\xi(\tilde{\xi}), \eta(\tilde{\eta}), \zeta(\tilde{\zeta})) \mathbf{x}_i = \mathbf{N}(\xi(\tilde{\xi}), \eta(\tilde{\eta}), \zeta(\tilde{\zeta})) \mathbf{x} \quad (2.26)$$

and applying chain rule of partial differentiation gives,

$$\begin{Bmatrix} \frac{\partial N}{\partial \xi} \\ \frac{\partial N}{\partial \eta} \\ \frac{\partial N}{\partial \zeta} \end{Bmatrix} = \begin{bmatrix} \frac{\partial x}{\partial \xi} & \frac{\partial y}{\partial \xi} & \frac{\partial z}{\partial \xi} \\ \frac{\partial x}{\partial \eta} & \frac{\partial y}{\partial \eta} & \frac{\partial z}{\partial \eta} \\ \frac{\partial x}{\partial \zeta} & \frac{\partial y}{\partial \zeta} & \frac{\partial z}{\partial \zeta} \end{bmatrix} \begin{Bmatrix} \frac{\partial N}{\partial x} \\ \frac{\partial N}{\partial y} \\ \frac{\partial N}{\partial z} \end{Bmatrix} \equiv \mathbf{J} \begin{Bmatrix} \frac{\partial N}{\partial x} \\ \frac{\partial N}{\partial y} \\ \frac{\partial N}{\partial z} \end{Bmatrix} \quad (2.27)$$

So,

$$\begin{Bmatrix} \frac{\partial N}{\partial x} \\ \frac{\partial N}{\partial y} \\ \frac{\partial N}{\partial z} \end{Bmatrix} = \mathbf{J}^{-1} \begin{Bmatrix} \frac{\partial N}{\partial \xi} \\ \frac{\partial N}{\partial \eta} \\ \frac{\partial N}{\partial \zeta} \end{Bmatrix} \quad (2.28)$$

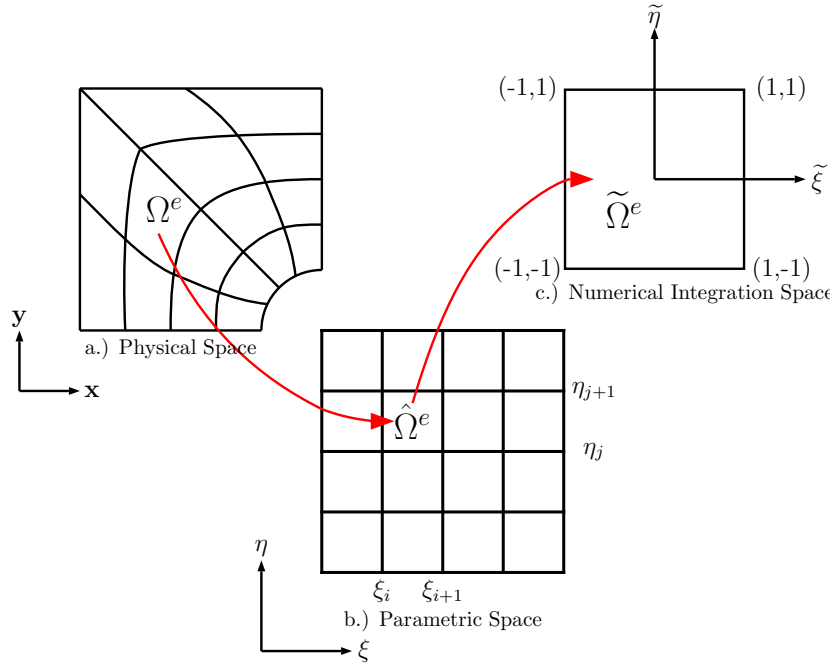


Figure 2.7: Mapping of the physical element to parametric domain and then to master element space.

Here, the index i in N_i is omitted for the purposes of clarity. The matrix \mathbf{J} is called the *Jacobian matrix* of transformation (2.26). Using transformation

(2.25), \mathbf{J} can be expanded as,

$$\mathbf{J} = \begin{bmatrix} \frac{\partial x}{\partial \xi} & \frac{\partial y}{\partial \xi} & \frac{\partial z}{\partial \xi} \\ \frac{\partial x}{\partial \eta} & \frac{\partial y}{\partial \eta} & \frac{\partial z}{\partial \eta} \\ \frac{\partial x}{\partial \zeta} & \frac{\partial y}{\partial \zeta} & \frac{\partial z}{\partial \zeta} \end{bmatrix} = \begin{bmatrix} \frac{\partial \xi}{\partial \xi} & 0 & 0 \\ 0 & \frac{\partial \eta}{\partial \eta} & 0 \\ 0 & 0 & \frac{\partial \zeta}{\partial \zeta} \end{bmatrix} \begin{bmatrix} \frac{\partial x}{\partial \xi} & \frac{\partial y}{\partial \xi} & \frac{\partial z}{\partial \xi} \\ \frac{\partial x}{\partial \eta} & \frac{\partial y}{\partial \eta} & \frac{\partial z}{\partial \eta} \\ \frac{\partial x}{\partial \zeta} & \frac{\partial y}{\partial \zeta} & \frac{\partial z}{\partial \zeta} \end{bmatrix} = \mathbf{A} \mathbf{B} \quad (2.29)$$

where

$$\mathbf{A} = \begin{bmatrix} \frac{\partial \xi}{\partial \xi} & 0 & 0 \\ 0 & \frac{\partial \eta}{\partial \eta} & 0 \\ 0 & 0 & \frac{\partial \zeta}{\partial \zeta} \end{bmatrix} \quad \text{and} \quad \mathbf{B} = \begin{bmatrix} \frac{\partial x}{\partial \xi} & \frac{\partial y}{\partial \xi} & \frac{\partial z}{\partial \xi} \\ \frac{\partial x}{\partial \eta} & \frac{\partial y}{\partial \eta} & \frac{\partial z}{\partial \eta} \\ \frac{\partial x}{\partial \zeta} & \frac{\partial y}{\partial \zeta} & \frac{\partial z}{\partial \zeta} \end{bmatrix} \quad (2.30)$$

So, the determinant of the Jacobian matrix becomes,

$$\begin{aligned} \det \mathbf{J} &= \det \mathbf{A} * \det \mathbf{B} \\ &= \frac{\partial \xi}{\partial \xi} * \frac{\partial \eta}{\partial \eta} * \frac{\partial \zeta}{\partial \zeta} * \det \mathbf{B} \end{aligned} \quad (2.31)$$

Equation (2.28) requires that the \mathbf{J} must be invertible, hence non-singular. And $\frac{\partial N}{\partial \xi}$, $\frac{\partial N}{\partial \eta}$ and $\frac{\partial N}{\partial \zeta}$ are evaluated by making use of relations (2.25). Applying chain rule to (2.25) gives,

$$\begin{Bmatrix} \frac{\partial N}{\partial \xi} \\ \frac{\partial N}{\partial \eta} \\ \frac{\partial N}{\partial \zeta} \end{Bmatrix} = \begin{bmatrix} \frac{\partial \xi}{\partial \xi} & 0 & 0 \\ 0 & \frac{\partial \eta}{\partial \eta} & 0 \\ 0 & 0 & \frac{\partial \eta}{\partial \eta} \end{bmatrix} \begin{Bmatrix} \frac{\partial N}{\partial \xi} \\ \frac{\partial N}{\partial \eta} \\ \frac{\partial N}{\partial \zeta} \end{Bmatrix} = \mathbf{A} \begin{Bmatrix} \frac{\partial N}{\partial \xi} \\ \frac{\partial N}{\partial \eta} \\ \frac{\partial N}{\partial \zeta} \end{Bmatrix} \quad (2.32)$$

Using equations (2.29) and (2.32), equation (2.28) becomes,

$$\begin{Bmatrix} \frac{\partial N}{\partial x} \\ \frac{\partial N}{\partial y} \\ \frac{\partial N}{\partial z} \end{Bmatrix} = \mathbf{B}^{-1} \begin{Bmatrix} \frac{\partial N}{\partial \xi} \\ \frac{\partial N}{\partial \eta} \\ \frac{\partial N}{\partial \zeta} \end{Bmatrix} \quad (2.33)$$

The entries of the matrix \mathbf{B} are evaluated from equation (2.23) as,

$$\begin{aligned} \frac{\partial x}{\partial \xi} &= \sum_{i=0}^n \frac{\partial N}{\partial \xi} x_i; & \frac{\partial x}{\partial \eta} &= \sum_{i=0}^n \frac{\partial N}{\partial \eta} x_i; & \frac{\partial x}{\partial \zeta} &= \sum_{i=0}^n \frac{\partial N}{\partial \zeta} x_i \\ \frac{\partial y}{\partial \xi} &= \sum_{i=0}^n \frac{\partial N}{\partial \xi} y_i; & \frac{\partial y}{\partial \eta} &= \sum_{i=0}^n \frac{\partial N}{\partial \eta} y_i; & \frac{\partial y}{\partial \zeta} &= \sum_{i=0}^n \frac{\partial N}{\partial \zeta} y_i \\ \frac{\partial z}{\partial \xi} &= \sum_{i=0}^n \frac{\partial N}{\partial \xi} z_i; & \frac{\partial z}{\partial \eta} &= \sum_{i=0}^n \frac{\partial N}{\partial \eta} z_i; & \frac{\partial z}{\partial \zeta} &= \sum_{i=0}^n \frac{\partial N}{\partial \zeta} z_i \end{aligned} \quad (2.34)$$

Computation of second derivatives of shape functions is presented in Appendix B.

Chapter 3

Formulation of Boundary Value Problems for Solids and Fluids

Formulation of a BVP is the process of deriving the governing differential equations which characterise the behaviour of a system one wants to study and identifying the associated boundary conditions. In solid and fluid mechanics BVPs are formulated based on continuum hypothesis.

Continuum hypothesis: At microscopic level a solid/fluid comprises individual molecules and its physical properties like density, velocity, etc., are time dependent and non-uniform. However, the phenomena studied in solid/fluid mechanics are macroscopic: the details at molecular levels are not taken into account. A solid/fluid body is treated as a continuum by viewing it at a scale coarse enough that any infinitesimally small solid/fluid element contains very large number of molecules and properties, like velocity, at any point in the body, are taken to be the average of molecular velocities. These locally averaged quantities vary smoothly within the continuum at the macroscopic scale. Formulation of a BVP in continuum mechanics requires a proper definition of many quantities which describe the kinematics, strains, stress measures and material constitutive laws. This chapter focusses on defining several important quantities required to formulate a BVP and then the formulation of BVPs in solid and fluid mechanics. The context is limited to the equations and materials used in the present work. For an elaborate discussion on these topics refer to [11, 20, 39].

3.1 Kinematics

Kinematics is the study of motion and deformation without consideration of the causes of the motion. Figure 3.1 shows the motion of a general deformable body in a three-dimensional Euclidean space. The body is assumed to be a collection of material particles denoted by position vector \mathbf{X} with respect to base \mathbf{E}_I in the initial configuration, Ω ; and by \mathbf{x} with respect to the base \mathbf{e}_i in the current configuration, ω . Current (or deformed) configuration, ω is

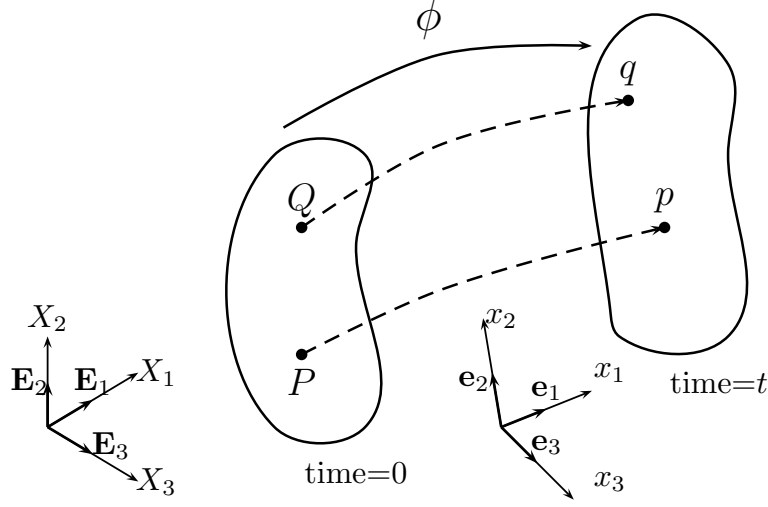


Figure 3.1: A general motion of a deformable body in space.

achieved by deformation of the body which is defined as a mapping,

$$\phi(\mathbf{X}) : \Omega \rightarrow \omega \quad (3.1)$$

that takes a point $\mathbf{X} \in \Omega$ to a point $\mathbf{x} \in \omega$. The displacement, \mathbf{u} , of a point from its initial position, \mathbf{X} , to its current position, \mathbf{x} , is given by,

$$\mathbf{u}(\mathbf{X}) = \phi(\mathbf{X}) - \mathbf{X} = \mathbf{x} - \mathbf{X} \quad (3.2)$$

In continuum mechanics two sets of coordinates are used to describe the motion of a particle — Lagrangian (or material) and Eulerian (or spatial). Lagrangian description refers to the motion where the observer follows an individual particle as it moves through space and time; whereas the Eulerian description refers to the motion of a particle that focuses on specific locations in the space through which the material flows as time passes. Lagrangian description is often used in solid mechanics and Eulerian description in fluid mechanics because of the underlying advantages of the corresponding description of the motion for the specific application.

3.1.1 Deformation gradient

The deformation gradient, \mathbf{F} , is one of the key quantities in the analysis of finite deformations. The deformation gradient can be defined as a mapping between relative positions of two particles from the reference configuration to the current configuration. Mathematically, the deformation gradient is defined as the gradient of current position vector with respect to the initial configuration, which is defined as,

$$\mathbf{F} = \frac{\partial \mathbf{x}}{\partial \mathbf{X}} = \nabla_{\mathbf{X}} \mathbf{x} \quad (3.3)$$

and the inverse of \mathbf{F} is,

$$\mathbf{F}^{-1} = \frac{\partial \mathbf{X}}{\partial \mathbf{x}} = \nabla_{\mathbf{x}} \mathbf{X} \quad (3.4)$$

Using (3.2), equation (3.3) can be expanded as,

$$\mathbf{F} = \mathbf{I} + \frac{\partial \mathbf{u}}{\partial \mathbf{X}} = \mathbf{I} + \nabla_{\mathbf{X}} \mathbf{u} \quad (3.5)$$

During the motion different fibres in the body experience rotation and distortion. The deformed quantities are related to the undeformed quantities via deformation gradient. Among the several such quantities, change in area and change in volume are two of the most important quantities in describing the equilibrium. For an infinitesimal element of volume $d\Omega$ in the reference configuration, the deformed volume is given by,

$$d\omega = J d\Omega \quad (3.6)$$

where, J is the determinant of the deformation gradient,

$$J = \det \mathbf{F} \quad (3.7)$$

that gives the amount of volume change. An infinitesimal area element $d\Gamma$ in the reference configuration is mapped to an infinitesimal area element $d\gamma$ in the current configuration by Nanson's formula, given as,

$$d\gamma = J \mathbf{F}^{-T} d\Gamma \quad (3.8)$$

where,

$$d\Gamma = \mathbf{N} d\Gamma \quad \text{and} \quad d\gamma = \mathbf{n} d\gamma \quad (3.9)$$

with \mathbf{N} and \mathbf{n} being the unit outward normals, respectively, in the reference and current configurations.

3.1.2 Strain measures

There is a multitude of strain measures defined in the literature of continuum mechanics. Among them the important ones used in the present work are: the right Cauchy-Green deformation tensor, \mathbf{C} ; the left Cauchy-Green deformation tensor, \mathbf{b} ; the Green-Lagrange strain tensor, \mathbf{E} ; Eulerian or Almansi strain tensor, \mathbf{e} ; and infinitesimal strain tensor, $\boldsymbol{\varepsilon}$, which are defined as,

$$\mathbf{C} = \mathbf{F}^T \mathbf{F} \quad (3.10)$$

$$\mathbf{b} = \mathbf{F} \mathbf{F}^T \quad (3.11)$$

$$\mathbf{E} = \frac{1}{2} (\mathbf{C} - \mathbf{I}) \quad (3.12)$$

$$\mathbf{e} = \frac{1}{2} (\mathbf{I} - \mathbf{b}^{-1}) \quad (3.13)$$

$$\boldsymbol{\varepsilon} = \frac{1}{2} (\nabla \mathbf{u} + (\nabla \mathbf{u})^T) \quad (3.14)$$

Time derivatives of kinematic quantities are very important in defining the conservation laws and governing equations; and whenever the motion of the body is time dependent. Material velocity $\mathbf{V}(\mathbf{X}, t)$ and material acceleration $\mathbf{A}(\mathbf{X}, t)$ of a particle are defined as the material time derivatives of $\mathbf{x}(\mathbf{X}, t)$ and $\mathbf{V}(\mathbf{X}, t)$, respectively.

$$\mathbf{V}(\mathbf{X}, t) = \frac{D\mathbf{x}(\mathbf{X}, t)}{Dt} = \frac{\partial \mathbf{x}(\mathbf{X}, t)}{\partial t} + \frac{\partial \mathbf{x}(\mathbf{X}, t)}{\partial \mathbf{X}} \frac{\partial \mathbf{X}}{\partial t} = \frac{\partial \mathbf{x}(\mathbf{X}, t)}{\partial t} \quad (3.15)$$

$$\mathbf{A}(\mathbf{X}, t) = \frac{D\mathbf{V}(\mathbf{X}, t)}{Dt} = \frac{\partial \mathbf{V}(\mathbf{X}, t)}{\partial t} + \frac{\partial \mathbf{V}(\mathbf{X}, t)}{\partial \mathbf{X}} \frac{\partial \mathbf{X}}{\partial t} = \frac{\partial \mathbf{V}(\mathbf{X}, t)}{\partial t} \quad (3.16)$$

Inverse mapping function, $\phi^{-1}(\mathbf{x}, t)$ is to be used in order to define spatial velocity and spatial acceleration. Spatial velocity is given by,

$$\mathbf{v}(\mathbf{x}, t) = \mathbf{V}(\mathbf{X}, t) = \mathbf{V}(\phi^{-1}(\mathbf{x}, t), t) \quad (3.17)$$

and the spatial acceleration is defined as,

$$\mathbf{a}(\mathbf{x}, t) = \dot{\mathbf{v}}(\mathbf{x}, t) = \frac{D\mathbf{v}(\mathbf{x}, t)}{Dt} = \frac{\partial \mathbf{v}(\mathbf{x}, t)}{\partial t} + \frac{\partial \mathbf{v}(\mathbf{x}, t)}{\partial \mathbf{x}} \frac{\partial \mathbf{x}}{\partial t} \quad (3.18)$$

In (3.18) the term $\frac{\partial \mathbf{v}(\mathbf{x}, t)}{\partial \mathbf{x}}$ is called as spatial velocity gradient, denoted by \mathbf{l} .

$$\mathbf{l} = \frac{\partial \mathbf{v}(\mathbf{x}, t)}{\partial \mathbf{x}} = \nabla_{\mathbf{x}} \mathbf{v}(\mathbf{x}, t) \quad (3.19)$$

Spatial velocity gradient can be decomposed into symmetric part, \mathbf{d} , and asymmetric part, \mathbf{w} , as,

$$\mathbf{d} = \frac{1}{2}(\mathbf{l} + \mathbf{l}^T) \quad (3.20)$$

$$\mathbf{w} = \frac{1}{2}(\mathbf{l} - \mathbf{l}^T) \quad (3.21)$$

3.2 Stress measures

Cauchy stress tensor, $\boldsymbol{\sigma}$, is the most ubiquitous stress measure in the study of continuum mechanics both in fluids and solids. It is a second order tensor that completely defines the state of stress, at a point, inside a material in the deformed configuration. It relates a unit normal, \mathbf{n} , to the traction (or stress) vector, $\mathbf{t}(\mathbf{n})$, across the surface perpendicular to \mathbf{n} , given by,

$$\mathbf{t}(\mathbf{n}) = \boldsymbol{\sigma} \cdot \mathbf{n} \quad (3.22)$$

Different components of Cauchy's stress tensor, along with the traction vector acting over an elemental cube, are shown in Figure. 3.2.

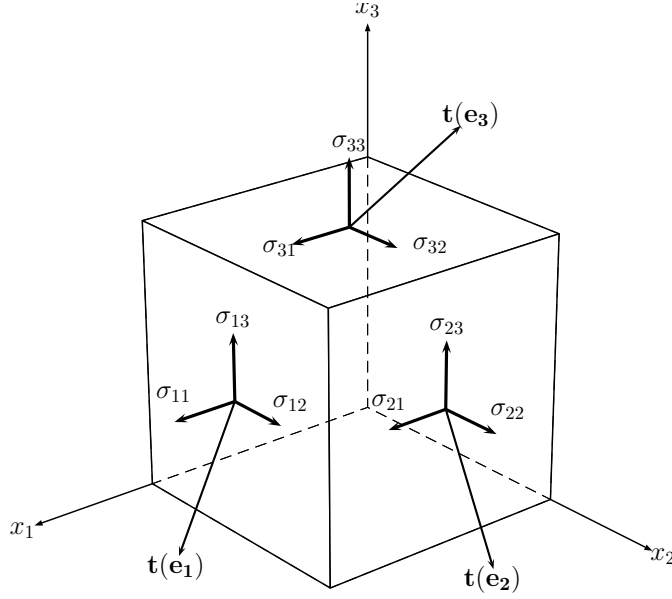


Figure 3.2: Components of Cauchy stress in three-dimensions.

Once the Cauchy stress is defined several other stress measures can be defined based on it. The first Piola-Kirchhoff stress tensor, \mathbf{P} , is given as,

$$\mathbf{P} = J\boldsymbol{\sigma}\mathbf{F}^{-T} \quad (3.23)$$

\mathbf{P} relates the force acting in the *current* configuration to the surface element in the *reference* configuration. Since it relates to both configurations, it is called as two-point tensor. While the Cauchy stress tensor is symmetric, the first Piola-Kirchhoff stress tensor is asymmetric.

The second Piola-Kirchhoff stress tensor, \mathbf{S} , another stress tensor referring to the reference configuration but a symmetric one, is defined as,

$$\mathbf{S} = J\mathbf{F}^{-1}\boldsymbol{\sigma}\mathbf{F}^{-T} \quad (3.24)$$

and is related to the first Piola-Kirchhoff stress tensor by the relation,

$$\mathbf{S} = \mathbf{F}^{-1}\mathbf{P} \quad (3.25)$$

Second Piola-Kirchhoff stress tensor is another widely used stress tensor in the study of solid mechanics, especially at finite strains.

3.3 Equilibrium

Balance of linear momentum: Assuming that the body is under the action of body forces per unit volume, \mathbf{f} ; and ignoring the inertia forces, balance of linear momentum gives equilibrium equations given as,

$$\text{div}\boldsymbol{\sigma} + \mathbf{f} = \mathbf{0} \quad \text{or} \quad \frac{\partial \sigma_{ij}}{\partial x_j} + f_i = 0 \quad (3.26)$$

where, $\text{div}\boldsymbol{\sigma}$ is the divergence of $\boldsymbol{\sigma}$ with respect to the current coordinates.

Balance of angular momentum: The rotational equilibrium (or balance of angular momentum) shows that $\boldsymbol{\sigma}$ is symmetric — having only six independent components instead of nine.

$$\boldsymbol{\sigma}^T = \boldsymbol{\sigma} \quad \text{or} \quad \sigma_{ji} = \sigma_{ij} \quad (3.27)$$

3.4 Boundary conditions

The solution of equilibrium equations is dictated by the type of boundary conditions present. Boundary conditions are divided into several types based on the condition of field variables to be satisfied on the boundary. Dirichlet and Neumann boundary conditions are the basic ones and other boundary conditions like Cauchy and Robin boundary conditions can be defined as a combination of these.

Dirichlet boundary condition specifies the value a solution needs to take on the boundary of the domain, specified as,

$$\mathbf{u} = \mathbf{g} \quad (3.28)$$

where as Neumann boundary condition specifies the values that the derivative of a solution has to take on the boundary of the domain. In the fields of solid and fluid mechanics the Neumann boundary condition is given as,

$$\boldsymbol{\sigma} \cdot \mathbf{n} = \mathbf{t} \quad (3.29)$$

where, \mathbf{n} is unit outward normal to the boundary and \mathbf{t} is the specified value.

3.5 Boundary Value Problem in solid mechanics

3.5.1 BVP in small strain regime

The boundary value problem of elasticity in small strain regime is stated as: Given $\mathbf{f} : \Omega \rightarrow \mathbb{R}^3$; $\mathbf{g} : \Gamma_D \rightarrow \mathbb{R}^3$; and $\mathbf{t} : \Gamma_N \rightarrow \mathbb{R}^3$, find $\mathbf{u} : \Omega \rightarrow \mathbb{R}^3$, such that:

$$\nabla \cdot \boldsymbol{\sigma} = \mathbf{f} \quad \text{in } \Omega, \quad (3.30)$$

$$\mathbf{u} = \mathbf{g} \quad \text{on } \Gamma_D, \quad (3.31)$$

$$\boldsymbol{\sigma} \cdot \mathbf{n} = \mathbf{t} \quad \text{in } \Gamma_N, \quad (3.32)$$

where, \mathbf{f} is the body force per unit volume; \mathbf{n} is the unit outward normal on the boundary, Γ , of Ω ; \mathbf{g} is the prescribed displacement on Γ_D ; and \mathbf{t} is the prescribed traction per unit area on Γ_N . Here, $\Gamma = \Gamma_D \cup \Gamma_N$ and $\Gamma_D \cap \Gamma_N = \emptyset$.

3.5.2 BVP in finite strain regime

In finite strain problems a clear distinction has to be made between the configurations with respect to which the governing equations are defined. The boundary value problem of elasticity, in large strain regime, in the reference configuration, can be derived from the momentum balance, as:
Given $\mathbf{f}_0 : \Omega \rightarrow \mathbb{R}^3$; $\mathbf{g} : \Gamma_D \rightarrow \mathbb{R}^3$; and $\mathbf{t}_0 : \Gamma_N \rightarrow \mathbb{R}^3$, find $\mathbf{u} : \Omega \rightarrow \mathbb{R}^3$, such that:

$$\nabla_{\mathbf{X}} \cdot \mathbf{P} = \mathbf{f}_0 \quad \text{in } \Omega, \quad (3.33)$$

$$\mathbf{u} = \mathbf{g} \quad \text{on } \Gamma_D, \quad (3.34)$$

$$\mathbf{P} \cdot \mathbf{N} = \mathbf{t}_0 \quad \text{in } \Gamma_N, \quad (3.35)$$

where, \mathbf{f}_0 is the body force per unit undeformed volume; \mathbf{N} is the unit outward normal on the boundary, Γ , of Ω ; \mathbf{g} is the prescribed displacement on Γ_D ; and \mathbf{t}_0 is the prescribed traction per unit undeformed area on Γ_N ; and $\Gamma = \Gamma_D \cup \Gamma_N$ and $\Gamma_D \cap \Gamma_N = \emptyset$.

Using Cauchy stress tensor as the stress measure, the boundary value problem of elasticity, in large strain regime, in the current configuration, is stated as:

Given $\mathbf{f} : \omega \rightarrow \mathbb{R}^3$; $\mathbf{g} : \gamma_D \rightarrow \mathbb{R}^3$; and $\mathbf{t} : \gamma_N \rightarrow \mathbb{R}^3$, find $\mathbf{u} : \omega \rightarrow \mathbb{R}^3$, such that:

$$\nabla_{\mathbf{x}} \cdot \boldsymbol{\sigma} = \mathbf{f} \quad \text{in } \omega, \quad (3.36)$$

$$\mathbf{u} = \mathbf{g} \quad \text{on } \gamma_D, \quad (3.37)$$

$$\boldsymbol{\sigma} \cdot \mathbf{n} = \mathbf{t} \quad \text{in } \gamma_N, \quad (3.38)$$

where, \mathbf{f} is the body force per unit volume in deformed configuration; \mathbf{n} is the unit outward normal on the deformed boundary, γ , of ω ; \mathbf{g} is the prescribed displacement on γ_D ; and \mathbf{t} is the prescribed traction per unit deformed area on γ_N . $\gamma = \gamma_D \cup \gamma_N$ and $\gamma_D \cap \gamma_N = \emptyset$.

Forces \mathbf{f} and \mathbf{t} are related to the corresponding terms in the reference configuration, \mathbf{f}_0 and \mathbf{t}_0 respectively, by the relations,

$$\mathbf{f} = \frac{1}{J} \mathbf{f}_0 \quad (3.39a)$$

$$\mathbf{t} = \frac{d\Gamma}{d\gamma} \mathbf{t}_0 \quad (3.39b)$$

where $d\Gamma$ and $d\gamma$ are the elemental areas, respectively, in the reference and deformed configurations.

3.6 Constitutive relations

The behaviour of a material is characterised by the relations between stress measures and kinematic quantities — called as *constitutive relations*. Constitutive relations describe how the material behaves when subjected to external

stimuli. There are a wide variety of material models available in the literature (see [20, 39, 61, 80, 92]) but in this section only those material models that are used in the present work are discussed.

3.6.1 Linear elasticity

For the simple linear elastic body the stress-strain relations are given by the generalized Hooke's law. Assuming that the elastic body is homogeneous and isotropic throughout the domain, the elasticity tensor, \mathbf{c} , can be simplified to,

$$c_{ijkl} = \lambda \delta_{ij} \delta_{kl} + \mu (\delta_{ik} \delta_{jl} + \delta_{il} \delta_{jk}) \quad (3.40)$$

where, μ and λ are the Lamé's constants, which can be written in terms of Young's modulus (E) and Poisson's ratio (ν) as,

$$\lambda = \frac{2\mu\nu}{1-2\nu}; \quad \mu = \frac{E}{2(1+\nu)} \quad (3.41)$$

and δ_{ij} is the Kronecker delta function, which is defined as,

$$\delta_{ij} = \begin{cases} 1, & \text{if } i = j \\ 0, & \text{if } i \neq j \end{cases} \quad (3.42)$$

Another important quantity which is useful in the subsequent sections is the Bulk modulus (κ), which is defined as,

$$\kappa = \lambda + \frac{2}{3}\mu = \frac{E}{3(1-2\nu)} \quad (3.43)$$

For the elasticity tensor given in (3.40), the Cauchy stress tensor becomes,

$$\boldsymbol{\sigma} = 2\mu\boldsymbol{\varepsilon} + \lambda(\nabla \cdot \mathbf{u})\mathbf{I} \quad (3.44)$$

where, \mathbf{I} is the second-order identity tensor.

It is very important to observe that the Cauchy stress (3.44) and elasticity tensor (3.40) are meaningful only when $\nu < 0.5$. But, when ν approaches the incompressible limit — 0.5, then λ goes to *infinity* and hence the components of the $\boldsymbol{\sigma}$ and \mathbf{c} . This poses a difficulty in obtaining accurate numerical solutions and calls for special treatments to deal with the problems involving incompressible and nearly incompressible materials.

3.6.2 Small strain elasto-plasticity

Plasticity describes the deformation of a material undergoing an irreversible change of shape when subjected to external forces. Theory of plasticity is a huge branch of engineering and the discussion here is restricted to only those aspects of plasticity that are used in the present work. For an elaborate discussion on theory of plasticity refer to [38, 55, 61, 80].

Three of the most important components of a model plasticity model are: a.) the yield function, b.) plastic flow rule which defines the evolution of the plastic strain and c.) hardening law which characterises the evolution of the yield limit. Each of these components has several different types, combinations of which lead to various types of plasticity models. In this work an associative plasticity model with von Mises yield criteria with linear isotropic hardening is considered.

In small strain plasticity, the strain tensor, $\boldsymbol{\varepsilon}$, is additively decomposed into an elastic component, $\boldsymbol{\varepsilon}^e$, and a plastic component, $\boldsymbol{\varepsilon}^p$, as,

$$\boldsymbol{\varepsilon} = \boldsymbol{\varepsilon}^e + \boldsymbol{\varepsilon}^p \quad (3.45)$$

and the elastic strain, $\boldsymbol{\varepsilon}^e$, is decomposed into deviatoric and volumetric components as,

$$\boldsymbol{\varepsilon}^e = \boldsymbol{\varepsilon}_{\text{dev}}^e + \boldsymbol{\varepsilon}_{\text{vol}}^e \quad (3.46)$$

The Cauchy stress is given by,

$$\boldsymbol{\sigma} = \mathbf{D}^e : \boldsymbol{\varepsilon}^e = 2\mu \boldsymbol{\varepsilon}_{\text{dev}}^e + \kappa \boldsymbol{\varepsilon}_{\text{vol}}^e \quad (3.47)$$

where, \mathbf{D}^e is the standard isotropic elasticity tensor.

According to the von Mises yield criterion, plastic yielding begins when the second deviatoric stress invariant, J_2 , reaches a critical value. For this reason it is also called the J_2 -plasticity or J_2 flow theory. The von Mises yield function is given as,

$$\Phi(\boldsymbol{\sigma}) = \sqrt{3J_2(\boldsymbol{\sigma})} - \sigma_y \quad (3.48)$$

where, σ_y is the yield stress and,

$$J_2(\boldsymbol{\sigma}) = \frac{1}{6} [(\sigma_1 - \sigma_2)^2 + (\sigma_2 - \sigma_3)^2 + (\sigma_3 - \sigma_1)^2] \quad (3.49)$$

where, σ_1 , σ_2 and σ_3 are the principal stresses.

The plastic flow rule, for the uniaxial case, is given as,

$$\dot{\boldsymbol{\varepsilon}}_p = \dot{\gamma} \text{sign}(\boldsymbol{\sigma}) \quad (3.50)$$

where,

$$\text{sign}(a) = \begin{cases} +1 & \text{if } a \geq 0 \\ -1 & \text{if } a < 0 \end{cases} \quad (3.51)$$

where, $\dot{\boldsymbol{\varepsilon}}_p$ is plastic strain rate and $\dot{\gamma}$ is called as plastic multiplier. The following set of constraints establish when plastic flow occurs.

$$\Phi \leq 0, \quad \dot{\gamma} \geq 0, \quad \dot{\gamma} \Phi = 0 \quad (3.52)$$

The associative linear hardening law is given as,

$$\sigma_y(\bar{\boldsymbol{\varepsilon}}^p) = \sigma_{y0} + H \bar{\boldsymbol{\varepsilon}}^p \quad (3.53)$$

where, H is termed the linear isotropic hardening modulus and $\bar{\boldsymbol{\varepsilon}}^p$ is the equivalent plastic strain. In case of perfectly-plastic material models, $H = 0$.

3.6.3 Hyperelastic materials

When the work done by the stresses during a deformation process depends only on the initial and final configurations of the continuum body then the material is termed as *hyperelastic*. For a stored strain energy function or elastic potential W , the first Piola Kirchhoff stress, \mathbf{P} ; second Piola Kirchhoff stress, \mathbf{S} ; the Cauchy stress, $\boldsymbol{\sigma}$; the material elasticity tensor, \mathbf{C} ; and the spatial elasticity tensor, \mathbf{c} ; are given, respectively, by,

$$\mathbf{P} = \frac{\partial W}{\partial \mathbf{F}} \quad (3.54)$$

$$\mathbf{S} = \frac{\partial W}{\partial \mathbf{E}} = 2 \frac{\partial W}{\partial \mathbf{C}} \quad (3.55)$$

$$\boldsymbol{\sigma} = \frac{2}{J} \frac{\partial W}{\partial \mathbf{b}} \mathbf{b} \quad (3.56)$$

$$\mathbf{C} = \frac{\partial \mathbf{S}}{\partial \mathbf{E}} = 2 \frac{\partial \mathbf{S}}{\partial \mathbf{C}} = 4 \frac{\partial^2 W}{\partial \mathbf{C} \partial \mathbf{C}} \quad (3.57)$$

$$\mathbf{c} = \frac{1}{J} \phi_*[\mathbf{C}] \quad (3.58)$$

where, ϕ_* is the push forward operator. For an *isotropic* elastic material the relation between W and \mathbf{C} is independent of the material axes chosen; hence, W is only a function of the invariants of \mathbf{C} .

In order to deal with the incompressibility constraint, deformation gradient, \mathbf{F} , is decomposed into deviatoric and volumetric components, as,

$$\mathbf{F} = \mathbf{F}_{\text{vol}} \mathbf{F}_{\text{dev}} \quad (3.59)$$

where,

$$\mathbf{F}_{\text{vol}} = J^{1/3} \mathbf{I}, \quad \mathbf{F}_{\text{dev}} = J^{-1/3} \mathbf{F} \quad (3.60)$$

It follows that

$$\det \mathbf{F}_{\text{vol}} = J \quad \text{and} \quad \det \mathbf{F}_{\text{dev}} = 1 \quad (3.61)$$

Similarly, the distortional component of the right Cauchy-Green tensor is defined as,

$$\bar{\mathbf{C}} = \mathbf{F}_{\text{dev}}^T \mathbf{F}_{\text{dev}} \quad (3.62)$$

For a nearly incompressible Neo-Hookean material the stored energy function, in general, is represented as the sum of deviatoric and volumetric parts, as,

$$W(J, \bar{\mathbf{C}}) = W_{\text{dev}}(J, \bar{\mathbf{C}}) + W_{\text{vol}}(J) \quad (3.63)$$

For materials that can be described by the split (3.63), \mathbf{S} and \mathbf{C} are given as,

$$\mathbf{S} = 2 \frac{\partial W_{\text{dev}}}{\partial \mathbf{C}} + p J \mathbf{C}^{-1} \quad (3.64)$$

$$\mathbf{C} = 4 \frac{\partial W_{\text{dev}}}{\partial \mathbf{C} \partial \mathbf{C}} + 2p \frac{\partial(J \mathbf{C}^{-1})}{\partial \mathbf{C}} + 2J \mathbf{C}^{-1} \otimes \frac{\partial p}{\partial \mathbf{C}} \quad (3.65)$$

$$\mathbf{c} = 4 \frac{\partial W_{\text{dev}}}{\partial \mathbf{C} \partial \mathbf{C}} - 2J \frac{\partial W_{\text{vol}}}{\partial J} \mathcal{I} + J \left(\frac{\partial W_{\text{vol}}}{\partial J} + J \frac{\partial^2 W_{\text{vol}}}{\partial J^2} \right) \mathbf{C}^{-1} \otimes \mathbf{C}^{-1} \quad (3.66)$$

where, \mathcal{I} is the fourth-order unit tensor and pressure, p , is given by the relation,

$$p = \frac{\partial W_{\text{vol}}(J)}{\partial J} \quad (3.67)$$

3.6.4 Large strain elasto-plasticity

In this work, widely followed hyperelastic based multiplicative plasticity model is used. According to this model, a hyperelastic material model is used in the elastic region and a plasticity model in the plastic portion. The main idea behind this framework is the multiplicative decomposition of the deformation gradient, \mathbf{F} , into elastic and plastic components, as given by,

$$\mathbf{F} = \mathbf{F}^e \mathbf{F}^p \quad (3.68)$$

where, \mathbf{F}^e and \mathbf{F}^p are called as the elastic and plastic deformation gradients, respectively. This multiplicative split is based on the assumption that a local unstressed intermediate configuration defined by the plastic deformation gradient, \mathbf{F}^p , exists.

Similar to the small-strain plasticity model this model also consists three important components: a.) a free-energy potential, which is used to derive the hyperelastic law, b.) a yield function to define the onset of plastic yielding, and c.) a dissipation potential, from which the plastic flow rule and the evolution laws for the internal variables are derived, (refer to Chapter 14 in [61]).

More specifically, a plasticity model with associative flow rule based on a von Mises yield criterion with isotropic nonlinear hardening is considered in all the examples studies in this work. The hyperelastic model varies for different test cases while the following nonlinear isotropic hardening law is used in all examples modelled with finite strain plasticity,

$$k(\bar{\varepsilon}^p) = \sigma_0 + (\sigma_\infty - \sigma_0) [1 - \exp(-\delta \bar{\varepsilon}^p)] + H \bar{\varepsilon}^p, \text{ with } \delta > 0 \quad (3.69)$$

where, $\bar{\varepsilon}^p$ is the equivalent plastic strain, σ_0 is the initial flow stress, σ_∞ is the saturation flow stress, δ is the saturation exponent, and H linear hardening coefficient. For the elaborate discussion on constitutive laws refer to [20, 39, 61, 80].

3.7 BVP in fluid mechanics

For an incompressible steady flow the boundary value problem is stated as: Given $\mathbf{f} : \Omega \rightarrow \mathbb{R}^3$; $\mathbf{g} : \Gamma_D \rightarrow \mathbb{R}^3$; and $\mathbf{t} : \Gamma_N \rightarrow \mathbb{R}^3$, find velocity, $\mathbf{v} : \Omega \rightarrow \mathbb{R}^3$; and pressure, $p : \Omega \rightarrow \mathbb{R}$, such that:

$$\rho(\mathbf{v} \cdot \nabla) \mathbf{v} - \nabla \cdot \boldsymbol{\sigma} = \mathbf{f} \quad \text{in } \Omega, \quad (3.70)$$

$$\nabla \cdot \mathbf{v} = 0 \quad \text{in } \Omega, \quad (3.71)$$

$$\mathbf{v} = \mathbf{g} \quad \text{on } \Gamma_D, \quad (3.72)$$

$$\boldsymbol{\sigma} \cdot \mathbf{n} = \mathbf{t} \quad \text{in } \Gamma_N, \quad (3.73)$$

where, ρ is the density of the fluid, \mathbf{f} is the body force per unit volume of the fluid; \mathbf{n} is the unit outward normal on the boundary, Γ , of Ω ; \mathbf{g} is the prescribed displacement on Γ_D ; and \mathbf{t} is the prescribed traction on Γ_N . Here, $\Gamma = \Gamma_D \cup \Gamma_N$ and $\Gamma_D \cap \Gamma_N = \emptyset$.

For a Newtonian fluid, the stress tensor is given as,

$$\boldsymbol{\sigma} = -p\mathbf{I} + \mu (\nabla \mathbf{v} + (\nabla \mathbf{v})^T) + \lambda (\nabla \cdot \mathbf{v})\mathbf{I} \quad (3.74)$$

where, μ is the dynamic viscosity of the fluid and λ is the so-called second coefficient of viscosity. So, for an incompressible fluid,

$$\boldsymbol{\sigma} = -p\mathbf{I} + \mu (\nabla \mathbf{v} + (\nabla \mathbf{v})^T) \quad (3.75)$$

Using (3.75) into (3.70) and after simplification,

$$\rho(\mathbf{v} \cdot \nabla)\mathbf{v} - \mu \nabla^2 \mathbf{v} + \nabla p = \mathbf{f} \quad (3.76)$$

Equation (3.76) along with the incompressibility constraint (3.71) are referred to as *stationary Navier-Stokes equations for an incompressible fluid flow*.

Flows are classified as laminar or turbulent based on the relative effects of inertial and viscous forces. Reynolds number, Re , is a non-dimensional parameter which is used to do such a classification. Reynolds number is defined as the ratio of inertial forces to the viscous forces.

$$Re = \frac{\text{inertial forces}}{\text{viscous forces}} = \frac{\rho \bar{V} L}{\mu} = \frac{\bar{V} L}{\nu} \quad (3.77)$$

where, \bar{V} is the characteristic velocity of the fluid, L is the characteristic length and $\nu = \mu/\rho$ is kinematic viscosity of the fluid. When the fluid velocity is low viscous forces dominate inertial forces and so, Re is low. Such a flow is called a laminar flow; and when the velocity of the fluid is very high, inertial forces dominate viscous forces and such a flow is called as turbulent flow. For turbulent flows Re is very high, usually $Re > 10000$. Fluid flows for which $Re \ll 1$ are called as creeping flows and such flows can be modelled with Stokes flow — a simplification of the Navier-Stokes — given as,

$$-\mu \nabla^2 \mathbf{v} + \nabla p = \mathbf{f} \quad \text{in } \Omega, \quad (3.78)$$

$$\nabla \cdot \mathbf{v} = 0 \quad \text{in } \Omega \quad (3.79)$$

along with the boundary conditions (3.72) and (3.73).

Chapter 4

Galerkin formulation

In the computational mechanics literature concerned with solution of BVPs one come across many methods to formulate weak forms of governing equations. In the present work variational formulation is used to derive the discretised equations. The formulations presented in this work are standard and can be found in [20, 80, 92].

This chapter discusses the displacement and mixed Galerkin formulations in small and finite strain regimes. Difficulties associated with solving matrix systems arising from mixed formulations are presented and equivalence of the two mixed methods — two-field and three-field — for the material models considered in the present work is derived.

4.1 Galerkin formulation in small strains

In small strain formulations, infinitesimal strain tensor, ε , is the most important strain measure. For a displacement vector $\mathbf{u} = \begin{Bmatrix} u_x & u_y & u_z \end{Bmatrix}^T$, the infinitesimal strain tensor, in index form, is given as,

$$\varepsilon_{ij} = \frac{1}{2} \left(\frac{\partial u_i}{\partial x_j} + \frac{\partial u_j}{\partial x_i} \right) \quad (4.1)$$

Strains can be written in the expanded form as,

$$\begin{aligned} \varepsilon_{xx} &= \frac{\partial u_x}{\partial x}, & \varepsilon_{xy} &= \frac{1}{2} \left(\frac{\partial u_x}{\partial y} + \frac{\partial u_y}{\partial x} \right) \\ \varepsilon_{yy} &= \frac{\partial u_y}{\partial y}, & \varepsilon_{xz} &= \frac{1}{2} \left(\frac{\partial u_x}{\partial z} + \frac{\partial u_z}{\partial x} \right) \\ \varepsilon_{zz} &= \frac{\partial u_z}{\partial z}, & \varepsilon_{yz} &= \frac{1}{2} \left(\frac{\partial u_y}{\partial z} + \frac{\partial u_z}{\partial y} \right) \end{aligned} \quad (4.2)$$

In Galerkin formulations it is convenient to work with strain, stress and elasticity tensors by representing them in the matrix form. Strains and stresses

transform into vectors, as,

$$\boldsymbol{\varepsilon} = \left\{ \varepsilon_{xx} \quad \varepsilon_{yy} \quad \varepsilon_{zz} \quad 2\varepsilon_{xy} \quad 2\varepsilon_{xz} \quad 2\varepsilon_{yz} \right\}^T \quad (4.3)$$

$$\boldsymbol{\sigma} = \left\{ \sigma_{xx} \quad \sigma_{yy} \quad \sigma_{zz} \quad \sigma_{xy} \quad \sigma_{xz} \quad \sigma_{yz} \right\}^T \quad (4.4)$$

The relations between strains and displacements can be written in matrix form as,

$$\boldsymbol{\varepsilon} = \mathbf{S} \mathbf{u} \quad (4.5)$$

where

$$\mathbf{S} = \begin{bmatrix} \frac{\partial}{\partial x} & 0 & 0 \\ 0 & \frac{\partial}{\partial y} & 0 \\ 0 & 0 & \frac{\partial}{\partial z} \\ \frac{\partial}{\partial y} & \frac{\partial}{\partial x} & 0 \\ \frac{\partial}{\partial z} & 0 & \frac{\partial}{\partial x} \\ 0 & \frac{\partial}{\partial z} & \frac{\partial}{\partial y} \end{bmatrix} \quad (4.6)$$

For isotropic linear elasticity the elasticity tensor in matrix form can be written as,

$$\mathbf{D} = 2\mu \mathbf{I}_0 + \lambda \mathbf{m} \mathbf{m}^T \quad (4.7)$$

where,

$$\mathbf{I}_0 = \text{diag} \left[1 \quad 1 \quad 1 \quad \frac{1}{2} \quad \frac{1}{2} \quad \frac{1}{2} \right] \quad (4.8)$$

$$\mathbf{m}^T = [1 \quad 1 \quad 1 \quad 0 \quad 0 \quad 0] \quad (4.9)$$

Therefore, in matrix notation, the Cauchy stress for linear elasticity becomes,

$$\boldsymbol{\sigma} = 2\mu \boldsymbol{\varepsilon} + \lambda (\nabla \cdot \mathbf{u}) \mathbf{m} \quad (4.10)$$

The main idea behind mixed formulations is to split the measure of deformation into deviatoric and volumetric components and replace the volumetric part by an improved value. In small strain formulation total strain $\boldsymbol{\varepsilon}$ is additively decomposed into deviatoric and volumetric parts as,

$$\boldsymbol{\varepsilon} = \boldsymbol{\varepsilon}_{\text{dev}} + \boldsymbol{\varepsilon}_{\text{vol}} \quad (4.11)$$

with,

$$\boldsymbol{\varepsilon}_{\text{dev}} = \mathbf{I}_{\text{dev}} \boldsymbol{\varepsilon} \quad \text{and} \quad \boldsymbol{\varepsilon}_{\text{vol}} = \mathbf{I}_{\text{vol}} \boldsymbol{\varepsilon} \quad (4.12)$$

where, \mathbf{I}_{dev} and \mathbf{I}_{vol} are the projection operators. They are fourth-order tensors which can be represented in the matrix form as,

$$\mathbf{I}_{\text{dev}} := \mathbf{I} - \frac{1}{3} \mathbf{m} \mathbf{m}^T \quad \text{and} \quad \mathbf{I}_{\text{vol}} := \frac{1}{3} \mathbf{m} \mathbf{m}^T \quad (4.13)$$

where \mathbf{I} is the fourth-order unit tensor, which in matrix notion becomes

$$\mathbf{I} = \text{diag}[1 \quad 1 \quad 1 \quad 1 \quad 1 \quad 1] \quad (4.14)$$

Likewise, the total stress, $\boldsymbol{\sigma}$, can be additively split into deviatoric and volumetric parts as,

$$\boldsymbol{\sigma} = \boldsymbol{\sigma}_{\text{dev}} + p \mathbf{m} \quad (4.15)$$

where, p is the hydrostatic pressure. p is related to the volumetric strain, ε_v , via the bulk modulus, κ , of the material, by the relation,

$$\varepsilon_v = \frac{p}{\kappa} \quad (4.16)$$

where, the volumetric strain is defined as,

$$\varepsilon_v = \mathbf{m}^T \boldsymbol{\varepsilon} = \varepsilon_{xx} + \varepsilon_{yy} + \varepsilon_{zz} \quad (4.17)$$

Similarly, the tangent matrix, \mathbf{D} , can be additively decomposed into deviatoric and volumetric components, as,

$$\mathbf{D} = \mathbf{D}_{\text{dev}} + \mathbf{D}_{\text{vol}} \quad (4.18)$$

where,

$$\mathbf{D}_{\text{dev}} = \mathbf{I}_{\text{dev}} \mathbf{D} \mathbf{I}_{\text{dev}} \quad \text{and} \quad \mathbf{D}_{\text{vol}} = \mathbf{I}_{\text{vol}} \mathbf{D} \mathbf{I}_{\text{vol}} \quad (4.19)$$

In the case of linear isotropic elastic material,

$$\mathbf{D}_{\text{dev}} = 2\mu \left(\mathbf{I}_0 - \frac{1}{3} \mathbf{m} \mathbf{m}^T \right) \quad \text{and} \quad \mathbf{D}_{\text{vol}} = \kappa \mathbf{m} \mathbf{m}^T \quad (4.20)$$

4.1.1 Displacement formulation

For a general continuum body Ω , in a three-dimensional Euclidean space, under the influence of body forces, \mathbf{f} ; and traction forces, \mathbf{t} ; the total potential energy is given by (see [92]),

$$\Pi(\mathbf{u}) = \int_{\Omega} \boldsymbol{\varepsilon}^T \boldsymbol{\sigma} \, d\Omega - \Pi_{\text{ext}} \quad (4.21)$$

where, Π_{ext} is the potential energy due to external forces acting on the body, given as,

$$\Pi_{\text{ext}} = \int_{\Omega} \mathbf{u}^T \mathbf{f} \, d\Omega + \int_{\Gamma} \mathbf{u}^T \mathbf{t} \, d\Gamma \quad (4.22)$$

Therefore,

$$\Pi = \int_{\Omega} \boldsymbol{\varepsilon}^T \boldsymbol{\sigma} \, d\Omega - \int_{\Omega} \mathbf{u}^T \mathbf{f} \, d\Omega - \int_{\Gamma} \mathbf{u}^T \mathbf{t} \, d\Gamma \quad (4.23)$$

For the system to be in equilibrium the potential energy has to be stationary and hence the first variation of total potential energy vanishes.

$$\delta\Pi = \int_{\Omega} \delta\boldsymbol{\varepsilon}^T \boldsymbol{\sigma} \, d\Omega - \int_{\Omega} \delta\mathbf{u}^T \mathbf{f} \, d\Omega - \int_{\Gamma} \delta\mathbf{u}^T \mathbf{t} \, d\Gamma = 0 \quad (4.24)$$

Equation (4.24), along with specified Dirichlet boundary conditions, describes the complete BVP in the so-called weak form. This is the simplest of the variational forms and requires only the knowledge of displacement field in the domain. This form is the basis for displacement based *irreducible* formulations.

In irreducible formulations, displacements, \mathbf{u} , are the only variables considered as degrees of freedom. Although u_x , u_y and u_z are independent of each other and can be approximated using different approximation functions, in general, they are approximated using the same type of approximation functions. So, displacement vector, \mathbf{u} , is approximated as,

$$\mathbf{u} = \mathbf{N} \bar{\mathbf{u}} \quad (4.25)$$

where, \mathbf{N} are the approximating functions and $\bar{\mathbf{u}}$ are the unknown values of displacements at the control variables.

$$\mathbf{N} = \begin{bmatrix} N_0 & 0 & 0 & N_1 & 0 & 0 & \dots & N_{n-1} & 0 & 0 \\ 0 & N_0 & 0 & 0 & N_1 & 0 & \dots & 0 & N_{n-1} & 0 \\ 0 & 0 & N_0 & 0 & 0 & N_1 & \dots & 0 & 0 & N_{n-1} \end{bmatrix} \quad (4.26)$$

$$\bar{\mathbf{u}} = \left\{ \bar{u}_0^x \quad \bar{u}_0^y \quad \bar{u}_0^z \quad \bar{u}_1^x \quad \bar{u}_1^y \quad \bar{u}_1^z \quad \dots \quad \bar{u}_{n-1}^x \quad \bar{u}_{n-1}^y \quad \bar{u}_{n-1}^z \right\}^T$$

There are n basis functions. Using (4.25), strains can be computed as,

$$\boldsymbol{\varepsilon} = \mathbf{B} \bar{\mathbf{u}} \quad (4.27)$$

where, \mathbf{B} is a $6 \times 3n$ matrix denoted the strain-displacement matrix.

$$\mathbf{B} = \begin{bmatrix} \frac{\partial N_0}{\partial x} & 0 & 0 & \frac{\partial N_1}{\partial x} & 0 & 0 & \dots & \frac{\partial N_{n-1}}{\partial x} & 0 & 0 \\ 0 & \frac{\partial N_0}{\partial y} & 0 & 0 & \frac{\partial N_1}{\partial y} & 0 & \dots & 0 & \frac{\partial N_{n-1}}{\partial y} & 0 \\ 0 & 0 & \frac{\partial N_0}{\partial z} & 0 & 0 & \frac{\partial N_1}{\partial z} & \dots & 0 & 0 & \frac{\partial N_{n-1}}{\partial z} \\ \frac{\partial N_0}{\partial y} & \frac{\partial N_0}{\partial x} & 0 & \frac{\partial N_1}{\partial y} & \frac{\partial N_1}{\partial x} & 0 & \dots & \frac{\partial N_{n-1}}{\partial y} & \frac{\partial N_{n-1}}{\partial x} & 0 \\ \frac{\partial N_0}{\partial z} & 0 & \frac{\partial N_0}{\partial x} & \frac{\partial N_1}{\partial z} & 0 & \frac{\partial N_1}{\partial x} & \dots & \frac{\partial N_{n-1}}{\partial z} & 0 & \frac{\partial N_{n-1}}{\partial x} \\ 0 & \frac{\partial N_0}{\partial z} & \frac{\partial N_0}{\partial y} & 0 & \frac{\partial N_1}{\partial z} & \frac{\partial N_1}{\partial y} & \dots & 0 & \frac{\partial N_{n-1}}{\partial z} & \frac{\partial N_{n-1}}{\partial y} \end{bmatrix} \quad (4.28)$$

From equations (4.25) and (4.27) variation of displacements and strains are given as,

$$\delta \mathbf{u} = \mathbf{N} \delta \bar{\mathbf{u}} \quad (4.29a)$$

$$\delta \boldsymbol{\varepsilon} = \mathbf{B} \delta \bar{\mathbf{u}} \quad (4.29b)$$

So, using equation (4.29) in (4.24),

$$\delta \Pi = \delta \bar{\mathbf{u}}^T \left[\int_{\Omega} \mathbf{B}^T \boldsymbol{\sigma} \, d\Omega - \int_{\Omega} \mathbf{N}^T \mathbf{f} \, d\Omega - \int_{\Gamma} \mathbf{N}^T \mathbf{t} \, d\Gamma \right] = 0 \quad (4.30)$$

In equation (4.30), $\delta \bar{\mathbf{u}}^T$ is arbitrary and the term inside the square brackets must be zero for the equation to be satisfied. This leads to a discrete system,

$$\Psi = \mathbf{P}(\boldsymbol{\sigma}) - \mathbf{f}_{\text{ext}} = 0 \quad (4.31)$$

where,

$$\mathbf{P}(\boldsymbol{\sigma}) = \int_{\Omega} \mathbf{B}^T \boldsymbol{\sigma} \, d\Omega \quad (4.32)$$

$$\mathbf{f}_{\text{ext}} = \int_{\Omega} \mathbf{N}^T \mathbf{f} \, d\Omega + \int_{\Gamma} \mathbf{N}^T \mathbf{t} \, d\Gamma \quad (4.33)$$

$\mathbf{P}(\boldsymbol{\sigma})$ is often denoted the stress divergence or internal force term. So far, in deriving (4.31) no assumption was made regarding the form of stress, whether it is a linear or nonlinear function of strain. If the stress is a linear function of strain, which is the case in linear elasticity, the resulting equations are linear and hence can be solved directly. However, if the stress is a nonlinear function of strain, which is the case with elasto-plastic materials, then an iterative scheme has to be employed in order to solve the resulting nonlinear equations. There are many such iterative methods available in literature and among them Newton-Raphson method is the widely used one because of its quadratic convergence property. The details of Newton-Raphson method can be found in Appendix A.

Applying Newton-Raphson method to solve (4.31) results in a matrix system of equations given by,

$$\mathbf{K} \, d\bar{\mathbf{u}} = -\mathbf{R}_u \quad (4.34)$$

where, $d\bar{\mathbf{u}}$ is the vector of increment in displacements and,

$$\mathbf{K} = \int_{\Omega} \mathbf{B}^T \mathbf{D} \mathbf{B} \, d\Omega \quad (4.35a)$$

$$\mathbf{R}_u = \int_{\Omega} \mathbf{B}^T \boldsymbol{\sigma} \, d\Omega - \mathbf{f}_{\text{ext}} \quad (4.35b)$$

4.1.2 Two-field mixed variational formulation

Depending upon the type of variables chosen as independent variables, many kinds of two-field mixed variational formulations are possible. In the current work, displacements (\mathbf{u}) and hydrostatic pressure (p) are considered as independent variables. By replacing $\boldsymbol{\sigma}$ in (4.24) with $\check{\boldsymbol{\sigma}}$ and imposing a weak form of (4.16), the weak forms of the two-field mixed variational formulation are given as (see [92]),

$$\int_{\Omega} \delta \boldsymbol{\varepsilon}^T \check{\boldsymbol{\sigma}} \, d\Omega = \int_{\Omega} \delta \mathbf{u}^T \mathbf{f} \, d\Omega + \int_{\Gamma} \delta \mathbf{u}^T \mathbf{t} \, d\Gamma \quad (4.36a)$$

$$\int_{\Omega} \delta p \left[\mathbf{m}^T \boldsymbol{\varepsilon} - \frac{p}{\kappa} \right] \, d\Omega = 0 \quad (4.36b)$$

where,

$$\check{\boldsymbol{\sigma}} = \bar{\boldsymbol{\sigma}}_{\text{dev}} + p \mathbf{m} \quad (4.37)$$

Here $\bar{\boldsymbol{\sigma}}_{\text{dev}}$, the deviatoric component of stresses, is calculated based on the strains, $\boldsymbol{\varepsilon}$; and p is evaluated from its independent approximation.

Taking independent approximations for \mathbf{u} and p as,

$$\mathbf{u} = \mathbf{N}_u \bar{\mathbf{u}}; \quad p = \mathbf{N}_p \bar{p} \quad (4.38)$$

and using them in (4.36), results in a nonlinear system of equations given as,

$$\Psi = \begin{Bmatrix} \mathbf{R}_u \\ \mathbf{R}_p \end{Bmatrix} = \mathbf{0} \quad (4.39)$$

where,

$$\mathbf{R}_u = \int_{\Omega} \mathbf{B}^T \check{\boldsymbol{\sigma}} \, d\Omega - \mathbf{f}_{\text{ext}} \quad (4.40a)$$

$$\mathbf{R}_p = \int_{\Omega} \mathbf{N}_p^T \left[\mathbf{m}^T \boldsymbol{\varepsilon} - \frac{p}{\kappa} \right] \, d\Omega \quad (4.40b)$$

Using Newton-Raphson iterative scheme to solve (4.39) leads to the following algebraic problem given by,

$$\begin{bmatrix} \mathbf{K}_{uu} & \mathbf{K}_{up} \\ \mathbf{K}_{pu} & -\mathbf{K}_{pp} \end{bmatrix} \begin{Bmatrix} d\bar{\mathbf{u}} \\ d\bar{p} \end{Bmatrix} = - \begin{Bmatrix} \mathbf{R}_u \\ \mathbf{R}_p \end{Bmatrix} \quad (4.41)$$

where, $d\bar{\mathbf{u}}$ and $d\bar{p}$ are vectors of increments in displacements and pressure respectively; and,

$$\mathbf{K}_{uu} = \int_{\Omega} \mathbf{B}^T \mathbf{D}_{\text{dev}} \mathbf{B} \, d\Omega \quad (4.42a)$$

$$\mathbf{K}_{up} = \int_{\Omega} \mathbf{B}^T \mathbf{m} \mathbf{N}_p \, d\Omega = \mathbf{K}_{pu}^T \quad (4.42b)$$

$$\mathbf{K}_{pp} = \int_{\Omega} \frac{1}{\kappa} \mathbf{N}_p^T \mathbf{N}_p \, d\Omega \quad (4.42c)$$

with \mathbf{f}_{ext} being the same as in (4.35).

4.1.3 Three-field mixed variational formulation

In the three-field mixed variational formulation, displacements, \mathbf{u} , volumetric strain, ε_v , and pressure, p , are treated as independent variables. By replacing $\boldsymbol{\sigma}$ in (4.24) with $\check{\boldsymbol{\sigma}}$ and imposing a weak form of (4.16) and (4.17), the weak

forms of the three-field mixed variational formulation, in small strains, are given as (see [92]),

$$\int_{\Omega} \delta \boldsymbol{\varepsilon}^T \boldsymbol{\sigma} \, d\Omega = \int_{\Omega} \delta \mathbf{u}^T \mathbf{f} \, d\Omega + \int_{\Gamma} \delta \mathbf{u}^T \mathbf{t} \, d\Gamma \quad (4.43a)$$

$$\int_{\Omega} \delta \varepsilon_v [\kappa \varepsilon_v - p] \, d\Omega = 0 \quad (4.43b)$$

$$\int_{\Omega} \delta p [\mathbf{m}^T \boldsymbol{\varepsilon} - \varepsilon_v] \, d\Omega = 0 \quad (4.43c)$$

where, $\bar{\boldsymbol{\sigma}}_{\text{dev}}$ of $\boldsymbol{\sigma}$, is calculated from the strains, $\check{\boldsymbol{\varepsilon}}$, which are computed as,

$$\check{\boldsymbol{\varepsilon}} = \boldsymbol{\varepsilon}_{\text{dev}} + \frac{1}{3} \varepsilon_v \mathbf{m} \quad (4.44)$$

where, $\boldsymbol{\varepsilon}_{\text{dev}}$ is the deviatoric component of strains calculated from displacements.

Taking approximations for variables \mathbf{u} , p and ε_v as,

$$\mathbf{u} = \mathbf{N}_u \bar{\mathbf{u}}; \quad p = \mathbf{N}_p \bar{p}; \quad \varepsilon_v = \mathbf{N}_{\theta} \bar{\theta} \quad (4.45)$$

and using them in (4.43) results in a nonlinear system of equations given as,

$$\Psi = \begin{Bmatrix} \mathbf{R}_u \\ \mathbf{R}_{\theta} \\ \mathbf{R}_p \end{Bmatrix} = \mathbf{0} \quad (4.46)$$

where,

$$\mathbf{R}_u = \int_{\Omega} \mathbf{B}^T \boldsymbol{\sigma} \, d\Omega - \mathbf{f}_{\text{ext}} \quad (4.47a)$$

$$\mathbf{R}_{\theta} = \int_{\Omega} \mathbf{N}_{\theta}^T [\kappa \varepsilon_v - p] \, d\Omega \quad (4.47b)$$

$$\mathbf{R}_p = \int_{\Omega} \mathbf{N}_p^T [\mathbf{m}^T \boldsymbol{\varepsilon} - \varepsilon_v] \, d\Omega \quad (4.47c)$$

Using Newton-Raphson iterative scheme to solve (4.46) leads to the following algebraic problem,

$$\begin{bmatrix} \mathbf{K}_{uu} & \mathbf{0} & \mathbf{K}_{up} \\ \mathbf{0} & \mathbf{K}_{\theta\theta} & \mathbf{K}_{\theta p} \\ \mathbf{K}_{pu} & \mathbf{K}_{p\theta} & \mathbf{0} \end{bmatrix} \begin{Bmatrix} d\bar{\mathbf{u}} \\ d\bar{\theta} \\ d\bar{p} \end{Bmatrix} = - \begin{Bmatrix} \mathbf{R}_u \\ \mathbf{R}_{\theta} \\ \mathbf{R}_p \end{Bmatrix} \quad (4.48)$$

where,

$$\mathbf{K}_{\theta\theta} = \int_{\Omega} \mathbf{N}_{\theta}^T \kappa \mathbf{N}_{\theta} \, d\Omega \quad (4.49a)$$

$$\mathbf{K}_{\theta p} = - \int_{\Omega} \mathbf{N}_{\theta}^T \mathbf{N}_p \, d\Omega = \mathbf{K}_{p\theta}^T \quad (4.49b)$$

and the remaining terms are same as those given in the two-field formulation.

4.2 Galerkin formulation in finite strains

For finite element formulations of finite deformation problems, the integral equations of weak forms can be constructed in either the reference or the current configuration. Usually, the derivations are carried out in the reference configuration and then transformed into the current configuration, as the integrals taken over the reference configuration do not change during the deformation process and hence are not affected during the variation or linearisation process. Most of the material presented in this section is extracted from [20, 92]. The interested reader can refer to those two excellent resources for a detailed discussion on these topics.

4.2.1 Displacement formulation

For a given stored energy function, W , the total energy functional in the reference configuration is given as,

$$\Pi(\mathbf{u}) = \int_{\Omega} W(\mathbf{C}) \, d\Omega - \Pi_{\text{ext}} \quad (4.50)$$

where, Π_{ext} is same as that given in (4.22). For the system to be in equilibrium the first variation of Π has to vanish, i.e.,

$$\delta\Pi = \int_{\Omega} \delta\mathbf{E}^T \mathbf{S} \, d\Omega - \delta\Pi_{\text{ext}} = \mathbf{0} \quad (4.51)$$

and in the current configuration,

$$\delta\Pi = \int_{\omega} \delta\boldsymbol{\varepsilon}^T \boldsymbol{\sigma} \, d\omega - \delta\Pi_{\text{ext}} = \mathbf{0} \quad (4.52)$$

By taking approximations for displacements as $\mathbf{u} = \mathbf{N}_u \bar{\mathbf{u}}$, equation (4.52) results in a nonlinear system of equations,

$$\mathbf{R}_u = \int_{\omega} \mathbf{B}^T \boldsymbol{\sigma} \, d\omega - \mathbf{f}_{\text{ext}} = \mathbf{0} \quad (4.53)$$

where, \mathbf{R}_u is termed as the residual and the load vector \mathbf{f}_{ext} is same as that given in (4.33). Newton-Raphson iterative scheme to solve (4.53) leads to the following algebraic problem given by,

$$\mathbf{K} \, d\bar{\mathbf{u}} = -\mathbf{R}_u \quad (4.54)$$

where, the stiffness matrix, \mathbf{K} , is given by,

$$\mathbf{K} = \mathbf{K}_M + \mathbf{K}_G + \mathbf{K}_L \quad (4.55)$$

where, \mathbf{K}_M and \mathbf{K}_G are the material stiffness and geometric stiffness, respectively, given as,

$$\mathbf{K}_M = \int_{\omega} \mathbf{B}^T \mathbf{D} \mathbf{B} \, d\omega \quad (4.56)$$

$$\mathbf{K}_{G,ab} = \int_{\omega} (\mathbf{N}_{a,i} \boldsymbol{\sigma}_{ij} \mathbf{N}_{b,j}) \mathbf{I} \, d\omega \quad (4.57)$$

and \mathbf{K}_L is the stiffness due to deformation dependent loads. When the loads are independent of the deformation, \mathbf{K}_L vanishes, [20, 92].

4.2.2 Two-field mixed variational formulation

Similar to the two-field formulation in small strains, here also, displacements (\mathbf{u}) and pressure (p) are considered as independent variables. A perturbed potential energy functional can be written as,

$$\Pi(\mathbf{u}, p) = \int_{\Omega} \left[W(\bar{\mathbf{C}}) + p(J - 1) - \frac{1}{2\kappa} p^2 \right] d\Omega - \Pi_{\text{ext}} \quad (4.58)$$

where, p can be viewed as a Lagrange multiplier which enforces the incompressibility constraints $J = 1$.

Taking approximations for variables \mathbf{u} and p as,

$$\mathbf{u} = \mathbf{N}_u \bar{\mathbf{u}}; \quad \text{and} \quad p = \mathbf{N}_p \bar{p} \quad (4.59)$$

and equating the first variation of (4.58) to zero, yields a nonlinear system of equations given as,

$$\Psi = \begin{Bmatrix} \mathbf{R}_u \\ \mathbf{R}_p \end{Bmatrix} = \mathbf{0} \quad (4.60)$$

where,

$$\mathbf{R}_u = \int_{\Omega} \mathbf{B}^T \check{\boldsymbol{\sigma}} J \, d\Omega - \mathbf{f}_{\text{ext}} \quad (4.61)$$

$$\mathbf{R}_p = \int_{\Omega} \mathbf{N}_p^T \left(J - 1 - \frac{p}{\kappa} \right) d\Omega \quad (4.62)$$

Using Newton-Raphson scheme to solve (4.60) leads to the following algebraic problem,

$$\begin{bmatrix} \mathbf{K}_{uu} & \mathbf{K}_{up} \\ \mathbf{K}_{pu} & -\mathbf{K}_{pp} \end{bmatrix} \begin{Bmatrix} d\bar{\mathbf{u}} \\ d\bar{p} \end{Bmatrix} = - \begin{Bmatrix} \mathbf{R}_u \\ \mathbf{R}_p \end{Bmatrix} \quad (4.63)$$

where,

$$\mathbf{K}_{uu} = \int_{\Omega} \mathbf{B}^T \bar{\mathbf{D}}_{11} \mathbf{B} J \, d\Omega + \mathbf{K}_G \quad (4.64)$$

$$\mathbf{K}_{up} = \int_{\Omega} \mathbf{B}^T \mathbf{m} \mathbf{N}_p J \, d\Omega = \mathbf{K}_{pu}^T \quad (4.65)$$

$$\mathbf{K}_{pp} = \int_{\Omega} \frac{1}{\kappa} \mathbf{N}_p^T \mathbf{N}_p \, d\Omega \quad (4.66)$$

$$\mathbf{K}_G = \int_{\omega} (\mathbf{N}_{a,i} \check{\boldsymbol{\sigma}}_{ij} \mathbf{N}_{b,j}) \mathbf{I} \, d\omega \quad (4.67)$$

where,

$$\bar{\mathbf{D}}_{11} = \mathbf{D}_{\text{dev}} - \frac{2}{3} (\mathbf{m} \bar{\boldsymbol{\sigma}}_{\text{dev}}^T + \bar{\boldsymbol{\sigma}}_{\text{dev}} \mathbf{m}^T) + 2(\bar{p} - p) \mathbf{I}_0 - \left(\frac{2}{3} \bar{p} - p \right) \mathbf{m} \mathbf{m}^T \quad (4.68)$$

$$\check{\boldsymbol{\sigma}} = \bar{\boldsymbol{\sigma}} + \mathbf{m}(p - \bar{p}) \quad (4.69)$$

$$\bar{p} = \frac{1}{3} \mathbf{m}^T \bar{\boldsymbol{\sigma}} \quad (4.70)$$

4.2.3 Three-field mixed variational formulation

Considering displacements, \mathbf{u} ; determinant of deformation gradient, J ; and pressure, p , as independent variables, the three-field Hu-Washizu type potential energy functional (see [20, 92]) can be written as,

$$\Pi_{HW}(\mathbf{u}, \bar{J}, p) = \int_{\Omega} [W(\bar{\mathbf{C}}) + p(J - \bar{J})] \, d\Omega - \Pi_{\text{ext}} \quad (4.71)$$

where, \bar{J} is an independent approximation of J and p works as a Lagrange multiplier which constraints J to \bar{J} . A new modified deformation gradient can now be defined by replacing J with its independent representation \bar{J} .

$$\bar{\mathbf{F}} = \left(\frac{\bar{J}}{J} \right)^{1/3} \mathbf{F} \quad \text{and} \quad \det \bar{\mathbf{F}} = \bar{J} \quad (4.72)$$

In order to simplify computations, consider,

$$\bar{J} = 1 + \theta \quad (4.73)$$

where, θ represents change in volume. In the reference configuration $\theta = 0$, so that no initial non-zero values need to be assigned.

By taking approximations for variables \mathbf{u} , p and θ as,

$$\mathbf{u} = \mathbf{N}_u \bar{\mathbf{u}}; \quad p = \mathbf{N}_p \bar{p}; \quad \theta = \mathbf{N}_{\theta} \bar{\theta} \quad (4.74)$$

and equating the first variation of (4.71) to zero results in a nonlinear system of equations given as,

$$\Psi = \begin{Bmatrix} \mathbf{R}_u \\ \mathbf{R}_p \\ \mathbf{R}_\theta \end{Bmatrix} = \mathbf{0} \quad (4.75)$$

where,

$$\mathbf{R}_u = \int_{\Omega} \mathbf{B}^T \check{\boldsymbol{\sigma}} \bar{J} \, d\Omega - \mathbf{f}_{\text{ext}} \quad (4.76)$$

$$\mathbf{R}_\theta = \int_{\Omega} \mathbf{N}_\theta^T (\bar{p} - p) \, d\Omega \quad (4.77)$$

$$\mathbf{R}_p = \int_{\Omega} \mathbf{N}_p^T (J - \bar{J}) \, d\Omega \quad (4.78)$$

The Newton-Raphson scheme to solve (4.75) gives the following algebraic problem,

$$\begin{bmatrix} \mathbf{K}_{uu} & \mathbf{K}_{u\theta} & \mathbf{K}_{up} \\ \mathbf{K}_{\theta u} & \mathbf{K}_{\theta\theta} & \mathbf{K}_{\theta p} \\ \mathbf{K}_{pu} & \mathbf{K}_{p\theta} & \mathbf{0} \end{bmatrix} \begin{Bmatrix} d\bar{\mathbf{u}} \\ d\bar{\boldsymbol{\theta}} \\ d\bar{p} \end{Bmatrix} = - \begin{Bmatrix} \mathbf{R}_u \\ \mathbf{R}_\theta \\ \mathbf{R}_p \end{Bmatrix} \quad (4.79)$$

where,

$$\mathbf{K}_{uu} = \int_{\Omega} \mathbf{B}^T \bar{\mathbf{D}}_{11} \mathbf{B} \, \bar{J} \, d\Omega + \mathbf{K}_G \quad (4.80)$$

$$\mathbf{K}_{u\theta} = \int_{\Omega} \mathbf{B}^T \bar{\mathbf{D}}_{12} \mathbf{N}_\theta \, d\Omega = \mathbf{K}_{\theta u}^T \quad (4.81)$$

$$\mathbf{K}_{up} = \int_{\Omega} \mathbf{B}^T \mathbf{m} \mathbf{N}_p \, J \, d\Omega = \mathbf{K}_{pu}^T \quad (4.82)$$

$$\mathbf{K}_{\theta\theta} = \int_{\Omega} \mathbf{N}_\theta^T \bar{\mathbf{D}}_{22} \mathbf{N}_\theta \frac{1}{\bar{J}} \, d\Omega \quad (4.83)$$

$$\mathbf{K}_{\theta p} = - \int_{\Omega} \mathbf{N}_\theta^T \mathbf{N}_p \, d\Omega = \mathbf{K}_{p\theta}^T \quad (4.84)$$

$$(4.85)$$

where,

$$\bar{\mathbf{D}}_{11} = \bar{\mathbf{D}}_{\text{dev}} - \frac{2}{3} (\mathbf{m} \bar{\boldsymbol{\sigma}}_{\text{dev}}^{\text{T}} + \bar{\boldsymbol{\sigma}}_{\text{dev}} \mathbf{m}^{\text{T}}) + 2(\bar{p} - \check{p}) \mathbf{I}_0 - \left(\frac{2}{3} \bar{p} - \check{p} \right) \mathbf{m} \mathbf{m}^{\text{T}} \quad (4.86)$$

$$\bar{\mathbf{D}}_{12} = \frac{1}{3} \mathbf{I}_{\text{dev}} \bar{\mathbf{D}} \mathbf{m} + \frac{2}{3} \bar{\boldsymbol{\sigma}}_{\text{dev}} \quad (4.87)$$

$$\bar{\mathbf{D}}_{22} = \frac{1}{9} \mathbf{m}^{\text{T}} \bar{\mathbf{D}} \mathbf{m} - \frac{1}{3} \bar{p} \quad (4.88)$$

$$\check{\boldsymbol{\sigma}} = \bar{\boldsymbol{\sigma}} + \mathbf{m}(\check{p} - \bar{p}) \quad (4.89)$$

$$\check{p} = \frac{J}{\bar{J}} p \quad (4.90)$$

4.2.4 Stability conditions for mixed formulations

Mixed Galerkin formulations lead to saddle-point problems which are unstable; hence, they impose certain constraints on the approximation order of the different field variables for the solutions to be stable. The stability condition relevant for mixed formulations is known as the Ladyzhenskaya-Brezzi-Babuška (LBB) condition or *inf-sup* condition, see [6, 23]. It is difficult to select the function spaces for displacement and pressure satisfying the LBB condition. It is almost impossible, in general, to test whether a particular pair of function spaces for displacement and pressure satisfy the LBB condition. Nevertheless, a condition — which the displacement and pressure DOFs have to satisfy — can be derived in a finite element setting (refer to [92]).

Assuming n_u , n_p and n_θ as the number of unknown displacements, pressures and volumetric strains, respectively, the constraint condition for a two-field mixed formulation is given as,

$$n_u \geq n_p \quad (4.91)$$

and for three-field mixed formulation as,

$$n_\theta \geq n_p \quad \text{and} \quad n_u \geq n_p \quad (4.92)$$

The above constraint conditions are just necessary but not sufficient to ensure that no locking occurs as incompressibility limit is approached. But they do provide a guideline to construct possible approximations for a particular problem.

Defining a constraint ratio, r_c , as,

$$r_c = \frac{n_u}{n_p} \quad (4.93)$$

it can be derived from the LBB condition, for a two-dimensional problem, that $r_c = 2$ would be an ideal value (refer to Chapter 4 in [40]). $r_c < 2$ indicates that the element has a tendency to lock; $r_c \leq 1$ means a severe locking problem; and $r_c \geq 2$ means that there are too few constraint variables to accurately represent

incompressibility. In terms of degree of the approximating polynomials, the general requirement is that primary variables, displacements in this context, should be one order higher than that of constraint variables — p , θ and \bar{J} .

4.3 NURBS spaces for mixed methods

As discussed in Section 2.4, the basic idea of IGA is to use the same basis functions used to represent the geometry of the domain as the approximating functions for the field variables. By using the NURBS as approximating functions, the field variables can be approximated as,

$$\mathbf{u} = \sum_{\alpha=0} \mathbf{N}_{\alpha}(\boldsymbol{\xi}) \bar{\mathbf{u}}_{\alpha}; \quad \mathbf{p} = \sum_{\alpha=0} \mathbf{N}_{\alpha}(\boldsymbol{\xi}) \bar{\mathbf{p}}_{\alpha}; \quad \boldsymbol{\theta} = \sum_{\alpha=0} \mathbf{N}_{\alpha}(\boldsymbol{\xi}) \bar{\boldsymbol{\theta}}_{\alpha} \quad (4.94)$$

where $\boldsymbol{\xi} = \{\xi, \eta, \zeta\}$ are the parametric coordinates; $\bar{\mathbf{u}}_{\alpha}$, $\bar{\mathbf{p}}_{\alpha}$ and $\bar{\boldsymbol{\theta}}_{\alpha}$ are the values at control points; and $\mathbf{N}(\boldsymbol{\xi})$ are the multivariate basis functions determined from the knot vectors and degrees of polynomial in each parametric direction. $\mathbf{N}(\boldsymbol{\xi})$ are computed as tensor products of univariate basis functions, as,

$$\mathbf{N}(\boldsymbol{\xi}) = \mathbf{M}(\xi) \otimes \mathbf{M}(\eta) \quad \text{in 2D} \quad (4.95)$$

$$\mathbf{N}(\boldsymbol{\xi}) = \mathbf{M}(\xi) \otimes \mathbf{M}(\eta) \otimes \mathbf{M}(\zeta) \quad \text{in 3D} \quad (4.96)$$

where, $\mathbf{M}(\xi)$, $\mathbf{M}(\eta)$ and $\mathbf{M}(\zeta)$ are the univariate basis functions in ξ , η , and ζ directions, respectively.

As a convention to represent NURBS spaces of different orders, let us denote Q_a as approximations of order a . The continuity of Q_a elements within a patch can be of any order k — varying from 0 to $(a - 1)$ — depending upon the multiplicity of the internal knots. All the knot vectors are assumed to be open: a patch constructed on such knot vectors would be interpolatory at the ends; hence, in case of problems modelled with multiple patches, only \mathcal{C}^0 continuity is achieved across the patch interfaces.

Using the above convention, a general element for displacement formulation is denoted as Q_a and for two-field and three-field mixed formulations as Q_a/Q_{a-1} , meaning that displacements are approximated using NURBS of order a and the constraint variables — like *pressures* and *volumetric strains* — are approximated using NURBS of one order lower i.e., $(a - 1)$. So if the displacements are \mathcal{C}^{a-1} continuous across the element boundaries then the constraint variables are \mathcal{C}^{a-2} continuous. As an example consider basis functions for a one-dimensional patch of four-elements for different orders as shown in Figure 4.1. All these functions are $\mathcal{C}^{a-1}/\mathcal{C}^{a-2}$ continuous because there are no internal knots with multiplicity > 1 . Figures on the left hand side are approximations for displacements and those on the right hand side are approximations for constraint variables. It can be observed that the lowest order NURBS element Q_1/Q_0 with three-field mixed formulation coincides with the standard mean-dilation quadrilateral element of Nagtegaal *et al.* [59] and well known B-bar method — given in Hughes [40] and Zienkiewicz and Taylor [92].

In case of domains modelled with multiple patches, where only \mathcal{C}^0 continuity is maintained across interfaces, displacements are assumed to be \mathcal{C}^0 continuous and constraint variables are assumed to be \mathcal{C}^{-1} continuous across a patch interface.

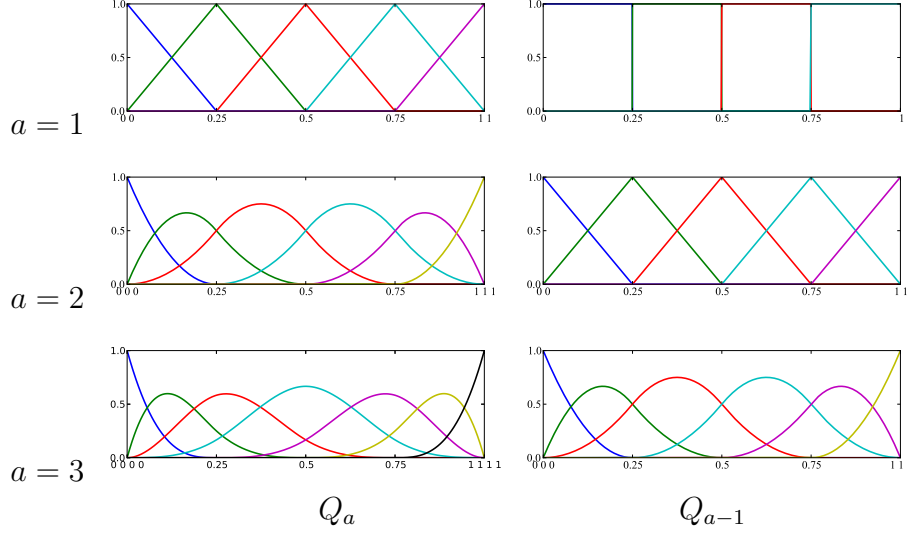


Figure 4.1: B-Spline basis functions for 1D patch of 4-elements with all the internal knots having multiplicity = 1. All the spaces have $\mathcal{C}^{a-1}/\mathcal{C}^{a-2}$ continuity.

4.3.1 Solving discrete equations arising from mixed formulations

If the constraint variables are assumed to be discontinuous across element boundaries then the global system of equations can be condensed as presented in [87]. But in the present work constraint variables are assumed to be continuous across the element boundaries — for all the orders ≥ 2 — and the discrete equations of mixed formulations are solved on the global level.

4.3.2 Equivalence of the two mixed formulations

The 3-field mixed Galerkin formulations proves to be superfluous for material models whose stored energy function can be decomposed into deviatoric and volumetric components. This can be demonstrated by numerical simulations with both formulations and comparing the results. But, this burden of performing numerical simulations can be avoided if it can be proved, mathematically, that the two formulations are equivalent by deducing the 2-field formulation from a 3-field formulation. The general 3-field mixed variational formulation,

for both the small strains and finite strains, can be written as,

$$\begin{bmatrix} \mathbf{K}_{uu} & \mathbf{K}_{u\theta} & \mathbf{K}_{up} \\ \mathbf{K}_{\theta u} & \mathbf{K}_{\theta\theta} & \mathbf{K}_{\theta p} \\ \mathbf{K}_{pu} & \mathbf{K}_{p\theta} & \mathbf{0} \end{bmatrix} \begin{Bmatrix} d\bar{\mathbf{u}} \\ d\bar{\boldsymbol{\theta}} \\ d\bar{\mathbf{p}} \end{Bmatrix} = - \begin{Bmatrix} \mathbf{R}_u \\ \mathbf{R}_\theta \\ \mathbf{R}_p \end{Bmatrix} \quad (4.97)$$

which can be condensed, on the global level, into,

$$\begin{bmatrix} \bar{\mathbf{K}}_{uu} & \bar{\mathbf{K}}_{up} \\ \bar{\mathbf{K}}_{pu} & -\bar{\mathbf{K}}_{pp} \end{bmatrix} \begin{Bmatrix} d\bar{\mathbf{u}} \\ d\bar{\mathbf{p}} \end{Bmatrix} = - \begin{Bmatrix} \bar{\mathbf{R}}_u \\ \bar{\mathbf{R}}_p \end{Bmatrix} \quad (4.98)$$

where,

$$\bar{\mathbf{K}}_{uu} = \mathbf{K}_{uu} - \mathbf{K}_{u\theta} \mathbf{K}_{\theta\theta}^{-1} \mathbf{K}_{\theta u} \quad (4.99)$$

$$\bar{\mathbf{K}}_{up} = \mathbf{K}_{up} - \mathbf{K}_{u\theta} \mathbf{K}_{\theta\theta}^{-1} \mathbf{K}_{\theta p} \quad (4.100)$$

$$\bar{\mathbf{K}}_{pu} = \mathbf{K}_{pu} - \mathbf{K}_{p\theta} \mathbf{K}_{\theta\theta}^{-1} \mathbf{K}_{\theta u} \quad (4.101)$$

$$\bar{\mathbf{K}}_{pp} = \mathbf{K}_{p\theta} \mathbf{K}_{\theta\theta}^{-1} \mathbf{K}_{\theta p} \quad (4.102)$$

$$\bar{\mathbf{R}}_u = \mathbf{R}_u - \mathbf{K}_{u\theta} \mathbf{K}_{\theta\theta}^{-1} \mathbf{R}_\theta \quad (4.103)$$

$$\bar{\mathbf{R}}_p = \mathbf{R}_p - \mathbf{K}_{p\theta} \mathbf{K}_{\theta\theta}^{-1} \mathbf{R}_\theta \quad (4.104)$$

4.3.2.1 Small Strain formulation

In small strain 3-field formulation, from (4.48),

$$\mathbf{K}_{u\theta} = \mathbf{K}_{\theta u}^T = \mathbf{0} \quad (4.105)$$

So,

$$\bar{\mathbf{K}}_{uu} = \mathbf{K}_{uu}; \quad \bar{\mathbf{K}}_{up} = \mathbf{K}_{up}; \quad \bar{\mathbf{K}}_{pu} = \mathbf{K}_{pu}; \quad \bar{\mathbf{R}}_u = -\mathbf{R}_u \quad (4.106)$$

Assuming that $\mathbf{N}_\theta = \mathbf{N}_p$, then equations (4.49b) and (4.49a) become,

$$\mathbf{K}_{p\theta} = \mathbf{K}_{\theta p}^T = - \int_{\Omega} \mathbf{N}_p^T \mathbf{N}_p \, d\Omega \quad (4.107)$$

$$\mathbf{K}_{\theta\theta} = -\kappa \mathbf{K}_{p\theta} = -\kappa \mathbf{K}_{\theta p} \quad (4.108)$$

Therefore,

$$\mathbf{K}_{p\theta} \mathbf{K}_{\theta\theta}^{-1} = -\frac{1}{\kappa} \quad (4.109)$$

So, from (4.102) and (4.104),

$$\bar{\mathbf{K}}_{pp} = \frac{1}{\kappa} \int_{\Omega} \mathbf{N}_p^T \mathbf{N}_p \, d\Omega \quad (4.110)$$

$$\begin{aligned} \text{and} \quad \bar{\mathbf{R}}_p &= \mathbf{R}_p + \frac{1}{\kappa} \mathbf{R}_\theta \\ &= \int_{\Omega} \mathbf{N}_p^T [\mathbf{m}^T \boldsymbol{\varepsilon} - \varepsilon_v] \, d\Omega + \frac{1}{\kappa} \int_{\Omega} \mathbf{N}_\theta^T [\kappa \varepsilon_v - p] \, d\Omega \\ &= \int_{\Omega} \mathbf{N}_p^T \left[\mathbf{m}^T \boldsymbol{\varepsilon} - \frac{p}{\kappa} \right] \, d\Omega \end{aligned} \quad (4.111)$$

It can be clearly observed that $\bar{\mathbf{K}}_{pp}$ and $\bar{\mathbf{R}}_p$ are exactly the same as (4.42c) and (4.40b). So, for the pressure-insensitive materials and when $\mathbf{N}_\theta = \mathbf{N}_p$, it is proven that 3-field formulation is equivalent to 2-field formulation in small strain regime.

4.3.2.2 Large Strain formulation

The equivalence of 3-field and 2-field formulations, for the considered assumptions, in large strain regime is presented by considering a material model whose free energy function can be additively decomposed into deviatoric and volumetric components, as,

$$W(J, \bar{\mathbf{b}}) = \bar{W}(\mathbf{I}_{\bar{\mathbf{b}}}, J) + \kappa U(J) \quad (4.112)$$

with

$$\mathbf{I}_{\bar{\mathbf{b}}} = \text{tr}(\bar{\mathbf{b}}) = J^{-2/3} \text{tr}(\mathbf{b}) = J^{-2/3} \mathbf{I}_{\mathbf{b}} \quad (4.113)$$

where $U(J)$ is the energy function corresponding to the volumetric part and the deviatoric part, \bar{W} , is assumed to be a function of $\mathbf{I}_{\bar{\mathbf{b}}}$ and J only. It is to be noted that, in the 3-field formulation, J is replaced by its approximation value \bar{J} .

For the free energy function (4.112), the elasticity matrix, $\bar{\mathbf{D}}$, is given by,

$$\bar{\mathbf{D}} = \bar{\mathbf{D}}_{\text{dev}} + \bar{\mathbf{D}}_{\text{vol}} \quad (4.114)$$

where,

$$\bar{\mathbf{D}}_{\text{dev}} = \frac{4}{\bar{J}} \begin{bmatrix} \mathbf{b} & \frac{1}{2} \bar{J} \mathbf{m} \end{bmatrix} \begin{bmatrix} \frac{\partial^2 \bar{W}}{\partial \mathbf{I}_{\bar{\mathbf{b}}}^2} & \frac{\partial^2 \bar{W}}{\partial \mathbf{I}_{\bar{\mathbf{b}}} \partial J} \\ \frac{\partial^2 \bar{W}}{\partial J \partial \mathbf{I}_{\bar{\mathbf{b}}}} & \frac{\partial^2 \bar{W}}{\partial J^2} \end{bmatrix} \begin{Bmatrix} \mathbf{b}^T \\ \frac{1}{2} \bar{J} \mathbf{m}^T \end{Bmatrix} + (\mathbf{m} \mathbf{m}^T - 2 \mathbf{I}_0) \frac{\partial \bar{W}}{\partial \bar{J}} \quad (4.115)$$

$$\bar{\mathbf{D}}_{\text{vol}} = \kappa \left(\frac{\partial U}{\partial \bar{J}} + \bar{J} \frac{\partial^2 U}{\partial \bar{J}^2} \right) \mathbf{m} \mathbf{m}^T - 2\kappa \frac{\partial U}{\partial \bar{J}} \mathbf{I}_0 \quad (4.116)$$

and the Cauchy stress tensor,

$$\bar{\boldsymbol{\sigma}} = \bar{\boldsymbol{\sigma}}_{\text{dev}} + \bar{p} \mathbf{m} \quad (4.117)$$

where,

$$\bar{\boldsymbol{\sigma}}_{\text{dev}} = \frac{2}{\bar{J}} \frac{\partial \bar{W}}{\partial \mathbf{I}_{\bar{\mathbf{b}}}} \bar{\mathbf{b}}_{\text{dev}} \quad \text{and} \quad \bar{p} = \kappa \frac{\partial U}{\partial \bar{J}} \quad (4.118)$$

So, after making use of (4.113) into (4.115) and further simplification,

$$\bar{\mathbf{D}} \mathbf{m} = -\frac{4}{\bar{J}} \frac{\partial \bar{W}}{\partial \mathbf{I}_{\bar{\mathbf{b}}}} \bar{\mathbf{b}}_{\text{dev}} + \kappa \left(\frac{\partial U}{\partial \bar{J}} + 3\bar{J} \frac{\partial^2 U}{\partial \bar{J}^2} \right) \mathbf{m} \quad (4.119)$$

Using equations (4.118) and (4.119),

$$\bar{\mathbf{D}}_{12} = \frac{1}{3} \mathbf{I}_{\text{dev}} \bar{\mathbf{D}} \mathbf{m} + \frac{2}{3} \bar{\boldsymbol{\sigma}}_{\text{dev}} = \mathbf{0} \quad (4.120)$$

Therefore,

$$\mathbf{K}_{u\theta} = \mathbf{K}_{\theta u}^T = \int_{\Omega} \mathbf{B}^T \bar{\mathbf{D}}_{12} \mathbf{N}_{\theta} \, d\Omega = \mathbf{0} \quad (4.121)$$

and, (4.106) follows. In addition,

$$\frac{\bar{\mathbf{D}}_{22}}{\bar{J}} = \frac{1}{\bar{J}} \left[\frac{1}{9} \mathbf{m}^T \bar{\mathbf{D}} \mathbf{m} - \frac{1}{3} \bar{p} \right] = \kappa \frac{\partial^2 U}{\partial \bar{J}^2} \quad (4.122)$$

In general $\bar{J} \approx 1.0$ and for all the models considered for $U(\bar{J})$,

$$\frac{\partial^2 U}{\partial \bar{J}^2} \approx 1.0 \quad (4.123)$$

Hence,

$$\mathbf{K}_{\theta\theta} = \int_{\Omega} \mathbf{N}_{\theta}^T \bar{\mathbf{D}}_{22} \mathbf{N}_{\theta} \frac{1}{\bar{J}} \, d\Omega = \kappa \int_{\Omega} \mathbf{N}_{\theta}^T \mathbf{N}_{\theta} \, d\Omega \quad (4.124)$$

Assuming that $\mathbf{N}_{\theta} = \mathbf{N}_p$, then equations (4.107) - (4.110) follow. In addition,

$$\begin{aligned} \bar{\mathbf{R}}_p &= \mathbf{R}_p + \frac{1}{\kappa} \mathbf{R}_{\theta} \\ &= \int_{\Omega} \mathbf{N}_p^T [J - \bar{J}] \, d\Omega + \frac{1}{\kappa} \int_{\Omega} \mathbf{N}_{\theta}^T [\bar{p} - p] \, d\Omega \\ &= \int_{\Omega} \mathbf{N}_p^T \left[J - \bar{J} + \frac{\partial U}{\partial \bar{J}} - \frac{p}{\kappa} \right] \, d\Omega \end{aligned} \quad (4.125)$$

Now $\bar{\mathbf{R}}_p$ is the only term that depends up on \bar{J} and replacing \bar{J} with J thereby eliminating the need to store the control variables for θ ,

$$\bar{\mathbf{R}}_p = \int_{\Omega} \mathbf{N}_p^T \left[\frac{\partial U}{\partial J} - \frac{p}{\kappa} \right] \, d\Omega \quad (4.126)$$

For the functions of U used in general, it can be observed that $\frac{\partial U}{\partial J} \approx J - 1$. So, (4.126) results in the same convergence pattern as that of (4.62) during every load step. This proves the equivalence of the two mixed formulations in finite strains.

Therefore, same level of accuracy can be obtained with 2-field formulation at a much less computational cost, as total number DOFs in 2-field formulation are less compared to the 3-field formulation. This reduction in computational time proves to be highly advantageous in real world engineering simulations using NURBS based isogeometric analysis to deal with incompressible materials whose material model can be additively decomposed into deviatoric and volumetric components.

Chapter 5

Galerkin formulation - Numerical Examples

In this chapter, numerical examples for mixed Galerkin formulation developed in Chapter 4 are presented. All examples considered to demonstrate the performance of the proposed methods are benchmark problems widely studied in the literature. The global system of equations are solved using direct solvers [1, 2].

The number of Gauss points used in evaluating the element matrices and vectors is equal to $(a + 1)$, in each coordinate direction, for NURBS basis functions of degree a .

5.1 Numerical examples - small strain

5.1.1 Elastic plate with a circular hole

In order to demonstrate the performance of NURBS based IGA, a linear elastic plate with a circular hole in plane-stress condition and under in-plane loading is considered. Only a quarter portion is modelled because of symmetry of geometry and loading conditions as shown in Figure (5.1) along with the material properties and loading condition. As Poisson's ratio is only 0.3, this example is studied with pure displacement formulation only. The initial geometry is defined using the coarsest possible mesh and k -refinement is performed to get the desired discretisation. Because of the presence of circular hole, quadratic NURBS are the minimum basis required to model the geometry. The coarse mesh is defined with two elements as shown in Figure 5.2(a) and its corresponding control net in Figure 5.2(b). Different h -refinements used for the analysis are shown in Figure 5.3. A reparameterisation, see [65, 41] is performed in the first knot direction to get a rather uniformly distributed knot spacing throughout the domain. Contour plots of x-directional stress, σ_{xx} , for mesh-1, mesh-3, mesh-4 and mesh-6 for Q_2 NURBS, shown in Figure 5.4, indicate an improvement in σ_{xx} with the mesh refinement. From the theory of stress concentration it can be calculated that the maximum stress, for the parameters chosen in the

present example, is 30.4 MPa and the current analysis with mesh-6 with Q_2 NURBS gives 31.3 MPa, which is 2.96% higher than the theoretical value. The accuracy of the results can be further improved by h -, p - or k - refinements.

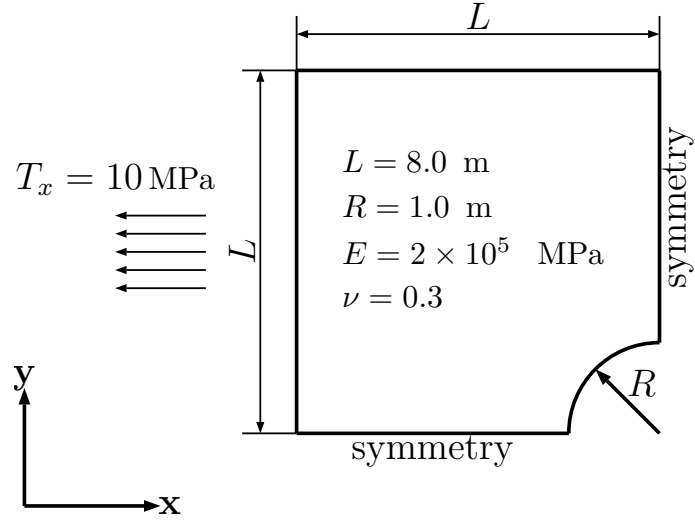


Figure 5.1: Plate with a circular hole: geometry, loading and material properties

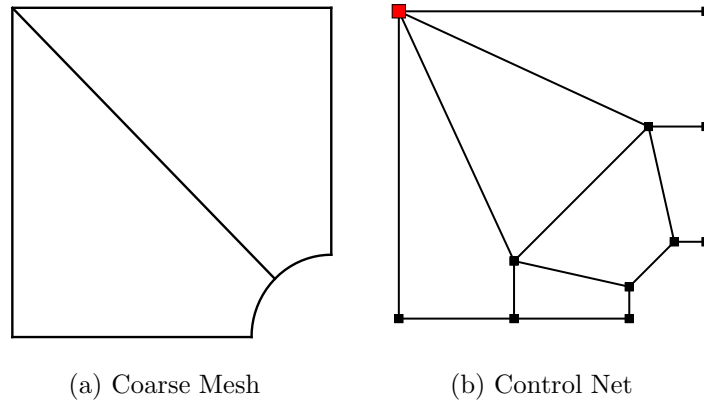


Figure 5.2: Plate with a circular hole: coarse mesh and its control net.

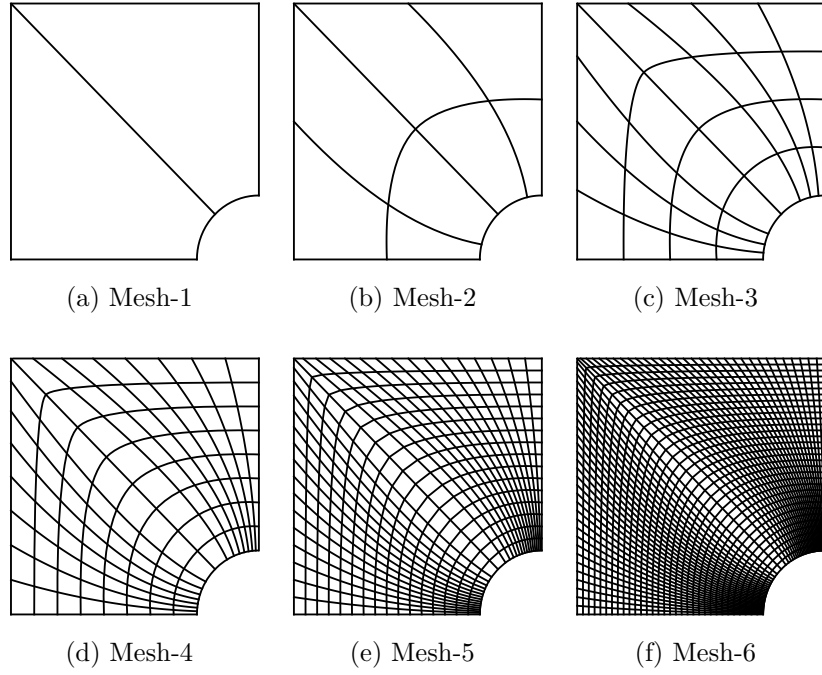


Figure 5.3: Plate with a circular hole: meshes generated by h -refinement, with reparameterization in first knot direction.

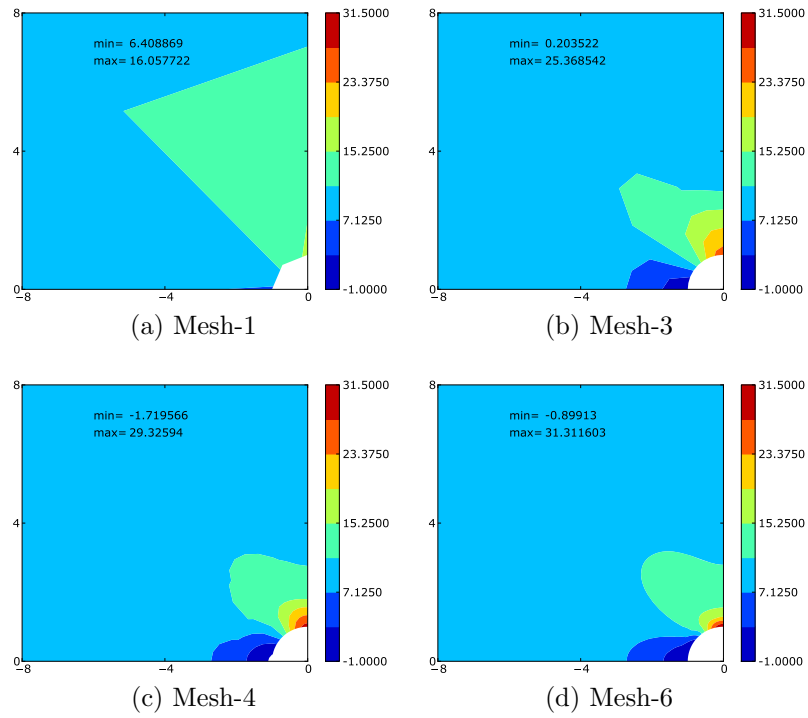


Figure 5.4: Plate with a circular hole: contour plots of stress σ_{xx} obtained with Q_2 NURBS.

5.1.2 Thick cylinder under internal pressure

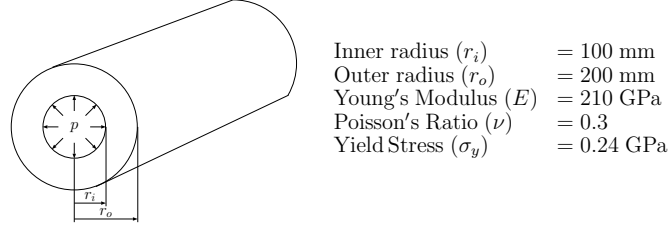


Figure 5.5: Thick cylinder under internal pressure: geometry, loading and material properties.

This example considers the analysis of a long metallic thick-walled cylinder subjected to internal pressure. The geometry of the problem and the material properties are shown in Figure 5.5. A perfectly elasto-plastic material with von Mises yield criteria is considered for the analysis. Plane strain condition is assumed because of geometry of the problem and only quarter portion of the cylinder is modelled because of the symmetry of geometry and loading conditions. A 32×32 mesh with quadratic NURBS is studied with pure displacement formulation. With the increase of internal pressure (p_i) plastic yielding starts at the inner surface (at radius r_i) and grows gradually towards the outer surface (at radius r_o) as shown in Figure 5.7. Failure occurs when the plastic front reaches the outer surface at which point entire cylinder has undergone yielding; after this point the cylinder will expand indefinitely without further increase in the load. For this problem analytical solutions derived by Hill [38, 61] are available for all the solution variables such as displacements, stresses and limit load. Using the analytical expression the limit load for the present problem is calculated to be 0.192 GPa. Analytical expressions for hoop stress ($\sigma_{\theta\theta}$) and radial stress (σ_{rr}) are given as:

- In the plastic region, i.e., for $r_i \leq r \leq r_c$,

$$\sigma_{rr} = \frac{\sigma_y}{\sqrt{3}} \left[-1 + \frac{r_c^2}{r_o^2} - 2 \ln \frac{r_c}{r_o} \right]; \quad \sigma_{\theta\theta} = \frac{\sigma_y}{\sqrt{3}} \left[1 + \frac{r_c^2}{r_o^2} - 2 \ln \frac{r_c}{r_o} \right] \quad (5.1)$$

- In the elastic region, i.e., for $r_c \leq r \leq r_o$,

$$\sigma_{rr} = \frac{p_c r_c^2}{r_o^2 - r_c^2} \left[1 - \frac{r_o^2}{r^2} \right]; \quad \sigma_{\theta\theta} = \frac{p_c r_c^2}{r_o^2 - r_c^2} \left[1 + \frac{r_o^2}{r^2} \right] \quad (5.2)$$

where p_c is the pressure acting on the elastic portion and r_c is the radius of elasto-plastic interface. Variation of radial displacement of a point on the external surface of the cylinder with respect to applied pressure, as shown in Figure 5.8, is in excellent agreement with the analytical solution. The

distribution of radial and hoop stresses along the thickness of the cylinder, as shown in Figure 5.10, also matches well with the analytical solution. Contour plots of von Mises stress for different values of applied pressure, as shown in Figure 5.9, show the propagation of plastic zone with the increase in pressure.

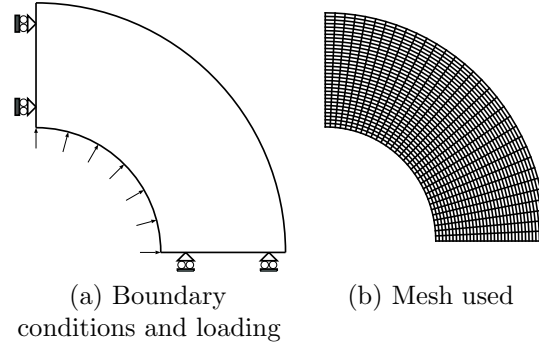


Figure 5.6: Thick cylinder under internal pressure.

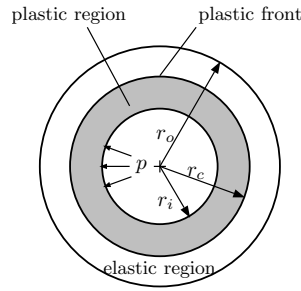


Figure 5.7: Thick cylinder under internal pressure: partly plastified cross-section.

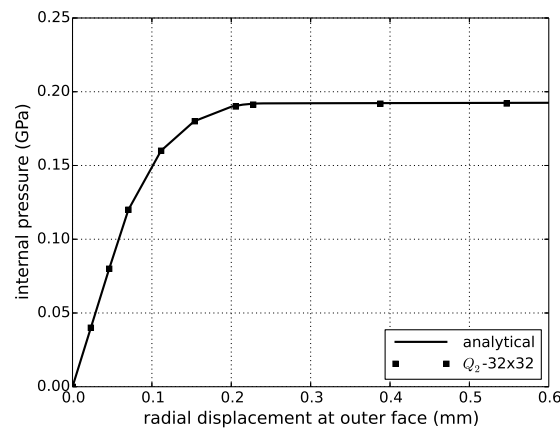


Figure 5.8: Thick cylinder under internal pressure: applied pressure versus displacement.

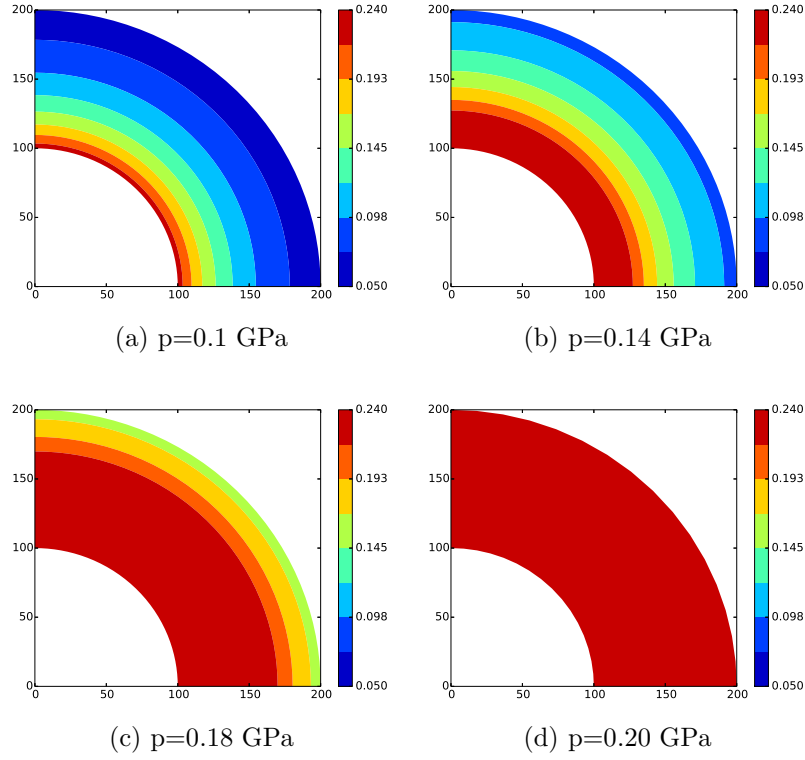


Figure 5.9: Thick cylinder under internal pressure: von Mises stress at different load levels for 32×32 mesh with Q_2 NURBS.

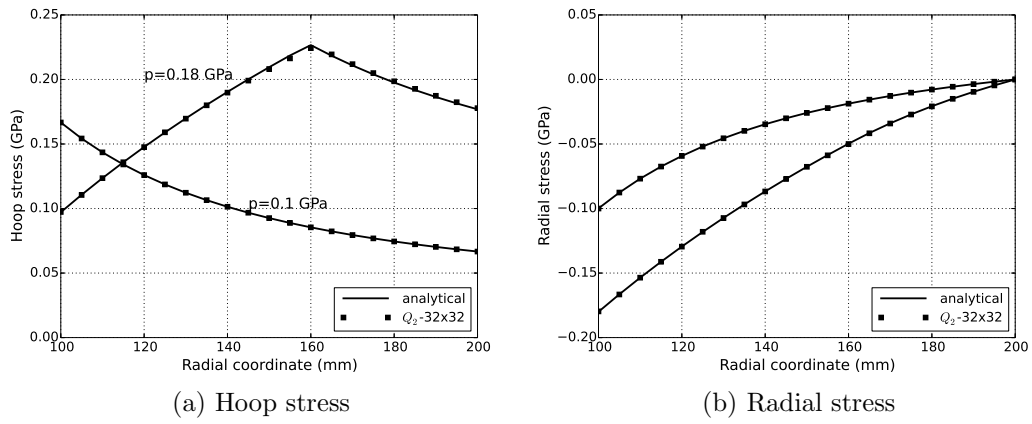


Figure 5.10: Thick cylinder under internal pressure: hoop and radial stress distribution along radial coordinate.

5.1.3 Cook's membrane with nearly incompressible linear elastic material

Cook's membrane is one of the benchmark problems used to study the quality of finite element formulation for incompressible solids. It has been studied by many authors [27, 60, 62] in the standard Finite Element formulations for large strains. To our knowledge only Elguedj *et al.* [33] studied Cook's membrane for small strains using NURBS based isogeometric analysis with $\bar{\mathbf{B}}$ formulation. Geometry, loading, boundary conditions and material properties are as shown in Figure 5.11. A load value of $F = 100$ N/mm is assumed to be uniformly distributed along the right edge. The initial mesh consists of a single element with linear NURBS; then k -refinement is performed to obtain the meshes shown in Figure 5.12. Analysis has been performed for different orders of NURBS, for each mesh, using both the displacement and mixed formulations in order to study their relative performances.

Figure 5.13 shows vertical displacement of the top right corner (point A in Figure 5.11) displayed against the number of elements per side for different orders of approximations. Lower order elements — linear and quadratic — with pure displacement formulation suffer from severe locking and the stiffening effect of locking disappears as the element order is increased. On the other hand, use of mixed formulation improves the accuracy of the results substantially: Q_1/Q_0 performs better than Q_2 ; Q_2/Q_1 performs better than Q_3 ; and Q_4/Q_3 element with just 2x2 mesh gives almost the converged value. Evidently, mixed formulation has helped to improve the accuracy of the result even for lower order elements. Figure 5.14 and Figure 5.15 show the contour plots of hydrostatic pressure and von Mises stress, respectively, for mesh-5 with Q_3 NURBS. As shown, mixed formulation gives a smooth variation of pressure compared to the displacement formulation.

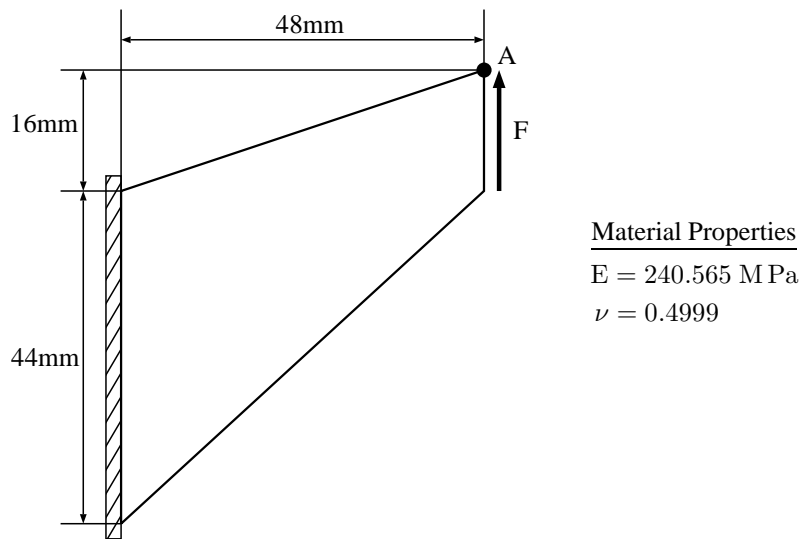


Figure 5.11: Cook's membrane: geometry, loading and material properties

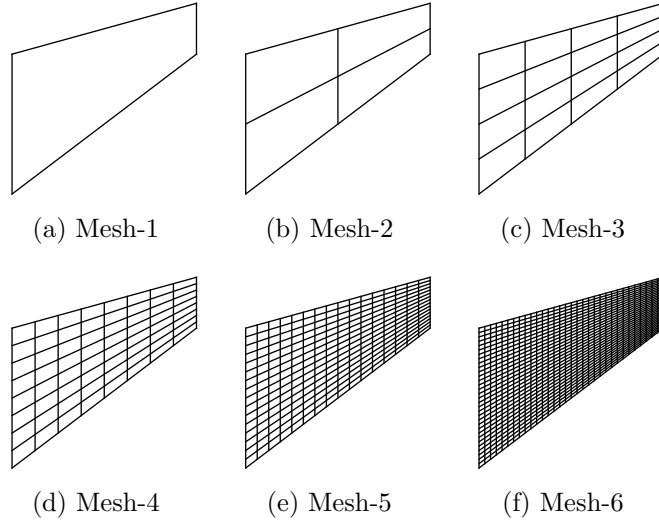


Figure 5.12: Cook's membrane: meshes generated by h -refinement

For this particular problem a closed form equation for constraint ratio (r_c) can be derived for 2-field mixed formulation, as,

$$r_c = \frac{2(n_e + a)}{(n_e + a - 1)} \quad (5.3)$$

where, n_e is the number of elements per side and a is the order of NURBS approximation for displacements — the order of NURBS approximation is assumed to be the same in both the directions. As n_e and/or a approach infinity r_c converges towards an optimal value, which is 2. This is immediately evident in the results.

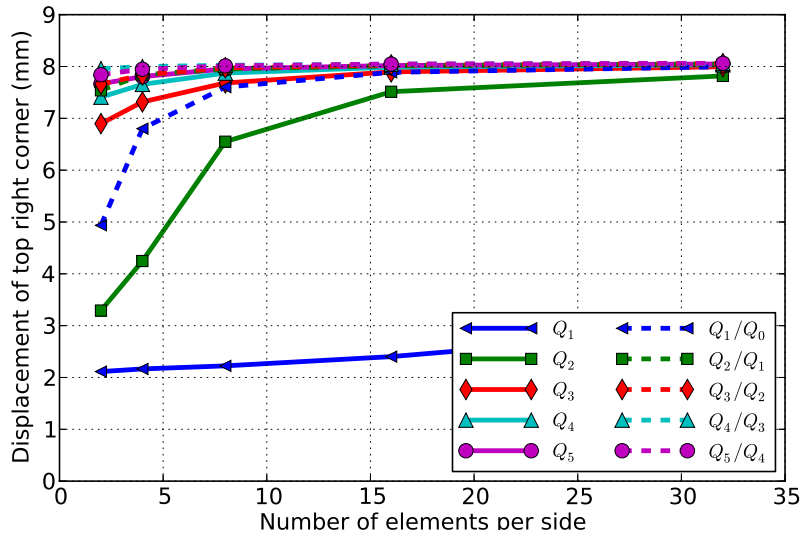
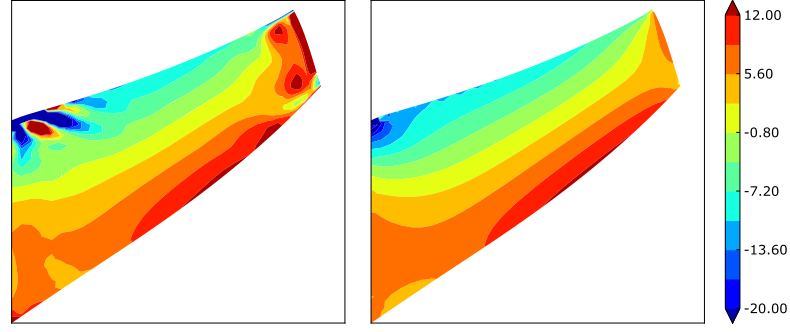


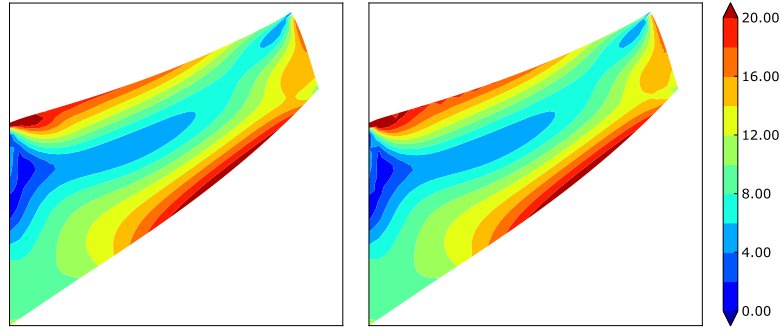
Figure 5.13: Cook's membrane with linear elastic material: vertical displacement of the top right corner against number of elements per side.



(a) displacement formulation

(b) mixed formulation

Figure 5.14: Cook's membrane with linear elastic material: hydrostatic pressure for mesh-5 with cubic NURBS.



(a) displacement formulation

(b) mixed formulation

Figure 5.15: Cook's membrane with linear elastic material: von Mises stress for mesh-5 with cubic NURBS

5.1.4 Strip Footing collapse

This example demonstrates the application of IGA to the determination of the limit load of a strip footing. This problem has been studied by de Souza Neto *et al.* [61] using the standard FEM. The problem consists of a long rectangular footing lying on soil. The footing is subjected to a vertical pressure and the purpose of analysis is to determine the collapse pressure, P_{lim} . The soil is assumed to be weightless and modelled as a perfectly plastic material with von Mises yield criteria. Due to the long length of the footing, the present problem is solved by assuming a plane strain state. Because of the symmetry of the problem geometry and loading, only one half of the cross-section is considered, as shown in Figure 5.16a, along with geometry, loading, boundary conditions and material properties. The footing is assumed to be rigid and footing/soil interface is assumed to be frictionless. This requires prescribing the vertical displacement u of the control points under the footing and allowing

their horizontal displacement to be unconstrained. A total displacement of $u = 0.002\text{m}$ is applied and the problem is solved in several load steps. The response is measured in terms of the normalized pressure (P/c), where P is total reaction on the footing and c is the cohesion or shear strength. For the von Mises model, $c = \sigma_y/\sqrt{3}$. Results from the current analysis are compared against the theoretical limit, calculated by Prandtl and Hill based on the slip-line theory, which for the chosen material properties is 5.14.

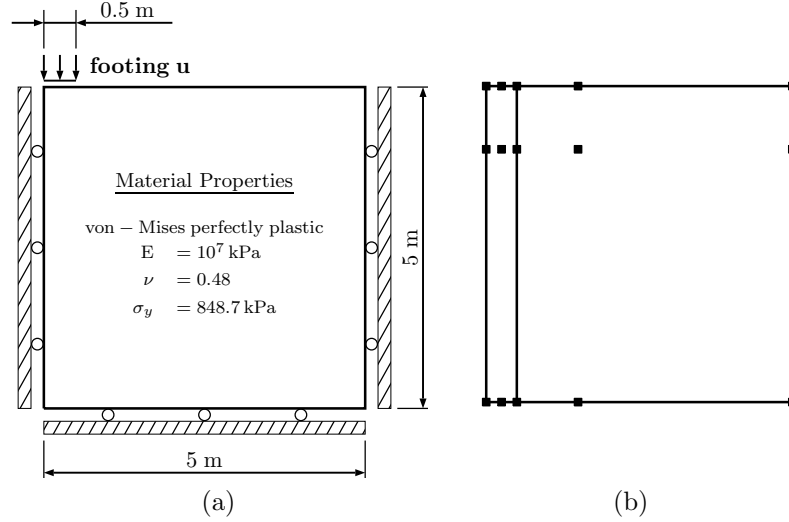


Figure 5.16: Strip footing collapse: a.) Geometry, loading, boundary conditions and material properties b.) Initial control mesh of two patch geometry.

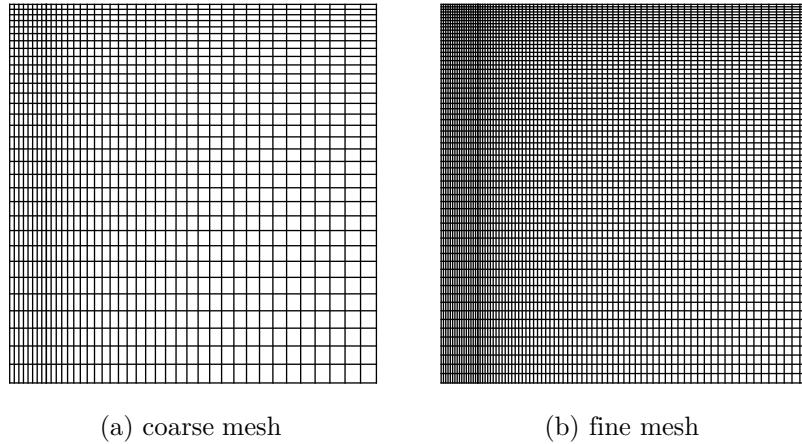


Figure 5.17: Strip footing collapse: meshes considered for the analysis.

The problem is modelled using two patches so that Dirichlet boundary conditions are applied exactly after refining the mesh using k -refinement. The initial mesh is modelled using quadratic NURBS with a single element in each patch and the initial control points used are as shown in Figure 5.16b. The

initial control points are chosen such that the mesh will be fine at the region of interest near the footing and coarse away from it. Two meshes, as shown in Figure 5.17, are considered to demonstrate the performance of IGA in computing the limit loads and slip lines. Analysis is performed for different orders of NURBS using both the displacement and mixed formulations.

5.1.4.1 Results for the coarse mesh

Figure 5.18(a) and Figure 5.18(b) show the computed normalized pressure (P/c) against normalized settlement (u/B), respectively, for displacement and mixed formulations and percentage errors in normalized pressure are tabulated in Table 5.1 to get a better picture of the variation of normalized pressure with different orders of approximations. Even though the collapse loads computed are within the acceptable limits for both displacement and mixed formulations, the accuracy of slip-lines from displacement formulation is very poor as shown in Figure 5.19. Use of mixed formulation substantially improves the accuracy of slip lines even for lower order elements, as shown in Figure 5.20. Contour plots of hydrostatic pressure for the displacement and mixed formulations are shown in Figure 5.21 and Figure 5.22, respectively.

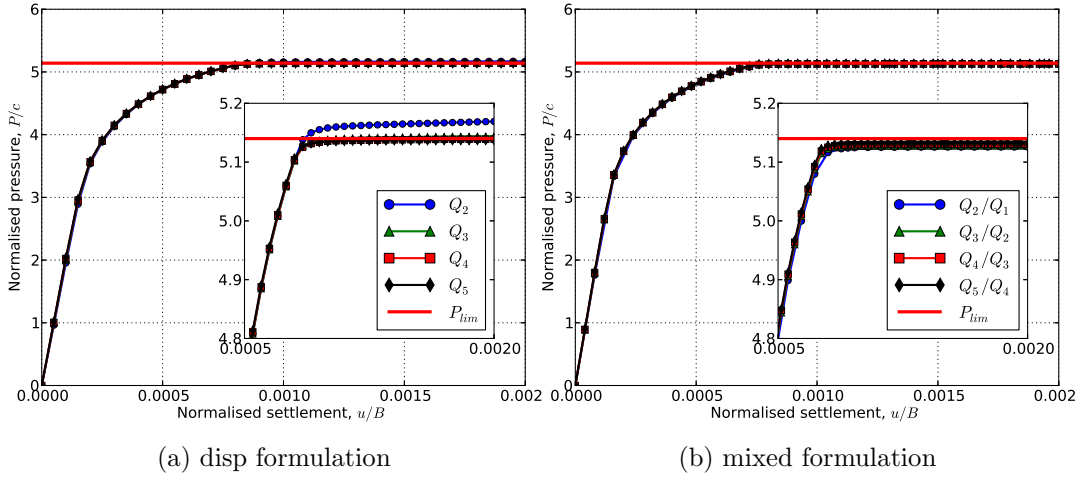


Figure 5.18: Strip footing collapse - coarse mesh: load-displacement curve.

Degree	disp-formulation	mixed formulation
Q_2	0.6	-0.3
Q_3	0.1	-0.2
Q_4	0.0	-0.2
Q_5	0.0	-0.1

Table 5.1: Strip footing collapse - coarse mesh: percentage error in normalized pressure for the coarse mesh

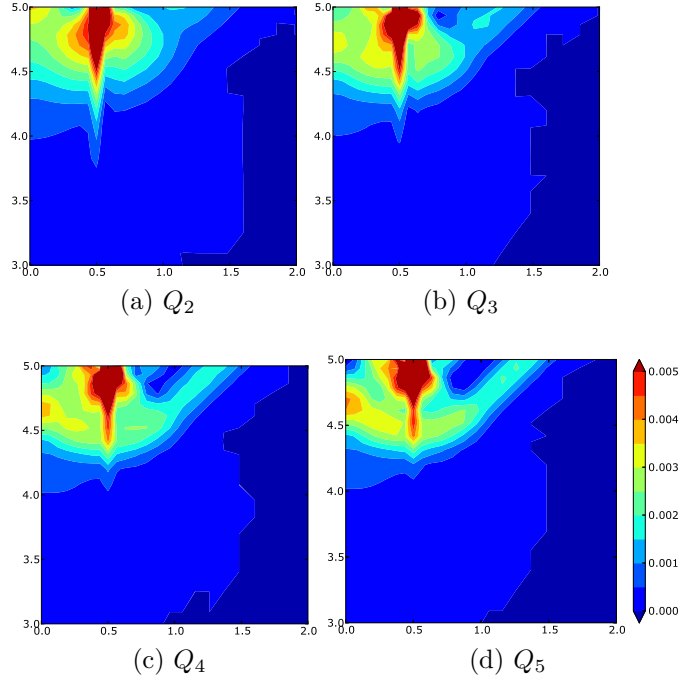


Figure 5.19: Strip footing collapse - coarse mesh: equivalent plastic strain with displacement formulation.

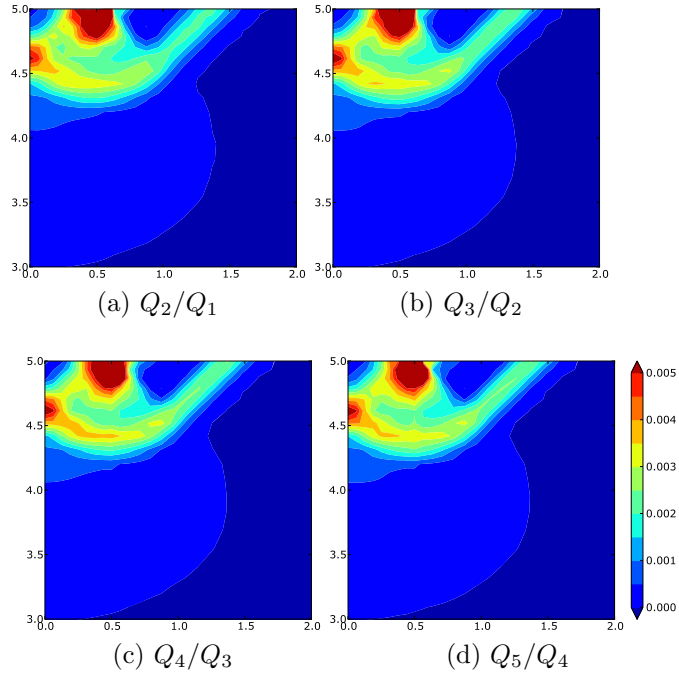


Figure 5.20: Strip footing collapse - coarse mesh: equivalent plastic strain with mixed formulation.

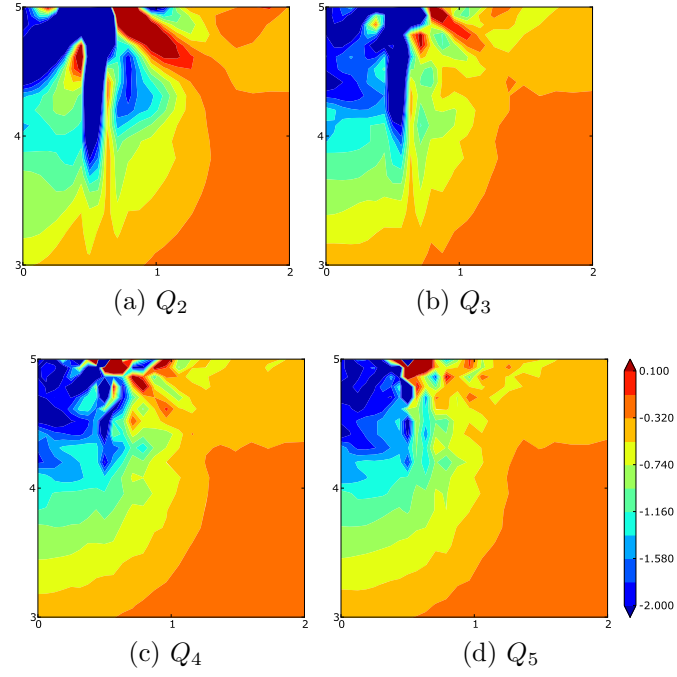


Figure 5.21: Strip footing collapse - coarse mesh: hydrostatic pressure with displacement formulation.

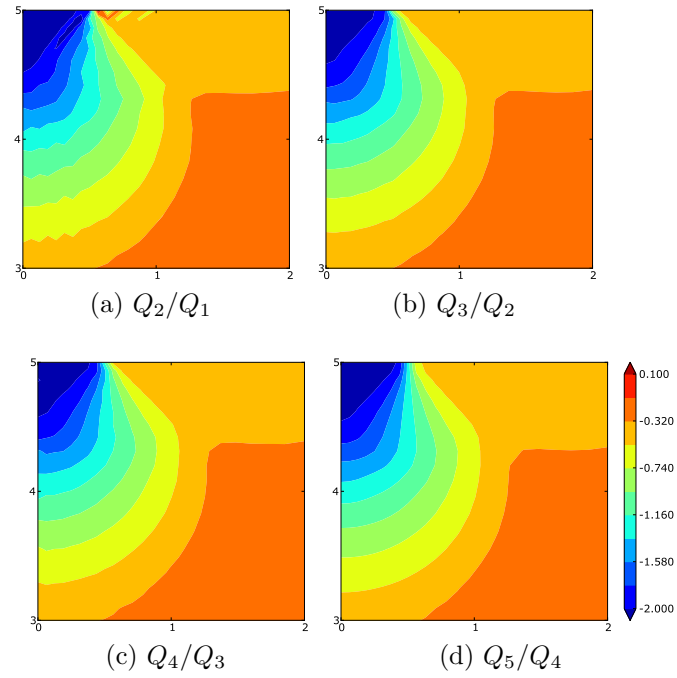


Figure 5.22: Strip footing collapse - coarse mesh: hydrostatic pressure with mixed formulation.

5.1.4.2 Results obtained with the fine mesh

Graphs of computed normalized pressure (P/c) against normalized settlement (u/B), are shown in Figure 5.23(a) and Figure 5.23(b) respectively, for displacement and mixed formulations, for different orders of approximations. Percentage errors in normalized pressure are tabulated in Table 5.2. Clearly, mixed formulation substantially improves the accuracy of slip lines, Figure 5.25, when compared to displacement formulation, Figure 5.24. Also, as the current mesh is obtained by h -refinement over the coarse mesh, the accuracy of slip lines improves significantly.

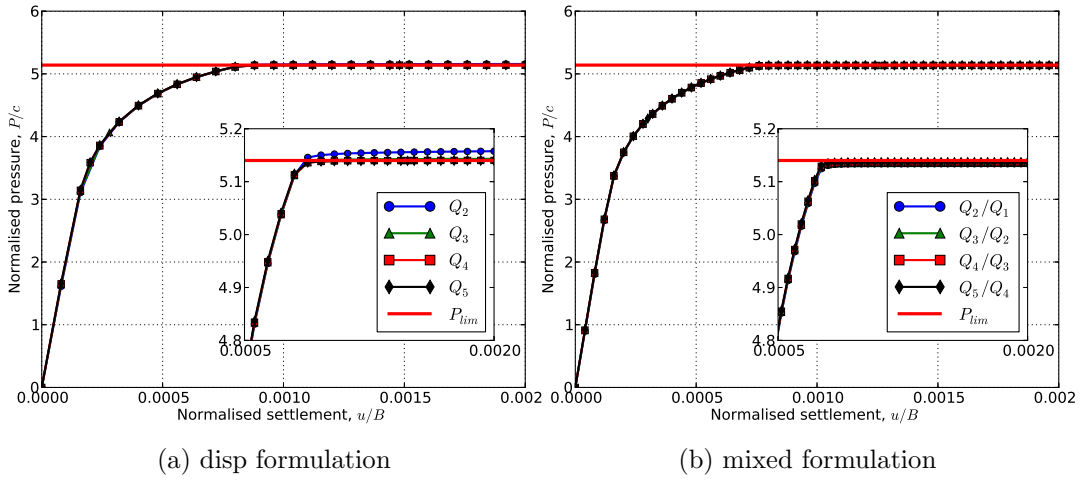


Figure 5.23: Strip footing collapse - fine mesh: load-displacement curve.

Degree	disp-formulation	mixed formulation
Q_2	0.3	-0.1
Q_3	0.1	-0.1
Q_4	0.0	-0.1
Q_5	0.0	0.0

Table 5.2: Strip footing collapse - fine mesh: percentage error in normalized pressure.

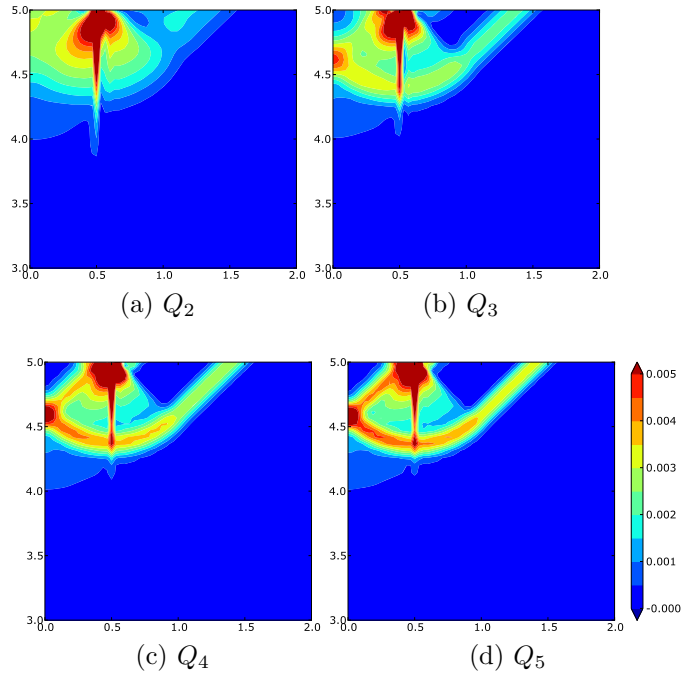


Figure 5.24: Strip footing collapse - fine mesh: equivalent plastic strain with displacement formulation.

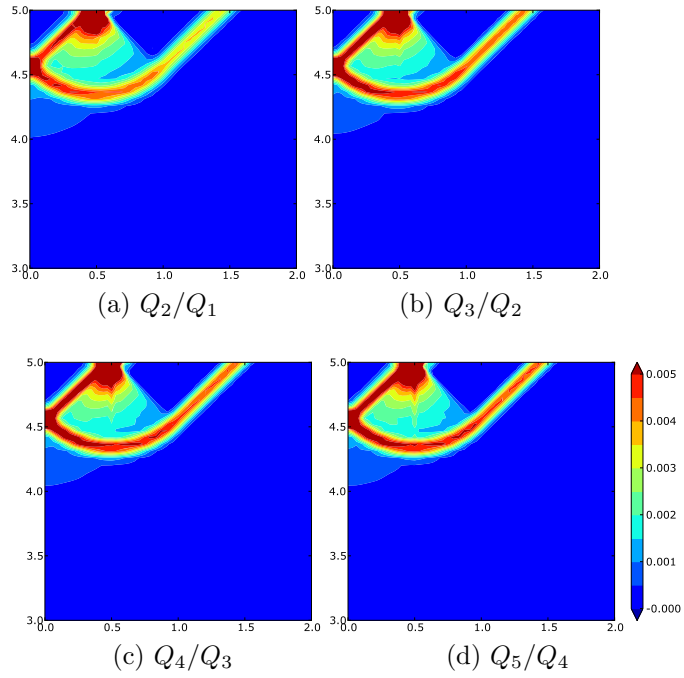


Figure 5.25: Strip footing collapse - fine mesh: equivalent plastic strain with mixed formulation.

5.1.5 Double-edge notched specimen

In this example, a deep double-edge notched specimen subjected to tensile loading is studied. This problem is a benchmark problem (see [59]), to test the finite element formulation for plasticity. Geometry, loading conditions and material properties are shown in Figure 5.26. The specimen is assumed to be in plane-strain condition. A perfectly plastic von Mises elasto-plastic material model is considered for the analysis. Because of obvious symmetry, only a quarter of the model is considered for the analysis and the geometry is modelled with two patches as in the previous example. A total displacement value of $u = 0.17$ is applied on the loading edge and the problem is solved in several load steps. Results are presented in terms of variation of normalized net stress, $\bar{\sigma}/\sigma_y$, versus the normalized edge deflection, \bar{u} , given as,

$$\bar{\sigma} = \frac{R}{B} \quad (5.4)$$

$$\bar{u} = 2uE/\sigma_y w \quad (5.5)$$

where, R is the total reaction on the restrained edge. For this problem, the limit value of normalized net stress, calculated by Prandtl, is 2.97. Similar to the previous problem, the analysis has been performed for different orders of NURBS discretisation using both displacement and mixed formulations. Figure 5.27 shows the variation of normalized net stress against normalized edge deflection for different orders of NURBS using both displacement and mixed formulations and percent errors in normalized net stress are shown in Table 5.3. Clearly mixed formulation improves the accuracy of the results and its advantages are clearly seen in the improved accuracy in prediction of slip lines, as shown in Figure 5.29, compared to the ones obtained using displacement formulation depicted in Figure 5.28.

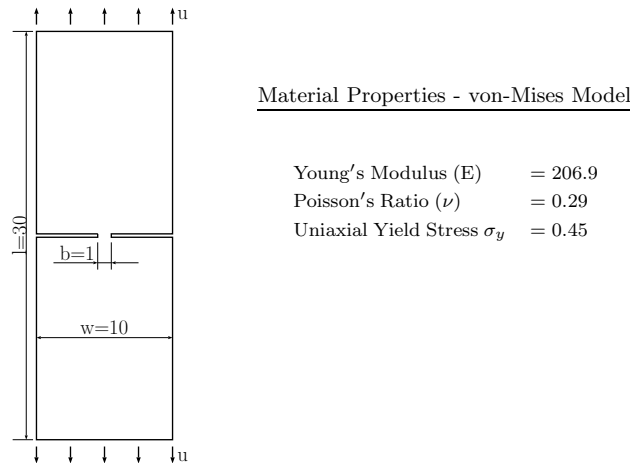


Figure 5.26: Double-edge notched tensile specimen: geometry, loading and material properties.

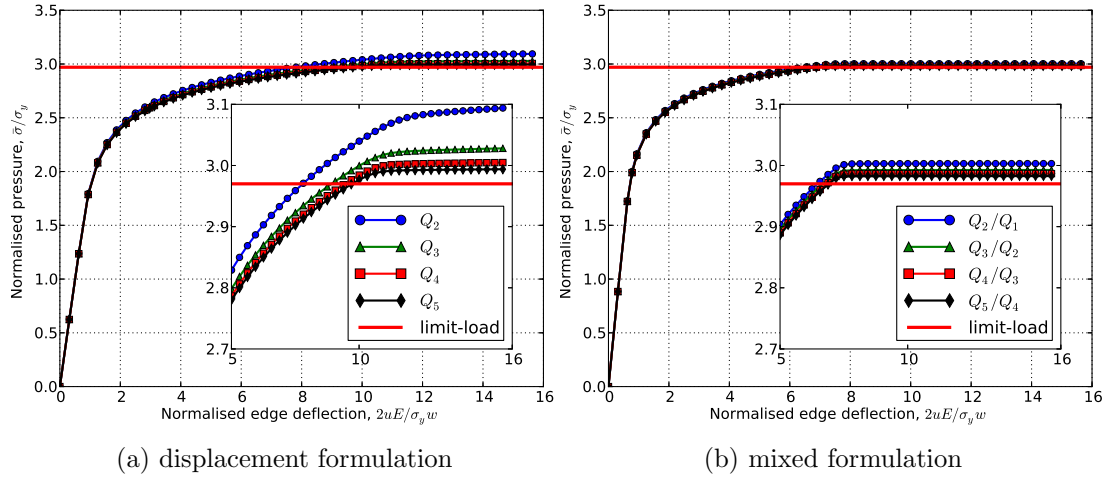


Figure 5.27: Double-edge notched specimen: load-displacement curve.

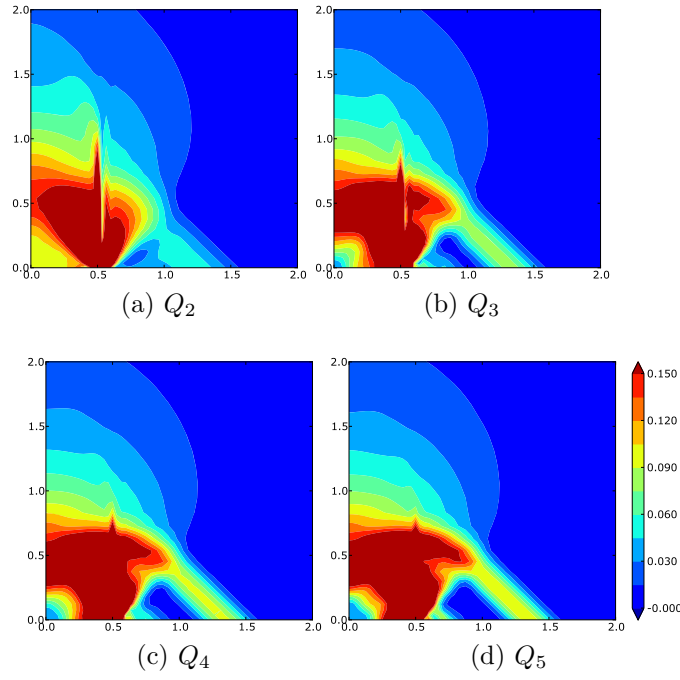


Figure 5.28: Double-edge notched specimen: equivalent plastic strain with displacement formulation.

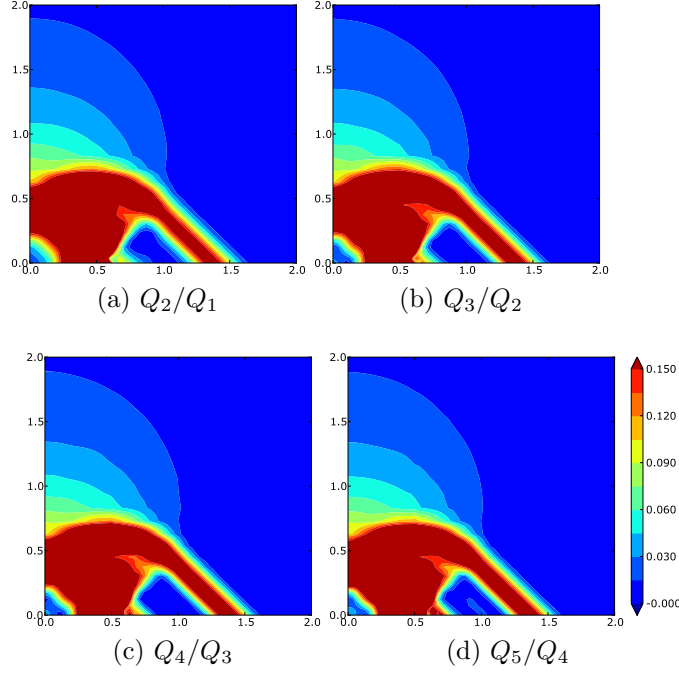


Figure 5.29: Double-edge notched specimen: equivalent plastic strain with mixed formulation.

Degree	disp-formulation	mixed formulation
Q_2	4.2	1.1
Q_3	1.9	0.8
Q_4	1.2	0.6
Q_5	0.8	0.4

Table 5.3: Double-edge notched specimen: percentage error in normalised pressure.

5.2 Numerical examples - Finite strain

5.2.1 Cook's membrane with Neo-Hookean material

The geometry, loading and boundary conditions of the problem are same as those in Figure 5.11 for small strain formulation. For the purpose of nonlinear analysis the material is modelled using the generalized Neo-Hookean hyperelastic material model whose stored energy function can be additively decomposed into distortional and volumetric parts, given by,

$$W(J, \bar{\mathbf{C}}) = \frac{1}{2}\mu (\text{I}_{\bar{\mathbf{C}}} - 3) + \frac{1}{2}\kappa \left(\frac{1}{2}(J^2 - 1) - \ln J \right) \quad (5.6)$$

The material properties considered are $\kappa = 40.0942 \times 10^4$ MPa and $\mu = 80.1938$ MPa. A load value of $F = 100$ N/mm is chosen and it is assumed

that the load is a "dead load" — a fixed load value equal to that in the reference configuration is assumed to act during the entire deformation. Similar to small strain formulation, analysis is performed for different orders of NURBS, for each of the 5 meshes in Figure 5.12, using both the displacement and mixed formulations. The response parameter, again, is the vertical displacement of the top right corner. Results are presented in Figure 5.30, in terms of response parameter against the number of elements per side and the converged pattern of results is exactly similar to that observed in small strain example.

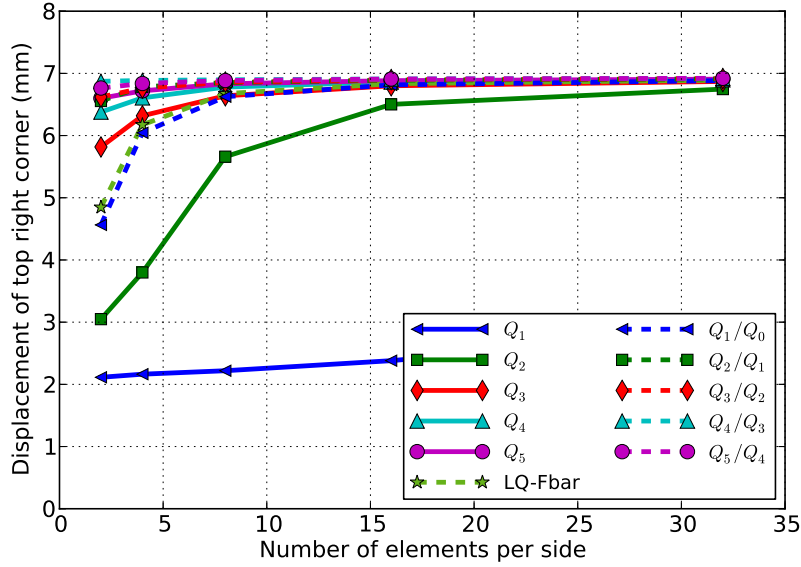


Figure 5.30: Cook's membrane with Neo-Hookean material: convergence of vertical displacement of top right corner with respect to number of elements.

In order to evaluate the performance of the present methods, results obtained with Q_1/Q_0 NURBS are compared with those obtained using the standard linear quadrilateral element with F-bar formulation of de Souza Neto [60] — denoted by LQ-Fbar. Lower order NURBS elements with pure displacement formulation suffer from severe locking problem and accuracy of the results improves with increasing the order of approximation. However, use of mixed formulation substantially improves the accuracy of results as observed in small strain formulation: Q_1/Q_0 gives improved results over Q_2 ; Q_2/Q_1 over Q_3 ; and Q_4/Q_3 with 2×2 mesh gives almost same result as that of Q_4 and Q_5 with 5×5 elements. To sum up, higher order NURBS elements with mixed formulation gives converged solution even for very coarse meshes.

Table 5.4 shows the evolution of L_2 norm of the residual over different iterations for the last substep of mesh-3 with quadratic NURBS for both the formulations. Figure 5.31 shows contour plots of hydrostatic pressure for cubic NURBS for mesh-5. Clearly, mixed formulations, as shown in Figure 5.31b, give a smooth variation of pressure compared to displacement formulation. In addition, as the von Mises stress is independent of hydrostatic pressure, both the formulations give almost identical smooth plots, as shown in Figure 5.32.

Iteration number	Norm of residue	
	Displacement formulation	Mixed formulation
1	4.4096 E+00	4.4096 E+00
2	6.1663 E+02	4.4412 E−01
3	5.7846 E−02	2.0535 E−04
4	1.7704 E−02	4.9694 E−11
5	1.2250 E−08	

Table 5.4: Cook’s membrane with NeoHookean material: evolution of norm of residual for the last sub-step for mesh-3 with Q_2 NURBS.

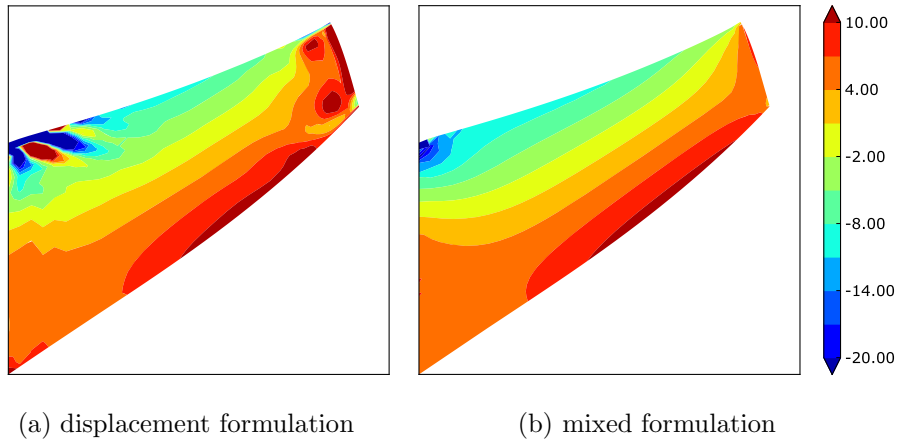


Figure 5.31: Cook’s membrane with Neo-Hookean material: hydrostatic pressure for mesh-5 with Q_3 NURBS.

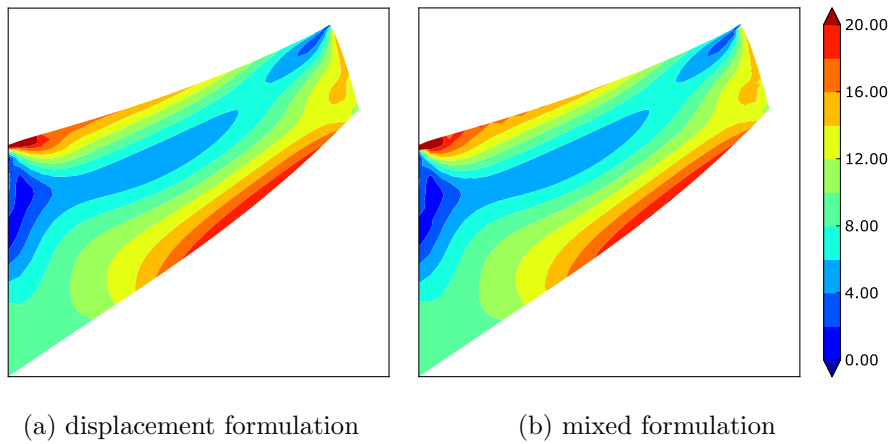


Figure 5.32: Cook’s membrane with Neo-Hookean material: equivalent stress for mesh-5 with Q_3 NURBS.

5.2.2 Cook's membrane with von Mises elasto-plastic material

In this example, Cook's membrane with elasto-plastic material model is studied. The material model consists of uncoupled stored energy with Neo-Hookean hyperelastic model for the elastic deformations and a plasticity model with associative flow rule based on a von Mises yield criterion with isotropic nonlinear hardening for the plastic portion. Neo-Hookean material model is identical to the one used in the previous example and the nonlinear isotropic hardening law is given by (3.69) with the material properties given in Table 5.5.

Bulk Modulus, κ	164.21 MPa
Shear Modulus, μ	80.1938 MPa
Initial flow stress, σ_0	0.45 MPa
Saturation flow stress, σ_∞	0.715 MPa
Saturation exponent, δ	16.93
Linear hardening coefficient, H	0.12924 MPa

Table 5.5: Material properties for Cook's membrane with elasto-plastic material.

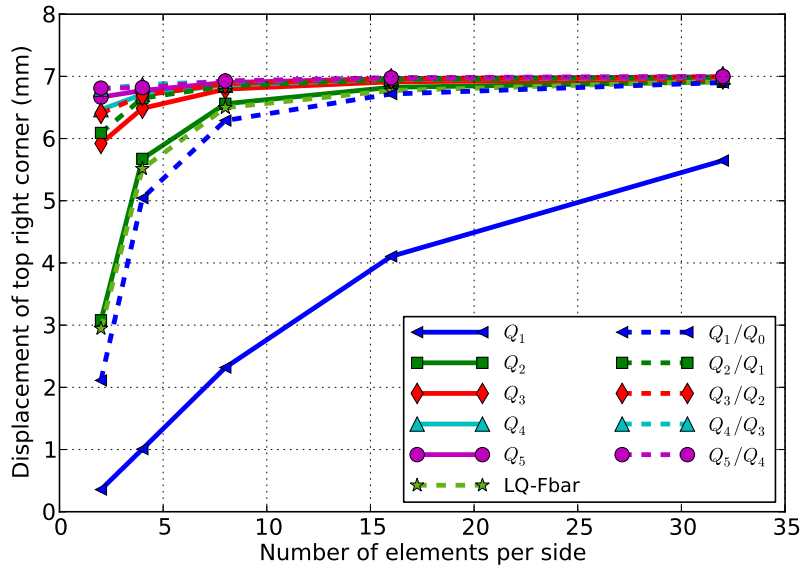


Figure 5.33: Cook's membrane with elasto-plastic material: convergence of vertical displacement of top right corner with respect to number of elements.

Similar to the previous example, analysis is performed for different orders of approximations for all the 5 meshes using both displacement and mixed formulations and a similar pattern in the convergence of results is observed. Variation of the displacement of top right corner against the number of elements per side, for different orders of approximations, is shown in Figure

5.33. As observed in the previous example, mixed formulations substantially improve the accuracy of the results. Table 5.6 shows the evolution of L_2 norm of the residual over different iterations for the last sub-step of mesh-3 with Q_2 NURBS for both the formulations. Figures 5.34 and 5.35 show the contour plots of equivalent plastic strain and von Mises stress, respectively, for both the formulations for mesh-5 with Q_3 NURBS.

Iteration number	Norm of residue	
	Displacement formulation	Mixed formulation
1	2.2048 E−01	2.2048 E−01
2	1.7653 E+00	1.7471 E+00
3	1.4690 E+01	2.3391 E+00
4	4.8451 E−01	7.1186 E−01
5	2.0579 E−01	8.8811 E−02
6	2.4905 E−04	4.3964 E−03
7	1.2486 E−06	1.3026 E−05
8	2.5026 E−09	8.9505 E−09

Table 5.6: Cook’s membrane with elasto-plastic material: evolution of norm of residual for the last substep for mesh-3 with Q_2 NURBS.

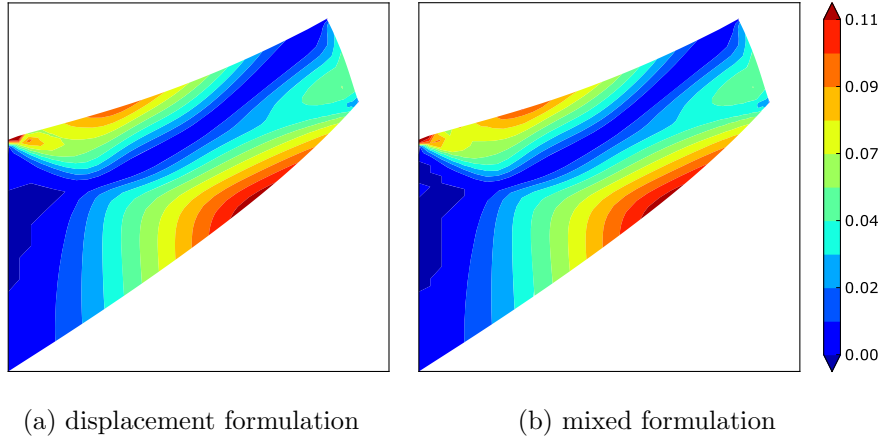


Figure 5.34: Cook’s membrane with elasto-plastic material: equivalent plastic strain for mesh-5 with Q_3 NURBS.

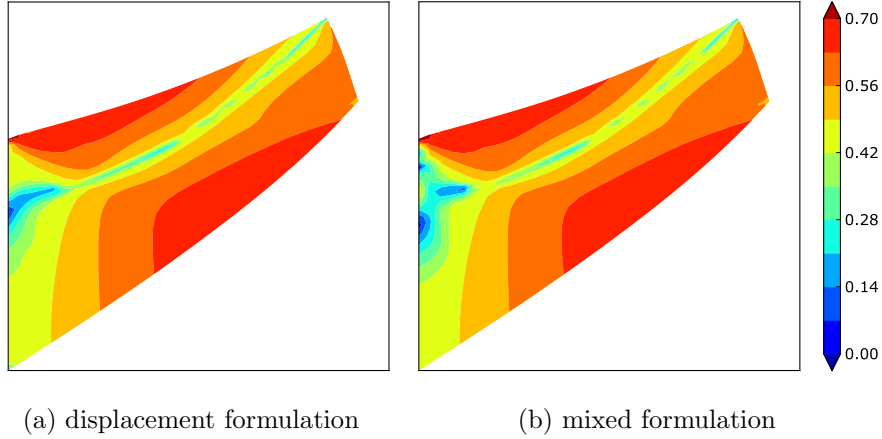


Figure 5.35: Cook's membrane with elasto-plastic material: von Mises stress for mesh-5 with Q_3 NURBS.

5.2.3 Compression of a plane-strain block

This problem consists of a block resting on a rigid surface and subjected to pressure loading at its middle portion. The geometry, boundary conditions and loading are as shown in Figure 5.36. This problem has been studied by Reese *et al.* [69] as a standard benchmark problem to study the performance of enhanced formulation to deal with incompressibility. Due to the symmetry of geometry, boundary and loading conditions, only half of the model is considered for the analysis. The material is modeled using Neo-Hookean material model with the following strain energy function,

$$W(J, \bar{\mathbf{C}}) = \frac{1}{2}\mu (\text{I}_{\bar{\mathbf{C}}} - 3) + \frac{1}{4}\lambda ((J^2 - 1) - 2\ln J) - \mu \ln J \quad (5.7)$$

with material parameters $\lambda = 400889.806$ MPa and $\mu = 80.1938$ MPa. The load is assumed to be *dead load* similar to Cook's membrane example. The quantity of interest is the compression level (vertical displacement) of top middle point, point A in Figure 5.36.

Variation of compression level is studied for different loading conditions - different p/p_0 values with $p_0 = 20$ — for different orders of NURBS approximation spaces using both the displacement and mixed formulations. Results obtained for Q_1/Q_0 NURBS are compared with those obtained using the standard four-node Linear-Quadrilateral element with F-bar formulation of de Souza Neto *et al.* [60] — denoted by LQ-Fbar. Convergence is obtained, for all the considered loading conditions, with a mesh of 16×16 and as shown in Figure 5.37, the present method performs better than the Fbar method for coarse meshes and coincides with Fbar method for finer meshes. Figure 5.38 shows the variation of compression level for different loading conditions — $p/p_0=20, 40, 60$ — using the displacement and mixed formulations for different orders of NURBS spaces. Convergence is obtained with 16×16 mesh for all NURBS

spaces considered, except for Q_1 NURBS. Q_1 NURBS for all the meshes and Q_2 NURBS for coarse meshes suffer from severe locking problems and increasing the order of NURBS improves the accuracy. Moreover, mixed formulation substantially improves the accuracy even for coarse meshes. Even though the improvement in accuracy with mixed formulation seems to be negligible for higher order NURBS with fine meshes, it has been observed that mixed formulation converges with substantially less number of load steps compared to the pure displacement formulation. Therefore, use of mixed formulation reduces the overall computational time and also gives more accurate results. Figures 5.39 and 5.40 show, respectively, the contour plots of hydrostatic pressure and von Mises stress with both the formulations for 32×32 mesh with cubic NURBS for the case of $p/p_0=60$.

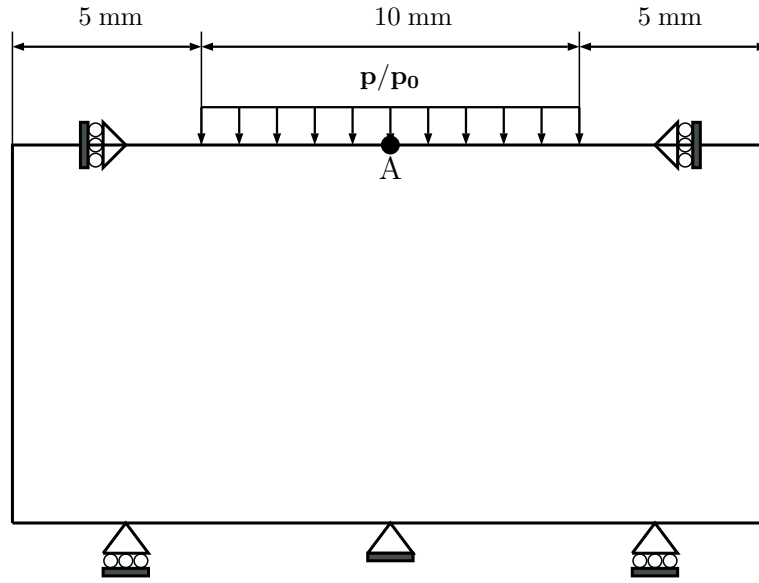


Figure 5.36: Plane-strain block under compression: geometry, loading and boundary conditions.

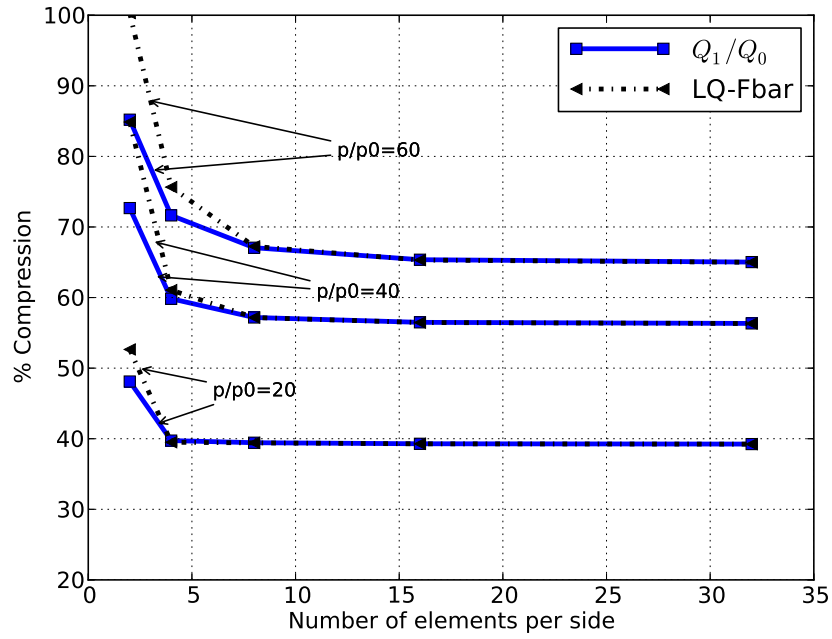


Figure 5.37: Plane-strain block under compression: compression level for Q_1/Q_0 NURBS compared to LQ-Fbar.

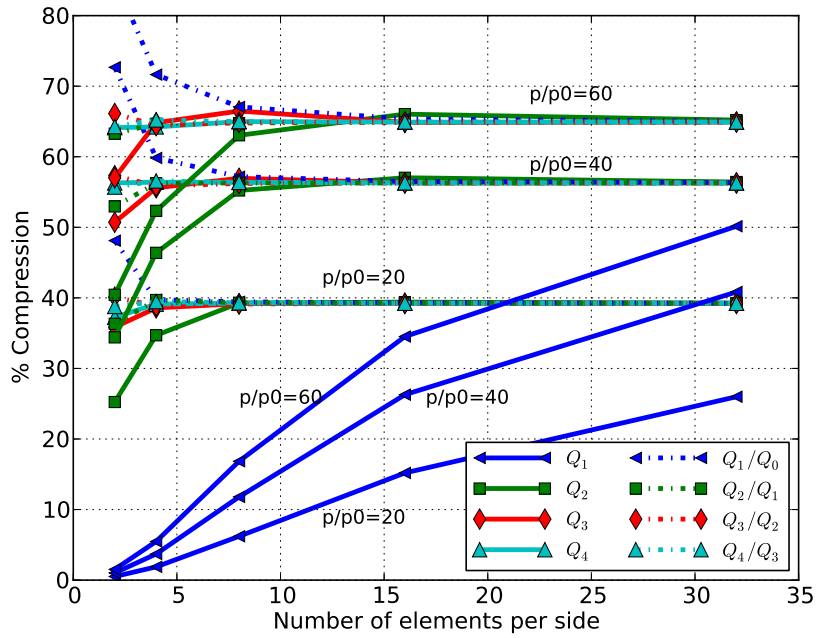


Figure 5.38: Plane-strain block under compression: compression level for different orders of NURBS under different loading conditions.

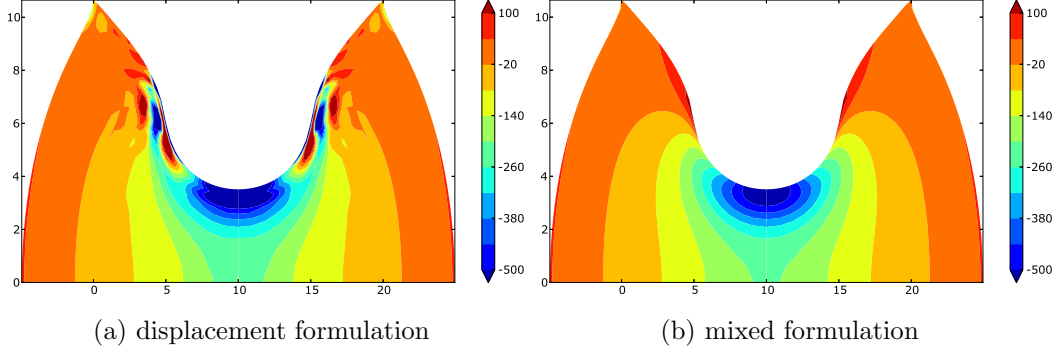


Figure 5.39: Plane-strain block under compression: contour plots of hydrostatic pressure for 32×32 mesh with Q_3 NURBS for $p/p_0=60$.

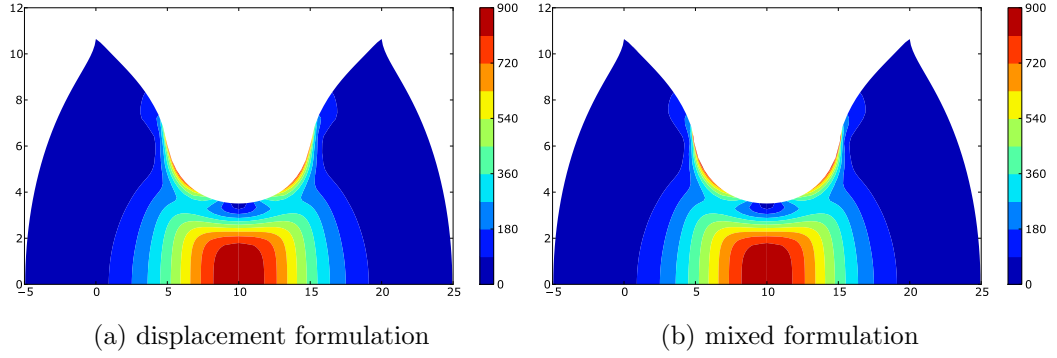


Figure 5.40: Plane-strain block under compression: contour plots of von Mises equivalent stress for 32×32 mesh with Q_3 NURBS for $p/p_0=60$.

5.2.4 Plane strain localization problem

In this example, plane strain localization of a strip subjected to uniform extension is studied. This problem has been studied by several authors [4, 57, 60, 62, 78, 87] and is considered as standard benchmark problem for testing finite element formulation in finite strains to deal with incompressibility problems posed by elasto-plastic material models. The geometry, loading and boundary conditions are as shown in Figure 5.41. The material model and material properties are same as those used in Cook's membrane with finite strain plasticity. Due to symmetry only quarter portion of the model is considered for the analysis; and in order to trigger strain localization a width reduction of 1.8% is introduced in the center of the bar. A total horizontal displacement of $u = 5.0$ is applied on the right edge and the problem is solved in several load steps.

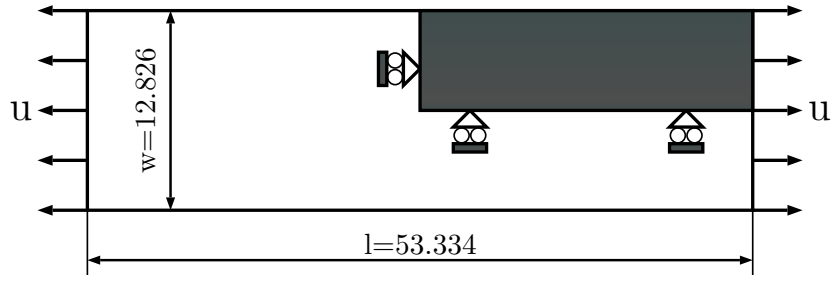
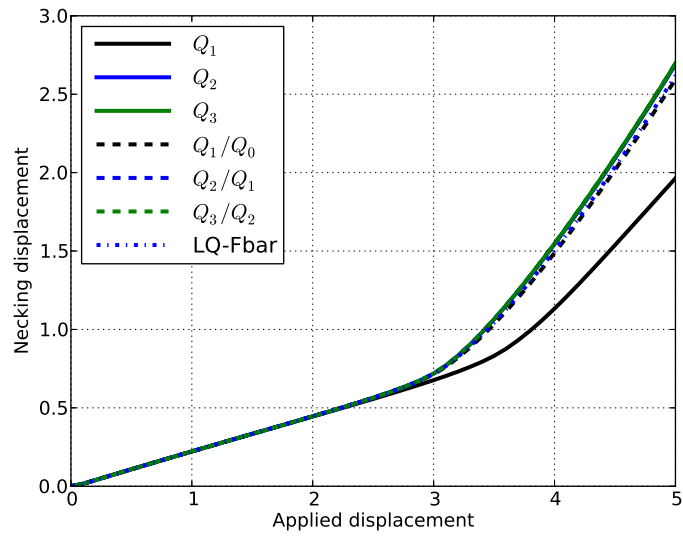
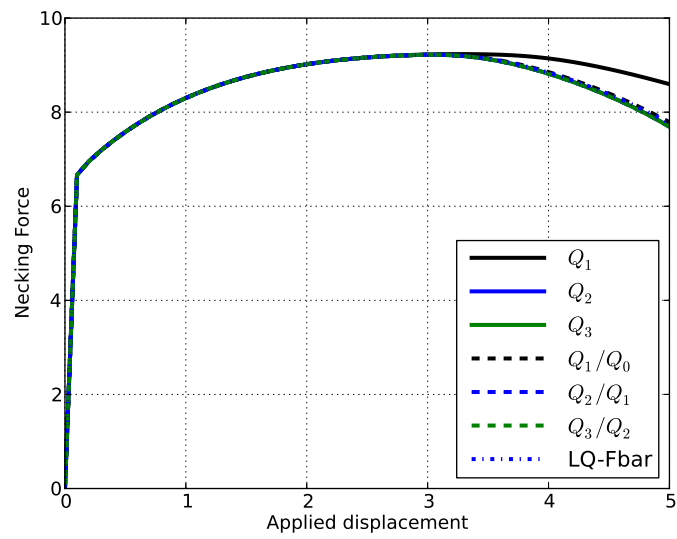


Figure 5.41: Necking of an elasto-plastic strip: geometry, loading and boundary conditions.



(a) Necking displacement



(b) Load-Vs-displacement curve

Figure 5.42: Necking of an elastoplastic strip.

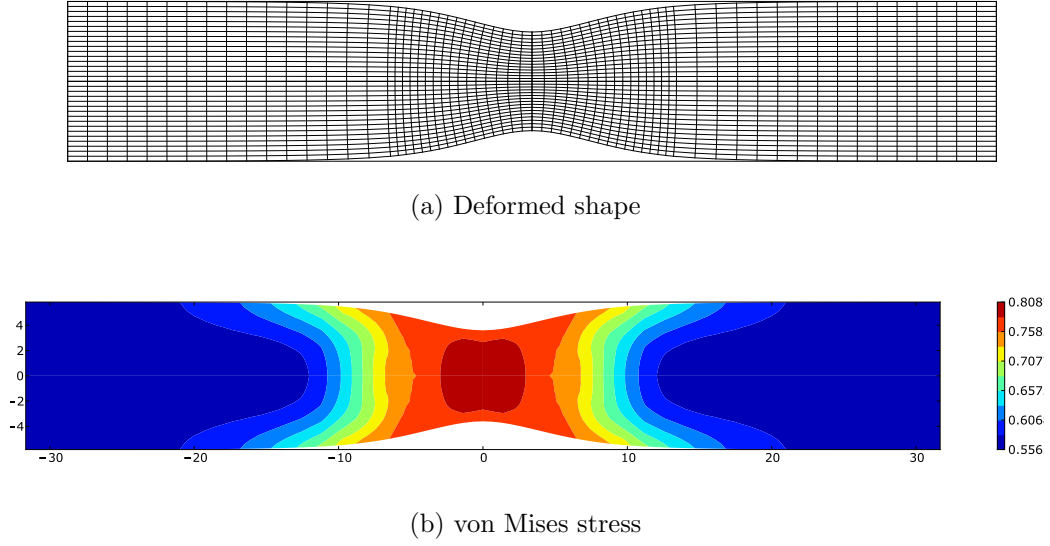


Figure 5.43: Necking of an elasto-plastic strip: deformed shape and von Mises stress for Q_3/Q_2 NURBS.

Figures 5.42(a) and 5.42(b) show the variation of necking displacement and necking force, respectively, with respect to applied displacement for different orders of NURBS spaces; as shown, mixed formulation clearly improves the accuracy of the results. Figure 5.43 shows the deformed shape and contour plot of von Mises stress for Q_3/Q_2 NURBS.

5.2.5 Pinched Torus

To our knowledge, this problem was first studied by Chavan *et al.* [27] in the context of developing locking-free linear brick elements and later by Elguedj *et al.* [33] using $\bar{\mathbf{F}}$ formulation with NURBS. Geometry of the problem can be modeled exactly using quadratic and higher order NURBS. The geometry, loading and boundary conditions are as shown in Figure 5.44. Due to symmetry only 1/8th of the total domain is considered for the purpose of analysis and Neo-Hookean hyperelastic material model (5.6) with $\kappa = 2833.333$ MPa and $\mu = 5.67$ MPa is considered and a load of $p_0 = 0.195$ MPa is considered to present the results. A mesh of $8 \times 2 \times 4$ elements (8 elements in small semi-circle, 2 elements in the radial direction of small circle and 4 elements in the circumference direction of large circle) is studied with Q_2 , Q_3 and Q_4 NURBS with both the formulations. The variation of vertical displacement of point A against the normalized load value during each load step is shown in Figure 5.45. Clearly, Q_2 NURBS suffer from severe locking problems and mixed formulation Q_2/Q_1 improves the result. Although Q_3 NURBS give almost the same result as that of Q_2/Q_1 , Q_3 NURBS require almost 5 times as many load steps to converge. So, 2-field mixed formulation, with few added degrees of freedom requires less computational time compared to the pure displacement formulation and also gives improved results. Contour plots of Cauchy stress component σ_{yy} for Q_2 ,

Q_2/Q_1 , Q_3/Q_2 NURBS, shown in Figure 5.46, clearly indicate that mixed formulation gives improved distribution of stresses compared to displacement formulation.

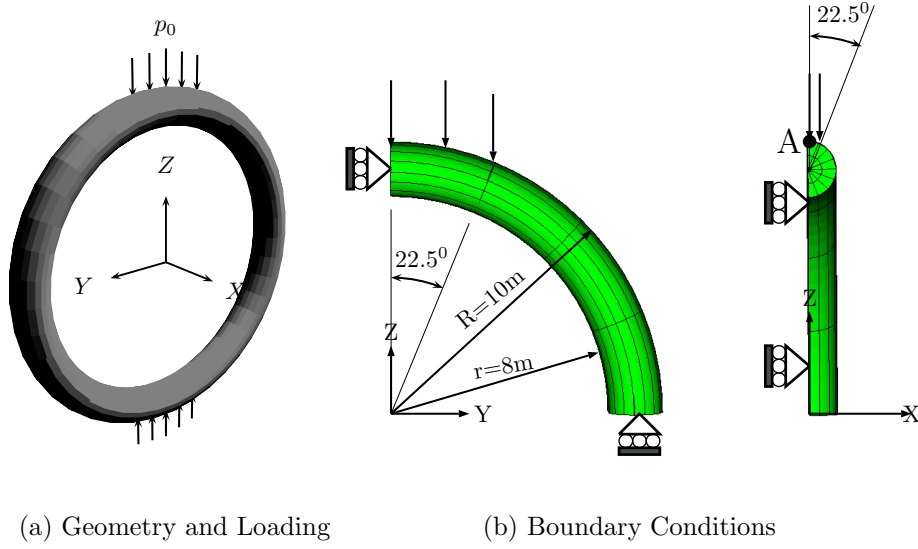


Figure 5.44: Pinched torus: geometry, loading and boundary conditions.

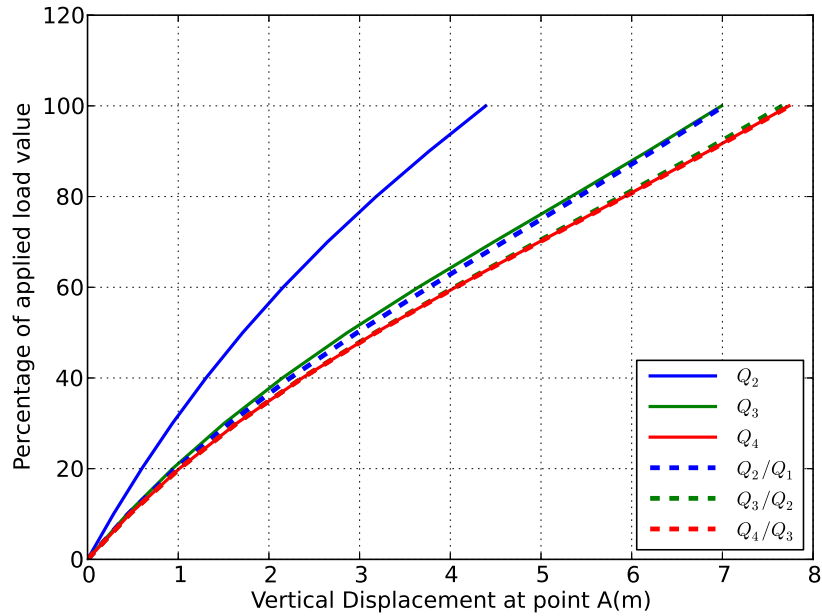


Figure 5.45: Pinched torus: load-displacement curve.

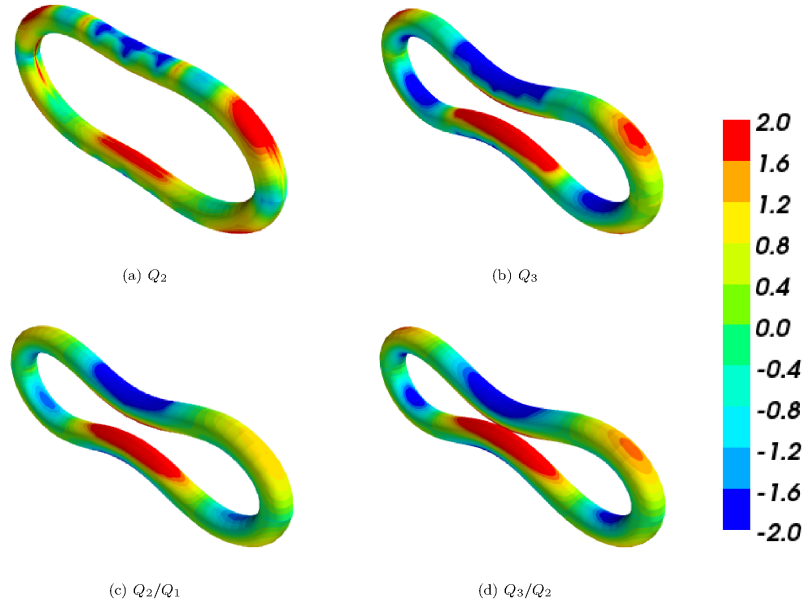


Figure 5.46: Pinched torus: contour plots of Cauchy stress component σ_{yy} .

5.2.6 Torsion of a square prism

This example is studied to demonstrate the performance of mixed formulations under severe mesh distortions. This problem was studied by Lipton *et al.* [52] using $\bar{\mathbf{F}}$ formulation with NURBS. Geometry and boundary conditions of the problems are as shown in Figure 5.47(a). Rotation (θ_z) on the top face is applied in the form X and Y directional displacements. Material model and material properties are same as those used in Cook’s membrane with Neo-Hookean hyperelastic material, see Section 5.2.1. Same discretizations as in [52] are considered: 4x4x16 elements for Q_1 NURBS, 3x3x15 for Q_2 NURBS, 2x2x14 for Q_3 NURBS and 1x1x13 for Q_4 NURBS. Each discretisation consists of 1381 DOF — 1125 displacement DOF + 256 pressure DOF.

The quantity of interest in the present example is the maximum angle of twist that a mesh can sustain before failing to converge. Failure angles for the displacement and the proposed mixed formulations, along with the values reported by Lipton *et al.* using $\bar{\mathbf{F}}$ formulation for NURBS [52], are presented in Table 5.7. As expected, mixed formulation improves the maximum sustainable angle for a given mesh. By comparing the failure angles, it can be concluded that the proposed two-field mixed formulation performs much better than the $\bar{\mathbf{F}}$ formulation used in [52]. Along with improving the failure angle, analyses performed with mixed formulation have shown exceptional reduction in computational time when compared with displacement formulation; mixed formulation converges with increments of 10 degrees while displacement formulation needs an increment of 1 degree or even less. On average, a 10-fold reduction in computational time is achieved using mixed formulation. This reduction in computational time proves to be extremely beneficial in large-scale

engineering simulations where number of DOF are usually very high. A typical deformed shape of the bar and von Mises stress distribution for an intermediate configuration — at $\theta = 720\text{deg}$ — are shown in Figure 5.47(b) and Figure 5.47(c), respectively.

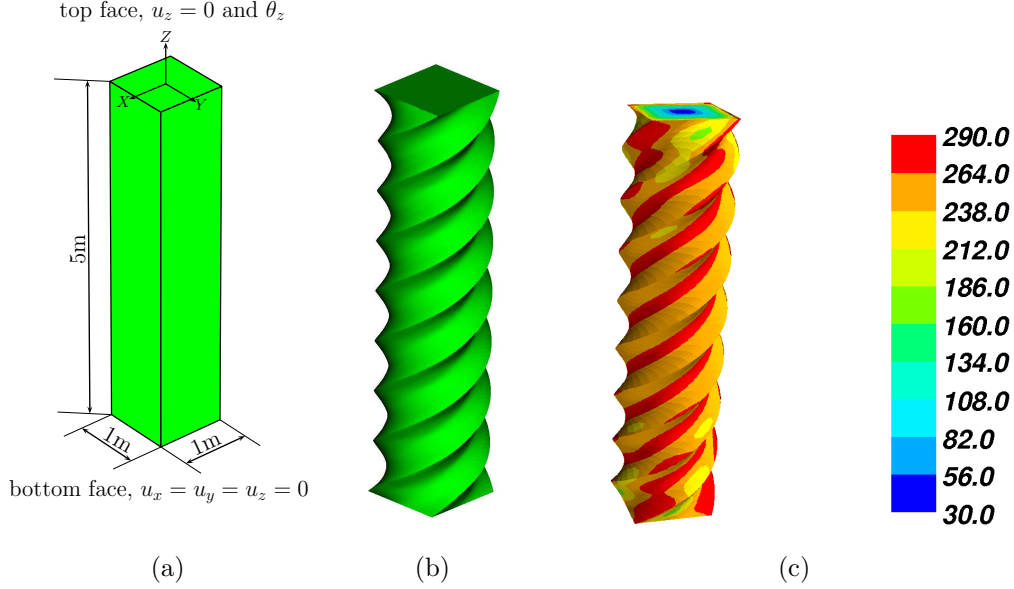


Figure 5.47: Torsion of a prism: (a) Geometry, loading and boundary conditions, (b) An intermediate deformed shape and (c) von Mises stress contour plot at 720 deg rotation for Q_2/Q_1 NURBS.

Table 5.7: Failure Angle in degrees

Degree	Grid	displacement formulation	mixed formulation	From [52]
Linear(Q_1)	4x4x16	988	1205	795
Quadratic(Q_2)	3x3x15	1153	1605	907
Cubic(Q_3)	2x2x14	902	1747	963.3
Quartic(Q_4)	1x1x13	160	935	NA

5.2.7 Necking of a cylindrical bar

In this example, necking of cylindrical bar in three-dimensions is studied. Length of the bar, $L = 53.334$ mm and its diameter, $D = 12.826$ mm. Due to symmetry, only $1/8^{th}$ of the total geometry is considered for the purpose of analysis, as depicted in Figure 5.48. As in two-dimensional necking example, a geometric imperfection of 1.8% of the radius is introduced at the center of the bar to trigger the necking. The material model and material properties are same as those used in two-dimensional necking problem. A displacement of 8mm is applied incrementally on the top face in the z-direction. A fixed

mesh with different orders of NURBS is studied with both the displacement and mixed formulations. Variation of reaction force and neck displacement with respect to applied displacement is as shown in Figures 5.49 and 5.50, respectively. Even though the mesh considered is coarse, higher order NURBS, coupled with mixed formulation, capture the necking phenomenon extremely well and as observed in other examples mesh refinement leads to more accurate results.

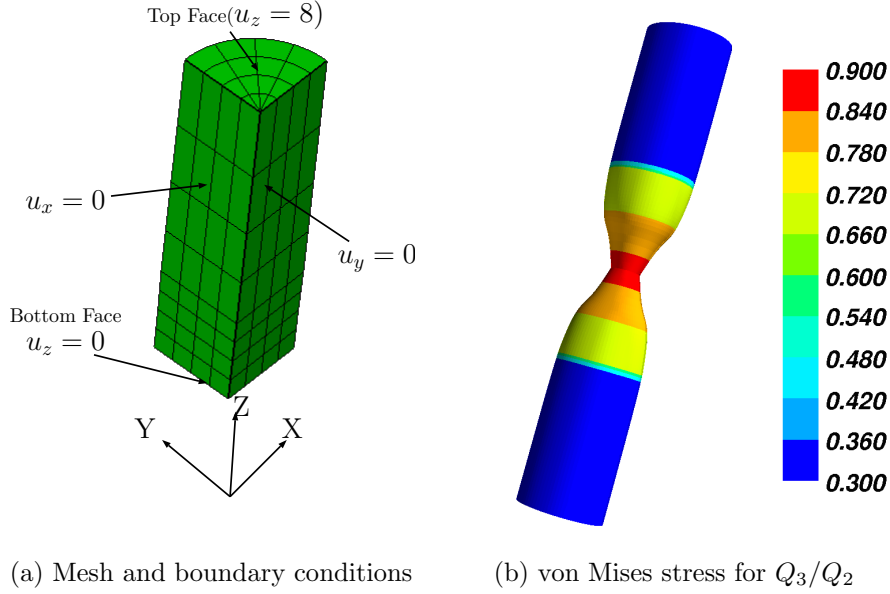


Figure 5.48: Necking of a cylindrical bar.

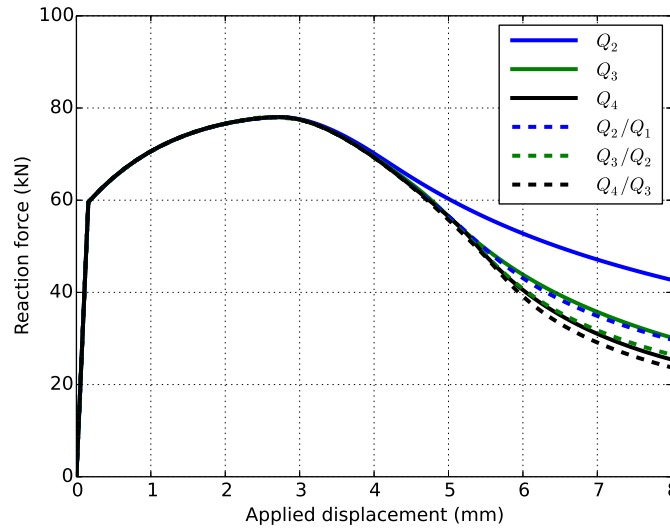


Figure 5.49: Necking of a cylindrical bar: variation of necking force with respect to applied displacement.

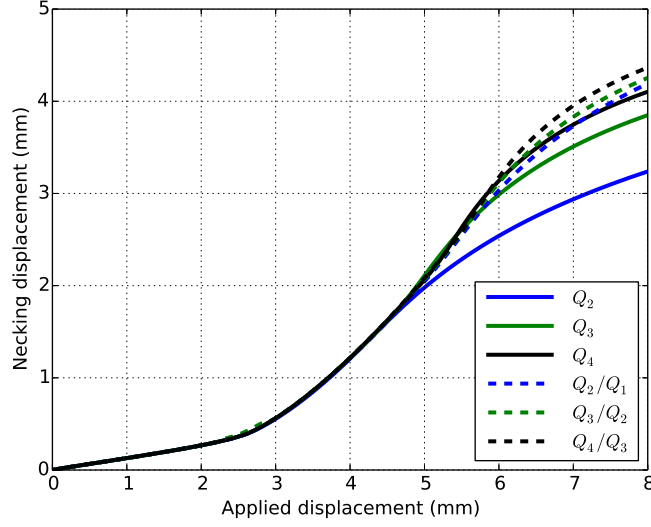


Figure 5.50: Necking of a cylindrical bar: variation of neck displacement with respect to applied displacement.

5.2.8 Compression of a block in three dimensions

This example is generalization of plane-strain block under compression studied earlier. This problem was studied in [70] as a benchmark for the three-dimensional version of the Q1SP element. The geometry, loading and boundary conditions of the problem are given in Figure 5.51. Due to symmetry of geometry and loading conditions only one quarter of the domain is considered for the analysis. A Neo-Hookean material model whose free energy function is given as,

$$\Psi(J, \bar{\mathbf{C}}) = \frac{1}{2}\mu (\text{tr}[\bar{\mathbf{C}}] - 3) - \mu \ln J + \frac{1}{2}\lambda (\ln J)^2 \quad (5.8)$$

with $\lambda = 400888.2$ MPa and $\mu = 80.19$ MPa, is considered. Analysis is performed for different mesh densities with different orders of NURBS using the mixed formulation. Each discretised model is studied for a maximum load value of $p/p_0 = 80$ with $p_0 = 4N/mm^2$ and the load is assumed to be a *dead load*. The evolution of the compression level, of point A shown in Figure 5.51, with respect to mesh refinement is studied. For the linear elements the results obtained with the present mixed formulation are compared with those obtained using the standard linear brick element with F-bar formulation of de Souza Neto [60] — denoted by LB-Fbar — as shown in Figure 5.52. Results obtained with the present formulation are well in agreement with those obtained with LB-Fbar. Compression levels obtained with NURBS spaces of different orders are shown in Figure 5.53. Use of higher order NURBS improves the accuracy for coarse meshes as observed in the two-dimensional example. Contour plots of vertical displacement and von Mises stress are shown in Figure 5.54.

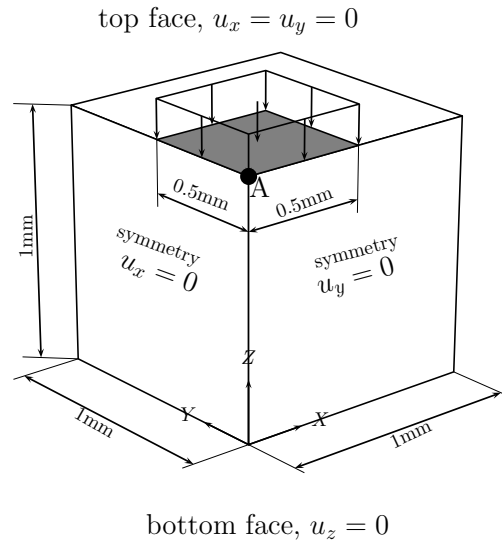


Figure 5.51: Block under compression in 3D: boundary conditions and loading.

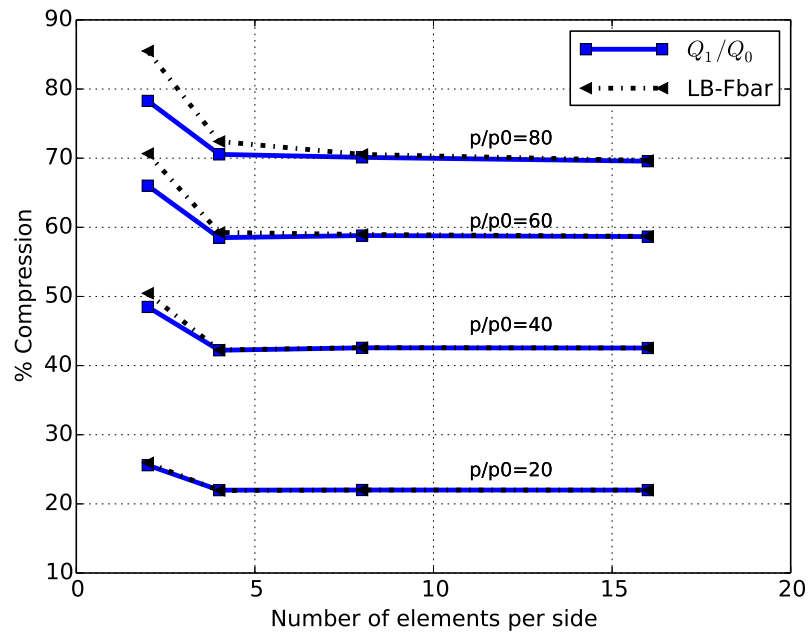


Figure 5.52: Block under compression in 3D: comparison, of convergence of compression level, between Q_1/Q_0 NURBS and standard F-bar element.

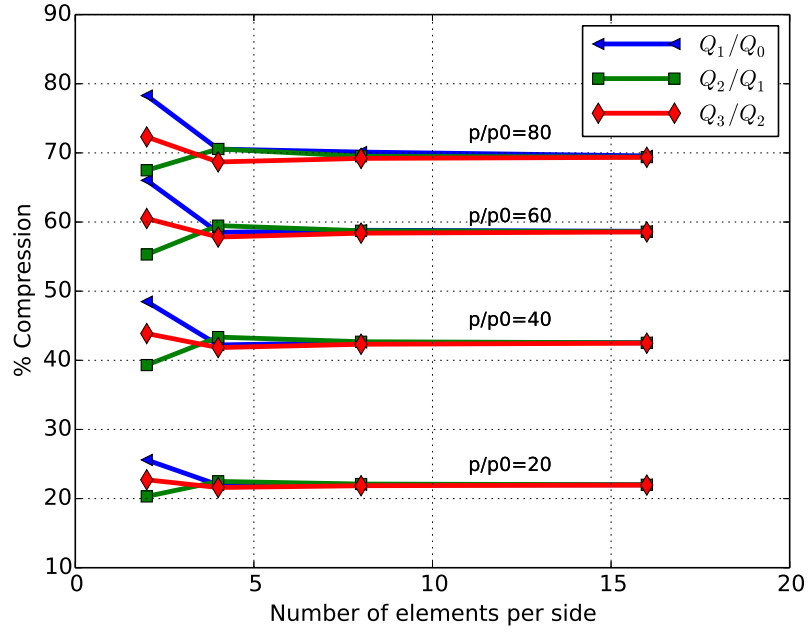


Figure 5.53: Block under compression in 3D: compression level for different orders of NURBS.

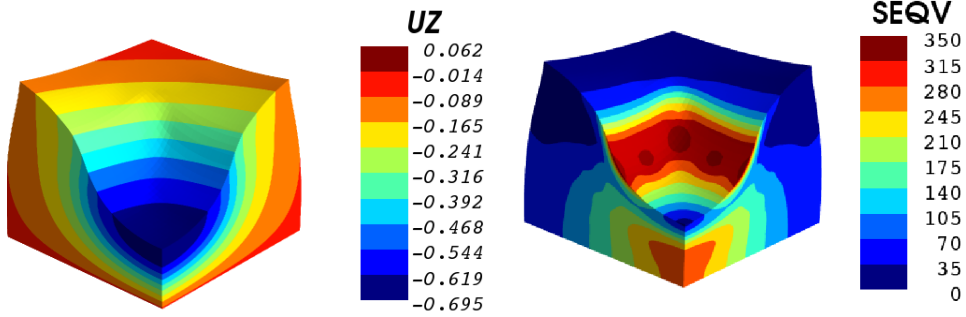


Figure 5.54: Block under compression in 3D: contour plots of vertical displacement (UZ) and von Mises equivalent stress.

5.2.9 Bending of a thick cylindrical shell

This example demonstrates the performance of the finite element formulations to deal with the issue of "shear locking" of shells. This problem was studied by [9, 27, 70]. The geometry, loading and material properties are as shown in Figure 5.55. No volumetric locking is expected as the Poisson's ratio is only 0.4; however, because of the geometry, this problem suffers from shear locking. Due to symmetry of geometry and loading conditions, only a 1/8th portion is considered for the analysis, as shown in Figure 5.56(a), along with boundary conditions and loading and a typical mesh used. As in previous examples, the

load is assumed to be *dead load* and the same Neo-Hookean material model used in the previous example is considered. The quantity of interest is the vertical displacement of point A shown in Figure 5.56(a).

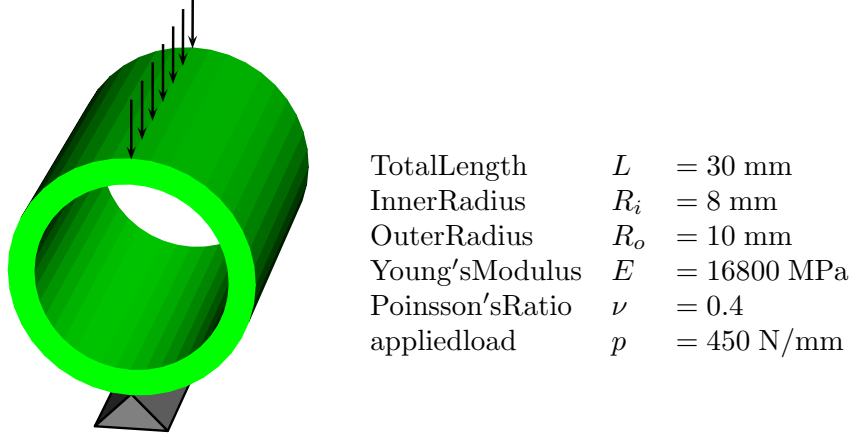


Figure 5.55: Thick cylindrical shell in 3D: geometry, loading and material properties.

Due to circular cross sections the initial geometry has to be modelled with quadratic NURBS. As in literature [9, 27, 70] only one element is considered in the thickness direction and different mesh densities are considered in the axial and circumferential directions. Each of the meshes, with densities 2x4x1, 4x8x1, 8x16x1 and 16x32x1, are analysed with Q_2 , Q_3 and Q_4 NURBS. 2x4x1 mesh implies that there are 2 elements in axial direction, 4 elements in circumferential direction and 1 element along thickness. Analysis has been performed with both the displacement and mixed formulations and vertical displacement at point A, for different discretisations, is shown in Figure 5.57. As expected Q_2 NURBS with pure displacement formulation suffers from shear locking and the accuracy improves with the h -, p - or k - refinements. Moreover, the use of mixed formulation improves the accuracy even for the coarse meshes as observed in the previous examples with significant volumetric locking. Therefore, as demonstrated with the current example, mixed formulation also deals with the problems of shear locking. Contour plots of vertical displacement and shear stress (σ_{xy}) are shown in Figure 5.58.

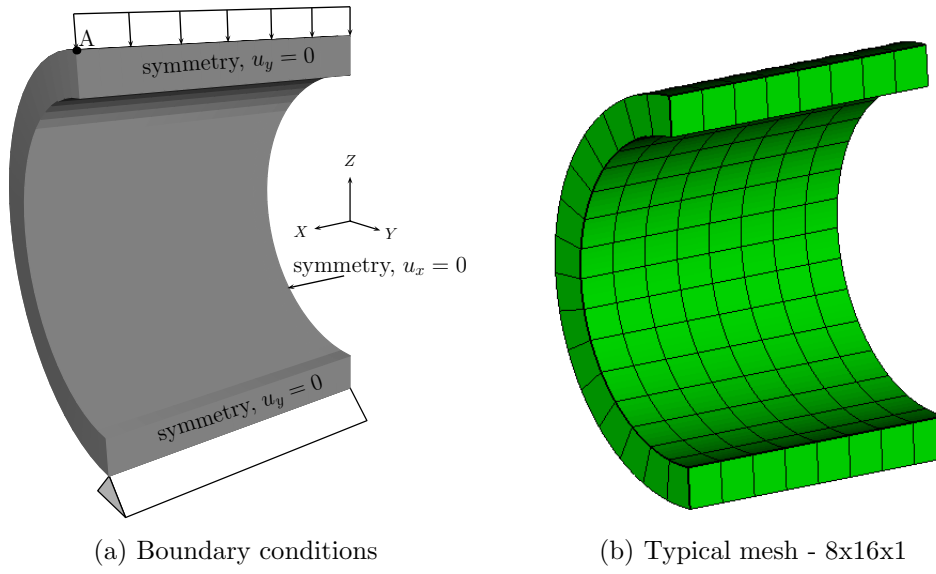


Figure 5.56: Thick cylindrical shell in 3D: boundary conditions and a typical mesh used for the analysis.

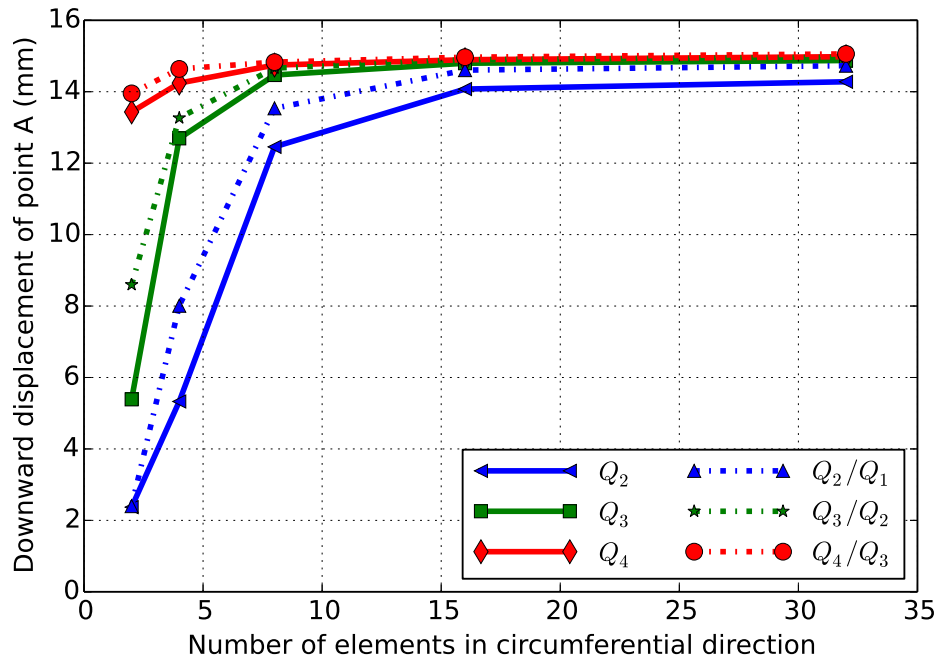
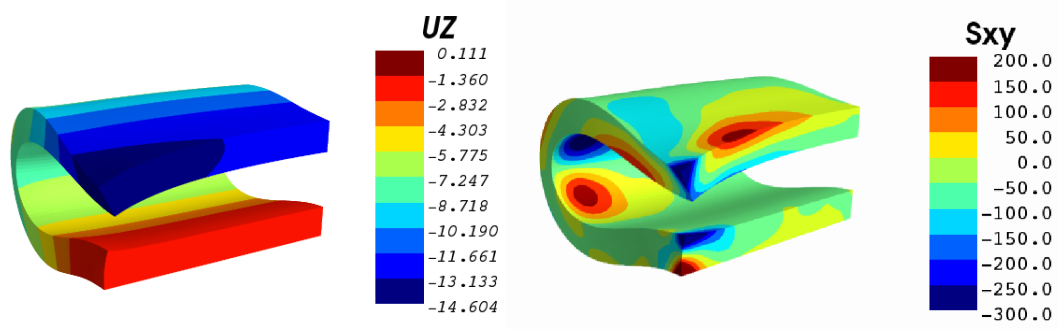


Figure 5.57: Thick cylindrical shell in 3D: vertical displacement of point A with respect to number of elements in the circumferential direction for different order of NURBS with displacement and mixed formulation.



(a) Vertical displacement

(b) Shear stress (σ_{xy})

Figure 5.58: Thick cylindrical shell in 3D: contour plots of vertical displacement (uz) and shear stress σ_{xy} .

Chapter 6

Least-Squares formulation

In this chapter, formulation of least-squares finite element methods for compressible and nearly incompressible elasticity in both the small strain and finite strains and incompressible Navier-Stokes is presented.

6.1 Formulation of general LSFEMs

The main motivation behind the development of LSFEMs is the desire to recover the advantages Rayleigh-Ritz methods, such as the avoidance of LBB condition and obtaining symmetric and positive definite (SPD) discrete systems. The basic idea behind a least-squares formulation is to define a least-squares functional as the sum of squares of the residuals of the governing equations. So, the least-squares functional is always positive and convex and leads to symmetric and positive definite bilinear forms even for the non-self-adjoint operators [19, 43].

Let Ω be a bounded domain in \mathbb{R}^n , $n = 1$ or 2 or 3 , with a Lipschitz boundary Γ . Let \mathcal{L} be a linear differential operator and \mathcal{R} be a boundary operator. Then, the governing differential equations along with the boundary conditions are given by,

$$\mathcal{L}\mathbf{u} = \mathbf{f} \quad \text{in } \Omega \quad (6.1a)$$

$$\mathcal{R}\mathbf{u} = \mathbf{g} \quad \text{on } \Gamma \quad (6.1b)$$

Defining a least-squares functional as,

$$\mathcal{J}(\mathbf{u}; \mathbf{f}, \mathbf{g}) = \frac{1}{2} (\|\mathcal{L}\mathbf{u} - \mathbf{f}\|_{\mathbf{H}_\Omega}^2 + \|\mathcal{R}\mathbf{u} - \mathbf{g}\|_{\mathbf{H}_\Gamma}^2) \quad (6.2)$$

where, $\|\cdot\|_{\mathbf{H}_\Omega}$ and $\|\cdot\|_{\mathbf{H}_\Gamma}$ are some norms in Hilbert spaces \mathbf{H}_Ω and \mathbf{H}_Γ respectively. Then, the general idea of LSFEM is to find $\mathbf{u} \in \mathbf{S}$, where, \mathbf{S} is a Sobolev space, which minimizes the least-squares functional $\mathcal{J}(\mathbf{u}; \mathbf{f}, \mathbf{g})$. This leads to an unconstrained minimization problem given by,

$$\min_{\mathbf{u} \in \mathbf{S}} \mathcal{J}(\mathbf{u}; \mathbf{f}, \mathbf{g}) \quad (6.3)$$

The unconstrained minimization problem given by (6.3) requires that the first variation of (6.2) is equal to zero, and results in the following system of equations.

$$\mathcal{B}(\mathbf{u}, \mathbf{v}) = \mathcal{F}(\mathbf{v}) \quad (6.4)$$

where,

$$\mathcal{B}(\mathbf{u}, \mathbf{v}) = (\mathcal{L}\mathbf{v}, \mathcal{L}\mathbf{u})_{\mathbf{H}_\Omega} + (\mathcal{R}\mathbf{v}, \mathcal{R}\mathbf{u})_{\mathbf{H}_\Gamma} \quad (6.5)$$

$$\mathcal{F}(\mathbf{v}) = (\mathcal{L}\mathbf{v}, \mathbf{f})_{\mathbf{H}_\Omega} + (\mathcal{R}\mathbf{v}, \mathbf{g})_{\mathbf{H}_\Gamma} \quad (6.6)$$

It can be easily observed that the bilinear operator $\mathcal{B}(\mathbf{u}, \mathbf{v})$ is always *symmetric* — even for non-self-adjoint differential operators — and *coercive*.

By taking approximations for \mathbf{u} and \mathbf{v} as,

$$\mathbf{u} = \mathbf{N}\bar{\mathbf{u}} \quad \text{and} \quad \mathbf{v} = \mathbf{N}\bar{\mathbf{v}} \quad (6.7)$$

Equation (6.4) can be written in matrix form given by,

$$\mathbf{K} \bar{\mathbf{u}} = \mathbf{F} \quad (6.8)$$

where, $\bar{\mathbf{u}}$ is the vector of knowns to solve for and

$$\mathbf{K} = \int_{\Omega} \mathbf{J}_1^T \mathbf{J}_1 \, d\Omega + \int_{\Gamma} \mathbf{J}_2^T \mathbf{J}_2 \, d\Gamma \quad (6.9)$$

$$\mathbf{F} = \int_{\Omega} \mathbf{J}_1^T \mathbf{f} \, d\Omega + \int_{\Gamma} \mathbf{J}_2^T \mathbf{g} \, d\Gamma \quad (6.10)$$

where, \mathbf{J}_1 and \mathbf{J}_2 are the Jacobians of residuals corresponding to the body and boundary terms, respectively, with respect to unknowns, $\bar{\mathbf{u}}$.

The approach discussed above is applicable only for linear governing equations. In case of nonlinear equations, one can follow the same approach and construct the least-squares functional in terms of non-linear residual equations and use Newton-Raphson method to find the solution of the resulting minimisation problem. But one of the important issues associated the standard Newton's method is that it requires the computation of the Hessian, terms involving the second derivatives of the residuals, which in most cases is always cumbersome and increases the computational cost. So, in order to circumvent this problem, Gauss-Newton method, which is often used to solve the problems of Nonlinear Least-squares, is adopted from the field of optimisation. However, Gauss-Newton method comes with a disadvantage of slower convergence compared to Newton's method. Nevertheless, it is often preferable as it does not require the computation of Hessian of residuals. For further information on Gauss-Newton's methods the reader can refer to [12, 48].

According to Gauss-Newton method, instead of linearising the least-squares functional, the nonlinear residuals are linearised first and then a new least-squares functional is constructed in terms of linearised residuals, i.e., a linear

least-squares problem is solved at each iteration. For a given set of n nonlinear residuals \mathbf{r} , a least-squares functional, at an iteration $(k + 1)$, is defined as,

$$\bar{\mathcal{J}}(\mathbf{u}^{k+1}; \mathbf{f}^{k+1}, \mathbf{g}^{k+1}) = \frac{1}{2} \sum_{i=1}^n \hat{r}_i(\mathbf{u}^{k+1}; \mathbf{f}^{k+1}, \mathbf{g}^{k+1})^2 \quad (6.11)$$

where,

$$\mathbf{u}^{k+1} = \mathbf{u}^k + d\mathbf{u} \quad (6.12)$$

with $d\mathbf{u}$ as increment in \mathbf{u} ; \mathbf{f}^{k+1} and \mathbf{g}^{k+1} are the force vectors at iteration $(k + 1)$; and \hat{r}_i is the linearised version of the residual r_i , given as,

$$\hat{r}_i(\mathbf{u}^{k+1}) = r_i(\mathbf{u}^k + d\mathbf{u}) \approx r_i(\mathbf{u}^k) + \mathcal{D}r_i(\mathbf{u}^k)[d\mathbf{u}] \quad (6.13)$$

where, $\mathcal{D}r_i(\mathbf{u}^k)[d\mathbf{u}]$ is the directional derivative of r_i , at \mathbf{u}^k , in the direction of $d\mathbf{u}$. The unconstrained minimization problem based on the modified least-squares functional is given as,

$$\min_{\mathbf{u}^{k+1} \in \mathbf{S}} \bar{\mathcal{J}}(\mathbf{u}^{k+1}; \mathbf{f}^{k+1}, \mathbf{g}^{k+1}) \quad (6.14)$$

And taking approximations for \mathbf{u} as, $\mathbf{u} = \mathbf{N}\bar{\mathbf{u}}$, equation (6.14) results in a matrix system,

$$\mathbf{K}(\mathbf{u}^k) d\bar{\mathbf{u}} = \mathbf{F}(\mathbf{u}^k) \quad (6.15)$$

The pseudo code for the entire Gauss-Newton procedure is given in Box 6.1.

1.) Linearise the residuals and derive the Jacobian matrix. 2.) Given an initial \mathbf{u} and a tolerance $\epsilon > 0$ for each load step, repeat a.) Compute \mathbf{K} and \mathbf{F} at \mathbf{u} b.) If $\ \mathbf{F}\ \leq \epsilon$, return \mathbf{u} c.) Solve $\mathbf{K} \delta\mathbf{u} = \mathbf{F}$ d.) Update: $\mathbf{u} = \mathbf{u} + d\mathbf{u}$ until maximum number of iterations is reached.

Box 6.1: Gauss-Newton procedure to solve nonlinear least-squares.

6.2 Boundary conditions and the issue of norm-equivalence

At this point it is very important to discuss the application of boundary conditions. Dirichlet boundary conditions can be imposed either strongly or in a

least-squares sense by including the corresponding residual in the least-squares functional. Neumann boundary conditions are always implemented in least-squares sense. The inclusion of the boundary residual in (6.2) allows the use of minimization spaces that are not constrained to satisfy the boundary condition (6.1b), i.e., such conditions are enforced weakly through the variational principle. This is advantageous whenever the condition (6.1b) is difficult to satisfy computationally and represents an additional beneficial feature of least-squares based methods.

Inclusion of boundary terms in the least-squares functional leads to the problem of norm-equivalence, see Chapter 2 in [19]. Least-squares formulations which are norm-equivalent result in optimal convergence rates and in order to define such norm-equivalent least-squares formulations, norms of boundary terms should be defined in appropriate fractional subspaces. However, such formulations are impractical to implement in a finite element framework and require to construct spectrally equivalent norms in order to make such formulations practical. But the main problem with spectrally equivalent norms is that they are extremely difficult to obtain in a general setting and even if such norms can be defined they add a lot of computational overhead. This issue adds to the disadvantages of least-squares based formulations.

In the present work all the boundary conditions are enforced in a least-squares sense, by including L_2 norms of the residuals of boundary terms into the corresponding least-squares functional. So, all the least-squares finite element formulations developed in the present work are non-norm-equivalent. But, this issue is alleviated by the use of higher order NURBS spaces as approximation functions.

6.3 Solid Mechanics

For the sake of completeness the governing equations for solid mechanics — in both the reference and current configurations — are given here.

6.3.1 Governing equations

The boundary value problem of elasticity in large strain regime for a body with reference configuration, Ω , is stated as:

Given $\mathbf{f}_0 : \Omega \rightarrow \mathbb{R}^3$, $\mathbf{g} : \Gamma_D \rightarrow \mathbb{R}^3$ and $\mathbf{t}_0 : \Gamma_N \rightarrow \mathbb{R}^3$, find $\mathbf{u} : \Omega \rightarrow \mathbb{R}^3$, such that:

$$\nabla_{\mathbf{x}} \cdot \mathbf{P} = \mathbf{f}_0 \quad \text{in } \Omega, \quad (6.16)$$

$$\mathbf{u} = \mathbf{g} \quad \text{on } \Gamma_D, \quad (6.17)$$

$$\mathbf{P} \cdot \mathbf{N} = \mathbf{t}_0 \quad \text{in } \Gamma_N, \quad (6.18)$$

where, \mathbf{u} is the displacement vector, \mathbf{f}_0 is the body force per unit undeformed volume, \mathbf{N} is the unit outward normal on the boundary, Γ , of Ω , \mathbf{g} is the

prescribed displacement on Γ_D and \mathbf{t}_0 is the prescribed traction per unit undeformed area on Γ_N , with $\Gamma = \Gamma_D \cup \Gamma_N$.

Using Cauchy stress tensor ($\boldsymbol{\sigma}$) as the stress measure, the boundary value problem of elasticity in large strain regime in the current configuration, ω , is stated as:

Given $\mathbf{f} : \omega \rightarrow \mathbb{R}^3$, $\mathbf{g} : \gamma_D \rightarrow \mathbb{R}^3$ and $\mathbf{t} : \Gamma_N \rightarrow \mathbb{R}^3$, find $\mathbf{u} : \omega \rightarrow \mathbb{R}^3$, such that:

$$\nabla \cdot \boldsymbol{\sigma} = \mathbf{f} \quad \text{in } \omega, \quad (6.19)$$

$$\mathbf{u} = \mathbf{g} \quad \text{on } \gamma_D, \quad (6.20)$$

$$\boldsymbol{\sigma} \cdot \mathbf{n} = \mathbf{t} \quad \text{in } \gamma_N, \quad (6.21)$$

where, \mathbf{f} is the body force per unit volume in deformed configuration, \mathbf{n} is the unit outward normal on the deformed boundary, γ , of ω , \mathbf{g} is the prescribed displacement on γ_D and \mathbf{t} is the prescribed traction per unit deformed area on γ_N . Here, $\gamma = \gamma_D \cup \gamma_N$. The Cauchy stress tensor $\boldsymbol{\sigma}$ depends upon the strain energy function under consideration. \mathbf{f} and \mathbf{t} are related to the corresponding terms in the reference configuration, \mathbf{f}_0 and \mathbf{t}_0 respectively, by the following relations.

$$\mathbf{f} = \frac{1}{J} \mathbf{f}_0 \quad (6.22a)$$

$$\mathbf{t} = \frac{dA}{da} \mathbf{t}_0 \quad (6.22b)$$

where dA and da are the elemental areas in the reference and deformed configurations respectively. For further details on this topic the reader can refer to [20].

6.3.2 Compressible linear elasticity

For the case of linear isotropic elastic material the governing equations can be written, in pure displacements, as,

$$\mu \Delta \mathbf{u} + (\mu + \lambda) \nabla (\nabla \cdot \mathbf{u}) = \mathbf{f}_0 \quad \text{in } \Omega, \quad (6.23)$$

$$\mathbf{u} = \mathbf{g} \quad \text{on } \Gamma_D, \quad (6.24)$$

$$[\mu (\nabla \mathbf{u} + (\nabla \mathbf{u})^T) + \lambda (\nabla \cdot \mathbf{u}) \mathbf{I}] \cdot \mathbf{n} = \mathbf{t}_0 \quad \text{in } \Gamma_N, \quad (6.25)$$

The governing differential equation (6.23) is called Navier-Cauchy equation. Then least-squares functional based on L^2 norms of the residuals is defined as,

$$\begin{aligned} \mathcal{J}(\mathbf{u}, p; \mathbf{f}, \mathbf{g}) = & \frac{1}{2} \left(\|\mu \Delta \mathbf{u} + (\mu + \lambda) \nabla (\nabla \cdot \mathbf{u}) - \mathbf{f}_0\|_0^2 + \|\mathbf{u} - \mathbf{g}\|_0^2 \right. \\ & \left. + \|\mu (\nabla \mathbf{u} + (\nabla \mathbf{u})^T) + \lambda (\nabla \cdot \mathbf{u}) \mathbf{I} \cdot \mathbf{n} - \mathbf{t}_0\|_0^2 \right) \end{aligned} \quad (6.26)$$

Taking approximations for displacements (\mathbf{u}) as,

$$\mathbf{u} = \mathbf{N}_u \bar{\mathbf{u}} \quad (6.27)$$

where,

$$\mathbf{N}_{\mathbf{u}} = \begin{bmatrix} N_{u,0} & 0 & 0 & N_{u,1} & 0 & 0 & \dots & N_{u,n-1} & 0 & 0 \\ 0 & N_{u,0} & 0 & 0 & N_{u,1} & 0 & \dots & 0 & N_{u,n-1} & 0 \\ 0 & 0 & N_{u,0} & 0 & 0 & N_{u,1} & \dots & 0 & 0 & N_{u,n-1} \end{bmatrix} \quad (6.28)$$

and using this in the least-squares functional (6.26) and making its first variation to zero, will yield a linear system of equations given in matrix form as,

$$\mathbf{K} \bar{\mathbf{u}} = \mathbf{F} \quad (6.29)$$

Matrix \mathbf{K} and vector \mathbf{F} are given by,

$$\mathbf{K} = \int_{\Omega} \mathbf{J}_1^T \mathbf{J}_1 \, d\Omega + \int_{\Gamma_D} \mathbf{J}_2^T \mathbf{J}_2 \, d\Gamma_D + \int_{\Gamma_N} \mathbf{J}_3^T \mathbf{J}_3 \, d\Gamma_N \quad (6.30)$$

$$\mathbf{F} = \int_{\Omega} \mathbf{J}_1^T \mathbf{f}_0 \, d\Omega + \int_{\Gamma_D} \mathbf{J}_2^T \mathbf{g} \, d\Gamma_D + \int_{\Gamma_N} \mathbf{J}_3^T \mathbf{t}_0 \, d\Gamma_N \quad (6.31)$$

where

$$\mathbf{J}_1 = \mu \Delta \mathbf{N}_{\mathbf{u}} + (\mu + \lambda) \nabla(\nabla \cdot \mathbf{N}_{\mathbf{u}}) \quad (6.32)$$

$$\mathbf{J}_2 = \mathbf{N}_{\mathbf{u}} \quad (6.33)$$

$$\mathbf{J}_3 = \mu (\nabla \otimes \mathbf{N}_{\mathbf{u}}) \mathbf{n} + \mu (\nabla \cdot \mathbf{N}_{\mathbf{u}}) \otimes \mathbf{n} + \lambda \mathbf{n} \otimes (\nabla \cdot \mathbf{N}_{\mathbf{u}}) \quad (6.34)$$

In the expanded form,

$$\mathbf{J}_1 = [\mathbf{A}_0 \quad \mathbf{A}_1 \quad \dots \quad \mathbf{A}_{n-1}] \quad (6.35)$$

$$\mathbf{J}_3 = [\mathbf{B}_0 \quad \mathbf{B}_1 \quad \dots \quad \mathbf{B}_{n-1}] \quad (6.36)$$

where,

$$\mathbf{A}_i = \mu (\Delta N_{u,i}) \mathbf{I} + (\mu + \lambda) \mathbf{H}(N_{u,i}) \quad (6.37)$$

where, $\Delta N_{u,i}$ and $\mathbf{H}(N_{u,i})$, respectively, are the Laplacian and Hessian of N_i ; and are given as,

$$\Delta N_{u,i} = \frac{\partial^2 N_{u,i}}{\partial x^2} + \frac{\partial^2 N_{u,i}}{\partial y^2} + \frac{\partial^2 N_{u,i}}{\partial z^2} \quad (6.38)$$

$$\mathbf{H}(N_{u,i}) = \begin{bmatrix} \frac{\partial^2 N_{u,i}}{\partial x^2} & \frac{\partial^2 N_{u,i}}{\partial x \partial y} & \frac{\partial^2 N_{u,i}}{\partial x \partial z} \\ \frac{\partial^2 N_{u,i}}{\partial y \partial x} & \frac{\partial^2 N_{u,i}}{\partial y^2} & \frac{\partial^2 N_{u,i}}{\partial y \partial z} \\ \frac{\partial^2 N_{u,i}}{\partial z \partial x} & \frac{\partial^2 N_{u,i}}{\partial z \partial y} & \frac{\partial^2 N_{u,i}}{\partial z^2} \end{bmatrix} \quad (6.39)$$

and,

$$\mathbf{B}_i = \begin{bmatrix} a_i + (\mu + \lambda) \frac{\partial N_{u,i}}{\partial x} n_x & \mu \frac{\partial N_{u,i}}{\partial x} n_y + \lambda \frac{\partial N_{u,i}}{\partial y} n_x & \mu \frac{\partial N_{u,i}}{\partial x} n_z + \lambda \frac{\partial N_{u,i}}{\partial z} n_x \\ \mu \frac{\partial N_{u,i}}{\partial y} n_x + \lambda \frac{\partial N_{u,i}}{\partial x} n_y & a_i + (\mu + \lambda) \frac{\partial N_{u,i}}{\partial y} n_y & \mu \frac{\partial N_{u,i}}{\partial y} n_z + \lambda \frac{\partial N_{u,i}}{\partial z} n_y \\ \mu \frac{\partial N_{u,i}}{\partial z} n_x + \lambda \frac{\partial N_{u,i}}{\partial x} n_z & \mu \frac{\partial N_{u,i}}{\partial z} n_y + \lambda \frac{\partial N_{u,i}}{\partial y} n_z & a_i + (\mu + \lambda) \frac{\partial N_{u,i}}{\partial z} n_z \end{bmatrix} \quad (6.40)$$

where,

$$a_i = \mu \left(\frac{\partial N_{u,i}}{\partial x} n_x + \frac{\partial N_{u,i}}{\partial y} n_y + \frac{\partial N_{u,i}}{\partial z} n_z \right) \quad (6.41)$$

6.3.3 Nearly incompressible linear elasticity

Similar to the 2-field mixed GFEMs pressure, p , is introduced as an additional variable in order to deal with the problems of incompressibility. Then, defining the Cauchy stress as,

$$\boldsymbol{\sigma} = 2\mu \boldsymbol{\varepsilon}_{\text{dev}} + p \mathbf{I} \quad (6.42)$$

where, $\boldsymbol{\varepsilon}_{\text{dev}}$, is the deviatoric strain given as,

$$\boldsymbol{\varepsilon}_{\text{dev}} = \boldsymbol{\varepsilon} - \frac{1}{d} \text{tr}(\boldsymbol{\varepsilon}) \mathbf{I} \quad (6.43)$$

where, d is the dimension of the problem and pressure is related to deformation via the relation,

$$p = \kappa \nabla \cdot \mathbf{u} \quad (6.44)$$

where, Bulk Modulus (κ) is defined as,

$$\kappa = \lambda + \frac{2}{d} \mu \quad (6.45)$$

Using the new definition of Cauchy stress from (6.42), the governing equations of linear elasticity in terms of displacements (\mathbf{u}) and pressure (p) are given as,

$$\mu \Delta \mathbf{u} + \alpha \nabla p = \mathbf{f}_0 \quad \text{in } \Omega \quad (6.46a)$$

$$\nabla \cdot \mathbf{u} = \frac{p}{\kappa} \quad \text{in } \Omega \quad (6.46b)$$

$$\mathbf{u} = \mathbf{g} \quad \text{on } \Gamma_D \quad (6.46c)$$

$$(2\mu \boldsymbol{\varepsilon}_{\text{dev}} + p \mathbf{I}) \cdot \mathbf{n} = \mathbf{t}_0 \quad \text{in } \Gamma_N \quad (6.46d)$$

where, $\alpha = \left(1 + \frac{(d-2)\mu}{d\kappa}\right)$. Then least-squares functional based on L^2 norms of the residuals of (6.46) is given by,

$$\begin{aligned} \mathcal{J}(\mathbf{u}, p; \mathbf{f}, \mathbf{g}) = \frac{1}{2} & \left(\|\mu \Delta \mathbf{u} + \alpha \nabla p - \mathbf{f}_0\|_0^2 + \left\| \nabla \cdot \mathbf{u} - \frac{p}{\kappa} \right\|_0^2 \right. \\ & \left. + \|\mathbf{u} - \mathbf{g}\|_0^2 + \|(2\mu \boldsymbol{\varepsilon}_{\text{dev}} + p \mathbf{I}) \cdot \mathbf{n} - \mathbf{t}_0\|_0^2 \right) \end{aligned} \quad (6.47)$$

Taking approximations for displacements (\mathbf{u}) and pressure (p) as,

$$\mathbf{u} = \mathbf{N}_{\mathbf{u}} \bar{\mathbf{u}} \quad \text{and} \quad p = \mathbf{N}_p \bar{p} \quad (6.48)$$

where, $\bar{\mathbf{u}}$ and \bar{p} are the unknown *dofs* at control points to be determined and $\mathbf{N}_{\mathbf{u}}$ is same as those given in (6.28) and \mathbf{N}_p is,

$$\mathbf{N}_p = [N_{p,0} \quad N_{p,1} \quad \dots \quad N_{p,m-1}] \quad (6.49)$$

By using (6.48) into the least-squares functional (6.47) and equating its first variation to zero, yields a linear system of equations given in matrix form, as,

$$\mathbf{K} \bar{\mathbf{U}} = \mathbf{F} \quad (6.50)$$

where,

$$\bar{\mathbf{U}} = \begin{Bmatrix} \bar{\mathbf{u}} \\ \bar{p} \end{Bmatrix} \quad (6.51)$$

Matrix \mathbf{K} and vector \mathbf{F} are given by,

$$\mathbf{K} = \int_{\Omega} \mathbf{J}_1^T \mathbf{J}_1 \, d\Omega + \int_{\Omega} \mathbf{J}_2^T \mathbf{J}_2 \, d\Omega + \int_{\Gamma_D} \mathbf{J}_3^T \mathbf{J}_3 \, d\Gamma_D + \int_{\Gamma_N} \mathbf{J}_4^T \mathbf{J}_4 \, d\Gamma_N \quad (6.52)$$

$$\mathbf{F} = \int_{\Omega} \mathbf{J}_1^T \mathbf{f}_0 \, d\Omega + \int_{\Gamma_D} \mathbf{J}_3^T \mathbf{g} \, d\Gamma_D + \int_{\Gamma_N} \mathbf{J}_4^T \mathbf{t}_0 \, d\Gamma_N \quad (6.53)$$

where,

$$\mathbf{J}_1 = [\mu \Delta \mathbf{N}_{\mathbf{u}} \quad \alpha \nabla \mathbf{N}_p] \quad (6.54)$$

$$\mathbf{J}_2 = (\nabla \cdot \mathbf{N}_{\mathbf{u}})^T \quad (6.55)$$

$$\mathbf{J}_3 = \mathbf{N}_{\mathbf{u}} \quad (6.56)$$

$$\mathbf{J}_4 = [\mu (\nabla \otimes \mathbf{N}_{\mathbf{u}}) \mathbf{n} + \mu (\nabla \cdot \mathbf{N}_{\mathbf{u}}) \otimes \mathbf{n} - \frac{2\mu}{d} \mathbf{n} \otimes (\nabla \cdot \mathbf{N}_{\mathbf{u}}) \quad \mathbf{n} \otimes \mathbf{N}_p] \quad (6.57)$$

In the expanded form,

$$\mathbf{J}_1 = [\mathbf{A}_0 \quad \mathbf{A}_1 \quad \dots \quad \mathbf{A}_{n-1} \quad \mathbf{B}_0 \quad \mathbf{B}_1 \quad \dots \quad \mathbf{B}_{m-1}] \quad (6.58)$$

$$\mathbf{J}_2 = [\mathbf{C}_0 \quad \mathbf{C}_1 \quad \dots \quad \mathbf{C}_{n-1}] \quad (6.59)$$

$$\mathbf{J}_4 = [\mathbf{L}_0 \quad \mathbf{L}_1 \quad \dots \quad \mathbf{L}_{n-1} \quad \mathbf{M}_0 \quad \mathbf{M}_1 \quad \dots \quad \mathbf{M}_{m-1}] \quad (6.60)$$

where,

$$\mathbf{A}_i = \mu(\Delta N_{u,i})\mathbf{I} \quad (6.61)$$

$$\mathbf{B}_i = \alpha \left[\frac{\partial N_{p,i}}{\partial x} \quad \frac{\partial N_{p,i}}{\partial y} \quad \frac{\partial N_{p,i}}{\partial z} \right]^T \quad (6.62)$$

$$\mathbf{C}_i = \left[\frac{\partial N_{u,i}}{\partial x} \quad \frac{\partial N_{u,i}}{\partial y} \quad \frac{\partial N_{u,i}}{\partial z} \right] \quad (6.63)$$

$$\mathbf{M}_i = \left[n_x \frac{\partial N_{p,i}}{\partial x} \quad n_y \frac{\partial N_{p,i}}{\partial y} \quad n_z \frac{\partial N_{p,i}}{\partial z} \right]^T \quad (6.64)$$

$$\mathbf{L}_i = \mu \begin{bmatrix} a_i + (1 - \frac{2}{d}) \frac{\partial N_{u,i}}{\partial x} n_x & \frac{\partial N_{u,i}}{\partial x} n_y - \frac{2}{d} \frac{\partial N_{u,i}}{\partial y} n_x & \frac{\partial N_{u,i}}{\partial x} n_z - \frac{2}{d} \frac{\partial N_{u,i}}{\partial z} n_x \\ \frac{\partial N_{u,i}}{\partial y} n_x - \frac{2}{d} \frac{\partial N_{u,i}}{\partial x} n_y & a_i + (1 - \frac{2}{d}) \frac{\partial N_{u,i}}{\partial y} n_y & \frac{\partial N_{u,i}}{\partial y} n_z - \frac{2}{d} \frac{\partial N_{u,i}}{\partial z} n_y \\ \frac{\partial N_{u,i}}{\partial z} n_x - \frac{2}{d} \frac{\partial N_{u,i}}{\partial x} n_z & \frac{\partial N_{u,i}}{\partial z} n_y - \frac{2}{d} \frac{\partial N_{u,i}}{\partial y} n_z & a_i + (1 - \frac{2}{d}) \frac{\partial N_{u,i}}{\partial z} n_z \end{bmatrix} \quad (6.65)$$

where,

$$a_i = \left(\frac{\partial N_{u,i}}{\partial x} n_x + \frac{\partial N_{u,i}}{\partial y} n_y + \frac{\partial N_{u,i}}{\partial z} n_z \right) \quad (6.66)$$

6.3.4 Compressible nonlinear elasticity

Now a least-square formulation for a compressible Neo-Hookean material is presented in both the reference and current configurations in order to assess the amount of effort required in terms of mathematics and computer programming in both the formulations. For the compressible Neo-Hookean material given by the free energy function,

$$\Psi = \frac{\mu}{2} (\mathbf{I}_C - 3) - \mu \ln J + \frac{\lambda}{2} (\ln J)^2 \quad (6.67)$$

First Piola-Kirchhoff stress (\mathbf{P}) and Cauchy stress ($\boldsymbol{\sigma}$) are given as,

$$\mathbf{P}(\mathbf{u}) = \mu \mathbf{F} + (\lambda \ln J - \mu) \mathbf{F}^{-T} \quad (6.68)$$

$$\boldsymbol{\sigma}(\mathbf{u}) = \frac{\mu}{J} \mathbf{b} + \frac{1}{J} (\lambda \ln J - \mu) \mathbf{I} \quad (6.69)$$

6.3.4.1 Least-square formulation in the reference configuration

In order to define a least-squares functional in the reference configuration the First Piola-Kirchhoff stress (\mathbf{P}) has to be linearised. Linearisation of \mathbf{P} at iteration $(k + 1)$ is,

$$\mathbf{P}(\mathbf{u}^k + d\mathbf{u}) \approx \mathbf{P}(\mathbf{u}^k) + \mathcal{D}_{\mathbf{u}}\mathbf{P}(\mathbf{u}^k)[d\mathbf{u}] = \mathbf{P}(\mathbf{u}^k) + \mathbf{A} \quad (6.70)$$

where, $\mathbf{A} = \mathcal{D}_{\mathbf{u}}\mathbf{P}(\mathbf{u}^k)[d\mathbf{u}]$ is the directional derivative of \mathbf{P} in the direction of $d\mathbf{u}$ at \mathbf{u}^k . The main purpose in denoting the directional derivative with \mathbf{A} is to avoid the complexity in writing the subsequent equations and make the formulation as generalised as possible. Using (6.70) the linearised governing equations, at iteration $(k + 1)$, are written as,

$$\nabla_{\mathbf{x}} \cdot \mathbf{A} = \mathbf{f}_0 - \nabla_{\mathbf{x}} \cdot \mathbf{P}(\mathbf{u}^k) \quad \text{in } \Omega, \quad (6.71a)$$

$$d\mathbf{u} = \mathbf{g}^{k+1} - \mathbf{u}^k \quad \text{on } \Gamma_D, \quad (6.71b)$$

$$\mathbf{A} \cdot \mathbf{N} = \mathbf{t}_0 - \mathbf{P}(\mathbf{u}^k) \cdot \mathbf{N} \quad \text{in } \Gamma_N, \quad (6.71c)$$

Now, using the linearised governing equations (6.71) a least-squares functional can be constructed as,

$$\begin{aligned} \mathcal{J}(\mathbf{u}; \mathbf{f}_0, \mathbf{g}_0, \mathbf{t}_0) = & \frac{1}{2} \left(\|\nabla_{\mathbf{x}} \cdot \mathbf{A} - (\mathbf{f}_0 - \nabla_{\mathbf{x}} \cdot \mathbf{P}(\mathbf{u}^k))\|_0^2 + \|d\mathbf{u} - (\mathbf{g}^{k+1} - \mathbf{u}^k)\|_0^2 \right. \\ & \left. + \|(\mathbf{A} \cdot \mathbf{N} - (\mathbf{t}_0 - \mathbf{P}(\mathbf{u}^k) \cdot \mathbf{N}))\|_0^2 \right) \end{aligned} \quad (6.72)$$

Taking approximations for displacements (\mathbf{u}) as,

$$\mathbf{u} = \mathbf{N}_{\mathbf{u}} \bar{\mathbf{u}} \quad (6.73)$$

gives,

$$d\mathbf{u} = \mathbf{N}_{\mathbf{u}} d\bar{\mathbf{u}} \quad (6.74)$$

and equating the first variation of the least-squares functional to zero results in a matrix system of equations given by,

$$\mathbf{K} d\bar{\mathbf{u}} = \mathbf{F} \quad (6.75)$$

where, $d\bar{\mathbf{u}}$ is the vector of unknowns. Matrix \mathbf{K} and vector \mathbf{F} are computed as,

$$\mathbf{K} = \int_{\Omega} \mathbf{J}_1^T \mathbf{J}_1 \, d\Omega + \int_{\Gamma_D} \mathbf{J}_2^T \mathbf{J}_2 \, d\Gamma_D + \int_{\Gamma_N} \mathbf{J}_3^T \mathbf{J}_3 \, d\Gamma_N \quad (6.76)$$

$$\begin{aligned} \mathbf{F} = & \int_{\Omega} \mathbf{J}_1^T (\mathbf{f}_0 - \nabla_{\mathbf{x}} \cdot \mathbf{P}(\mathbf{u}^k)) \, d\Omega + \int_{\Gamma_D} \mathbf{J}_2^T (\mathbf{g}^{k+1} - \mathbf{u}^k) \, d\Gamma_D \\ & + \int_{\Gamma_N} \mathbf{J}_3^T (\mathbf{t}_0 - \mathbf{P}(\mathbf{u}^k) \cdot \mathbf{N}) \, d\Gamma_N \end{aligned} \quad (6.77)$$

where, \mathbf{J}_1 , \mathbf{J}_2 , and \mathbf{J}_3 can be computed similar to the procedure followed in the previous cases. For the First Piola-Kirchhoff stress given by (6.68),

$$\begin{aligned} \mathbf{A} = & \mathcal{D}_{\mathbf{u}}\mathbf{P}(\mathbf{u}^k)[d\mathbf{u}] \\ = & \mu \nabla_{\mathbf{x}}(d\mathbf{u}) + \lambda \operatorname{div}(d\mathbf{u}) \mathbf{F}^{-T} - (\lambda \ln J - \mu) \mathbf{F}^{-T} d\mathbf{F}^T \mathbf{F}^{-T} \end{aligned} \quad (6.78)$$

6.3.4.2 Least-square formulation in the current configuration

Along similar lines, in order to define a least-squares functional in the current configuration the Cauchy's stress given by (6.69) has to be linearised. Linearisation of the Cauchy's stress at iteration $(k + 1)$ is,

$$\boldsymbol{\sigma}(\mathbf{u}^k + d\mathbf{u}) \approx \boldsymbol{\sigma}(\mathbf{u}^k) + \mathcal{D}_{\mathbf{u}}\boldsymbol{\sigma}(\mathbf{u}^k)[d\mathbf{u}] = \boldsymbol{\sigma}(\mathbf{u}^k) + \mathbf{A} \quad (6.79)$$

where, $\mathbf{A} = \mathcal{D}_{\mathbf{u}}\boldsymbol{\sigma}(\mathbf{u}^k)[d\mathbf{u}]$ is the directional derivative of $\boldsymbol{\sigma}$ in the direction of $d\mathbf{u}$ at \mathbf{u}^k . So, using (6.79) the governing equations are written as,

$$\nabla_{\mathbf{x}} \cdot \mathbf{A} = \mathbf{f} - \nabla_{\mathbf{x}} \cdot \boldsymbol{\sigma}(\mathbf{u}^k) \quad \text{in } \omega, \quad (6.80a)$$

$$d\mathbf{u} = \mathbf{g} - \mathbf{u}^k \quad \text{on } \gamma_D, \quad (6.80b)$$

$$\mathbf{A} \cdot \mathbf{n} = \mathbf{t} - \boldsymbol{\sigma}(\mathbf{u}^k) \cdot \mathbf{n} \quad \text{in } \gamma_N, \quad (6.80c)$$

Here we would like to point out that the body force, \mathbf{f} , and traction, \mathbf{t} , given by (6.22) are not linearised in the present work. Now, using the linearised governing equations (6.80) we can construct a least-squares functional as,

$$\begin{aligned} \mathcal{J}(\mathbf{u}; \mathbf{f}_0, \mathbf{g}_0, \mathbf{t}_0) = & \frac{1}{2} \left(\|\nabla_{\mathbf{x}} \cdot \mathbf{A} - (\mathbf{f}^{k+1} - \nabla_{\mathbf{x}} \cdot \boldsymbol{\sigma}(\mathbf{u}^k))\|_0^2 + \|d\mathbf{u} - (\mathbf{g}^{k+1} - \mathbf{u}^k)\|_0^2 \right. \\ & \left. + \|(\mathbf{A} \cdot \mathbf{n} - (\mathbf{t}^{k+1} - \boldsymbol{\sigma}(\mathbf{u}^k) \cdot \mathbf{n}))\|_0^2 \right) \end{aligned} \quad (6.81)$$

Taking approximations for displacements (\mathbf{u}) as,

$$\mathbf{u} = \mathbf{N}_{\mathbf{u}} \bar{\mathbf{u}} \quad (6.82)$$

gives,

$$d\mathbf{u} = \mathbf{N}_{\mathbf{u}} d\bar{\mathbf{u}} \quad (6.83)$$

and equating the first variation of the least-squares functional to zero results in a matrix system of equations given by,

$$\mathbf{K} d\bar{\mathbf{u}} = \mathbf{F} \quad (6.84)$$

where, $d\bar{\mathbf{u}}$ is the vector of unknowns. Matrix \mathbf{K} and vector \mathbf{F} are computed as,

$$\mathbf{K} = \int_{\omega} \mathbf{J}_1^T \mathbf{J}_1 d\omega + \int_{\gamma_D} \mathbf{J}_2^T \mathbf{J}_2 d\gamma_D + \int_{\gamma_N} \mathbf{J}_3^T \mathbf{J}_3 d\gamma_N \quad (6.85)$$

$$\begin{aligned} \mathbf{F} = & \int_{\omega} \mathbf{J}_1^T (\mathbf{f}^{k+1} - \nabla_{\mathbf{x}} \cdot \boldsymbol{\sigma}(\mathbf{u}^k)) d\omega + \int_{\gamma_D} \mathbf{J}_2^T (\mathbf{g}^{k+1} - \mathbf{u}^k) d\gamma_D \\ & + \int_{\gamma_N} \mathbf{J}_3^T (\mathbf{t}^{k+1} - \boldsymbol{\sigma}(\mathbf{u}^k) \cdot \mathbf{n}) d\gamma_N \end{aligned} \quad (6.86)$$

For the Cauchy's stress given by (6.69),

$$\begin{aligned}\mathbf{A} &= \mathcal{D}_{\mathbf{u}}\boldsymbol{\sigma}(\mathbf{u}^k)[d\mathbf{u}] \\ &= \frac{\mu}{J} \left[\nabla_{\mathbf{x}}(d\mathbf{u})\mathbf{b} + \mathbf{b}(\nabla_{\mathbf{x}}(d\mathbf{u}))^T \right] - \frac{1}{J} [\mu(\mathbf{b} - \mathbf{I}) - \lambda(1 - \ln J)\mathbf{I}] \operatorname{div}(d\mathbf{u})\end{aligned}\quad (6.87)$$

An important difference to be noted at this point is that the integrals in equations (6.85) and (6.86) are with respect to the current configuration. While minimising the least-squares functional (6.81) the quantities $d\omega$, $d\gamma_D$ and $d\gamma_N$ are assumed to be constant.

6.3.5 Nearly incompressible non-linear elasticity

As an example, consider a Neo-Hookean hyperelastic material model whose stored energy function, W , can be represented as the additive decomposition of deviatoric and volumetric parts, as,

$$W(J, \mathbf{C}) = W^{\text{dev}}(J, \mathbf{C}) + W^{\text{vol}}(J) \quad (6.88)$$

$$W(J, \bar{\mathbf{C}}) = \frac{1}{2}\mu(\mathbf{I}_{\bar{\mathbf{C}}} - 3) + \frac{1}{2}\kappa \left(\frac{1}{2}(J^2 - 1) - \ln J \right) \quad (6.89)$$

where $\bar{\mathbf{C}}$ is the distortional component of the right Cauchy-Green tensor given by 3.62. For the above strain energy function Cauchy stress can be derived as,

$$\boldsymbol{\sigma}(\mathbf{u}, p) = \frac{\mu}{J^{1/3}} \left(\mathbf{b} - \frac{1}{3}\mathbf{I}_{\mathbf{b}}\mathbf{I} \right) + p\mathbf{I} \quad (6.90)$$

and pressure p is related to the material model by

$$p = \frac{\partial W^{\text{vol}}(J)}{\partial J} = \frac{\kappa}{2} \left(J - \frac{1}{J} \right) \quad (6.91)$$

which can be rewritten as,

$$r_p = \frac{1}{2} \left(J - \frac{1}{J} \right) - \frac{p}{\kappa} \quad (6.92)$$

For the sake of brevity the least-squares formulation is given only in terms of the current configuration. Now, in order to construct a least-squares functional, equations (6.90) and (6.92) have to be linearised. Linearisation of the Cauchy's stress at iteration $(k+1)$ gives,

$$\begin{aligned}\boldsymbol{\sigma}(\mathbf{u}^k + d\mathbf{u}, p^k + dp) &\approx \boldsymbol{\sigma}(\mathbf{u}^k, p^k) + \mathcal{D}_{\mathbf{u}}\boldsymbol{\sigma}[d\mathbf{u}] + \mathcal{D}_p\boldsymbol{\sigma}[dp] \\ &= \boldsymbol{\sigma}(\mathbf{u}^k, p^k) + \mathbf{A}\end{aligned}\quad (6.93)$$

where, $\mathcal{D}_{\mathbf{u}}\boldsymbol{\sigma}[d\mathbf{u}]$ and $\mathcal{D}_p\boldsymbol{\sigma}[dp]$ are the directional derivatives of $\boldsymbol{\sigma}$ in the direction of $d\mathbf{u}$ and dp respectively. And linearisation of (6.91) gives,

$$\begin{aligned}r_p(\mathbf{u}^k + d\mathbf{u}, p^k + dp) &\approx r_p(\mathbf{u}^k, p^k) + \mathcal{D}_{\mathbf{u}}r_p[d\mathbf{u}] + \mathcal{D}_pr_p[dp] \\ &= r_p(\mathbf{u}^k, p^k) + B\end{aligned}\quad (6.94)$$

where, $\mathcal{D}_{\mathbf{u}}r_p[d\mathbf{u}]$ and $\mathcal{D}_{\mathbf{u}}r_p[dp]$ are the directional derivatives of r_p in the direction of $d\mathbf{u}$ and dp , respectively. \mathbf{A} and B are given as,

$$\mathbf{A} = \frac{\mu}{J^{5/3}} \left[\nabla(d\mathbf{u})\mathbf{b} + \mathbf{b}(\nabla(d\mathbf{u}))^T - \frac{2}{3}\text{tr}(\nabla(d\mathbf{u})\mathbf{b})\mathbf{I} - \frac{5}{3} \left(\mathbf{b} - \frac{1}{3}\mathbf{I}_b\mathbf{I} \right) (\nabla \cdot d\mathbf{u}) \right] + dp\mathbf{I} \quad (6.95)$$

$$B = \frac{1}{2} \left(J + \frac{1}{J} \right) (\nabla \cdot d\mathbf{u}) - \frac{dp}{\kappa} \quad (6.96)$$

Using (6.93) and (6.94) the governing equations can be rewritten as,

$$\nabla \cdot \mathbf{A} = \mathbf{f}^{k+1} - \nabla \cdot \boldsymbol{\sigma}(\mathbf{u}^k, p^k) \quad \text{in } \Omega \quad (6.97a)$$

$$B = -r_p(\mathbf{u}^k, p^k) \quad \text{in } \Omega \quad (6.97b)$$

$$d\mathbf{u} = \mathbf{g}^{k+1} - \mathbf{u}^k \quad \text{on } \Gamma_D \quad (6.97c)$$

$$\mathbf{A} \cdot \mathbf{n} = \mathbf{t}^{k+1} - \boldsymbol{\sigma}(\mathbf{u}^k, p^k) \cdot \mathbf{n} \quad \text{on } \Gamma_N \quad (6.97d)$$

Here it is to be pointed out that the body force, \mathbf{f} , and traction, \mathbf{t} , given by (6.22) are not linearised in the present work. Now, using the linearised governing equations given in (6.97), a least-squares functional can be constructed as,

$$\begin{aligned} \mathcal{J}(\mathbf{u}, p; \mathbf{f}, \mathbf{g}) = & \frac{1}{2} \left(\|\nabla \cdot \mathbf{A} - (\mathbf{f}^{k+1} - \nabla \cdot \boldsymbol{\sigma}(\mathbf{u}^k, p^k))\|_0^2 + \|B + r_p(\mathbf{u}^k, p^k)\|_0^2 \right. \\ & + \|d\mathbf{u} - (\mathbf{g}^{k+1} - \mathbf{u}^k)\|_0^2 \\ & \left. + \|(\mathbf{A} \cdot \mathbf{n} - (\mathbf{t}^{k+1} - \boldsymbol{\sigma}(\mathbf{u}^k, p^k) \cdot \mathbf{n}))\|_0^2 \right) \end{aligned} \quad (6.98)$$

Taking approximations for displacements (\mathbf{u}) and pressure (p) as,

$$\mathbf{u} = \mathbf{N}_u \bar{\mathbf{u}} \quad \text{and} \quad p = \mathbf{N}_p \bar{p} \quad (6.99)$$

and following the similar approach used earlier in case of Navier-Stokes equations and linear elasticity, results in a matrix system of equations.

$$\mathbf{K} = \int_{\omega} \mathbf{J}_1^T \mathbf{J}_1 \, d\omega + \int_{\omega} \mathbf{J}_2^T \mathbf{J}_2 \, d\omega + \int_{\gamma_D} \mathbf{J}_3^T \mathbf{J}_3 \, d\gamma_D + \int_{\gamma_N} \mathbf{J}_4^T \mathbf{J}_4 \, d\gamma_N \quad (6.100)$$

$$\begin{aligned} \mathbf{F} = & \int_{\omega} \mathbf{J}_1^T (\mathbf{f}^{k+1} - \nabla \cdot \boldsymbol{\sigma}(\mathbf{u}^k, p^k)) \, d\omega + \int_{\gamma_D} \mathbf{J}_3^T (\mathbf{g}^{k+1} - \mathbf{u}^k) \, d\gamma_D \\ & + \int_{\gamma_N} \mathbf{J}_4^T (\mathbf{t}^{k+1} - \boldsymbol{\sigma}(\mathbf{u}^k, p^k) \cdot \mathbf{n}) \, d\gamma_N \end{aligned} \quad (6.101)$$

6.4 Fluid Mechanics

6.4.1 The incompressible Navier-Stokes

The governing equations of incompressible Navier-Stokes, presented in Section 3.7, are summarised below.

$$\rho(\mathbf{v} \cdot \nabla)\mathbf{v} - \mu\Delta\mathbf{u} + \nabla p = \mathbf{f} \quad \text{in } \Omega \quad (6.102a)$$

$$\nabla \cdot \mathbf{v} = 0 \quad \text{in } \Omega \quad (6.102b)$$

$$\mathbf{v} = \mathbf{g} \quad \text{on } \Gamma_D \quad (6.102c)$$

$$[-p\mathbf{I} + \mu(\nabla\mathbf{v} + (\nabla\mathbf{v})^T)] \cdot \mathbf{n} = \mathbf{t} \quad \text{on } \Gamma_N \quad (6.102d)$$

For the examples considered in the present work no Neumann boundary conditions are present. Therefore, the term corresponding to Neumann boundary conditions is not considered in the present least-squares formulation. But it is pointed out that the inclusion of Neumann boundary conditions is exactly similar to the method followed in least-squares formulations for elasticity, presented above.

As discussed in Section 6.1, in order to use Gauss-Newton method, the governing equations have to be linearised first. The linearised equations of the above governing equations (6.102) – at iteration $(k + 1)$ – are given as,

$$\rho(\mathbf{v}^k \cdot \nabla)d\mathbf{v} + \rho(d\mathbf{v} \cdot \nabla)\mathbf{v}^k - \mu\Delta(d\mathbf{v}) + \nabla(dp) = \mathbf{f}^{k+1} - \mathbf{R}(\mathbf{v}^k) \quad (6.103a)$$

$$\nabla \cdot d\mathbf{v} = -\nabla \cdot \mathbf{v}^k \quad (6.103b)$$

$$d\mathbf{v} = \mathbf{g}^{k+1} - \mathbf{v}^k \quad (6.103c)$$

where,

$$\mathbf{R}(\mathbf{v}^k) = \rho(\mathbf{v}^k \cdot \nabla)\mathbf{v}^k - \mu\Delta\mathbf{v}^k + \nabla p^k \quad (6.104)$$

Then, the least-squares functional based on L^2 norms of the linearised residuals is given by,

$$\begin{aligned} \mathcal{J}(\mathbf{v}, p; \mathbf{f}, \mathbf{g}) = & \frac{1}{2} \left(\|\rho(\mathbf{v}^k \cdot \nabla)d\mathbf{v} + \rho(d\mathbf{v} \cdot \nabla)\mathbf{v}^k - \mu\Delta(d\mathbf{v}) + \nabla(dp) - \mathbf{f}^{k+1} + \mathbf{R}(\mathbf{v}^k)\|_0^2 \right. \\ & \left. + \|\nabla \cdot d\mathbf{v} + \nabla \cdot \mathbf{v}^k\|_0^2 + \|d\mathbf{v} - (\mathbf{g}^{k+1} - \mathbf{v}^k)\|_0^2 \right) \end{aligned} \quad (6.105)$$

Taking approximations for velocities (\mathbf{v}) and pressure (p) as,

$$\mathbf{v} = \mathbf{N}_v \bar{\mathbf{v}} \quad \text{and} \quad p = \mathbf{N}_p \bar{p} \quad (6.106)$$

where, $\bar{\mathbf{v}}$ and \bar{p} are the unknown DOFs at control points to be determined. Then,

$$d\mathbf{v} = \mathbf{N}_v d\bar{\mathbf{v}} \quad \text{and} \quad dp = \mathbf{N}_p d\bar{p} \quad (6.107)$$

Using (6.107) in the least-squares functional (6.105) and equating its first variation to zero, yields a linear system of equations given in matrix form as,

$$\mathbf{K} d\bar{\mathbf{V}} = \mathbf{F} \quad (6.108)$$

where,

$$d\bar{\mathbf{V}} = \left\{ d\bar{\mathbf{v}} \right\} \quad (6.109)$$

is the vector of unknowns. Matrix \mathbf{K} and vector \mathbf{F} are given by,

$$\mathbf{K} = \int_{\Omega} \mathbf{J}_1^T \mathbf{J}_1 \, d\Omega + \int_{\Omega} \mathbf{J}_2^T \mathbf{J}_2 \, d\Omega + \int_{\Gamma_D} \mathbf{J}_3^T \mathbf{J}_3 \, d\Gamma_D \quad (6.110)$$

$$\mathbf{F} = \int_{\Omega} \mathbf{J}_1^T (\mathbf{f}^{k+1} - \mathbf{R}(\mathbf{v}^k)) \, d\Omega + \int_{\Gamma_D} \mathbf{J}_3^T (\mathbf{g}^{k+1} - \mathbf{v}^k) \, d\Gamma_D \quad (6.111)$$

with,

$$\mathbf{J}_1 = [\mathbf{A}_0 \quad \mathbf{A}_1 \quad \dots \quad \mathbf{A}_{n-1} \quad \mathbf{B}_0 \quad \mathbf{B}_1 \quad \dots \quad \mathbf{B}_{m-1}] \quad (6.112)$$

$$\mathbf{J}_2 = (\nabla \cdot \mathbf{N}_v)^T = [\mathbf{C}_0 \quad \mathbf{C}_1 \quad \dots \quad \mathbf{C}_{n-1}] \quad (6.113)$$

$$\mathbf{J}_3 = \mathbf{N}_v \quad (6.114)$$

and,

$$\mathbf{A}_i = \begin{bmatrix} a_i + \rho \frac{\partial v_1}{\partial x} N_{v,i} & \rho \frac{\partial v_1}{\partial y} N_{v,i} & \rho \frac{\partial v_1}{\partial z} N_{v,i} \\ \rho \frac{\partial v_2}{\partial x} N_{v,i} & a_i + \rho \frac{\partial v_2}{\partial y} N_{v,i} & \rho \frac{\partial v_2}{\partial z} N_{v,i} \\ \rho \frac{\partial v_3}{\partial x} N_{v,i} & \rho \frac{\partial v_3}{\partial y} N_{v,i} & a_i + \rho \frac{\partial v_3}{\partial z} N_{v,i} \end{bmatrix} \quad (6.115)$$

$$\mathbf{B}_i = \left[\frac{\partial N_{p,i}}{\partial x} \quad \frac{\partial N_{p,i}}{\partial y} \quad \frac{\partial N_{p,i}}{\partial z} \right]^T \quad (6.116)$$

$$\mathbf{C}_i = \left[\frac{\partial N_{v,i}}{\partial x} \quad \frac{\partial N_{v,i}}{\partial y} \quad \frac{\partial N_{v,i}}{\partial z} \right] \quad (6.117)$$

$$a_i = \rho \left(v_1 \frac{\partial N_{v,i}}{\partial x} + v_2 \frac{\partial N_{v,i}}{\partial y} + v_3 \frac{\partial N_{v,i}}{\partial z} \right) - \mu(\Delta N_{u,i}) \quad (6.118)$$

Chapter 7

Least-Squares Formulation - Numerical Examples

In this chapter, numerical examples to demonstrate the performance of LSFEMs proposed in Chapter 6 are presented. Examples chosen for compressible elasticity — one dimensional bar and two-dimensional block under body force — are simple yet sufficiently complex to make clear comparisons between different schemes. Cook’s membrane used to present results for nearly compressible linear and nonlinear elasticity; and both the examples used for fluid mechanics — Kovasznay flow and flow in a lid-driven cavity — are benchmark problems in the literature. It is important to point out that straightforward LSFEMs lead to matrix systems with high condition numbers (see [19]). However, the present work is not concerned about this issue as the resulting matrix systems are solved using direct solvers [1, 2].

7.1 NURBS spaces

As discussed in Chapters 1 and 6, LSFEMs are not required to satisfy LBB condition. So, basis functions of any arbitrary order can be used to approximate different field variables; but this results in complicated programming routines. Therefore, equal order NURBS basis functions are used. Naming convention followed for LSFEMs is: NURBS shape functions of degree a are denoted as Q_a , meaning that the degree of approximation spaces for both the displacements (or velocities in fluid mechanics) and pressure is the same and is equal to a .

All of the LSFEMs developed in this work require that basis functions are at least C^1 continuous across element boundaries. This puts a stringent requirement on the continuity across patch interfaces, which is very difficult to achieve in general. This issue can be solved by defining patches with higher-order continuities across their interfaces or by enforcing the jump conditions in the field variables across the patch-interfaces in a least-squares sense. Both of these options are difficult to implement and therefore all the examples con-

sidered in this chapter are modelled with a single patch without any multiple internal knots. Thus, the continuity across element interfaces is always \mathcal{C}^{a-1} for a NURBS patch of degree a . And, for two dimensional examples, the patch is modelled with NURBS spaces of equal order in both directions.

Similar to the mixed Galerkin formulations, the number of Gauss points used in evaluating the element matrices and vectors is equal to $(a + 1)$, in each coordinate direction, for NURBS basis functions of degree a .

7.2 Numerical Examples - Solid Mechanics

7.2.1 Cook's membrane with nearly incompressible linear elasticity

Geometry, material and boundary conditions of the problem are as used in Section 5.1.3 of Chapter 5. A load value of $F = 100$ N/mm is considered in the present example. This problem has a singularity at top left corner where the boundary condition suddenly changes from clamped to traction-free. As in Section 5.1.3, in this example also, five h -refinements, each with different orders of NURBS, are studied with the proposed least-squares formulation. The quantity of interest, again, is the vertical displacement of top-right corner and its variation against number of elements per side for different orders of approximations, is shown Figure 7.1. As the analytical solution is not available for this problem, the displacement value obtained with an extremely fine mesh is used as the reference value. Linear shape functions are not considered as the minimum degree of shape functions required for the current LSFEM is two. Solution obtained with Q_2 NURBS, as expected, is not very good for coarse meshes; however, the accuracy improves as the mesh is refined. Moreover, use of higher order NURBS yields tremendous improvement in the accuracy of solutions. Results obtained with higher-order NURBS spaces are indistinguishable. Contour plots of hydrostatic pressure and von Mises stress, as shown in Figure 7.2, indicate that the distribution of hydrostatic pressure is very smooth and the corner singularity is captured well.

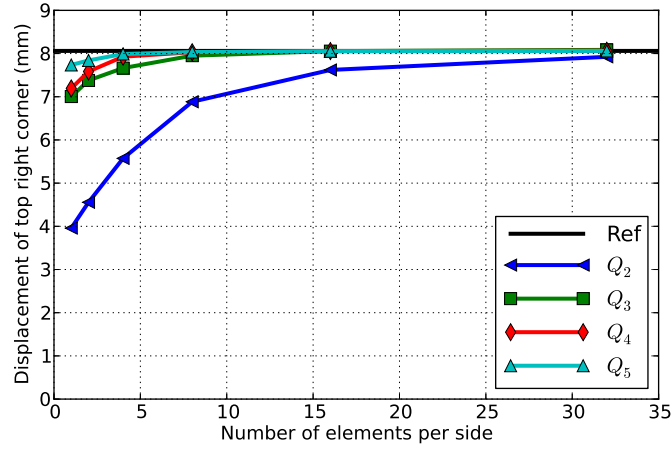


Figure 7.1: Cook's membrane with nearly incompressible linear elasticity: vertical displacement of the top right corner against number of elements per side with different orders of NURBS basis functions.

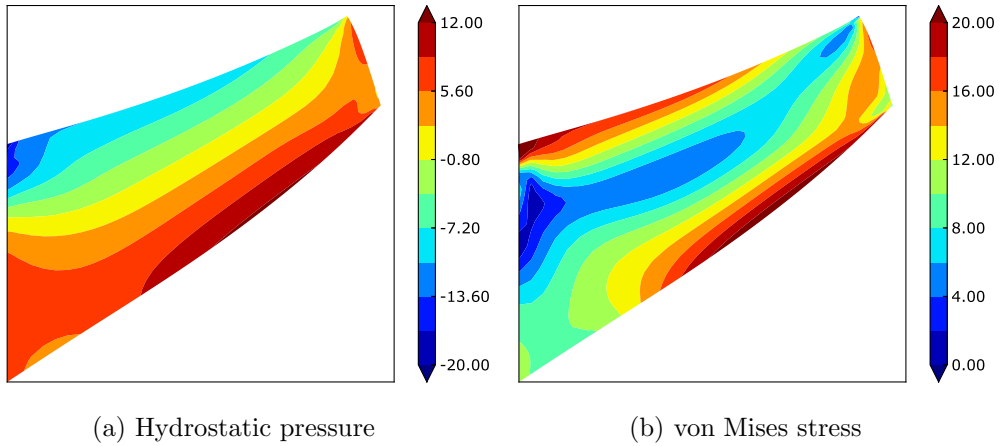


Figure 7.2: Cook's membrane with nearly incompressible linear elasticity: contour plots of hydrostatic pressure and von Mises stress for mesh-5 with Q_3 NURBS.

7.2.2 1-D bar under body force

In this example the performance of LSFEM in the finite strain regime, in both the reference and current configurations, is studied by considering a one-dimensional bar problem under body force. Geometry, loading and boundary conditions are shown in Figure 7.3.

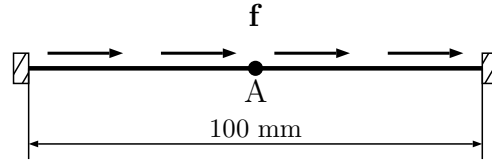


Figure 7.3: 1-D bar under body force: geometry, loading and boundary conditions.

The material properties are: Young's modulus, $E = 240.565$ MPa, and Poisson's ratio, $\nu = 0.0$. A body force, $\mathbf{f}_0 = \{-2.5, 0.0, 0.0\}$ is considered. The quantity of interest is the displacement of the midpoint of the bar, point A in Figure 7.3. Analysis has been performed for different mesh sizes; each with different orders of NURBS basis functions with LSFEM in both the current and reference configurations, denoted by LSFEM-CC and LSFEM-RC respectively. As shown in Figure (7.4), there is no observable difference between the results obtained with LSFEM-CC and LSFEM-RC. For the purpose of validation these results are compared with those obtained with GFEM based on pure displacements, as shown in Figure (7.5). Convergence of the iterations of the Gauss-Newton algorithm is also studied in order to assess its performance. Both the LSFEMs converge exactly in the same manner and convergence of Gauss-Newton iterations improves with the refinement of discretisation in both the formulations, as shown in Table 7.1.

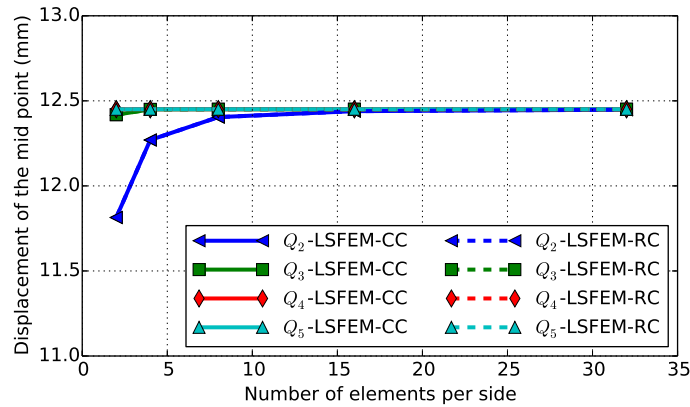


Figure 7.4: 1-D bar under body force: displacement of mid point against number of elements per side with different orders of NURBS basis functions with LSFEM LSFEM-CC and LSFEM-RC.

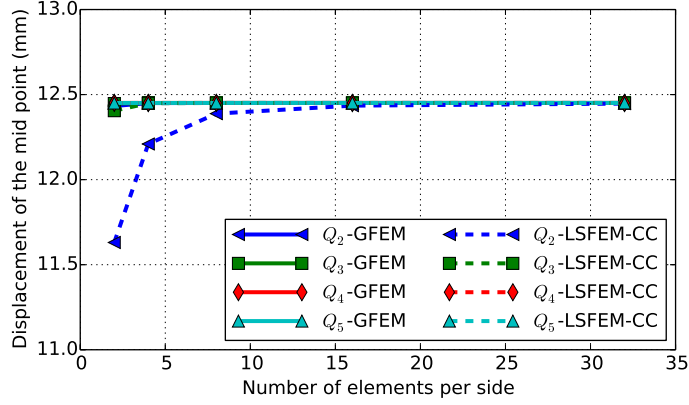


Figure 7.5: 1-D bar under body force: displacement of mid point against number of elements per side with different orders of NURBS basis functions with LSFEM-CC and GFEM.

The most important observation is that the amount of effort required — in terms of mathematics and number of terms to be computed in programming — in current configuration is less than that required in the reference configuration. It can be easily verified from (6.78) and (6.87), respectively, for LSFEM-RC and LSFEM-CC that the term $\nabla_{\mathbf{x}} \cdot \mathbf{A}$ in the current configuration is easier to evaluate and results in a smaller number of terms, hence less computation, than the term $\nabla_{\mathbf{x}} \cdot \mathbf{A}$ in the reference configuration. Even though the difference is negligible for the one dimensional problem, it would be significant in higher dimensions. Hence LSFEM-CC is superior to LSFEM-RC, as it requires less effort — both mathematically and computationally.

Iteration number	Norm of rhs			
	2 elements with Q_2		16 elements with Q_4	
	LSFEM-CC	LSFEM-RC	LSFEM-CC	LSFEM-RC
1	4.8113 E+01	4.8113 E+01	7.6981 E+02	7.6981 E+02
2	1.4326 E+02	8.2654 E+01	4.7143 E+03	2.3102 E+03
3	1.0144 E+01	5.8667 E+00	6.7246 E+02	3.8744 E+02
4	3.7442 E−01	1.9649 E−01	2.0321 E+01	1.1968 E+01
5	2.7038 E−02	1.1698 E−02	1.0688 E−02	6.2914 E−03
6	1.9115 E−03	6.8603 E−04	1.3858 E−09	8.4113 E−10
7	1.3516 E−04	4.0189 E−05		
8	9.5494 E−06	2.3527 E−06		
9	6.7446 E−07	1.3769 E−07		
10	4.7628 E−08	8.0573 E−09		

Table 7.1: 1-D bar under body force: evolution of norm of rhs for the different discretisations with LSFEM-CC and LSFEM-RC.

7.2.3 Plane-strain block under body force

In this example a plane-strain block which is totally fixed on all the boundaries and subject to a body force is studied. The main purpose of this example is to study the effect of application of Dirichlet boundary conditions in strong and weak sense and study the relative performance. The geometry, loading and boundary conditions of the problem are as shown in Figure (7.6). The material properties are: Young's modulus, $E = 240.565$ MPa, and Poisson's ratio, $\nu = 0.3$. A body force, $\mathbf{f}_0 = \{0.0, -2.5, 0.0\}$ is considered. The quantity of interest in this example is the downward displacement of mid point of the block, point A in Figure (7.6). Analysis has been performed for different mesh sizes and different orders of NURBS basis functions for each mesh size using LSFEM-CC; and results obtained are compared with those obtained with GFEM with pure displacements. As shown in Figure (7.7), they match well. The evolution of the norm of rhs for two different discretisations is shown in Figure 7.8. Similar to one-dimensional bar problem, convergence of Gauss-Newton iterations improves with the discretisation but the rate of convergence is slow owing to missing contribution from the Hessian matrix; nevertheless, *super-linear* convergence is achieved in the present case. Contour plots of displacements, shear stress and von Mises stress are shown in Figure 7.10 for 32×32 mesh for Q_4 NURBS.

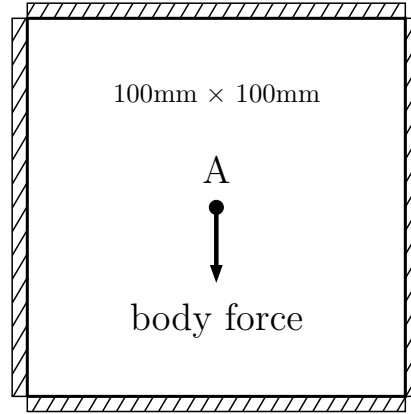


Figure 7.6: Plane-strain block under body force: geometry, loading and boundary conditions.

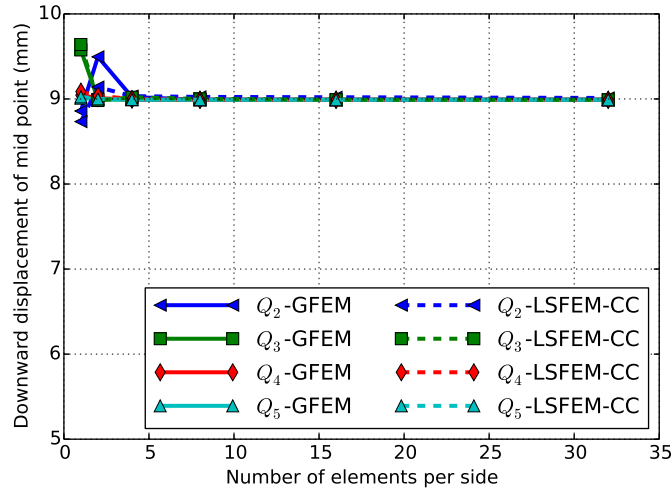


Figure 7.7: Plane-strain block under body force: displacement of mid point against number of elements per side, for different orders of NURBS, with LSFEM-CC and GFEM; Dirichlet boundary conditions are enforced strongly for GFEM and weakly for LSFEM-CC.

Results shown in Figure (7.7) are obtained by applying the boundary conditions weakly — in the least-square sense. A study is also performed by enforcing the boundary conditions strongly in order to assess the relative performance. As NURBS are interpolatory at the boundaries it is expected that the results obtained by enforcing Dirichlet boundary conditions strongly should be better or at least on par with those obtained by enforcing them weakly. But surprisingly, as shown in Figure (7.9), the results obtained by enforcing Dirichlet boundary conditions strongly are less accurate than those obtained by enforcing them weakly. Reasons for this behaviour are unknown and need to be investigated.

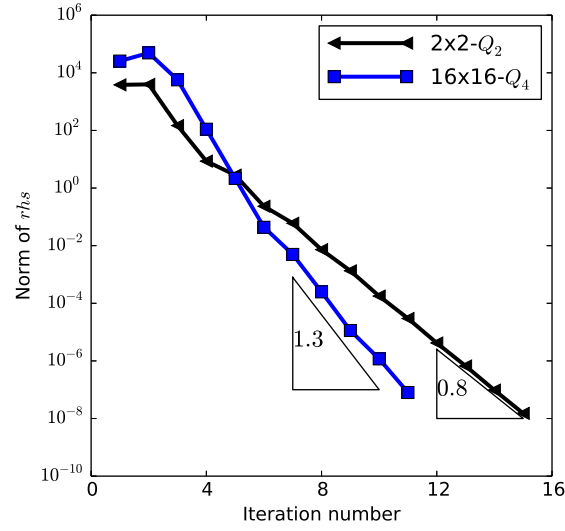


Figure 7.8: Plane-strain block under body force: convergence of Gauss-Newton iterations for two different discretisations with LSFEM-CC; Dirichlet boundary conditions are enforced weakly.

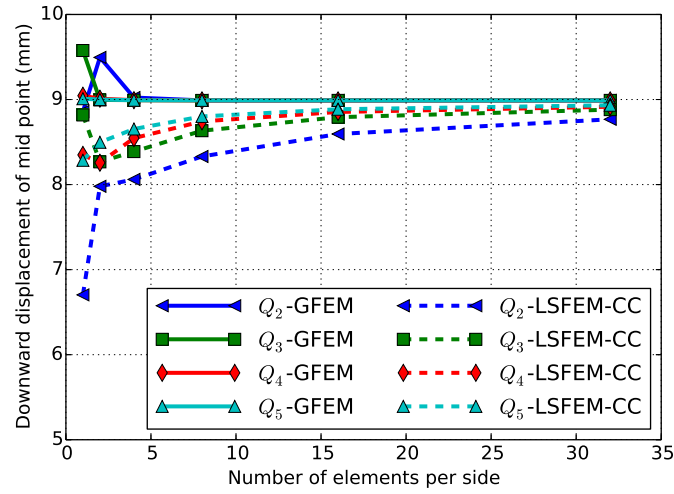


Figure 7.9: Plane-strain block under body force: downward displacement of mid point against number of elements per side with different orders of NURBS with LSFEM-CC and GFEM; Dirichlet boundary conditions are enforced strongly for both GFEM and LSFEM-CC.

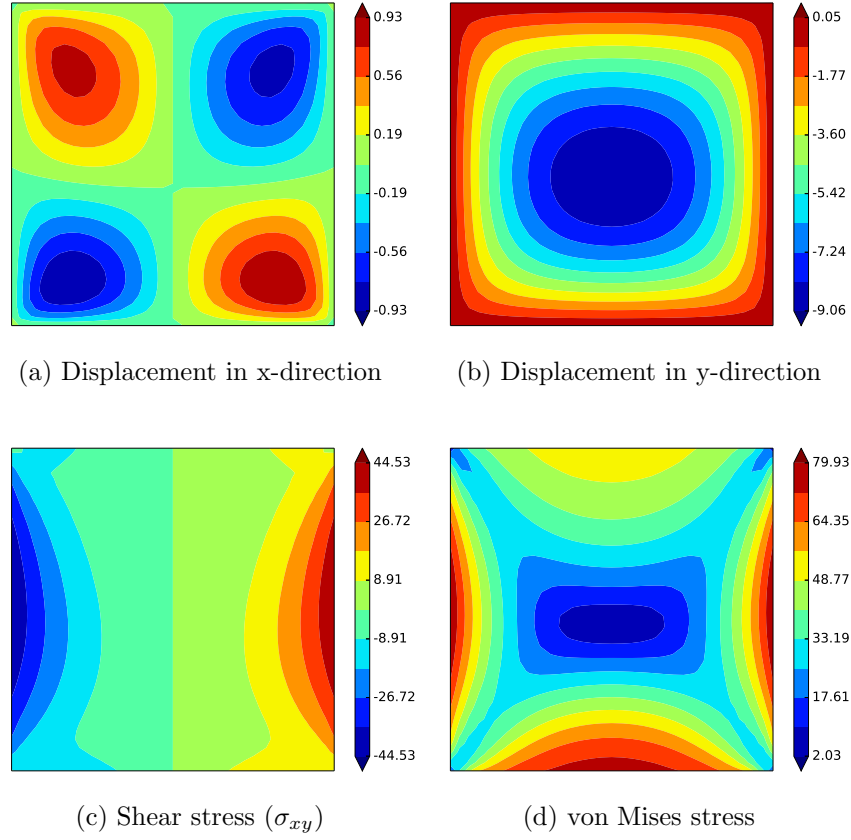


Figure 7.10: Plane-strain block under body force: contour plots of displacements, shear stress and von Mises stress for 32×32 mesh for Q_4 NURBS with LSFEM-CC; Dirichlet boundary conditions are enforced weakly.

7.2.4 Cook's membrane with compressible Neo-Hookean material

Geometry, loading, boundary conditions and material properties are the same as those used in the small-strain example. The load is assumed to be a "dead load" — a fixed load value equal to that in the reference configuration. The response parameter, again, is the vertical displacement of the top right corner and its variation for different discretisations is shown in Figure 7.11. As shown, the accuracy of the results improves with the increase in order of NURBS; however, LSFEM-CC converges slowly compared to GFEM. Convergence of Gauss-Newton iterations, as shown in Figure (7.12), improves with the discretisation.

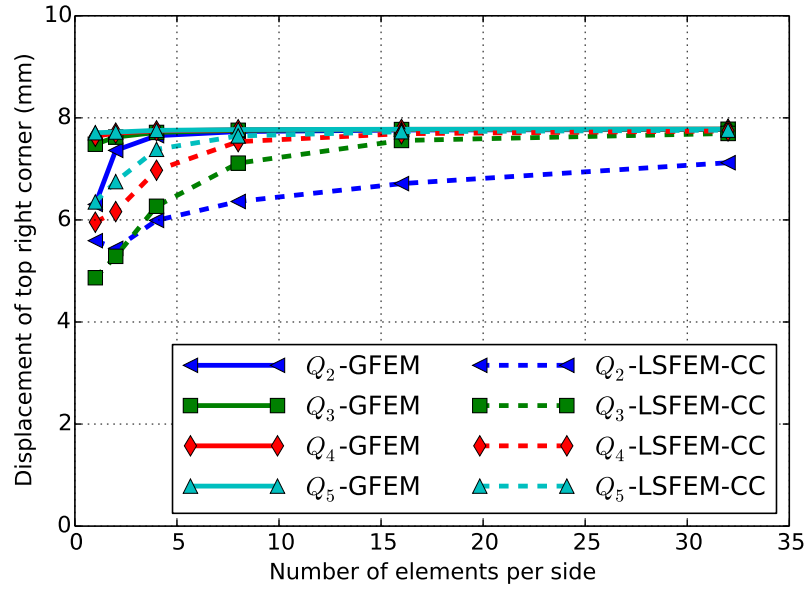


Figure 7.11: Cook's membrane with compressible Neo-Hookean material: vertical displacement of the top right corner against number of elements per side with different orders of NURBS basis functions with LSFEM-CC and GFEM.

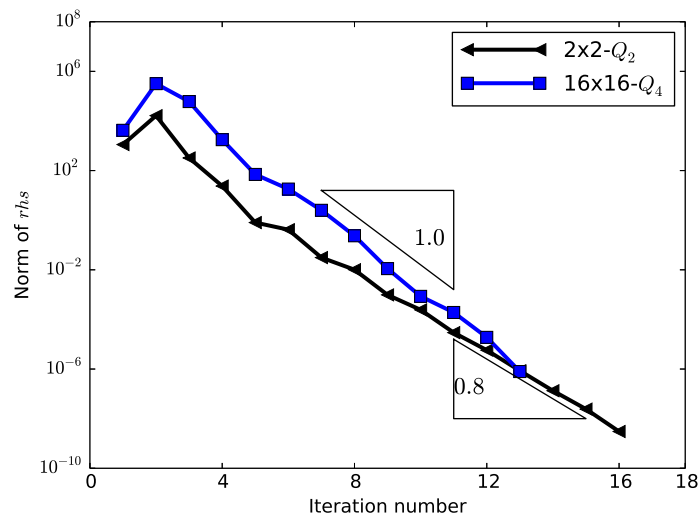


Figure 7.12: Cook's membrane with compressible Neo-Hookean material: convergence of Gauss-Newton iterations for two different discretisations with LSFEM-CC.

7.2.5 Cook's membrane with nearly incompressible Neo-Hookean material

The geometry, loading and boundary conditions of the problem are same as those used in the example for small strain formulation. Neo-Hookean hyperelastic material model discussed in Section 6.3.5 is considered for the analysis. The load is assumed to be a "dead load" as in the previous example and the response parameter, again, is the vertical displacement of the top right corner. Results are presented in Figure 7.13, in terms of response parameter against the number of elements per side; displacement value obtained with a very fine mesh is used as the reference value as the analytical solution is not available; and the converge pattern of results is exactly similar to that observed in small strain example. Contour plots of hydrostatic pressure and von Mises stress are shown in Figure 7.14, for Q_3 NURBS for mesh-5.

Convergence of Gauss-Newton iterations is rather poor in this example. Such a behaviour is expected due to the fact that the contribution made by the Hessian matrix is significant because of the nonlinearities involved and number of terms present. Use of Gauss-Newton procedure helps to circumvent the need to calculate the complicated terms, though, at the expense of good convergence ratio.

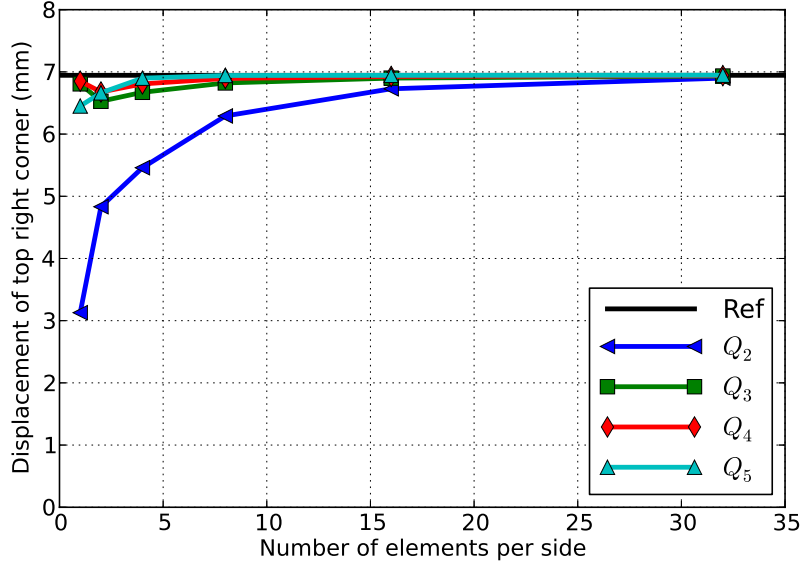


Figure 7.13: Cook's membrane with nearly incompressible Neo-Hookean material: vertical displacement of the top right corner against number of elements per side with different orders of NURBS.

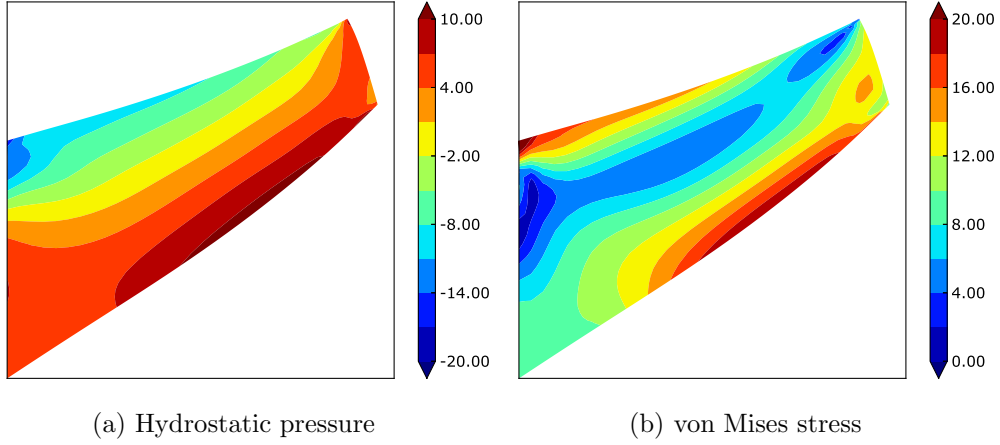


Figure 7.14: Cook's membrane with nearly incompressible Neo-Hookean material: contour plots of hydrostatic pressure and von Mises stress for mesh-5 with Q_3 NURBS.

7.3 Numerical Examples - Fluid Mechanics

7.3.1 Kovasznay flow

The performance of the current formulation for incompressible Navier-Stokes is studied by considering a two-dimensional stationary problem due to Kovasznay [49]. Even though this problem is relatively simple, it establishes confidence in the numerical method by allowing one to compute the error estimates which provide a meaningful measure of the approximation error — even for a nonlinear problem. The domain of the problem is $\Omega = [-0.5, 1.5] \times [-0.5, 1.5]$ and its analytical solution is given by,

$$u(x, y) = 1.0 - e^{\lambda x} \cos(2\pi y) \quad (7.1a)$$

$$v(x, y) = \frac{\lambda}{2\pi} e^{\lambda x} \sin(2\pi y) \quad (7.1b)$$

$$p(x, y) = p_0 - \frac{1}{2} e^{2\lambda x} \quad (7.1c)$$

where,

$$\lambda = \frac{Re}{2} - \sqrt{\frac{Re^2}{4} + 4\pi^2} \quad (7.2)$$

where, Re is the Reynolds number and p_0 is a reference pressure. A case with $Re = 40$ ($\rho = 1.0$ and $\mu = 0.025$) is considered to study the convergence of L_2 norm of components of velocity and pressure and H_1 norm of velocity, as the mesh is refined with both p -refinement and h -refinement. All the meshes considered in this problem are uniform — meaning equal knot spans — in both the directions. The exact solution, given by (7.1), is used to prescribe

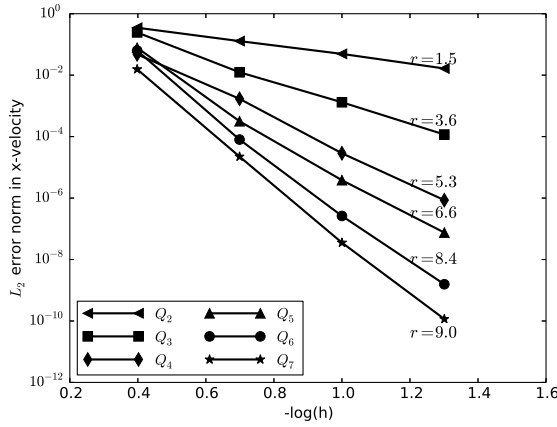
Dirichlet boundary conditions on Γ_D and a pressure value of zero is specified at the bottom-left corner.

Convergence plots are shown in Figure (7.15); the values of r indicated at every curve represents the convergence ratio corresponding to that particular degree of NURBS basis function. From approximation theory it is known that, for basis functions of degree a , the optimal convergence ratio of L_2 norm in velocity components must be $(a+1)$ and optimal convergence ratio of L_2 norm of pressure and H_1 norm of velocity must be a . It can be observed from the convergence plots that the convergence ratio for Q_2 and Q_3 NURBS is not optimal and it improves and reaches better than optimal value for higher degree NURBS. The reason for this sub-optimal convergence for Q_2 and Q_3 NURBS is that the proposed least-squares formulation is not norm-equivalent. However, this issue of non-norm-equivalence is alleviated by the use of higher order NURBS and leads to better than optimal convergence rates as shown with numerical results. Therefore, the proposed least-square formulations, with higher order NURBS as basis functions, yield optimal convergence rates as well as straightforward implementation. Table 7.2 presents the convergence of norm of the right hand side (*rhs*) of matrix system at each iteration of the Gauss-Newton procedure for different mesh densities with Q_4 NURBS. This clearly shows that convergence of the norm of *rhs* improves with the refinement and quadratic convergence of Newton-Raphson method can be recovered without the need to use full Newton-Raphson method. Contour plots of velocity components, pressure and streamlines for 20×20 mesh with Q_2 and Q_3 NURBS is shown in Figure (7.16). As shown, Q_2 NURBS give poor results, as the second derivatives do not get resolved properly with; Q_3 NURBS clearly improves the results; and contour plots obtained with other higher degree NURBS are indistinguishable from those obtained with Q_3 NURBS.

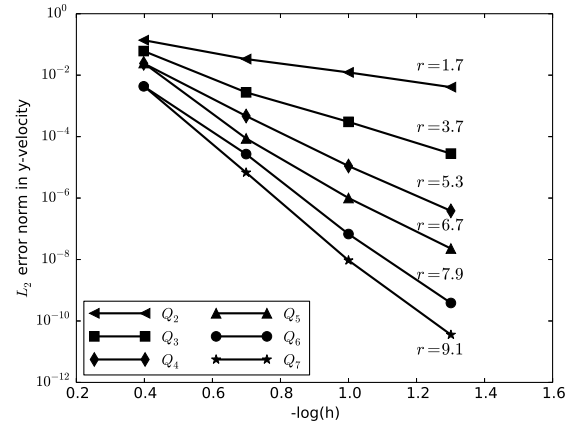
The most important observation to be made, at this point, is that there is absolutely no stabilisation technique used and still solutions obtained are free of spurious oscillations. This essential aspect, of the current formulation, that governing equations are not transformed into lower-order equations and no external stabilisation techniques are required to get accurate results makes the proposed formulation very efficient, robust and stable.

Iteration number	Norm of rhs		
	5×5 mesh	10×10 mesh	20×20 mesh
1	2.5010 E+00	2.1437 E+00	1.8358 E+00
2	7.3951 E+00	7.7189 E+00	7.8856 E+00
3	6.8924 E-01	1.1707 E+00	8.3107 E-01
4	2.3512 E-02	2.9692 E-02	2.0521 E-02
5	4.0363 E-04	1.4740 E-05	1.3929 E-05
6	4.0116 E-05	1.5498 E-08	3.7139 E-11
7	4.7320 E-06		
8	5.7093 E-07		
9	7.5774 E-08		

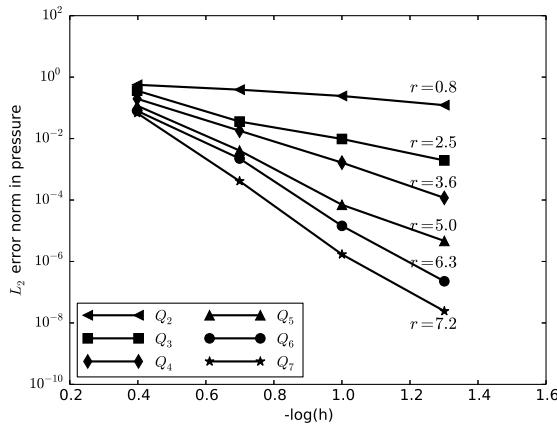
Table 7.2: Kovasznay flow: evolution of norm of rhs for the different meshes with Q_4 NURBS.



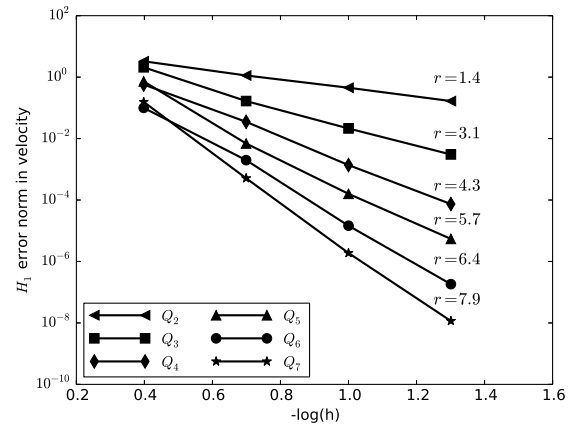
(a) L_2 norm of x-velocity



(b) L_2 norm of y-velocity

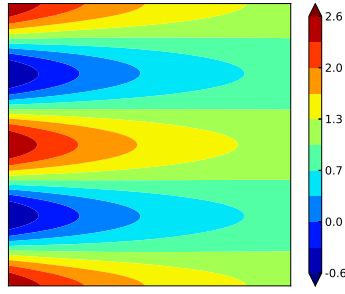


(c) L_2 norm of pressure

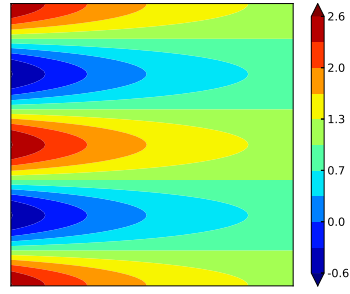


(d) H_1 norm of velocity

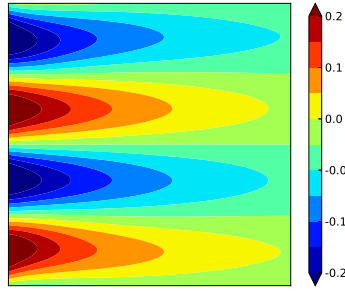
Figure 7.15: Kovasznay flow: error norms for $Re = 40$.



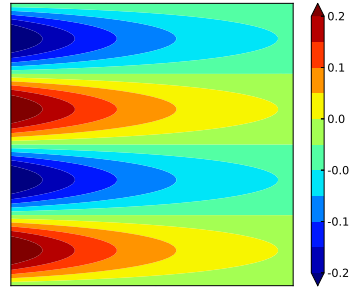
(a) X-velocity with Q_2 NURBS



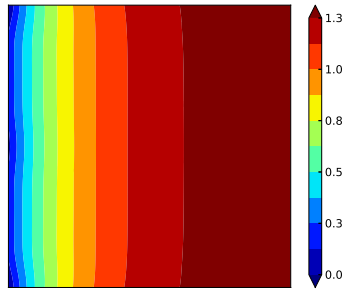
(b) X-velocity with Q_3 NURBS



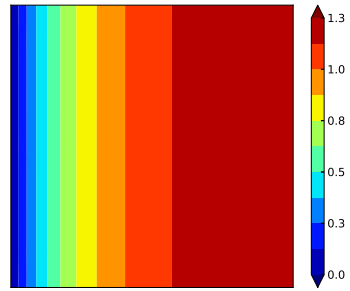
(c) Y-velocity with Q_2 NURBS



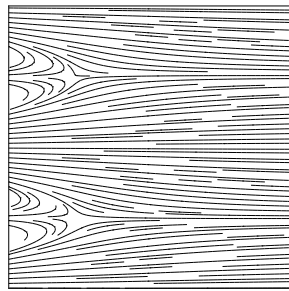
(d) Y-velocity with Q_3 NURBS



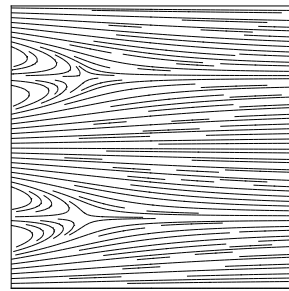
(e) Pressure with Q_2 NURBS



(f) Pressure with Q_3 NURBS



(g) Streamlines with Q_2 NURBS



(h) Streamlines with Q_3 NURBS

Figure 7.16: Kovasznay flow: Contour plots for 20×20 mesh with Q_2 and Q_3 NURBS.

7.3.2 Flow in lid driven cavity

This is a benchmark example considered to demonstrate the performance of numerical method applied to incompressible fluid flow. Geometry and boundary conditions of the problem are as shown in Figure (7.17a). Fluid velocity is zero on all the boundaries except at the lid where the velocity is equal to the velocity of the lid, which is taken as unity in this example. Horizontal velocity at the top corners is assumed to be equal to that of lid, making it a "leaking cavity". For this example a non-uniform mesh, as shown in Figure (7.17b), is considered as finer discretisation is needed at the corners in order to resolve vortices accurately. Different mesh densities are used to study the flow with different Reynold's numbers. Fluid density, ρ , is fixed as 1.0 and viscosity, μ , is adjusted based on the value of Reynold's number. Meshes with densities 20×20 , 40×40 and 150×150 are used for Reynold's number 100, 1000 and 10000, respectively. Each case is studied with NURBS basis functions of different orders and the velocity profiles are compared against the widely accepted values from Ghia *et al* [36], as shown in Figures (7.18) - (7.20). Results obtained using the current formulation agree well with the benchmark values; for $Re = 10000$ the solution failed to converge for Q_2 NURBS. For all the Reynold's numbers considered there is no difference in results with the NURBS spaces of different orders, except for Q_2 NURBS; because of the reason that Q_2 NURBS are not good enough to accurately resolve second derivatives. Contour plots of streamlines and pressure for different Reynold's numbers for Q_4 NURBS are presented in Figures (7.21) - (7.23).

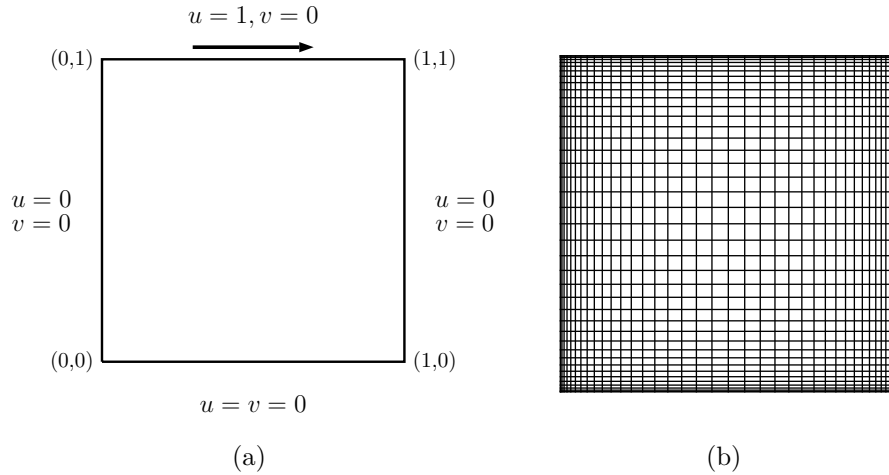
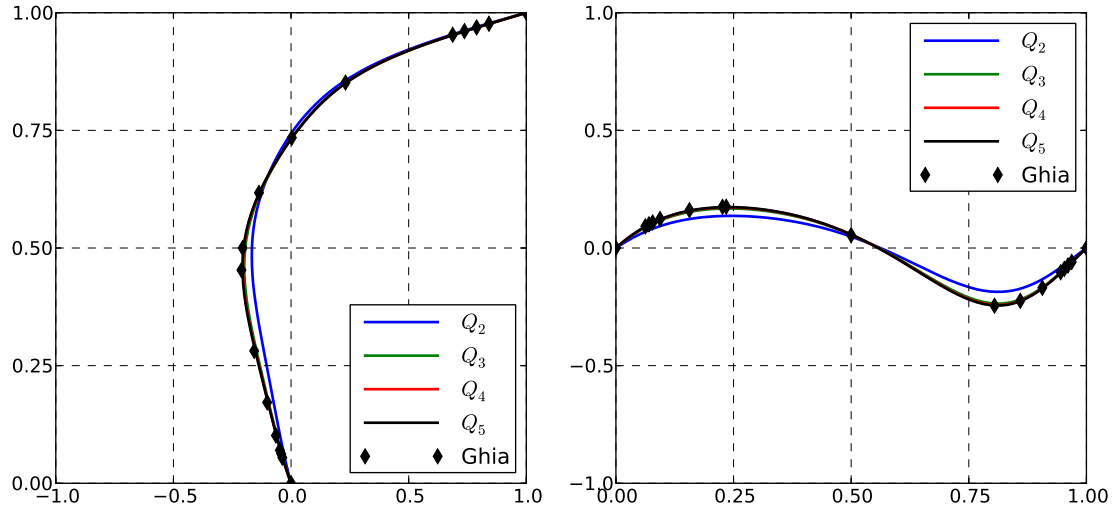
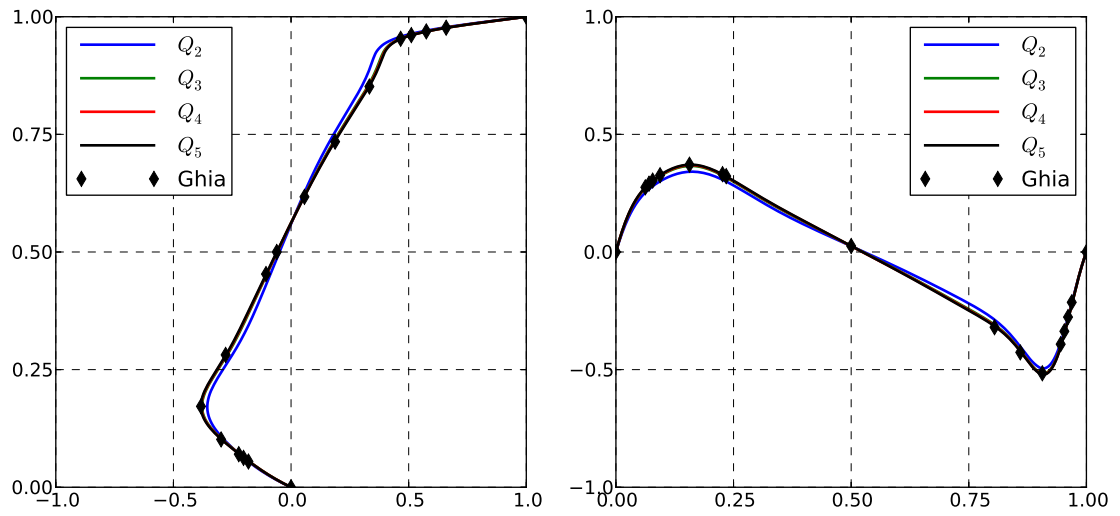


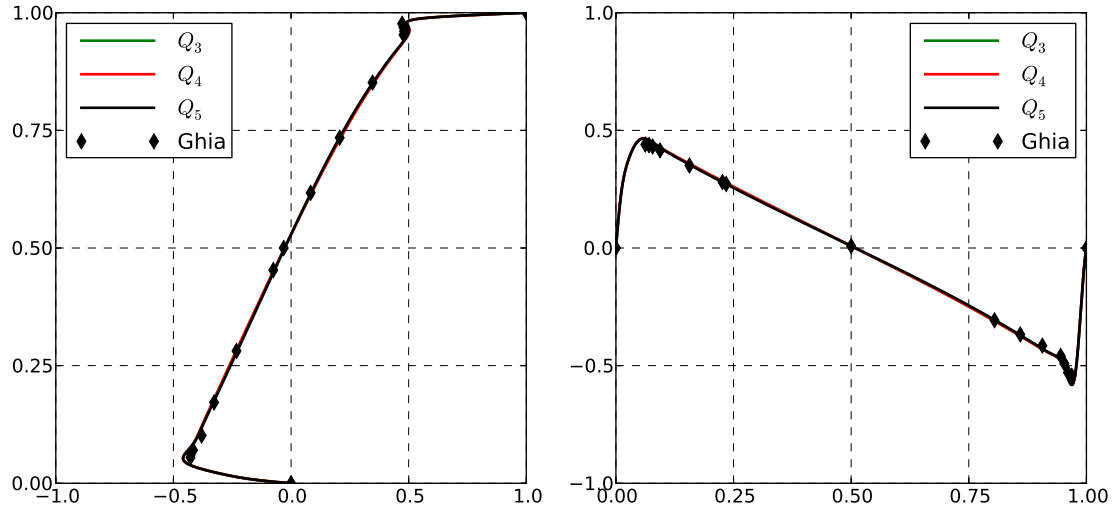
Figure 7.17: Lid driven cavity: a.) Geometry and boundary conditions and b.) A typical mesh used for the analysis.



(a) y -velocity profile along horizontal center line (b) x -velocity profile along vertical center line
Figure 7.18: Lid driven cavity: velocity profiles for 20×20 mesh with $Re = 100$.

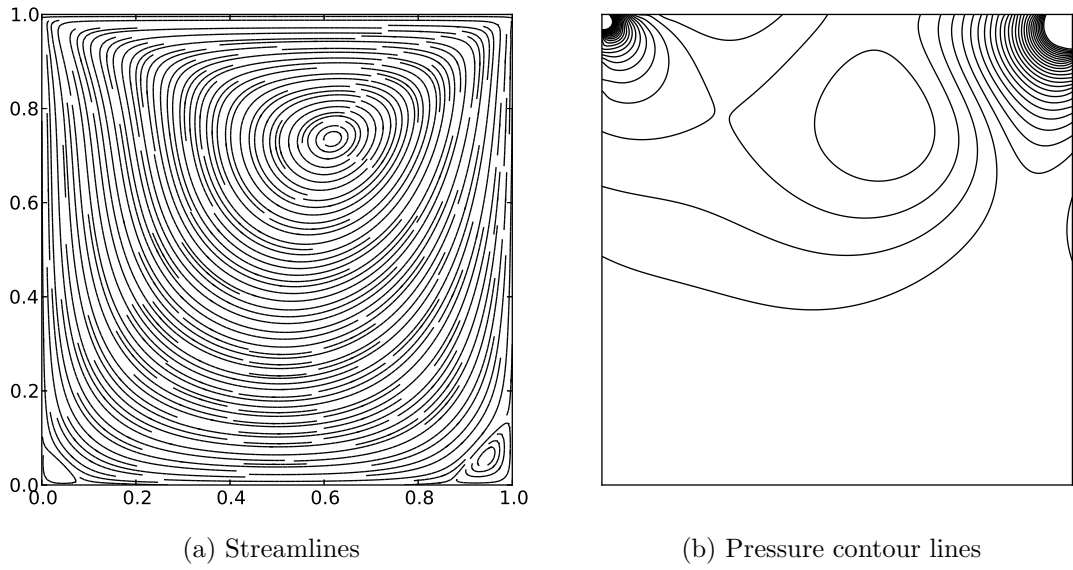


(a) y -velocity profile along horizontal center line (b) x -velocity profile along vertical center line
Figure 7.19: Lid driven cavity: velocity profiles for 40×40 mesh with $Re = 1000$.



(a) y -velocity profile along horizontal center line (b) x -velocity profile along vertical center line

Figure 7.20: Lid driven cavity: velocity profiles for 150×150 mesh with $Re = 10000$.



(a) Streamlines

(b) Pressure contour lines

Figure 7.21: Lid driven cavity: streamlines and pressure contour lines for 20×20 mesh with Q_4 NURBS for $Re = 100$.

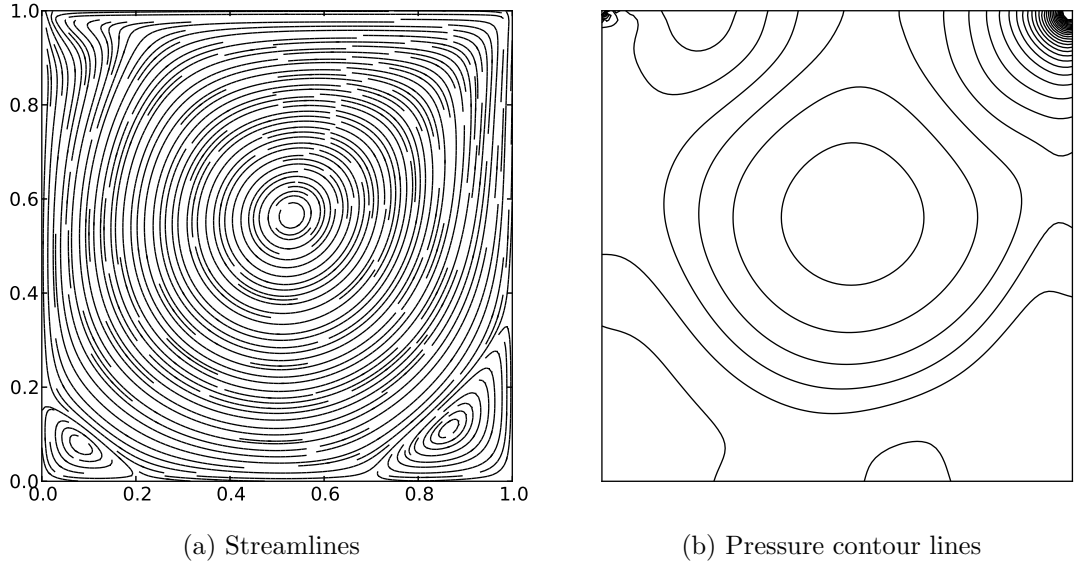


Figure 7.22: Lid driven cavity: streamlines and pressure contour lines for 40×40 mesh with Q_4 NURBS for $Re = 1000$.

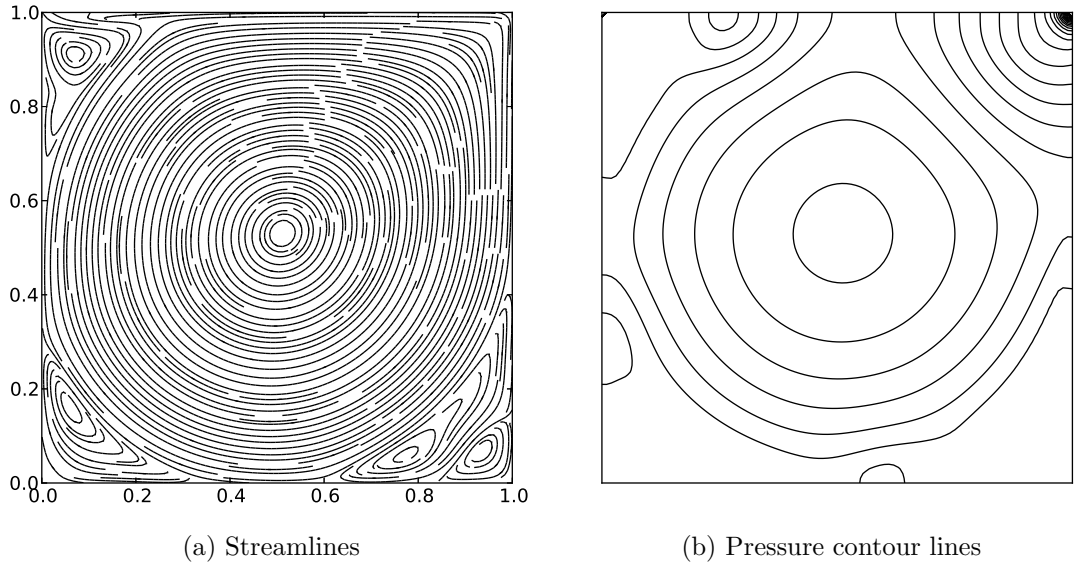


Figure 7.23: Lid driven cavity: streamlines and pressure contour lines for 150×150 mesh with Q_4 NURBS for $Re = 10000$.

Chapter 8

Conclusions

The aim of the thesis — the development of efficient, accurate and robust numerical techniques using NURBS based isogeometric analysis — has been achieved. Two-field and three-field mixed Galerkin formulations have been presented in order to deal with the problems of incompressibility in small and finite strains. Subsequently, straightforward least-squares based finite element formulations have been proposed to deal with the issues of incompressibility in small and finite strain elasticity and incompressible Navier-Stokes. The methods proposed are simple, robust and can be implemented straightforwardly. The performance of the proposed formulations is assessed using several benchmark examples from the literature and results obtained are shown to be well in agreement with the reference values.

8.1 Achievements and Conclusions

Mixed Galerkin formulations

Numerical results show that higher order NURBS with mixed formulations perform excellently even for coarse meshes; and with the presented numerical examples it has been demonstrated that 2-field mixed formulations — for both small and finite strains — are sufficient to deal with the problems of incompressibility posed by the material models (whose strain energy function can be represented as the sum of deviatoric and volumetric components) encountered in engineering simulations, without the need to implement 3-field formulation. Important observations and conclusions for mixed GFEMs:

- Pure displacement formulation with higher order NURBS gives converged results; however, it requires the load to be applied in small increments (or more number of load-steps). Also, the distribution of stresses is erratic.
- Mixed formulations require a much smaller number of load-steps to converge, though at the expense of increased DOF; but, the overall computational cost is less compared to pure displacement formulation. Moreover, the distribution of stresses is smooth.

- Mixed formulations are superior to $\bar{\mathbf{F}}$ formulation under severe mesh distortions. This is demonstrated with "Torsion of square prism" example, Section 5.2.6.
- The presented mixed formulations, in finite strains, also deals with shear locking — along with the intended motivation to resolve volumetric locking. This is demonstrated with "Bending of a thick cylindrical shell" example, Section 5.2.9.
- Same level of accuracy can be obtained using 2-field formulations – compared to 3-field formulations – for the material models considered in the present work.
- Huge savings in computational time can be obtained as the proposed 2-field formulations lead to fewer DOF compared to 3-field formulations.

Least-Square formulations

We have shown the advantages of using the Gauss-Newton procedure instead of the Newton-Raphson method as a solution scheme to solve nonlinear equations. Even though it lacked the efficiency in case of nonlinear elasticity, it is shown, however, that in case of Navier-Stokes near quadratic convergences of iterations can be obtained at a less computational effort compared to full Newton-Raphson's method. The poor convergence in case of nonlinear elasticity can be attributed to the fact the contribution made by the Hessian is more significant in this case than in Navier-Stokes. Least-square based formulations offer many computational advantages over traditional Galerkin formulations. Important observations and conclusions for LSFEMs are:

- LSFEMs combined with NURBS can be directly applied to any type of governing equations without the need to formulate the governing equations into lower-order system. Therefore, by using the current formulations, accurate results can be obtained at less DOF count; hence less computational effort as there are no auxiliary variables being introduced.
- LSFEMs always result in unconstrained minimisation problems which always result in symmetric positive definite matrix systems and are not subjected to stability issues, like LBB. Hence, equal order shape functions are used, which eased the effort of computer implementation compared to mixed GFEMs.
- LSFEMs based on higher order NURBS result in numerical schemes with optimal convergence rates even for non-norm-equivalence least-square formulations.
- No stabilisation techniques are required to get accurate results using LSFEMs for incompressible fluid flow which is demonstrated with the

benchmark examples: Kovasznay flow and flow in lid-driven cavity. This is one of the essential features of LSFEMs which makes them very robust and possibly more suitable for large scale computations than GFEMs.

Publications

Results of this research work have been submitted to prestigious international journals and was also presented in international conferences.

8.2 Scope for future research work

Mixed Galerkin formulations

Even though the mixed formulations improved the accuracy of the results and reduced the computational cost, NURBS still lack local refinement capabilities — which lead to DOF which are not necessary for the purpose of the analysis but still need to be carried along. Thus, it is necessary to develop local refinement schemes which result in smaller number of DOF. The extension of the mixed formulations to the following local refinement schemes should be investigated: T-Splines [32, 77, 76]; Hierarchical B-Splines [73, 74, 90]; and PHT-Splines [63].

Least-square finite element formulations

It is suggested that LSFEMs combined with NURBS based IGA have huge potential for further research because of their advantages and practicality. The following future research topics are suggested:

- 1.) Use of local refinement schemes with the proposed LSFEMs, thereby making IGA as a versatile numerical method in computational mechanics.
- 2.) Developing stress-displacement based LSFEMs, using NURBS, for the solutions of BVPs in solid mechanics.
- 3.) Developing LSFEMs, using NURBS, by transforming the governing system of equations to lower-order equations (by introducing auxiliary variables).
- 3.) Extending the proposed formulation to solve BVPs in other fields of science and engineering — either by using straightforward least-square formulations or formulations based on reduced lower-order equations.
- 4.) Another important area of future research work with huge potential that we can foresee is *immersed boundary methods* with LSFEMs based on B-Splines and hierarchical B-Splines as the background cartesian mesh.

Appendix A

Newton-Raphson method

Newton-Raphson method is the most widely used numerical iterative scheme to solve a nonlinear system of equations. Consider a system of nonlinear equations given as

$$\Psi(\mathbf{x}) = \mathbf{0} \quad (\text{A.1})$$

In this iterative method, given a solution estimate \mathbf{x}_k at iteration k , a new solution $\mathbf{x}_{k+1} = \mathbf{x}_k + d\mathbf{x}$ is obtained by taking a linearised approximation of equation (A.1) given as,

$$\Psi(\mathbf{x}_{k+1}) = \Psi(\mathbf{x}_k) + \nabla_{\mathbf{x}} \Psi(\mathbf{x}_k)[d\mathbf{x}_k] \quad (\text{A.2})$$

where, $\nabla_{\mathbf{x}} \Psi(\mathbf{x}_k)[d\mathbf{x}_k]$ is the directional derivative of $\Psi(\mathbf{x})$, at \mathbf{x}_k , in the direction of $[d\mathbf{x}_k]$, which can be represented as,

$$\nabla_{\mathbf{x}} \Psi(\mathbf{x}_k)[d\mathbf{x}_k] = \mathbf{K} d\mathbf{x}_k \quad (\text{A.3})$$

where, \mathbf{K} , called as *tangent matrix*, is,

$$K_{ij}(\mathbf{x}_k) = \left. \frac{\partial \Psi_i}{\partial x_j} \right|_{\mathbf{x}_k} \quad (\text{A.4})$$

Combining equations (A.2) and (A.4) a Newton-Raphson iteration can be summarised as,

$$\mathbf{K}(\mathbf{x}_k) d\mathbf{x} = -\Psi(\mathbf{x}_k) \quad (\text{A.5})$$

$$\mathbf{x}_{k+1} = \mathbf{x}_k + d\mathbf{x}$$

The iteration process continues until a certain convergence criteria is satisfied. In general, the L_2 norm of residue $\Psi(\mathbf{x}_k)$ is compared against a tolerance value, say ϵ , specified by the user. So, the iteration process continues until,

$$\|\Psi(\mathbf{x}_k)\| \leq \epsilon \quad (\text{A.6})$$

In the finite element methods the function Ψ is usually is a set of equilibrium equations given as the sum of internal forces, \mathbf{R} , and external forces, \mathbf{F} , as,

$$\Psi = \mathbf{R} - \mathbf{F} \quad (\text{A.7})$$

In general the external load is applied in several steps in order to enhance the convergence. The pseudo code for the Newton-Raphson method is given in Box A.1.

- 1.) Input initial geometry, \mathbf{X} , and tolerance, ϵ .
- 2.) Initialise: $\mathbf{x} = \mathbf{X}$, $\mathbf{F} = \mathbf{0}$
- 3.) For each load step
 - a.) Compute $\Delta \mathbf{F}$
 - b.) Set $\mathbf{F} = \mathbf{F} + \Delta \mathbf{F}$
 - c.) **repeat**
 - * Compute \mathbf{K} and \mathbf{R} at \mathbf{x}
 - * Set $\Psi = \mathbf{R} - \mathbf{F}$
 - * if $\|\Psi\| \leq \epsilon$, **return**
 - * Solve: $\mathbf{K} d\mathbf{x} = -\Psi$
 - * Update: $\mathbf{x} = \mathbf{x} + d\mathbf{x}$

Box A.1: Pseudo-code for Newton-Raphson method to solve nonlinear equations.

Appendix B

Computing second derivatives

Equation (2.33) can also be written as,

$$\nabla_{\xi} N = \mathbf{B} \nabla_{\mathbf{x}} N \quad (\text{B.1})$$

where,

$$\mathbf{B} = (\nabla_{\xi} \mathbf{x})^T \quad (\text{B.2})$$

Gradient of (B.1) with respect to parametric coordinates $\xi = (\xi, \eta, \zeta)$ gives,

$$\begin{aligned} \nabla_{\xi} \nabla_{\xi} N &= \nabla_{\xi} (\mathbf{B} \nabla_{\mathbf{x}} N) \\ &= \mathbf{B} (\nabla_{\xi} \nabla_{\mathbf{x}} N) + (\nabla_{\xi} \mathbf{B}) (\nabla_{\mathbf{x}} N) \\ &= \mathbf{B} (\nabla_{\mathbf{x}} \nabla_{\mathbf{x}} N) (\nabla_{\mathbf{x}} \mathbf{x}) + (\nabla_{\xi} \mathbf{B}) (\nabla_{\mathbf{x}} N) \\ &= \mathbf{B} (\nabla_{\mathbf{x}} \nabla_{\mathbf{x}} N) \mathbf{B}^T + (\nabla_{\xi} \mathbf{B}) (\nabla_{\mathbf{x}} N) \\ &= \mathbf{B} (\mathbf{H}_{\mathbf{x}} N) \mathbf{B}^T + (\mathbf{H}_{\xi x}) \frac{\partial N}{\partial x} + (\mathbf{H}_{\xi y}) \frac{\partial N}{\partial y} + (\mathbf{H}_{\xi z}) \frac{\partial N}{\partial z} \end{aligned} \quad (\text{B.3})$$

where, $\mathbf{H}_{\mathbf{x}} N$ is the Hessian of N with respect to coordinates $\mathbf{x} = (x, y, z)$ and $\mathbf{H}_{\xi x}$, $\mathbf{H}_{\xi y}$ and $\mathbf{H}_{\xi z}$ are Hessians of x , y and z respectively with respect to parametric coordinates $\xi = (\xi, \eta, \zeta)$. So,

$$\mathbf{H}_{\mathbf{x}} N = \mathbf{B}^{-1} \left(\mathbf{H}_{\xi} N - (\mathbf{H}_{\xi x}) \frac{\partial N}{\partial x} - (\mathbf{H}_{\xi y}) \frac{\partial N}{\partial y} - (\mathbf{H}_{\xi z}) \frac{\partial N}{\partial z} \right) \mathbf{B}^{-T} \quad (\text{B.4})$$

In three dimensions,

$$\nabla_{\boldsymbol{\xi}} \mathbf{x} = \begin{bmatrix} \frac{\partial x}{\partial \xi} & \frac{\partial x}{\partial \eta} & \frac{\partial x}{\partial \zeta} \\ \frac{\partial y}{\partial \xi} & \frac{\partial y}{\partial \eta} & \frac{\partial y}{\partial \zeta} \\ \frac{\partial z}{\partial \xi} & \frac{\partial z}{\partial \eta} & \frac{\partial z}{\partial \zeta} \end{bmatrix} \quad (\text{B.5})$$

$$\mathbf{H}_{\boldsymbol{\xi}} N = \nabla_{\boldsymbol{\xi}} \nabla_{\boldsymbol{\xi}} N = \begin{bmatrix} \frac{\partial^2 N}{\partial \xi^2} & \frac{\partial^2 N}{\partial \xi \partial \eta} & \frac{\partial^2 N}{\partial \xi \partial \zeta} \\ \frac{\partial^2 N}{\partial \eta \partial \xi} & \frac{\partial^2 N}{\partial \eta^2} & \frac{\partial^2 N}{\partial \eta \partial \zeta} \\ \frac{\partial^2 N}{\partial \zeta \partial \xi} & \frac{\partial^2 N}{\partial \zeta \partial \eta} & \frac{\partial^2 N}{\partial \zeta^2} \end{bmatrix} \quad (\text{B.6})$$

$$\mathbf{H}_{\mathbf{x}} N = \nabla_{\mathbf{x}} \nabla_{\mathbf{x}} N = \begin{bmatrix} \frac{\partial^2 N}{\partial x^2} & \frac{\partial^2 N}{\partial x \partial y} & \frac{\partial^2 N}{\partial x \partial z} \\ \frac{\partial^2 N}{\partial y \partial x} & \frac{\partial^2 N}{\partial y^2} & \frac{\partial^2 N}{\partial y \partial z} \\ \frac{\partial^2 N}{\partial z \partial x} & \frac{\partial^2 N}{\partial z \partial y} & \frac{\partial^2 N}{\partial z^2} \end{bmatrix} \quad (\text{B.7})$$

$$\mathbf{H}_{\boldsymbol{\xi}} x = \nabla_{\boldsymbol{\xi}} \nabla_{\boldsymbol{\xi}} x = \begin{bmatrix} \frac{\partial^2 x}{\partial \xi^2} & \frac{\partial^2 x}{\partial \xi \partial \eta} & \frac{\partial^2 x}{\partial \xi \partial \zeta} \\ \frac{\partial^2 x}{\partial \eta \partial \xi} & \frac{\partial^2 x}{\partial \eta^2} & \frac{\partial^2 x}{\partial \eta \partial \zeta} \\ \frac{\partial^2 x}{\partial \zeta \partial \xi} & \frac{\partial^2 x}{\partial \zeta \partial \eta} & \frac{\partial^2 x}{\partial \zeta^2} \end{bmatrix} \quad (\text{B.8})$$

$\mathbf{H}_{\boldsymbol{\xi}} y$ and $\mathbf{H}_{\boldsymbol{\xi}} z$ are similar to $\mathbf{H}_{\boldsymbol{\xi}} x$. And their entries are evaluated from equation 2.23 as,

$$\begin{aligned} \frac{\partial^2 x}{\partial \xi^2} &= \sum_{i=0}^n \frac{\partial^2 N}{\partial \xi^2} x_i & \frac{\partial^2 x}{\partial \eta \partial \xi} &= \sum_{i=0}^n \frac{\partial^2 N}{\partial \eta \partial \xi} x_i & \frac{\partial^2 x}{\partial \eta^2} &= \sum_{i=0}^n \frac{\partial N}{\partial \eta^2} x_i \\ \frac{\partial^2 y}{\partial \xi^2} &= \sum_{i=0}^n \frac{\partial^2 N}{\partial \xi^2} y_i & \frac{\partial^2 y}{\partial \eta \partial \xi} &= \sum_{i=0}^n \frac{\partial^2 N}{\partial \eta \partial \xi} y_i & \frac{\partial^2 y}{\partial \eta^2} &= \sum_{i=0}^n \frac{\partial N}{\partial \eta^2} y_i \\ \frac{\partial^2 z}{\partial \xi^2} &= \sum_{i=0}^n \frac{\partial^2 N}{\partial \xi^2} y_i & \frac{\partial^2 z}{\partial \eta \partial \xi} &= \sum_{i=0}^n \frac{\partial^2 N}{\partial \eta \partial \xi} y_i & \frac{\partial^2 z}{\partial \eta^2} &= \sum_{i=0}^n \frac{\partial N}{\partial \eta^2} y_i \end{aligned} \quad (\text{B.9})$$

B.1 For an uniform cartesian grid

In the case of an uniform cartesian grid,

$$x = x(\xi), y = y(\eta), z = z(\zeta) \quad (\text{B.10})$$

So,

$$\frac{\partial x}{\partial \eta} = \frac{\partial x}{\partial \zeta} = 0 \quad (\text{B.11})$$

$$\frac{\partial y}{\partial \xi} = \frac{\partial y}{\partial \zeta} = 0 \quad (\text{B.12})$$

$$\frac{\partial z}{\partial \xi} = \frac{\partial z}{\partial \eta} = 0 \quad (\text{B.13})$$

and all the second derivatives of x , y and z with respect to parametric coordinates $\boldsymbol{\xi} = (\xi, \eta, \zeta)$ vanish. Hence,

$$\mathbf{H}_{\boldsymbol{\xi}}x = \mathbf{H}_{\boldsymbol{\xi}}y = \mathbf{H}_{\boldsymbol{\xi}}z = \mathbf{0} \quad (\text{B.14})$$

Assuming that

$$J_x = \frac{\partial x}{\partial \xi}, \quad J_y = \frac{\partial y}{\partial \eta}, \quad J_z = \frac{\partial z}{\partial \zeta}, \quad (\text{B.15})$$

the matrix \mathbf{B} becomes,

$$\mathbf{B} = \begin{bmatrix} J_x & 0 & 0 \\ 0 & J_y & 0 \\ 0 & 0 & J_z \end{bmatrix} \quad (\text{B.16})$$

So, the second derivatives of shape function N with respect to coordinate axes (x, y, z) are given by,

$$\begin{bmatrix} \frac{\partial^2 N}{\partial x^2} & \frac{\partial^2 N}{\partial x \partial y} & \frac{\partial^2 N}{\partial x \partial z} \\ \frac{\partial^2 N}{\partial y \partial x} & \frac{\partial^2 N}{\partial y^2} & \frac{\partial^2 N}{\partial y \partial z} \\ \frac{\partial^2 N}{\partial z \partial x} & \frac{\partial^2 N}{\partial z \partial y} & \frac{\partial^2 N}{\partial z^2} \end{bmatrix} = \begin{bmatrix} \frac{1}{J_x^2} \frac{\partial^2 N}{\partial \xi^2} & \frac{1}{J_x J_y} \frac{\partial^2 N}{\partial \xi \partial \eta} & \frac{1}{J_x J_z} \frac{\partial^2 N}{\partial \xi \partial \zeta} \\ \frac{1}{J_x J_y} \frac{\partial^2 N}{\partial \eta \partial \xi} & \frac{1}{J_y^2} \frac{\partial^2 N}{\partial \eta^2} & \frac{1}{J_y J_z} \frac{\partial^2 N}{\partial \eta \partial \zeta} \\ \frac{1}{J_x J_z} \frac{\partial^2 N}{\partial \zeta \partial \xi} & \frac{1}{J_y J_z} \frac{\partial^2 N}{\partial \zeta \partial \eta} & \frac{1}{J_z^2} \frac{\partial^2 N}{\partial \zeta^2} \end{bmatrix} \quad (\text{B.17})$$

Bibliography

- [1] HSL. A collection of Fortran codes for large-scale scientific computation. <http://www.hsl.rl.ac.uk/>.
- [2] PARDISO Solver Project. <http://www.pardiso-project.org/>.
- [3] W.T. Ang. *A Beginner's Course in Boundary Element Methods*. Universal Publishers, Florida, 2007.
- [4] F. Armero and S. Glaser. On the formulation of enhanced strain finite elements in finite deformations. *Engineering. Computations*, 14:759–791, 1997.
- [5] Refaat El Attar. *Special functions and orthogonal polynomials*. Lulu press, 2006.
- [6] I. Babuška. The finite element method with Lagrangian multipliers. *Numerische Mathematik*, 20:179–192, 1973.
- [7] K.J. Bathe. *Finite Element Procedures*. Prentice Hall Inc., New Jersey, 1996.
- [8] Y. Bazilevs, V.M. Calo, T.J.R. Hughes, and Y. Zhang. Isogeometric fluid-structure interaction: theory, algorithms, and computations. *Computational Mechanics*, 43:3–37, 2008.
- [9] N. Büchter, E. Ramm, and D. Roehl. Three-dimensional extension of non-linear shell formulation based on the enhanced assumed strain concept. *In*, 37:25512568, 1994.
- [10] G. Beer, I. Smith, and C. Deunser. *The Boundary Element Method with Programming For Engineers and Scientists*. Springer, Germany, 2008.
- [11] T. Belytschko, W.K. Liu, and B. Moran. *Nonlinear Finite Elements for Continua and Structures*. John Wiley and Sons, 1st edition, 2000.
- [12] A. Björck. *Numerical methods for least-squares problems*. SIAM, 1996.
- [13] P. Bochev. *Least-squares finite element methods for the Stokes and Navier-Stokes equations*. PhD thesis, 1994.

- [14] P. Bochev. Analysis of least-squares finite element methods for the Navier-Stokes equations. *SIAM Journal on Numerical Analysis*, 34:1817–1844, 1997.
- [15] P. Bochev and M. Gunzburger. A least-squares Finite element method for the Navier-Stokes equations. *Applied Mathematics Letters*, 6:27–30, 1993.
- [16] P. Bochev and M. Gunzburger. Accuracy of least-squares methods for the Navier-Stokes equations. *Computers & Fluids*, 22:549–563, 1993.
- [17] P. Bochev and M. Gunzburger. Analysis of least-squares Finite element methods for the Stokes equations. *Mathematics of Computation*, 63:479–506, 1994.
- [18] P. Bochev and M. Gunzburger. Analysis of weighted least-squares Finite element method for the Navier-Stokes equations. *Proc. 14th IMACS World Congress*, pages 584–587, 1994.
- [19] P. Bochev and M. Gunzburger. *Least-Squares Finite Element Methods*. Springer, New York, USA, 2009.
- [20] J. Bonet and R.D. Wood. *Nonlinear continuum mechanics for finite element analysis*. Cambridge University Press, 1997.
- [21] J. H. Bramble and J. Pasciak. Least-squares method for Stokes equations based on a discrete minus one inner product. *Journal of Computational and Applied Mathematics*, 74:155–173, 1996.
- [22] C. A. Brebbia and J. Dominguez. *Boundary Elements, An Introductory Course*. WIT Press, United Kingdom, 1992.
- [23] F. Brezzi. On the existence, uniqueness and approximation of saddle-point problems arising from Lagrange multipliers. *RFAIRO*, 8:129–151, 1974.
- [24] Z. Cai, J. Korsawe, and G. Starke. An Adaptive Least Squares Mixed Finite Element Method for the Stress-Displacement Formulation of Linear Elasticity. *Numerical Methods for Partial Differential Equations*, 21:132–148, 2005.
- [25] Z. Cai and G. Starke. First-Order System Least Squares for the Stress-Displacement Formulation: Linear Elasticity. *SIAM Journal on Numerical Analysis*, 41:715–730, 2003.
- [26] Z. Cai and G. Starke. Least-Squares Methods for Linear Elasticity. *SIAM Journal on Numerical Analysis*, 42:826–842, 2004.
- [27] K. S. Chavan, B. P. Lamichhane, and B. I. Wohlmuth. Locking-free finite element methods for linear and nonlinear elasticity in 2D and 3D. *Computer Methods in Applied Mechanics and Engineering*, 196:4075–4086, 2007.

- [28] Y. Chen, J. Lee, and A. Eskandarian. *Meshless Methods in Solid Mechanics*. Springer, United States of America, 2006.
- [29] J. A. Cottrell, Y. Bazilevs, and T. J. R. Hughes. *Isogeometric Analysis: Toward Integration of CAD and FEA*. John Wiley & Sons, Chichester, England, 2009.
- [30] J. A. Cottrell, A. Reali, Y. Bazilevs, and T. J. R. Hughes. Isogeometric analysis of structural vibrations. *Computer Methods in Applied Mechanics and Engineering*, 195:5257–5296, 2006.
- [31] G. Danisch and G. Starke. First-Order System Least-Squares for Darcy-Stokes Flow. *SIAM Journal on Numerical Analysis*, 45:731–745, 2007.
- [32] M. R. Dörfel, B. Jüttler, and B. Simeon. Adaptive isogeometric analysis by local h-refinement with T-splines. *Computer Methods in Applied Mechanics and Engineering*, 199:264–275, 2010.
- [33] T. Elguedj, Y. Bazilevs, V.M. Calo, and T.J.R. Hughes. \bar{B} and \bar{F} Projection Methods for Nearly Incompressible Linear and Non-linear Elasticity and Plasticity using Higher-order NURBS Elements. *Computer Methods in Applied Mechanics and Engineering*, 197:2732–2762, 2008.
- [34] G. Farin. *Curves and Surfaces for CAGD, A practical guide*. Academic Press, San Diego, CA, first edition, 2002.
- [35] L. Gaul, M. Kógl, and M. Wagner. *Boundary Element Methods for Engineers and Scientists*. Springer, Berlin, 2003.
- [36] U. Ghia, K.N. Ghia, and C.T. Shin. High-resolution for incompressible flow using the Navier–Stokes equations and the multigrid method. *Journal of Computational Physics*, 48:387–411, 1982.
- [37] H. Gomez, T.J.R. Hughes, X. Nogueira, and V.M. Calo. Isogeometric analysis of the isothermal Navier–Stokes–Korteweg equations. *Computer Methods in Applied Mechanics and Engineering*, 199:1828–1840, 2010.
- [38] R. Hill. *The Mathematical Theory of Plasticity*. Oxford University Press, London, 1950.
- [39] G.A. Holzapfel. *Nonlinear Continuum Mechanics - A Continuum Approach for Engineering*. John Wiley and Sons, 2000.
- [40] T. J. R. Hughes. *The Finite Element Method: Linear Static and Dynamic Finite Element Analysis*. Dover Publications, Mineola, NewYork, 2000.
- [41] T. J. R. Hughes, Y. Bazilevs, and J. A. Cottrell. Isogeometric Analysis: CAD, Finite Elements, NURBS, Exact Geometry and Mesh Refinement. *Computer Methods in Applied Mechanics and Engineering*, 194:4135–4195, 2005.

- [42] Bo-Nan Jiang. A least-squares finite element method for incompressible Navier-Stokes problems. *International Journal for Numerical Methods in Fluids*, 14:843–859, 1992.
- [43] Bo-Nan Jiang. *The Least-Squares Finite Element Method: Theory and Applications in Computational Fluid Dynamics and Electromagnetics*. Springer-Verlag, Germany, 1998.
- [44] Bo-Nan Jiang. The least-squares finite element method in elasticity. Part II: Bending of thin plates. *International Journal for Numerical Methods in Engineering*, 54:1459–1475, 2002.
- [45] Bo-Nan Jiang and G. F. Carey. A stable least-squares finite element method for non-linear hyperbolic problems. *International Journal for Numerical Methods in Fluids*, 8:933–942, 1988.
- [46] Bo-Nan Jiang and G. F. Carey. Least-squares finite element methods for compressible Euler equations. *International Journal for Numerical Methods in Fluids*, 10:557–568, 1990.
- [47] Bo-Nan Jiang and Jie Wu. The least-squares finite element method in elasticity—Part I: Plane stress or strain with drilling degrees of freedom. *International Journal for Numerical Methods in Engineering*, 53:621–636, 2002.
- [48] D. Kalyanmoy. *Optimization for Engineering Design - Algorithms and Examples*. Prentice-Hall of India Pvt Ltd, New Delhi, 2005.
- [49] L. I. G. Kovasznay. Laminar flow behind a two-dimensional grid. *Mathematical Proceedings of the Cambridge Philosophical Society*, 44(1):58–62, 1948.
- [50] R. J. Leveque. *Finite Volume Methods for Hyperbolic Problems*. Cambridge University Press, United Kingdom, 2002.
- [51] H Li and S. S. Mulay. *Meshless Methods and their Numerical Properties*. CRC Press, Taylor & Francis Group, 2013.
- [52] S. Lipton, J.A. Evans, Y. Bazilevs, T. Elguedj, and T.J.R. Hughes. Robustness of isogeometric structural discretizations under severe mesh distortion. *Computer Methods in Applied Mechanics and Engineering*, 199:357–373, 2010.
- [53] G. R. Liu. *Meshfree methods: Moving beyond the Finite Element Method*. CRC Press, United States of America, 2000.
- [54] G. R. Liu and Y. T. Gu. *An introduction to meshfree methods and their programming*. Springer, New York, 2005.

- [55] J. Lubliner. *Plasticity Theory*. Macmillan, 1990.
- [56] T. A. Manteuffel, S. F. McCormick, J.G. Schmidt, and C.R. Westphal. First-Order System Least Squares for Geometrically Nonlinear Elasticity. *SIAM Journal on Numerical Analysis*, 44:2057–2081, 2006.
- [57] K. M. Mathisen, K. M. Okstad, T. Kvamsdal, and S. B. Raknes. Isogeometric analysis of finite deformation nearly incompressible solids. *Journal of Structural Mechanics*, 44(3):260–278, 2011.
- [58] S. Müntenmaier and G. Starke. First-Order System Least Squares for Coupled Stokes-Darcy Flow. *SIAM Journal on Numerical Analysis*, 49:387–404, 2011.
- [59] I.C. Nagtegaal, D.M. Parks, and J.R. Rice. On numerically accurate finite element solutions in the plastic range. *Computer Methods in Applied Mechanics and Engineering*, 4:153–177, 1974.
- [60] E. A. de Souza Neto, D. Perić, M. Dutko, and D. R. J. Owen. Design of simple low order finite elements for large strain analysis of nearly incompressible solids. *International Journal of Solids Structures*, 33:3277–3296, 1996.
- [61] E. A. de Souza Neto, D. Perić, and D. R. J. Owen. *Computational Methods for Plasticity, Theory and Applications*. John Wiley and Sons, United Kingdom, 2008.
- [62] E. A. de Souza Neto, F. M. A. Pires, and D. R. J. Owen. F-bar-based linear triangles and tetrahedra for finite strain analysis of nearly incompressible solids. Part I: formulation and benchmarking. *International Journal for Numerical Methods in Engineering*, 62:353–383, 2005.
- [63] N. Nguyen-Thanh, H. Nguyen-Xuan, S.P.A. Bordas, and T. Rabczuk. Iso-geometric analysis using polynomial splines over hierarchical T-meshes for two-dimensional elastic solids. *Computer Methods in Applied Mechanics and Engineering*, 200:1892–1908, 2010.
- [64] T. H. H. Pian and C. C. Wu. *Hybrid and Incompatible Finite Element Methods*. Chapman and Hall/CRC, 2006.
- [65] L. Piegl and W. Tiller. *The NURBS Book (Monographs in Visual Communication)*. Springer-Verlag, New York, 1997.
- [66] J. P. Pontaza and J. N. Reddy. Least-squares finite element formulations for viscous incompressible and compressible fluid flows. *Computer Methods in Applied Mechanics and Engineering*, 195:2454–2494, 2006.
- [67] J.P. Pontaza and J.N. Reddy. Space-time coupled spectral/*hp* least-squares finite element formulation for the incompressible Navier–Stokes equations. *Journal of Computational Physics*, 197:418–459, 2004.

- [68] J. N. Reddy. *An Introduction to the Finite Element Method*. Tata McGraw Hill, New York, third edition, 2006.
- [69] S. Reese, M. Kussner, and B. D. Reddy. A new stabilization technique for finite elements in non-linear elasticity. *International Journal for Numerical Methods in Engineering*, 44:1617–1652, 1999.
- [70] S. Reese, P. Wriggers, and B. D. Reddy. A new locking-free brick element technique for large deformation problems in elasticity. *Computers and Structures*, 75:291–304, 2000.
- [71] D. F. Rogers. *An Introduction to NURBS With Historical Perspective*. Academic Press, San Diego, CA, 2001.
- [72] S.A. Sauter and C. Schwab. *Boundary Element Methods*. Springer, Berlin, 2011.
- [73] D. Schillinger, L. Dedè, M. A. Scott, J. A. Evans, M. J. Borden, E. Rank, and T. J. R. Hughes. An isogeometric design-through-analysis methodology based on adaptive hierarchical refinement of NURBS, immersed boundary methods, and T-spline CAD surfaces. *Computer Methods in Applied Mechanics and Engineering*, page In press, 2012.
- [74] D. Schillinger and E. Rank. An unfitted hp-adaptive finite element method based on hierarchical B-splines for interface problems of complex geometry. *Computer Methods in Applied Mechanics and Engineering*, 200:3358–3380, 2011.
- [75] A. Schwarz, J. Schröder, and G. Starke. Least-Squares Mixed Finite Elements for Small Strain Elasto-Viscoplasticity. *International Journal for Numerical Methods in Engineering*, 77:1351–1370, 2009.
- [76] M. A. Scott. *T-splines as a Design-Through-Analysis Technology*. PhD thesis, The University of Texas at Austin, 2011.
- [77] M. A. Scott, M. J. Borden, C. V. Verhoosel, T. W. Sederberg, and T. J. R. Hughes. Isogeometric finite element data structures based on Bézier extraction of T-splines. *International Journal for Numerical Methods in Engineering*, 88:126–156, 2011.
- [78] J. C. Simo and F. Armero. Geometrically non-linear enhanced strain mixed methods and the method of incompatible modes. *International Journal for Numerical Methods in Engineering*, 33:1413–1449, 1992.
- [79] J. C. Simo and T. J. R. Hughes. On the variational foundations of assumed strain methods. *Journal of Applied Mechanics*, 53:51–54, 1986.
- [80] J. C. Simo and T. J. R. Hughes. *Computational Inelasticity*, volume 7 of *Interdisciplinary Applied Mathematics*. Springer, Berlin, Germany, 1998.

- [81] J. C. Simo and M. S. Rifai. A class of mixed assumed strain methods and the method of incompatible modes. *International Journal for Numerical Methods in Engineering*, 29:1595–1638, 1990.
- [82] J. C. Simo, R. L. Taylor, and K. S. Pister. Variational and Projection Methods for the Volume Constraint in Finite Deformation Elastoplasticity. *Computer Methods in Applied Mechanics and Engineering*, 51:177–208, 1985.
- [83] G. D. Smith. *Numerical Solutions of Partial Differential Equations, Finite Difference Methods*. Oxford University Press, Great Britain, 2004.
- [84] G. Starke. An Adaptive Least-Squares Mixed Finite Element Method for Elasto-Plasticity. *SIAM Journal on Numerical Analysis*, 45:371–388, 2007.
- [85] G. Starke, A Schwarz, and J. Schröder. Analysis of a Modified First-Order Least Squares Method for Linear Elasticity with Improved Momentum Balance. *SIAM Journal on Numerical Analysis*, 49:1006–1022, 2011.
- [86] Santiago Alves Tavares. *Generation of multivariate Hermite interpolating polynomials*. Chapman and Hall/CRC, 2006.
- [87] R. L. Taylor. Isogeometric Analysis of Nearly Incompressible Solids. *International Journal for Numerical Methods in Engineering*, 87:273–288, 2011.
- [88] J. W. Thomas. *Numerical Partial Differential Equations, Finite Difference Methods*. Springer, 1995.
- [89] H. K. Versteeg and W. Malalasekara. *An Introduction to Computational Fluid Dynamics, The Finite Volume Method*. Prentice Hall, Glasgow, 2007.
- [90] A.-V. Vuong, C. Giannelli, B. Jüttler, and B. Simeon. A Hierarchical Approach to Adaptive Local Refinement in Isogeometric Analysis. *Computer Methods in Applied Mechanics and Engineering*, 200:3554–3567, 2011.
- [91] Sheng-Tao Yu, Bo-Nan Jiang, Nan-Suey Liu, and Jie Wu. The least-squares finite element method for low-mach-number compressible viscous flows. *International Journal for Numerical Methods in Engineering*, 38:3591–3610, 1995.
- [92] O. C. Zienkiewicz and R. L. Taylor. *The Finite Element Method for Solid and Structural Mechanics*. Elsevier Butterworth and Heinemann, Oxford, England, sixth edition, 2005.